transactions of the ASME

Published Quarterly by
The American Society of
Mechanical Engineers

Volume 92 • Series C • Number 4

NOVEMBER 1970

journal of heat transfer

EDITORIAL OFFICES are at ASME Headquarters, United Engineering Center, 345 East 47th Street, New York, N. Y. 10017. Cable address, "Mechaneer," New York.
PUBLISHED QUARTERLY at 20th and Northampton Streets, Easton, Pa. 18042. Second-class postage paid at Easton.
CHANGES OF ADDRESS must be received at Society headquarters seven weeks before they are to be effective. Please send old label and new address.
PRICES: to members, $2.25 a copy, $7.50 annually; to nonmembers, $4.50 a copy, $15.00 annually.
Add 75 cents for postage to countries outside the U. S. and Canada.

INDEXED by the Engineering Index, Inc.

C. A. BANKSTON
Staff Member,
Los Alamos Scientific Laboratory,
Los Alamos, N. M.
Assoc. Mem. ASME

The Transition From Turbulent to Laminar Gas Flow in a Heated Pipe[1]

Experimental results are reported on the heat transfer and fluid friction of heated hydrogen and helium gas flows undergoing transition from turbulent to laminar flow in a circular tube. The entering Reynolds numbers range from 2350 to 12,500 and the nondimensional heat-flux parameter ranges from 0.0021 to 0.0061. Local heat-transfer coefficients and friction factors are obtained, and the flow transition, which is evident in these results, is verified at small heat fluxes by measuring directly the turbulence intensity at the center line with a hot-wire anemometer. At large heat fluxes, laminarization is found to occur at local bulk Reynolds numbers well in excess of the minimum number for fully turbulent adiabatic flow, and the resulting heat-transfer coefficients are much lower than those associated with fully turbulent flow at the same Reynolds number. The relation between laminarization in heated tubes and in severely accelerated external boundary layers is investigated and some similarities are noted. The acceleration and pressure-gradient parameters used to predict boundary-layer laminarization are modified for tube flow and used to correlate the initiation and completion of laminarization in the heated tube.

Introduction

A TURBULENT boundary layer subjected to a strong favorable pressure gradient may revert to a laminar state. This process, known as "laminarization" or "reverse transition" is not yet fully explained, but the conditions under which it is likely to occur have been established [1–5].[2] It will occur, for example, when the acceleration parameter K exceeds a certain value for a sufficient distance along the layer. The parameters used to define incipient laminarization and their critical values vary, but there is general agreement that strong increases in free-stream velocity lead to laminarization and to an attendant reduction in heat transfer. The event appears to be substantially independent of the boundary-layer Reynolds number.

A heated turbulent gas flow in a tube[3] may also revert to laminar flow, but there is an additional mechanism—not present in boundary layers—which may be responsible for the transition. The viscosity of gases increases with temperature, and hence the turbulence eddies are subjected to increasing viscous damping as they move through the tube. Thus, any turbulent gas flow should eventually revert to laminar if the heating were continued over a sufficient length of conduit. If the heat flux is very small, its main effect is to increase the viscosity and thereby to decrease the Reynolds number so that the transition should start at about the same Reynolds number at which it begins in an unheated tube when the flow is decreased. The minimum Reynolds number at which fully turbulent, unheated pipe flow can be maintained is usually about 3000 [5], and for small heat fluxes the transition does begin when the Reynolds number, based on bulk fluid conditions, reaches approximately this value.

When the heat flux is large enough to cause significant distortions of the normal fully developed velocity profile, the transition may begin at considerably higher bulk Reynolds numbers. The tendency of strongly heated gas flow to laminarize prematurely has been noted previously [6, 7]. Certain aspects of the premature transition of heated gas flows seem to resemble strongly the laminarization of accelerated boundary layers. In both cases, an acceleration of the fluid is accompanied by an apparent thickening of the viscous sublayer and by a flattening of the velocity profile outside the sublayer relative to the law of the wall. Thus, the combined effects of fluid acceleration and increasing viscosity in heated flows may have the same consequences as acceleration of external flows. In fact, one finds that the parameters used to define incipient laminarization of boundary layers may be modified for internal flows with little change in their critical values.

---

[1] Work performed under the auspices of the U. S. Atomic Energy Commission. Part of the material in this paper is based on a D.Sc. dissertation submitted in 1965 to the Department of Mechanical Engineering, University of New Mexico.

[2] Numbers in brackets designate References at end of paper.

[3] Unless specified differently, the heat flux at the wall of the tube will be assumed to be independent of x.

Contributed by the Heat Transfer Division of THE AMERICAN SOCIETY OF MECHANICAL ENGINEERS and presented at the ASME-AIChE Heat Transfer Conference, Minneapolis, Minn., August 3–6, 1969. Manuscript received at ASME Headquarters, May 16, 1969. Paper No. 69-HT-54.

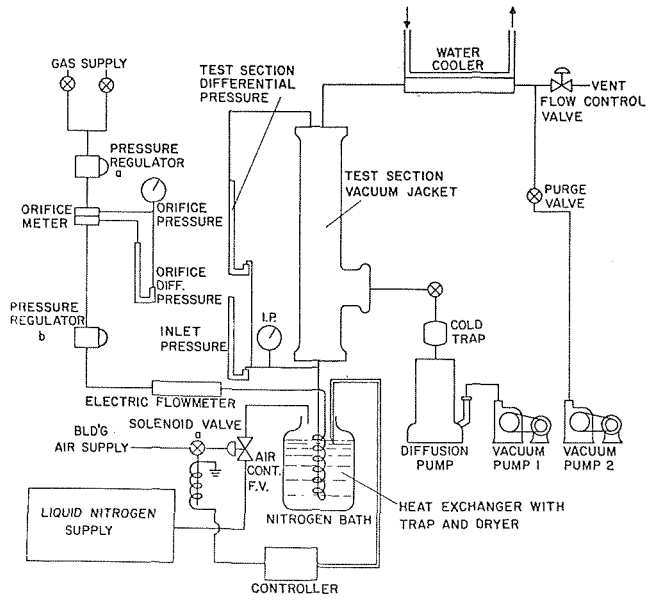

Fig. 1 General arrangement of the experimental apparatus

This paper reports the results of an experimental investigation in which heat transfer and fluid friction were measured in hydrogen and helium gas flows undergoing the transition from turbulent to laminar flow in long, slender tubes. Results for transitions which occur at low heating rates in a normal manner are included as well as for those which occur at bulk Reynolds numbers well in excess of 3000. Local Nusselt numbers and friction factors were obtained, and a series of measurements of center-line turbulence intensities was made to verify laminarization. Although the results are useful in nuclear rocket design and could have other heat-transfer applications, their greatest value may lie in helping to understand the mechanism of the reverse transition phenomena.

Experimental Investigation

The experimental investigation was designed to produce special results applicable to nuclear rocket systems. Therefore, the tubes had a greater length-to-diameter ratio than usually used in heat-transfer studies, and the experiments were conducted with hydrogen as the primary test gas. Both features have some advantages in studying the reverse transition phenomena. The longer tubes permit the completion of the transition process and the verification of the stability of the resulting laminar flow. Also, it is easier to comply with accuracy considerations for convective heat-transfer experiments which require that the ratio of convection to total heat transfer be maximum. For fixed heat losses and flow conditions this may obviously be achieved best by maximizing the thermal conductivity of the gas. Thus, hydrogen and helium are logical choices from an accuracy viewpoint, and both exhibit well-behaved and reasonably well-known property variations over a broad temperature range.

The experimental apparatus as well as the procedures for its calibration and operation and the data-processing procedures have been described in detail elsewhere [8]; they are summarized below for completeness.

Apparatus. The general arrangement of the apparatus is shown in Fig. 1. High-pressure hydrogen was supplied to the liquid-nitrogen heat exchanger through two pressure-regulating valves and two independent flowmeters. The heat exchanger consisted of a length of copper tubing and a series of flow-reversing traps and filters immersed in a dewar of liquid nitrogen whose level was maintained by a controller. This arrangement supplied dry hydrogen at a temperature of 135 deg R to the inlet of the electrically heated tube. The effluent gas was cooled in a gas-to-water heat exchanger before being discharged through the flow-controlling needle valve. The jacket surrounding the test section was maintained at a pressure of less than 10^{-3} torr, and a separate vacuum pump was provided to purge the system and reactivate the filters when the system was not in use.

The test sections were made from $\frac{3}{16}$-in-OD by 0.035-in-thick commercial tubing, of an 80:20 percent nickel-chromium alloy. The inside diameters of the tubes were determined from samples

Nomenclature

A = cross-sectional area of tube wall
A_{cs} = cross-sectional area of tube, $\pi D^2/4$
C = electrical parameter, $\int \frac{\rho I^2}{A}\, dx/EI$
c_p = specific heat at constant pressure
D = diameter
E = electrical potential
f = friction factor, $-8\tau_w/\rho_b U_b^2$
G = mass flow velocity, $\dot{m}/A_{cs}$
H = enthalpy
HB = heat-balance parameter, $(P - Q - Q_L)/P$
h = convective heat-transfer coefficient, $q_w''/(T_w - T_b)$
I = electrical current
K = acceleration parameter, $(\nu/U_\infty^2) \times dU_\infty/dx$
K' = modified acceleration parameter for tube flow, $(\nu_b/U_b^2)dU_b/dx$
k = thermal conductivity
L = heated length of tube
$\dot{m}$ = mass flow rate
Nu = Nusselt number, hD/k
n = exponent for temperature dependence of viscosity, i.e., $\mu = \mu_0(T/T_0)^n$
P = power input, EI
Pr = Prandtl number, $\mu c_p/k$
p = pressure
Q = convective heat transfer, $\dot{m}[H(L) - H(0)]$
Q_L = total heat loss from outside of tube
q_i^+ = wall heat-flux parameter, $q_w''/(Gc_{p,i}T_i)$, $q^+ = q_w''/(Gc_{p,b}T_b)$
q_w'' = heat flux from wall to gas
R = tube radius
Re = Reynolds number, $4\dot{m}/(\pi D\mu)$
r = radial coordinate
St = Stanton number, h/Gc_p
T = absolute temperature
U, u = gas velocity in axial direction
u' = fluctuating component of velocity in axial direction
U_τ = shear velocity, $\sqrt{\tau/\rho}$
x = axial coordinate, measured from start of heating
x^+ = axial distance parameter, $(2x/D)/(\mathrm{RePr})$
x_h = axial coordinate, measured from tube entrance
y = transverse coordinate
α = shear-stress gradient, $\partial\tau/\partial y$
Δ_p = pressure-gradient parameter, $(\nu/\rho U_\tau^3)dp/dx$
Δ_τ = shear-gradient parameter, $\nu\alpha/\rho U_\tau^3$
δT = bulk temperature adjustment, $T(L)_{\text{measured}} - T(L)_{\text{calculated}}$
η = ratio of heat convected to heat generated, Q/P
μ = viscosity
ν = kinematic viscosity, μ/ρ
ρ = density
τ = shear stress

Subscripts

b = evaluated at bulk temperature
i = inlet
l = laminar
t = turbulent
w = evaluated at wall
x = evaluated at local conditions
∞ = evaluated at free-stream conditions

Omission of a subscript implies the quantity is evaluated at the bulk conditions at x.

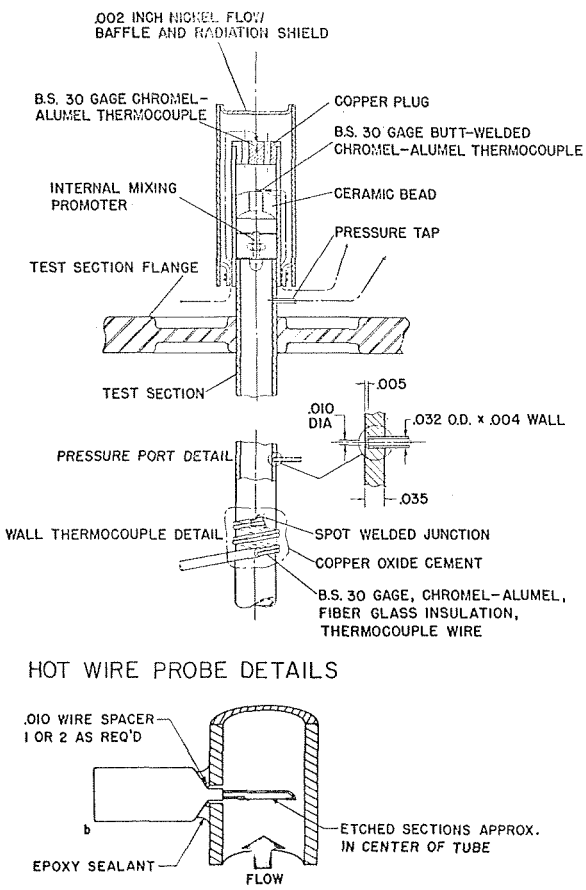

Fig. 2 Details of the test section instrumentation

cut from each end of the original tubing. The tubes were gold-plated to reduce radiation losses and to provide a stable surface; aluminum radiation shields were used in some of the tests. The tube entrance was cut square and sharp to produce a definite and reproducible entrance condition, and a 4-in-long unheated section was provided at the end by brazing the tube into a heavy copper sleeve.

Details of the tube's instrumentation are shown in Fig. 2. The exit temperature was measured by a chromel-alumel thermocouple which was brazed into a perforated copper plug attached to the end of the tube by a ceramic sleeve. A flow-reversing baffle forced the gas to flow back over both the sleeve and the exit flange to further reduce the heat exchange between the end of the tube and the guard heated exhaust chamber. Fourteen BS-30 gage chromel-alumel thermocouples were spot-welded to the tube at 0.0625, 1.25, 2.5, 5.0, 10.0, 15.0, 20.0, 25.0, 30.0, 35.0, 40.0, 45.0, 49.0, and 50.0 in. from the upstream electrode. The thermocouple leads were wrapped around the tube and secured with copper oxide cement. Piezometer holes of 0.010-in. dia were electric-discharge machined through the wall and connected to manometers through 0.032-in-OD by 0.004-in-thick Inconel tubing. The pressure ports were located at -0.1, 12.6, 25.6, and 50.1 in. from the upstream electrode.

The hot-wire probes shown in Fig. 2 were installed at four locations, 0.5, 12.5, 25.0, and 51 in. from the start of heating, in a tube operated especially to obtain turbulence-intensity data. They were operated by a single constant-current anemometer through a switching arrangement.

Procedures. Each test section, or tube, was individually calibrated by determining the local resistivity of the tube wall and the local effective heat-exchange coefficient between the outer wall of the tube and the environment over as much of the operating temperature range as the apparatus could tolerate without gas flow. The calibration range for tube resistance was from 135 to 1260 deg R, whereas the calibration range for heat-exchange coefficients was from 450 to 1450 deg R. The resistivity and heat-exchange coefficients were extrapolated to temperatures beyond these ranges, but wall temperatures for data reported in this paper ranged only from 162 to 1472 deg R. The thermocouples used for inlet gas temperature measurements were individually calibrated at the saturation temperature of liquid nitrogen ($\sim$135 deg R at 580 mm Hg). A continuous calibration from 135 to 1410 deg R was performed for several samples taken from the spool of wire from which the wall thermocouples and exit-gas temperature thermocouples were made using a certified platinum resistance thermometer and a certified platinum/platinum-10-percent-rhodium thermocouple as standards. A uniformity check of the installed thermocouples at 135 and 533 deg R detected only negligible deviations. Electrical instruments and flowmeters were calibrated before, after, and, in many cases, during the investigation.

The hot-wire probes were individually calibrated in air prior to their installation, using a specially designed wind tunnel, and in helium and hydrogen after installation in the tube. All calibrations were performed near ambient temperature. Although generally accepted heat-transfer laws and detailed gas-property information were used to correlate the calibration results, at the very low temperatures encountered in the experiments these correlations were not very satisfactory. A procedure was therefore devised for calculating the hot-wire sensitivities from the estimated velocity profiles in the experiments. Although the two procedures gave quite different results for average velocities, the relative intensity of turbulence usually agreed within 15 percent. The failure of accepted hot-wire calibration and processing techniques at low temperature is not fully understood, but surface effects are suspected. The uncertainty in the accommodation coefficient is large under these conditions, and the corrections for free molecular effects were fairly large for helium and hydrogen.

Local heat-transfer coefficients and wall shear stresses were calculated from measured outside wall temperatures in a computer program where radial and axial conduction (including the effects of temperature-dependent wall thermal conductivity, electrical resistivity, and diameter) and radiation from the outer surface of the tube were taken into account. Radiation from the inner wall was neglected because the temperature was very low near the entrance and because temperature gradients were small near the exit. A nondimensional total enthalpy distribution was calculated by dividing the integral of the convective heat flow obtained from a local heat balance from 0 to x by its integral over the entire heated length. This nondimensional distribution was multiplied by the total enthalpy rise of the gas, as determined by the inlet and exit temperature measurements, to obtain an adjusted enthalpy distribution from which temperatures could be calculated. This procedure was adopted because calculations showed it reduced the uncertainty in the measured heat-transfer coefficient. The adjustment was generally equivalent to less than ± 2 percent of the convective heat transfer; runs for which it exceeded ± 5 percent were excluded. The local heat-transfer coefficient was computed from the adjusted total gas temperature and from the temperature of the inner wall. Gas properties were also computed at the total bulk gas temperature since the greatest Mach number was only 0.12.

The apparent wall shear stresses and friction factors were calculated from a one-dimensional analysis of the flow. The derivatives of the impulse function, $p + \rho U^2$, were obtained by fitting a second-order polynomial in log (x_h) to the five known values of log $(p + \rho U^2)$ at the pressure-tap locations by the method of least squares. This procedure permitted calculation of local friction factors at the locations of the thermocouples, but introduced some bias by forcing a particular function to fit only five pressure measurements.

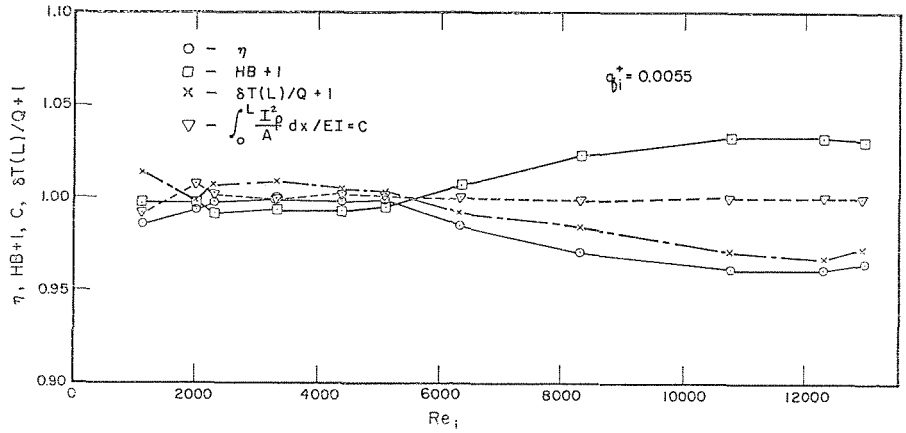

Fig. 3 Performance parameters indicating the overall accuracy of data for a typical heating rate

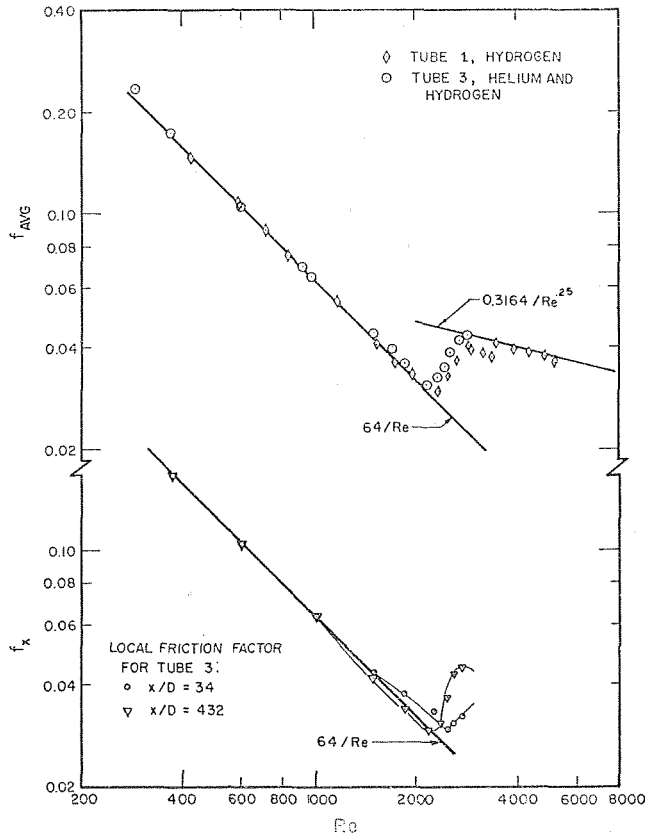

Fig. 4 Average adiabatic friction factors for Tubes 1 and 3 and local adiabatic friction factors for Tube 3

The properties of normal hydrogen were taken from reference [9]. The thermal conductivity and viscosity data for helium were from reference [10], and the specific heat of helium was taken to be 1.248 Btu/lb-deg R.

Experimental Results

Scope and Accuracy. The results presented in this paper were drawn from data obtained in the investigation described in references [7, 8]. Only the data from runs in which a transition from turbulent to laminar flow occurs or from runs which illustrate the limiting behavior in fully laminar or fully turbulent flows have been included. This includes results from 77 heated hydrogen runs and five heated helium runs, as well as some results for adiabatic flows and some laminar hydrogen flows. The range of transition data included is summarized in Table 1.

Table 1 Range of variables for hydrogen transition flow results

q_i^+	$T_b(L)$	Number of runs	Entering Reynolds number maximum	minimum
0.0021	530	11	9419	2393
0.0025	600	9	9714	2762
0.0031	700	14	9201	2440
0.0037	800	10	8980	2708
0.0043	900	10	8942	2392
0.0049	1000	7	9114	2668
0.0055	1100	9	12950	2467
0.0061	1200	7	13412	3457
		77	13412	2392

The accuracy and consistency of the overall measurements is illustrated in Fig. 3, in which the ratio of convection to heat generation, η, the heat balance, HB, the bulk temperature adjustment factor, $\delta T/T_L - T_i$, and parameter C (which represents the ratio of generated heat as computed by integrating $I^2\rho dx/A$ to the power computed from EI) are plotted as functions of the entering Reynolds number for a typical series of runs with $q_i^+ = 0.0055$.

Adiabatic Flow Results. The friction factors in unheated flow were measured for each tube used in the investigation to establish the character of the adiabatic transition and to verify that the entry configuration did give reproducible transitions. Fig. 4 shows the average friction factors obtained for Tubes 1 and 3 in the upper part of the figure and the local friction factors for Tube 3 in the lower part. The average friction factors are in good agreement with the Hagen-Poiseuille law for Re < 2000 and with the Blasius relation for Re > 3000. The transition appears to begin at a Reynolds number between 2200 and 2350 for both tubes, and is essentially complete at Re > 2800. The local friction factors shown in the lower part of the figure indicate that the transition is rather gradual near the entry and more abrupt near the tube exit. At a Reynolds number of 2461, for example, the friction factor near the entrance is about 1.25 times the laminar prediction and the ratio increases to about 1.5 at 450 diameters, but the result of the Blasius relation at Re $= 2461$ is 1.7 times the laminar value. This indicates that a very long tube would be required to establish a "fully" turbulent flow when the Reynolds number is in the transition region. The friction factors were obtained both with increasing and decreasing flow rates, without any evidence of "hysteresis" in the results.

Because the friction factors cited above were obtained for Tubes 1 and 3, which did not contain any hot-wire anemometer probes, turbulence in these tubes could not be observed directly. However, Tube 2 was instrumented with such probes, and turbu-

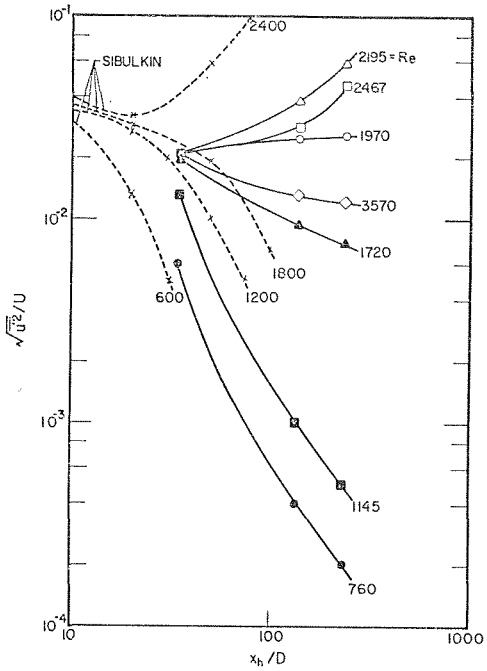

Fig. 5 Axial variation of turbulence intensities for adiabatic flow in Tube 2

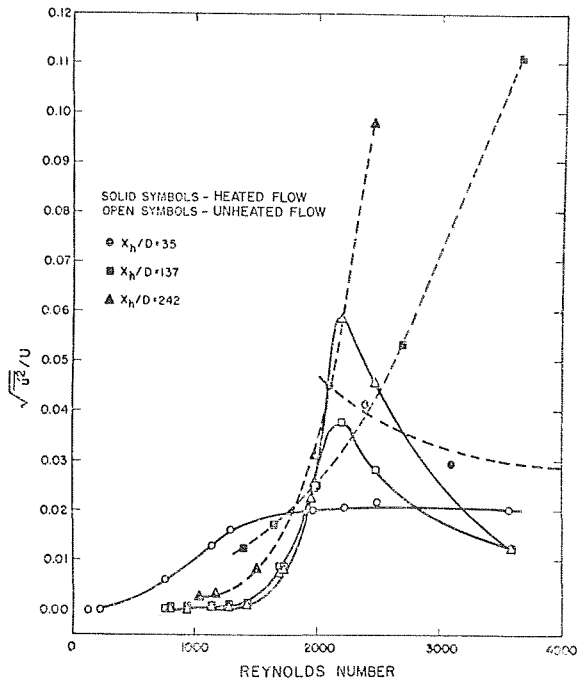

Fig. 7 Comparison of turbulence intensities in heated and adiabatic flow in Tube 2

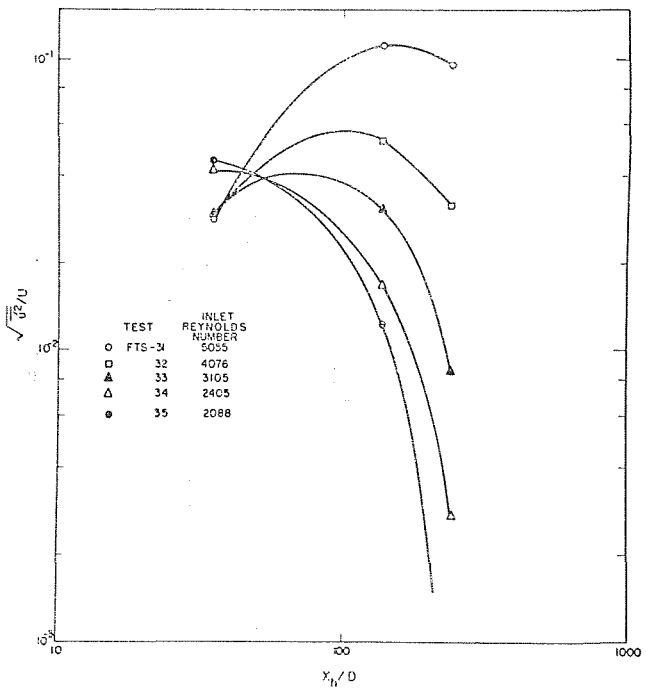

Fig. 6 Axial variation of turbulence intensities for heated flow in Tube 2

lence measurements were made. The results for adiabatic flow are shown in Fig. 5. The turbulence intensity near the entrance is seen to be relatively constant for Re > 1700, but the intensity downstream decays for Re > 1900, grows for 1900 < Re < 2800, and remains fairly constant for higher Reynolds numbers. The results of Sibulkin [11], which are included in the figure for comparison, were obtained from hot-wire measurements along the axis of a pipe downstream from a sudden enlargement. In the present experiments, the source of turbulence is primarily the separated-flow zone caused by the sharply cut entrance. Still, the trends are similar and the growth and decay rates are quite close at corresponding Reynolds numbers. Because the intensities shown in Fig. 5 were obtained with an rms voltmeter having a long averaging time, the effect of intermittency is included in the intensity data. The oscilloscope traces, however, did display pronounced intermittency for Reynolds numbers in the transition range. No intermittency was observed at Reynolds numbers greater than 3000.

Local adiabatic friction factors for the tube containing hot-wire probes (Tube 2) were in good agreement with the results from the clean tubes at very low Reynolds numbers and for fully turbulent flows, but were in marked disagreement at high laminar Reynolds numbers and in the transition region. Because these deviations were larger than could be ascribed to normal probe interference effects, they were attributed to interactions between the turbulent (or sometimes periodic) wake of the hot-wire supports and the mean flow. These effects could be eliminated either with probes small enough to produce only laminar wakes for all flow conditions or with probes that could be readily withdrawn from the flow. Because neither alternative was available at the time of the investigation, the usefulness of the tube with the hot-wire probes had to be restricted to verifying the transition from turbulent to laminar flow. Although some of the turbulence detected by downstream probes probably originated at upstream probes, this does not preclude their use to distinguish flows in which the turbulence is decaying from those in which the turbulence is stable or growing.

Taken together, the observations cited above of adiabatic laminar-to-turbulent transition seem to be in excellent accord, qualitatively and quantitatively, with the more complete and detailed transitions studies of Rotta [12]. The values obtained for the upper and lower transition Reynolds numbers are also in good agreement with the recent results of Head and Patel [5].

Heated Helium Flow. Results obtained during intensity measurements in heated helium flows are introduced at this point to present some direct evidence of turbulent-to-laminar transition. Heat-transfer and friction data were obtained at the same time, but, because of the probe interference effects just discussed, the results are not considered as reliable as those obtained with hydrogen in clean tubes. The turbulence intensities for a series of

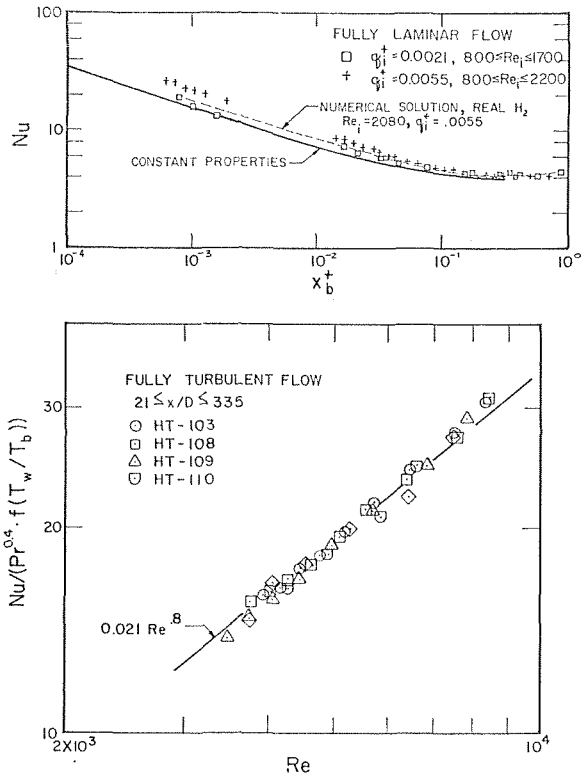

Fig. 8 Comparison of heat-transfer results for fully laminar and fully turbulent flow with theory and accepted correlations

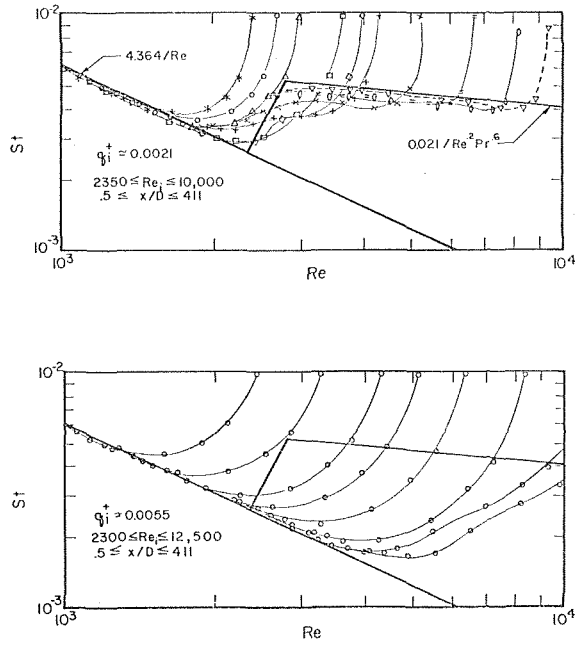

Fig. 9 Heat-transfer results for transition flows with small and large heating rates. Light lines connect data points for a single run; x/D increases from right to left

five runs with entering Reynolds numbers ranging from 2088 to 5055 and an exit temperature of 880 deg R are plotted in Fig. 6 as a function of the distance from the tube entrance x_h/D. At the higher Reynolds numbers the intensities start to grow initially, but in all cases follow a reversed trend further downstream. The runs with entering Reynolds numbers of 3100 or less decay almost from the start, and by the end of the tube they have decreased to levels that can only be classified as laminar.

The same results are presented differently in Fig. 7 in which the turbulence intensities for heated and unheated flow are compared. For Re > 2000 the intensities in heated flow are considerably higher than in unheated flow. This discrepancy may be due in part to difficulties in calibrating the probes for low temperatures, but higher apparent velocity fluctuations are expected in heated flow due to temperature fluctuations.[4] The significant conclusion to be drawn from this figure is the fact that downstream turbulence intensities for heated flows approach those for unheated flows at bulk Reynolds numbers below 2000 despite different upstream histories. This is regarded as evidence of turbulent flow reverting to laminar flow. Although hot-wire measurements were not made in the strongly heated hydrogen flows in which premature laminarization was indicated by the heat-transfer results, the results cited above certainly support the view that the character of the flow is laminar under such conditions.

Heated Hydrogen Flow. Results which best illustrate the heat-transfer and friction characteristics of gas flow undergoing turbulent-to-laminar transition are discussed in this section. Therefore, only data from Tube 3, which contained no hot-wire probes, and from hydrogen flows, for which the results are more reliable, will be discussed.

Nusselt numbers obtained for fully laminar and fully turbulent flows are shown in Fig. 8 and are included here to indicate the reliability of the results. In the upper part of the figure, experimental results for completely laminar flow at two heat-flux levels, $q_i^+ = 0.0021$ and 0.0055, are compared with theoretical results. The solid line represents the eigenvalue solution of reference [13] with 40 eigenvalues obtained by extrapolating with the method of Kays [14]. The dashed curve represents the results of a numerical solution of the boundary-layer equations by the methods of reference [15] which includes the effects of variable hydrogen properties, partially developed velocity profiles at the start of heating, and the experimental variation of heat flux with distance. For $x^+ > 10^{-2}$ the agreement between the numerical solution and the experimental results is better than ±5 percent. At smaller values of x^+ the experimental results for the lower heating rate agree well with the constant-property solution, but the Nusselt numbers for the higher heating rate are 20 percent higher than the numerical results. The poorer agreement at small x^+ and large q_i^+ may be due to several factors: (1) the boundary-layer approximations are not strictly valid when $x^+ \lesssim 10^{-3}$ [16], (2) the calculation assumes a uniform entering-velocity profile, whereas the real flow must separate at the sharp entrance edge and form a vena contracta, and (3) the experimental results for $x^+ < 10^{-2}$ are all from data at the first thermocouple ($x/D = 0.52$) where the approximations used in processing the data may be less accurate. Buoyancy effects were made negligible in the experiments by operating at low pressures.

The results for several fully turbulent flow runs are plotted in the lower part of Fig. 8. The effects of property variations were reduced by dividing the experimental Nusselt numbers by the ratio of the variable-property to the constant-property Nusselt number obtained for higher Reynolds numbers by numerical methods [17]. This ratio approaches $(T_w/T_b)^{-0.3}$ for $T_w/T_b \to 1$, which was shown to be appropriate for moderate temperature ratios [18]. Although the range of the results for fully turbulent flow is quite limited, they do agree with the modified Dittus-Boelter correlation for constant properties when plotted as in Fig. 8.

Transitional results for $q_i^+ = 0.0021$ and 0.0055 are presented in Fig. 9 as Stanton numbers versus Reynolds numbers. This common method of representing average heat-transfer results has the advantage of showing the response of the wall tempera-

[4] In subsequent experiments, the effects of temperature and velocity fluctuations were separated by operating the wire at several overheat ratios, but in this series of runs, only one overheat was used.

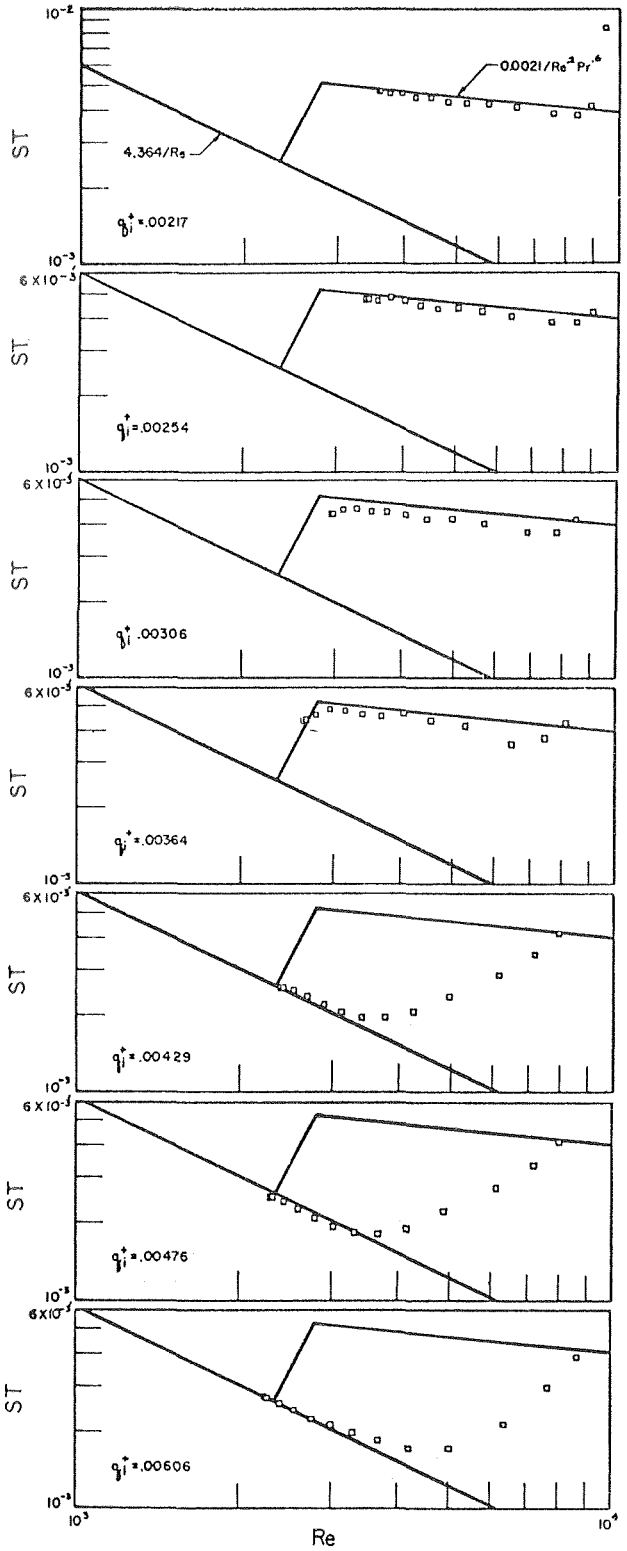

Fig. 10 Variation of Stanton number with heating rate for nearly constant entering Reynolds number; x/D increases from right to left, heat flux increases from top to bottom

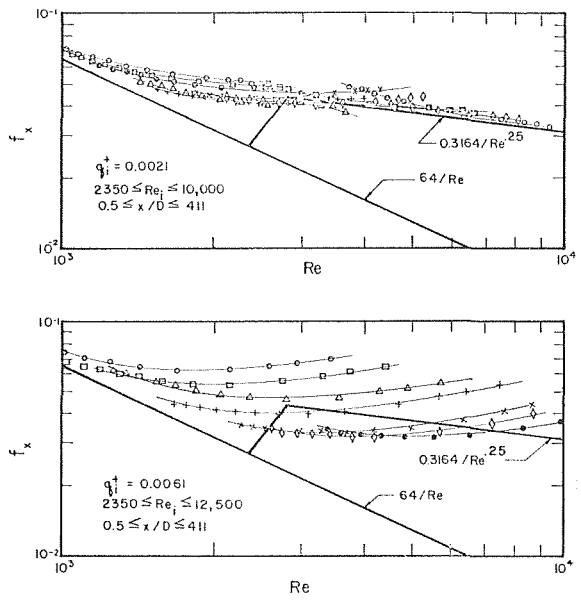

Fig. 11 Friction factor for transition flow with small and large heating rates. Light lines connect data points for a single run. x/D increases from right to left

ture to changes in Reynolds number directly [19], but, in applying the method to local results, one must remember that the local Reynolds number is a function of x/D. Thus, in Fig. 9, the points connected by light lines have the same entering Reynolds number, and x/D increases from right to left. The solid lines plotted in the figure represent the fully developed flow, constant-properties limits for both turbulent and laminar flows, and values along a line joining the two at Reynolds numbers corresponding to the adiabatic transition.

The smaller heat flux yields results which correspond to what could be called a normal transition. In fact, for several entering Reynolds numbers, a turbulent entry region may be discerned followed by a region of fully developed turbulent flow, a transition region, and finally a region of fully developed laminar flow. The transition occurs in about the same Re range as in adiabatic flow. For the highest Reynolds numbers shown, the flow is fully turbulent throughout.

The results for $q_i^+ = 0.0055$, shown in the lower part of Fig. 9, exhibit a very different transition to laminar flow. None of the runs considered in this figure have heat-transfer characteristics of a fully turbulent flow. Even the runs with entering Reynolds numbers in excess of 12,000 show a continuous approach to the heat-transfer characteristic of laminar flow. Furthermore, for the high entering Reynolds numbers, the transition appears to be essentially complete when the local Reynolds number is still nearly 4000. Although the results do approach the flow characteristics of fully developed laminar flow smoothly, the approach is much steeper than that of a hypothetical laminar flow with the same entering Reynolds number. Thus, the entry region must be turbulent.

In Fig. 10, which depicts a series of runs with about the same entering Reynolds number as in Fig. 9, but with increasing values of q_i^+, we see that the change from a fully turbulent flow to a laminarizing flow occurs abruptly when the heat-flux parameter exceeds 0.004. Although the value of the heat-flux parameter at which the change occurs varies with entering Re_i the transition remains rather abrupt, which suggests that a "critical" value for some parameter may exist that will determine whether a flow remains turbulent or laminarizes.

The variation of the local friction factor in the transition region is quite different from that of the Stanton number. Fig. 11 shows local friction factors for a small and a large q_i^+. For a given Re_i the transition appears to be quite gradual for either large or small values of q_i^+ although at the higher q_i^+ level f is more sensitive to Re_i. This behavior may be explained by noting that the friction factors for laminar flow are quite sensitive to property variations (T_w/T_b), but the friction factors for fully developed turbulent flow are not. Thus, as the flow begins to revert to laminar, the wall-to-bulk-temperature ratio increases

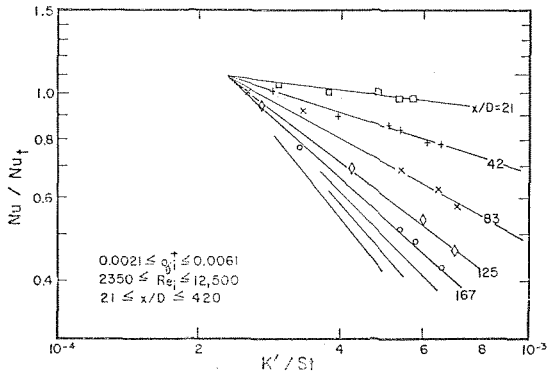

Fig. 12 Correlation of Nusselt number in terms of the modified acceleration parameter K′/St. The number of data points shown have been limited for clarity. Trends are shown by solid lines

due to the decrease in Stanton number and this results in an increased friction factor. The net result, at least for moderate heating rates, is the fact that the friction factor may be approximated by extending the Blasius relation down to the intersection with the laminar-flow relation in the manner of a hysteresis loop, but this should not be interpreted as a lag in the transition. It was shown in reference [8] that the transition friction factors could be correlated by either laminar or turbulent relations if suitable functions of the wall-to-bulk-temperature ratio are used. Note that the friction factors described here were calculated from the data on the assumption that the velocity profile (or at least the momentum coefficient β) is invariant; therefore they do not reflect the distribution of the wall shear stresses accurately when the flow is undergoing transition.

Discussion

Comparison With Boundary-Layer Flows. The results discussed in the preceding sections indicated a tendency for strongly heated gas flows to become laminar at bulk Reynolds numbers considerably in excess of those associated with adiabatic flow transition; because this premature laminarization is similar in some respects to phenomena observed in external boundary layers, we now consider how these transition phenomena may be related. In particular, we want to determine if the parameters that have been found useful in predicting laminarization of boundary layers may be used to correlate the present results.

In the external boundary layers the pressure-gradient term in the momentum equation may be regarded as a known quantity, imposed upon the boundary layer by the external flow field. The magnitude of this term determines the extent of deviation of the boundary-layer flow from equilibrium. For external flows in which the velocity is uniform in the direction normal to the boundary layer, the severity of the pressure gradient is quite conveniently expressed in terms of the acceleration of the free stream. The nondimensional form $K = \nu/U_\infty^2(dU_\infty/dx)$ is often used. The pressure gradient for a confined flow cannot be considered independent but must be just sufficient to overcome the retarding forces at the wall and to accelerate the entire flow to the velocities required by continuity. Consequently, a parameter similar to K but defined in terms of the average velocity of a confined flow will not have exactly the same significance it has for external flows. Still, it is a convenient parameter to calculate, and it is large when the heating is severe so that it may be useful in correlating transition results. We therefore define

$$K' = \frac{\nu_b}{U_b^2}\frac{dU_b}{dx} \tag{1}$$

and note that for constant-area flow of ideal gases with small changes in pressure

$$K' \cong \frac{1}{\mathrm{Re}}\left(\frac{1}{T_b}\frac{dT_b}{d(x/D)}\right) = \frac{4q^+}{\mathrm{Re}} = \frac{4q_i^+}{\mathrm{Re}}\left(\frac{T_i}{T_b}\right) \tag{2}$$

Nusselt numbers normalized according to the turbulent correlation of Fig. 8 are plotted in Fig. 12 against the acceleration parameter K' divided by the local Stanton number as suggested by the work of Moretti and Kays [3]. In this figure the values of K' were calculated from equation (1) by using the experimental bulk velocities. The number of data points in the figure has been limited for clarity, but the trends indicated by the solid lines are evident when the entire set of results is included. When the value of K'/St is less than $\sim 2 \times 10^{-4}$, the measured Nusselt number agrees reasonably well with the result for fully turbulent heat transfer. For larger values of K'/St, there is a systematic decrease in the Nusselt-number ratio which becomes progressively more severe as x/D increases. If 2×10^{-4} is taken as the largest value of K'/St for which the heat-transfer process can be considered fully turbulent, K' varies from about 8.0×10^{-7} to 1.14×10^{-6} over the range of variables included in the present investigation. This compares with values from about 2.0×10^{-6} to 3.5×10^{-6} reported by boundary-layer investigators

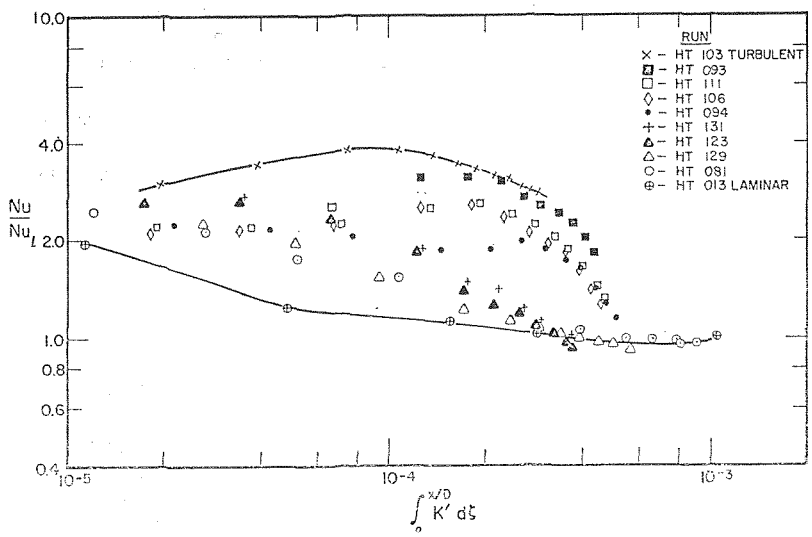

Fig. 13 Correlation of Nusselt number in terms of the integral of the acceleration parameter K′. Upper curve represents a fully turbulent run and lower curve a nearly fully laminar run

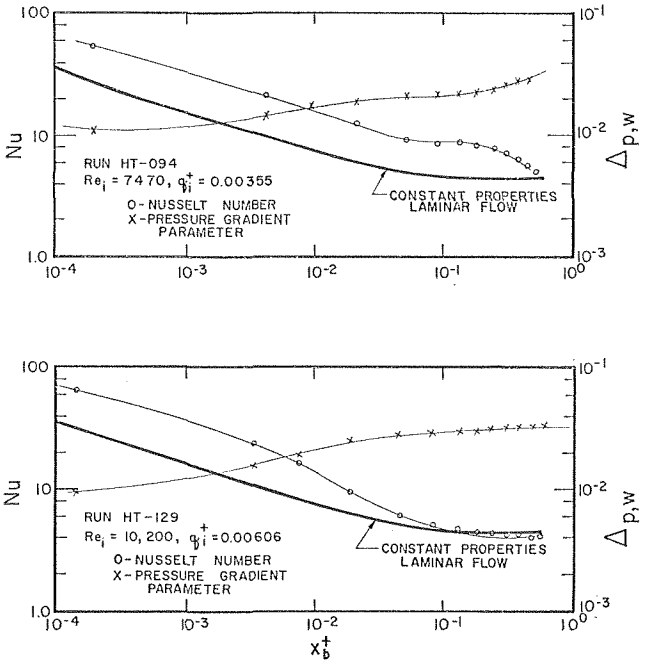

Fig. 14 Axial variation of the pressure-gradient parameter and Nusselt number for two transitional runs

[2–4], and with a value of 1.5×10^{-6} recently reported by Perkins and Coon [20] for internal flow.

Even if the previous evidence is accepted as providing a means of predicting when laminarization will occur, there is no indication of how long the process will take. If, indeed, the magnitude of K' is related to the onset of laminarization, the rate of decay of turbulence must also be related to K' so that the length required for the completion of laminarization should depend upon the initial intensity of turbulence and the magnitude of K'. Because the turbulence measurements reported earlier indicate that the initial turbulence does not vary greatly for $\mathrm{Re}_i > 2000$, the above hypothesis can be tested by plotting a normalized Nusselt number against the integral of K' as shown in Fig. 13. In this figure the ordinate is the local Nusselt number normalized by the constant-property solution for laminar flow shown in Fig. 8. The lowest set of points shown in this figure represents a run for which $\mathrm{Re}_i = 2400$ and $q_i{}^+ = 0.0021$ and could be considered to represent an almost fully laminar run while the uppermost set is for a fully turbulent run. Transition results fall between these two and approach the laminar limit, $\mathrm{Nu}/\mathrm{Nu}_l = 1$, as the integral increases. Although the rate of approach varies considerably, perhaps due to slight differences in initial conditions, laminarization is essentially complete when the integral of K' attains a value of about 5×10^{-4}. Using this value and equation (2), we can obtain a simple expression for the nondimensional distance required for laminarization

$$x_i{}^+ = \frac{(5 \times 10^{-4} n \mathrm{Re}_i + 1)^{1/n} - 1}{2 q_i{}^+ \mathrm{Re}_i \mathrm{Pr}_i} \tag{3}$$

where n is the exponent of the temperature-dependence of the viscosity, and the specific heat has been assumed constant.

In a recent study of reverse transition, Head and Patel [5] suggest that the shear stress in the wall region is the important parameter in initiating the reversion. They define a shear-stress-gradient parameter $\Delta_\tau = \nu\alpha/\rho U_\tau{}^3$ in terms of the shear velocity $U_\tau = \sqrt{\tau_w/\rho}$ and the slope of the shear-stress distribution near the wall, $\alpha = \partial\tau/\partial y$. Their results seem to indicate that a fully turbulent flow will begin to break down when $\Delta_\tau < -0.009$. They argue that this value should apply to pipe flow as well as to external flow and show that the critical value above, corresponding to a pipe Reynolds number of 3000, is where adiabatic turbulent flows start to break down.

Unfortunately, there is no way of obtaining the slope of the shear stress in developing flows unless detailed profiles are available. However, calculations using the methods of reference [15] do indicate a sharp decrease in α near the wall and a flattening of the velocity profile in the core under conditions which lead to laminarization.

In fully developed pipe flow, it can easily be shown that the pressure-gradient parameter, defined as $\Delta_p = (\nu/\rho U_\tau{}^3)\, dp/dx$, is just $2\Delta_\tau$. This simple relation does not hold for developing flows, but it does suggest that the pressure-gradient parameter might be useful in flows where Δ_τ cannot be determined. The parameter Δ_p can be evaluated directly from the experimental results, and, using the data-reduction equations of reference [8], it can be shown that

$$\Delta_p = -\frac{4\mu}{D} \frac{1}{\sqrt{\rho \tau_w}} \tag{4}$$

Both μ and ρ are functions of temperature and because the primary concern here is the wall region, both are evaluated at the temperature of the wall. This pressure-gradient parameter is designated $\Delta_{p,w}$ and its variation with axial location for two transitional runs is shown, along with the corresponding Nusselt-number variations, in Fig. 14. An obvious advantage of the pressure-gradient parameter over the acceleration parameter is its change from values associated with fully turbulent flow toward values characteristic of laminar flow as the distance from the start of heating increases. The acceleration parameter decreases with distance and can therefore only be used to distinguish those flows in which conditions near the entrance are severe enough to lead eventually to laminarization. Thus, for Run HT-094 shown in the upper part of the figure, the criterion $K'/\mathrm{St} > 2 \times 10^{-4}$ would allow prediction of laminarization somewhere, but by taking -0.02 as the critical value of $\Delta_{p,w}$ it would be possible to anticipate the rapid approach to laminar flow beginning at $x^+ \cong 0.2$. The lower part of Fig. 14 indicates that the same value would be appropriate for Run HT-129 which has a high heating rate and exhibits a more gradual transition beginning at about $x^+ = 10^{-2}$.

Fig. 15 was constructed to find a more sensitive indicator of incipient laminarization. The ordinate is the difference between the observed Nusselt number and the constant-properties solution for laminar flow divided by the difference between the correlation of Fig. 8 for turbulent flow and the laminar solution; the abscissa is $\Delta_{p,w}$. So long as the flow is essentially turbulent the derivative of this function should be relatively small, but, as the conditions leading to laminarization are approached, the derivative should decrease sharply. Unfortunately, in the entry region the sensitivity of the function is apparently too great for the precision of the experimental results and for the turbulent correlation so that a rather large negative slope is exhibited for small x/D even for fully turbulent flows. However, several runs do have a plateau followed by a rather sharp decrease which is evidently the onset of laminarization. The solid curves again represent almost fully laminar and fully turbulent flow situations. The number of runs plotted in the figure was limited for clarity. For the runs shown, and most of the others, it is possible to identify a decrease in slope in the range $0.014 < \Delta_{p,w} < 0.023$, but there does not seem to be a definite "critical" value. The adiabatic-transition result, i.e., $\Delta_p = 0.018$, does fall close to the center of this range.

Although the present results cannot offer strong support for the proposals of reference [5] they are in no way contradictory. Possibly, better agreement might be achieved if a direct indication of the shear distribution near the wall were available.

Correlation of Heat-Transfer and Friction Results. An empirical correlation for the entire set of results obtained in the investi-

gation upon which this paper is based was presented in reference [7]. Although this correlation, which relied upon a classification of the flow regimes, was useful in calculating the stability of parallel-channel heat exchangers and presumably would be useful for other design purposes, it did not help in understanding the transition phenomena.

Finally, it should be noted that an effort is underway to obtain a better understanding of the laminarization process by detailed numerical solutions of the boundary-layer equations under transition conditions using various models for the turbulent transport properties. Some results of this effort, relating to the experimental work presented here and by others [6, 20, 21], are presented in another paper [22]. It is hoped that the insight into the mechanism gained via this approach will correlate or explain transfer processes in laminarizing flows in a more meaningful way than is presently possible.

Conclusions

The study of turbulent-to-laminar-flow transition presented in this paper justifies the following conclusions:

1 The reversion of a fully turbulent flow to a laminar one as evidenced by the magnitude of the resulting transfer processes has been verified by direct observations of turbulence intensities for modest heat fluxes and Reynolds numbers.

2 The heat-transfer measurements indicate that transition may occur at local bulk Reynolds numbers well in excess of the lower limit of fully turbulent adiabatic pipe flow (i.e., Re > 2800); the resulting Stanton numbers are much smaller than those corresponding to turbulent flow at the same Reynolds number.

3 Many aspects of the reversion of turbulent pipe flow are similar to the phenomena of laminarization of turbulent boundary layers in severely accelerated external flows. In fact, the onset and completion of flow laminarization in a heated pipe can be correlated reasonably well by suitable modifications of the acceleration and pressure-gradient parameters used for boundary layers. The results presented here indicate that transition to laminar flow is likely to begin when

$$\Delta_{p,w} = (\nu_w/\rho_w U_\tau^3)dp/dx \lesssim -0.02$$

or when

$$K' = 4q^+/\mathrm{Re} \geq 2 \times 10^{-4}(0.021\ \mathrm{Re}^{-0.2}\mathrm{Pr}^{-0.6})$$

and will be essentially complete when

$$x_i^+ = \frac{(5 \times 10^{-4} n\ \mathrm{Re}_i + 1)^{1/n} - 1}{2q_i^+\ \mathrm{Re}_i\ \mathrm{Pr}_i}$$

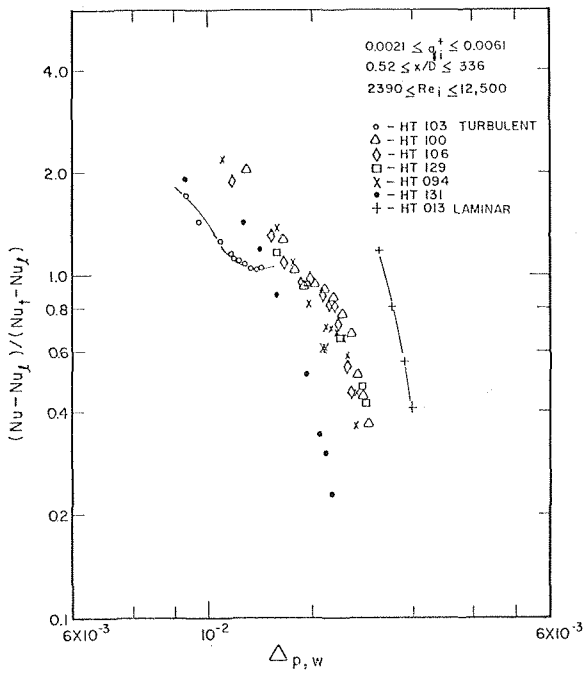

Fig. 15 Determination of the critical range of pressure-gradient parameters from transitional heat-transfer results

Acknowledgments

The author wishes to thank Dr. W. L. Sibbitt, LASL, and Professor V. J. Skoglund, University of New Mexico, for their encouragement and advice during the experimental phases of this work and Professor D. M. McEligot, University of Arizona, for many helpful discussions.

References

1 Launder, B. E., and Lockwood, F. C., "An Aspect of Heat Transfer in Accelerating Turbulent Boundary Layers," JOURNAL OF HEAT TRANSFER, TRANS. ASME, Series C, Vol. 91, No. 2, May 1969, pp. 229–234.

2 Launder, B. E., "Laminarization of the Turbulent Boundary Layer by Acceleration," Gas Turbine Lab. Report 77, M.I.T., Nov. 1964.

3 Morretti, P. M., and Kays, W. M., "Heat Transfer to a Turbulent Boundary Layer with Varying Free-Stream Velocity and Varying Surface Temperature—An Experimental Study," *International Journal of Heat and Mass Transfer*, Vol. 8, 1965, p. 1187.

4 Back, L. H., and Seban, R. A., "Flow and Heat Transfer in a Turbulent Boundary Layer with Large Acceleration Parameter," *Heat Transfer and Fluid Mechanics Institute*, Stanford University Press, 1967.

5 Patel, V. C., and Head, M. R., "Reversion of Turbulent to Laminar Flow," *Journal of Fluid Mechanics*, Vol. 34, Pt. 2, 1968, pp. 371–392.

6 Perkins, H. C., and Worsoe-Schmidt, P. M., "Turbulent Heat and Momentum Transfer for Gases in a Circular Tube at Wall-to-Bulk Temperature Ratios to Seven," *International Journal of Heat and Mass Transfer*, Vol. 8, 1965, pp. 1011–1031. Data tabulated in Tech. Report SU 247-7, Mech. Eng. Dept., Stanford University, Sept. 1964.

7 Bankston, C. A., Sibbitt, W. L., and Skoglund, V. J., "Stability of Gas Flow Distribution Among Parallel Heated Channels," AIAA 2nd Propulsion Joint Specialist Conference, AIAA Paper 66-589, 1966.

8 Bankston, C. A., "Fluid Friction, Heat Transfer, Turbulence and Interchannel Flow Stability in the Transition from Turbulent to Laminar Flow in Tubes," Sc.D. thesis, University of New Mexico, 1965.

9 Hilsenrath, J., et al., "Tables of Thermal Properties of Gases," NBS Circular 564, 1955.

10 Hilsenrath, J., and Touloukian, Y. S., "Viscosity, Thermal Conductivity and Prandtl Number for Air, O_2, N_2, NO, H_2, CO, CO_2, H_2O, He, and A," TRANS. ASME, Vol. 76, Aug. 1954, pp. 967–985.

11 Sibulkin, M., "Transition from Turbulent to Laminar Pipe Flow," *The Physics of Fluids*, Vol. 5, 1962, p. 280.

12 Rotta, J., "Experimentaller Beitrag zur Entstehung Turbulenter Stromung in Rohr," *Ingr-Arch.*, Vol. 24, 1956, p. 258.

13 Siegel, R., Sparrow, E. M., and Hallman, T. M., "Steady-Laminar Heat Transfer in a Circular Tube with Prescribed Wall Heat Flux," *Applied Science Research*, Vol. A7, 1958, pp. 386–391.

14 Kays, W. M., *Convective Heat and Mass Transfer*, McGraw-Hill, New York, 1966.

15 Bankston, C. A., and McEligot, D. M., "Turbulent and Laminar Heat Transfer to Gases with Varying Properties in the Entry Region of Circular Ducts," *International Journal of Heat and Mass Transfer*, Vol. 13, 1970, pp. 319–334.

16 Worsoe-Schmidt, P. M., and Leppert, G., "Heat Transfer and Friction for Laminar Flow of a Gas in a Circular Tube at High Heating Rate," *International Journal of Heat and Mass Transfer*, Vol. 8, 1965, pp. 1281–1301.

17 McEligot, D. M., Smith, S. B., and Bankston, C. A., "Quasi-Developed Turbulent Pipe Flow with Heat Transfer," JOURNAL OF HEAT TRANSFER, TRANS. ASME, Series C, Vol. 92, No. 4, Nov. 1970, pp. 641–650.

18 McEligot, D. M., "Internal Gas Flow Heat Transfer with Slight Property Variation," *Bull. Mech. Engng. Educ.*, Vol. 6, 1967, p. 251.

19 Jakob, M., *Heat Transfer*, Vol. 1, John Wiley and Sons, New York, N. Y., 1957.

20 Coon, C. W., and Perkins, H. C., "Transition From the Turbulent to the Laminar Regime for Internal Convective Flow With Large Property Variations," JOURNAL OF HEAT TRANSFER, TRANS. ASME, Series C, Vol. 92, No. 3, Aug. 1970, pp. 506–512.

21 McEligot, D. M., "The Effect of Large Temperature Gradients on Turbulent Flow of Gases in the Downstream Regions of Tubes," Ph.D. dissertation, Stanford University (TID-19446), 1963.

22 McEligot, D. M., and Bankston, C. A., "Numerical Predictions for Circular Tube Laminarization by Heating," ASME Paper No. 69-HT-52, presented at 11th National Heat Transfer Conference, Minneapolis, Minn., Aug. 1969.

J. F. HUMPHREYS[1]
H. BARROW
W. D. MORRIS[2]

Department of Mechanical Engineering,
University of Liverpool, Liverpool,
England

Transient Free Convection in a Revolving Tube

An experimental study has been made of transient free convection in a tube which revolves about an axis parallel to the tube axis. Three fluids have been studied for one tube diameter and one radius of rotation for centrifugal accelerations in the range 0 to 100 g. The measurement of transient temperature and heat transfer coefficient shows that significant changes result from rotational buoyancy effects. A correlation of all the data to within ±20 percent has been effected by the use of a quasi-steady relation between a modified heat transfer coefficient and a rotational Rayleigh number as

$$\textit{Nusselt number} = 0.107\ (\textit{Rayleigh number})^{0.35}$$

Introduction

This paper is concerned with the subject of heat transfer to a revolving fluid system. The free convection mechanism which results from the system motion is induced predominantly by the centrifugal force field and, out of necessity, is time-dependent.

Such a situation could be found in engineering practice if, for example, the blowers used for the forced internal cooling of the rotors of electrical machines were to fail suddenly. The fluid which is contained in the revolving coolant passages is heated transiently in the presence of centrifugal forces giving rise to free convection in a plane perpendicular to the axis of revolution. Similar problems in space technology which are of interest here are those in which the body force field on the fluid system is due to rapid linear acceleration or deceleration. One example which is readily called to mind is that of a fuel storage tank of a space vehicle which is subject to thermal and nuclear radiation. The ensuing free convection is likewise time-dependent.

The majority of the earlier studies of free convection which are relevant to the present inquiry fall into two main categories. Firstly, there are those which were concerned with rotationally induced free convection in the steady-state condition; and secondly, there are those which were time-dependent but restricted to the influence of the earth's gravitational field. In the former category, the studies of Bayley and Cohen [1][3], Martin and Cresswell [2], Morris [3], Davies and Morris [4], Humphreys, Morris, and Barrow [5] are worthy of note, these investigations having their origin in the problem of the cooling of rotating components in steady flow. Of the transient studies, referred to in the second category, the works of Siegel [6], Goldstein and Briggs

[1] Presently, The Electricity Council Research Centre, Capenhurst, Chester, England.

[2] Presently, School of Applied Sciences, University of Sussex, Falmer, Brighton, England.

Contributed by the Heat Transfer Division and presented at the Fluids Engineering, Heat Transfer, and Lubrication Conference, Detroit, Mich., May 24–27, 1970, of THE AMERICAN SOCIETY OF MECHANICAL ENGINEERS. Manuscript received at ASME Headquarters, December 10, 1969. Paper No. 70-HT-10.

[3] Numbers in brackets designate References at end of paper.

Nomenclature

$\alpha(=\kappa/c_p\rho)$ = thermal diffusivity
$A(=H\Omega^2/g)$ = acceleration ratio
b, K = constants
$B(\tau - t)$ = response of a transient system at time τ to unit $E(t)$
$E(t)$ = excitation at time t
$C(=H\Omega d\rho/\mu)$ = nondimensional parameter
β = volumetric coefficient of expansion
c_p = specific heat at constant pressure
d = diameter
ϵ = emissivity
$e(=d/H)$ = eccentricity parameter
f = function
g = acceleration due to gravity
$F(=\alpha t/d^2)$ = Fourier number
$\mathrm{Gr}\left(=\dfrac{H\Omega^2\beta d^3(\theta_w-\theta_c)\rho^2}{\mu^2}\right)$ = Grashoff number
$h(=q/(\theta_w-\theta_c))$ = heat transfer coefficient

(Continued on next page)

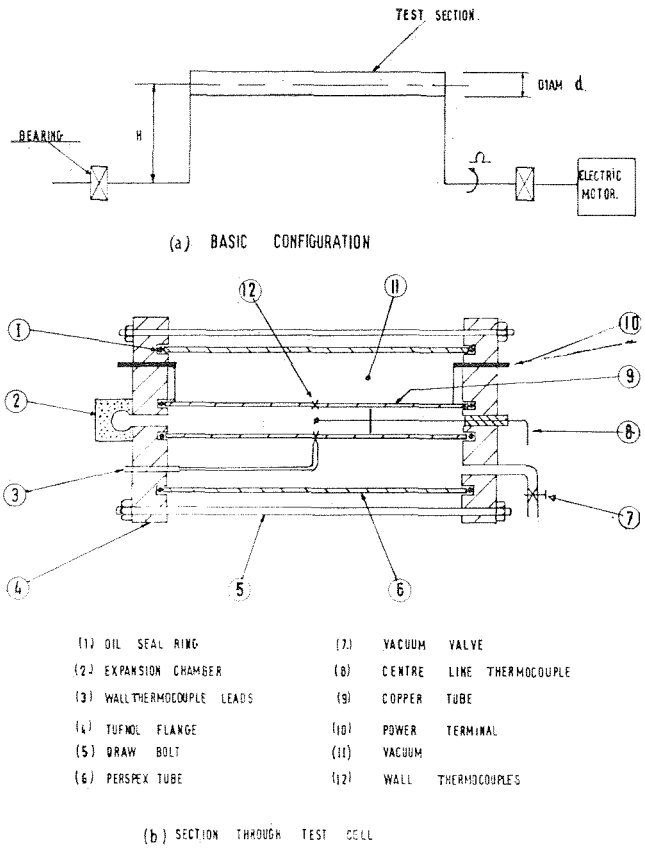

Fig. 1 Transient free convection apparatus

[7], both of which pertain to free convection in an infinite fluid system, are relevant here, but the investigations of Maahs [8] and Evans and Stefany [9] are of special interest in that they refer to fluid systems contained in cylindrical enclosures. Evans and Stefany [9] briefly review the transient studies in other containing geometries. While the foregoing studies deal with either the force field aspect or the transient aspect of free convection in fluid systems, there is only a limited amount of information on the combined effects. Some qualitative data on the case of time-dependent heat transfer in an accelerating fluid system are to be found in the report by Anderson and Kolar [10] who studied heating of a fuel storage tank in a space vehicle.

The present paper is intended as a contribution to transient free convection heat transfer under the effects of centrifugal body forces associated with the revolution of the fluid system. At the outset it was considered that the nature of the fluid and the magnitude of the force field would be of interest, and accordingly provision was made for effecting variation in the Prandtl number of the test fluid and the speed of revolution of the fluid system.

The thermal boundary condition in this investigation was that of uniform heat release at the outer boundary of the containing geometry which in this study was a pipe. Accordingly, the heat transfer system includes both the fluid system and its container. Further reference to this point is made in later sections and it is sufficient to state at this stage that the type of heating is consistent with that met with in many engineering situations. The idealized model geometry is shown in Fig. 1(*a*), and the component which simulates the thermodynamic system for the experimental work is illustrated in Fig. 1(*b*).

The equations of continuity, momentum, and energy for the theoretical system are complex in the extreme and a solution for the temperature and hence heat transfer is unobtainable. Recourse may be made however to a dimensional analysis approach to the problem. Consideration of the variables involved in the problem yields the following relationship

$$\mathrm{Nu} = f[\mathrm{Gr}, F, \mathrm{Pr}, e, C] \tag{1}$$

where the dimensionless groups are defined in the Nomenclature. The first four groups are familiar, while the last two parameters, viz., e and C in equation (1), are included to account for the geometry of the revolving system and coriolis forces, respectively. The parameter C which equals $H\Omega\rho/(\mu/d)$ measures the significance of the coriolis forces to the viscous forces. The nature of the problem makes the determination of the functional relationship in equation (1) difficult to determine as independent variation of the parameters containing fluid properties is almost impossible. It is shown later, however, that a simplified form of this relationship suffices to correlate the data of the present tests within acceptable limits. This technique employs the idea of a quasi-steady situation and has been used previously. The transient nature of the heat transfer process can be meaningfully presented by a comparison of the temperature of the system in the transient state with that in the case when conduction alone takes place. A single fluid temperature measurement is convenient for this purpose as the temperature fields in both the case of convection and conduction at a given time are uniquely defined; it has the advantage that it quantitatively indicates the behavior of the fluid flow in the rotationally induced convection. Furthermore, it is possible to compare the transient heat transfer by the employment of a heat transfer coefficient based on the difference between the temperature of the wall and that at the specific location of the single temperature measurement.

Both the dimensional analysis approach and the temperature comparison technique are used in a later section in connection with a discussion of the experimental data of the tests reported in this work. The following section describes the equipment and procedure which was adopted in the experimental program.

Experimental Apparatus and Procedure

A rotating framework which has been described by the present authors [5] was available in the Department of Mechanical En-

Nomenclature

H = distance between axis of tube and axis of rotation
κ = thermal conductivity
μ = dynamic viscosity
L = water equivalent
$\mathrm{Nu}\ (= hd/\kappa)$ = Nusselt number
P = energy release
$\mathrm{Pr}(= c_p\mu/\kappa)$ = Prandtl number
q = heat flux at wall
Q = heat transfer rate to test fluid
R = radiation heat loss
ρ = density
s = surface area
θ = temperature
t, τ = times
$Y(t)$ = response of a transient system
Ω = angular velocity
$\mathrm{Ra}(= \mathrm{Gr} \times \mathrm{Pr})$ = Rayleigh number
$\Theta\left(= \dfrac{\theta_w - \theta_c}{\theta_w - \theta_i}\right)$ = temperature parameter

Subscripts

a = ambient
w = wall
c = at axis of tube
i = initial

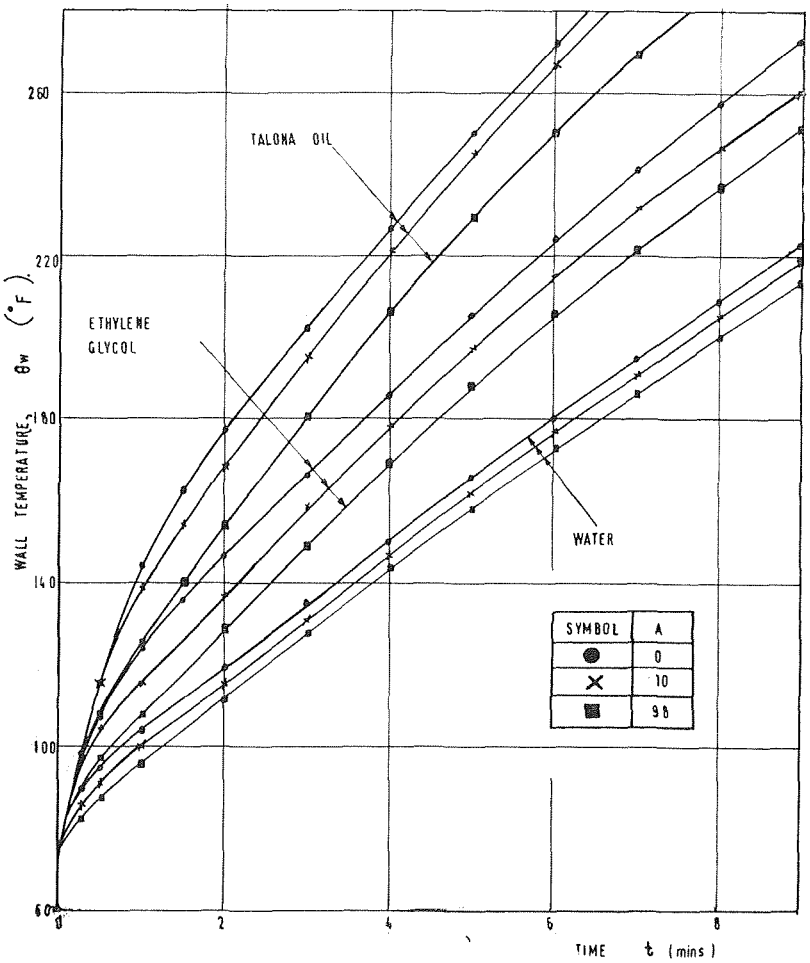

Fig. 2 Wall temperatures

gineering, University of Liverpool, and it was decided to construct a transient heat transfer test section which could be readily fitted to this (see Fig. 1(*a*)). A copper tube 1 in. dia and 16 in. long was found to be suitable for these purposes. The length of the tube was considered to be sufficiently large to justify the assumption that there would be no end effects at the central cross section. It was reasoned that the heat loss from the exterior of the tube could be best calculated under conditions of vacuum insulation and this method was adopted. A diagram of the test section is shown in Fig. 1(*b*). Two "tufnol" (an insulating material) flanges were machined as shown to be push fits with the copper tube and the outer concentric perspex tube. "O-ring" seals and draw bolts were employed to achieve vacuum-tight joints. The copper tube was wound with glass fiber tape and then with resistance wire to provide for heat transfer. Two copper–constantan thermocouples were located diametrically opposite each other on the outer surface of the tube at the central section as shown in Fig. 1(*b*), the fluid temperature on the center line being measured by an axial thermocouple probe. Expansion of the test fluid during transient heating was catered for by the provision of a small flexible and insulated reservoir as shown. The thermocouple signals and electric heating power were transmitted via slip rings. Rotation of the test section up to speeds of 560 rpm was provided by a belt drive from a 1-hp electric motor. The radius of rotation in all tests was 11 in.

The preparation of the test section for each experiment was conducted remote from the rotating rig. The annular chamber was exhausted using a small rotary vacuum pump with a view to minimizing heat loss due to free convection effects. The vacuum was found to hold satisfactorily for a day without further extraction being necessary. The test tube was then completely filled with the test fluid and sealed. After installation of the test section in the rotating rig, the apparatus was set running at the desired speed and left for a time to allow the fluid to rotate "solidly" with its containing tube. After the preliminary running-up period, the power was switched on and readings of tube wall and fluid temperature were made at convenient intervals of time over a period of about 10 min. The ambient temperature was noted.

Three fluids, viz., water, ethylene glycol, and a commercial light heat transfer oil "Shell Talona 10 W," were used. For all fluids, the total electric heating power was maintained at a fixed value of 3.6 watt/cm^3 with a view to producing a thermal boundary condition of uniform heat sources at the outer boundary of the tube. Tests were conducted at rotational speeds which gave accelerations of the center line of the test section equal to 0, 10, 24, 45, 59, and 98 g.

Method of Calculation

In order to calculate the heat transfer coefficient for this flow system, it is necessary to know the variation of heat flux to the fluid with time. Owing to the finite heat capacity of the heater wire, insulation, and tube wall, and also because of heat loss to the atmosphere, the energy dissipated by the heater is not entirely transferred to the fluid. Tests indicated that the rate of temperature change for the wire, insulation, and tube wall rapidly equalize, so that an energy balance may be written as

$$P = L\frac{\partial\theta}{\partial t} + R + Q \qquad (2)$$

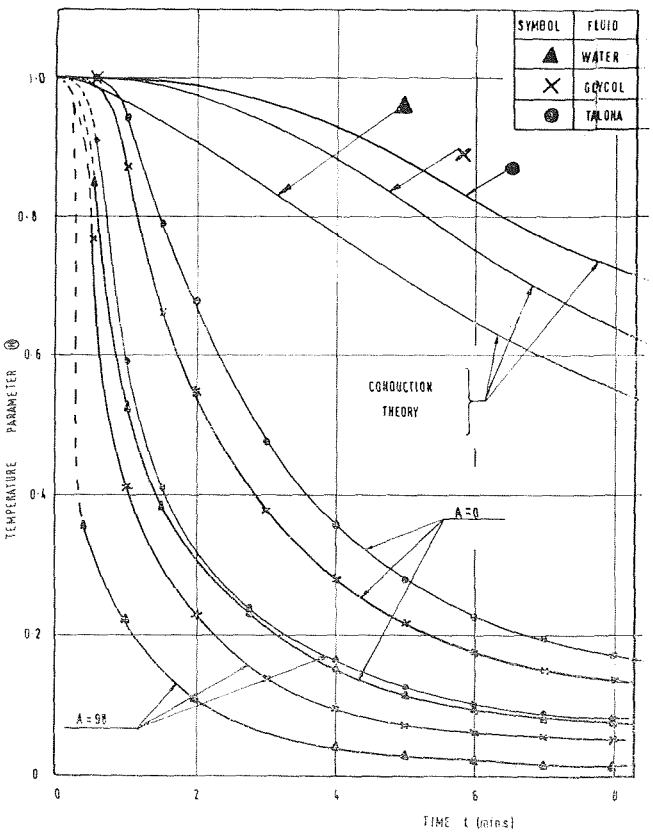

Fig. 3 Normalized temperatures

where P is the energy release per unit time in the wire, L is the water equivalent of the wire, insulation, and tube wall, R is the heat loss, and Q is the heat transfer to the fluid in appropriate units.

The heat loss comprises conduction through the vacuum jacket and net radiation heat transfer between the test tube and its containing perspex tube. Rigorous calculation of these losses is complex in the extreme on account of the geometry and nature of the radiating surfaces. Preliminary calculations showed that the radial conduction loss was significantly smaller than the radiation loss and was neglected. The radiation loss has been calculated from the simplified Stefan-Boltzmann formula

$$R = 17.3 \times 10^{-10} \cdot \epsilon \cdot S(\theta_w^4 - \theta_a^4) \qquad (3)$$

which assumes that the radiation surface of the heated tube is small in comparison with the surface area of the confining perspex tube and that the latter is at the ambient temperature θ_a. Accordingly, the heat flow to the fluid can be calculated from equations (2) and (3) when the variation of the wall temperature is known. With the variation of heat flow to the fluid, whose mass, initial temperature, and heat capacity are known, the bulk temperature at any time could be evaluated. However, on account of the small differences between the wall temperature and the fluid bulk temperature, an alternative method which employs the fluid center-line temperature in the assessment of heat transfer was considered. This is warranted because the bulk and center-line temperatures are uniquely related and the center-line temperature is more easily determined. The alternative technique can be particularly useful in the study of transient heat transfer to contained fluids. It is frequently necessary, for example, to know the temperature history at a specific location within the fluid system. Such a problem occurs in many situations in the chemical processing industry. The center-line temperature in the actual transient convection case when compared with that in the transient heat conduction case provides a positive measure of the enhancement of heat transfer due to fluid flow. These considerations are included in the next section in addition to a more conventional approach to the problem.

Results and Discussion

The history of the wall temperature for the particular thermal boundary condition considered here is shown in Fig. 2 for various fluids at various rotational speeds. At any time, the amount of energy transferred to all fluids is greater at the larger rotational speeds, this being in keeping with a decrease in wall temperature as the speed increases. Differences in wall temperatures with speed variation occur first in the case of water, then with glycol, and finally with "Talona," which indicates that the effects of rotation are experienced earlier in the case of water than in the case of the other fluids. A more comprehensive presentation of temperature history is presented in Fig. 3 where the effects of convection in the stationary and rotating cases are to be seen more clearly. The curves indicate that the center-line temperature increases more rapidly in the rotational case than in the stationary case. While these trends are to be expected, the magnitude of such are here clearly determined and seen to be most significant. The difference between the center-line temperature when the tube is stationary and that according to conduction theory (Appendix) shows the inherent free convection in any stationary geometry. The differences between the curves for $A = 0$ and $A = 98$ result from the enhancement of fluid motion in planes perpendicular to the tube axis and can be attributed to the additional effects of centrifugal buoyancy and coriolis forces. The coincidence of the experimental temperature curves and the curves from the conduction theory near the origin is compatible with the mechanism of heat transfer by conduction alone at the beginning of heating as observed by Evans and Stefany [9]. The increasing departure from the curves by conduction theory at later times is consistent with a free convection regime. However, a decrease in $(\theta_w - \theta_c)$ means that the temperature differences within the fluid are becoming smaller with a corresponding reduction in the motive force for the convection. This ultimately results in a reduction of the temperature slope at larger times as shown in Fig. 3. Physically, the situation may be explained in terms of "stratification" of the fluid, i.e., relatively hot fluid once located near to the axis of rotation tends to stay there, giving a so-called stable region of stagnant fluid.

It can be seen that the effect of rotation in each of the fluids is to establish the onset of free convection sooner and also to substantially increase the rate of free convection in the free convection regime referred to earlier. However, because with rotation, Θ at first decreases very rapidly compared with the zero-speed case, then at greater times the rate at which Θ decreases must be less in the rotational case than in the stationary case for the reasons given previously. From the curves this is seen to be so. Fig. 3 also shows that free convection occurs noticeably sooner in the case of water, illustrating that water is a better free convection fluid than glycol, which in turn is better than Talona. This is consistent with a quasi-steady approach to a correlation of the present data.

The center-line temperature history study given in the foregoing paragraphs provides for physical insight into the behavior of the fluid flow across the tube. The center-line thermocouple probe measures the temperature of a stream of fluid moving diametrically outward across the tube, its temperature varying with time and speed of rotation, and is useful in assessing the effects on heat transfer. The use of heat transfer coefficient is, however, more familiar and this measure has been adopted in Fig. 4 where the heat transfer coefficient based on wall to center-line temperature difference is plotted against time. Initially, at $t = 0$, the heat transfer coefficient is infinitely large and must decrease at times soon after $t = 0$ since the geometry is closed. At larger times, see Fig. 4, because of the onset of free convection an increasing heat transfer coefficient results as shown in the diagram. As the time further increases, the rate of increase

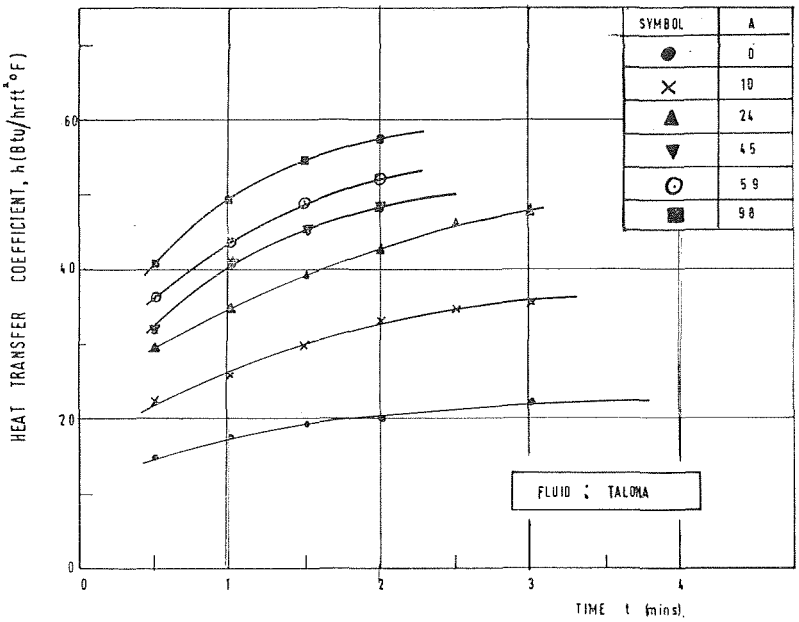

Fig. 4 Heat transfer coefficients

Table 1 Percentage increases in heat transfer coefficient due to rotation

TIME	PERCENTAGE INCREASE IN 'h' FOR A = 98.		
(MINS)	WATER	GLYCOL	TALONA
1	240	180	160
2	260	200	190

of h decreases which is consistent with the form of the temperature curves. Some examples of the very large increases in h with increase in rotational speed are quoted in Table 1.

It will be recalled that in the conventional approach to the study of steady-state free convection, the following type of equation is employed:

$$\text{Nusselt number} = f(\text{Rayleigh number}) \tag{4}$$

and that a particular form of this equation, viz., Nusselt number $= K$ (Rayleigh number), has been used [9] in the transient heat transfer case for average heat transfer coefficients on a quasi-steady basis. A detailed consideration of the basic equations of momentum and energy for the present geometry reveals that additional parameters have to be included with the Nusselt and Rayleigh numbers for a complete correlation. It was decided, however, that because complete coverage of all such variables, which include the Fourier number and a further geometry parameter, could not be catered for in the present experimental work, a quasi-steady equation

$$\text{Nu} = f(\text{Ra}) \tag{5}$$

might suffice. The temperature difference in the parameters of equation (5) was chosen to be that between the wall and the center line instead of the more usual bulk temperature basis. This is justifiable because the ratio of the two temperature differences is determined by the temperature field which is governed by the energy equation. The energy equation in turn yields some of the appropriate parameters.

Fig. 5 shows a plot of Nu versus Ra for all fluids at all rotational speeds. The zero-speed case could be considered separately because it is not to be expected that these results should correlate with those in rotation when coriolis forces are present. It is noteworthy that in Fig. 5 the water results are most scattered around the mean line but this is primarily due to the larger errors involved in determining the heat flux in that case. It will be seen that the majority of the experimental data are correlated to within ±20 percent by the equation

$$\text{Nu} = 0.107(\text{Ra})^{0.35} \tag{6}$$

it being remembered that both Nu and Ra are based on wall to center-line temperature difference and fluid properties evaluated at the instantaneous center-line temperature. While the zero-speed results are not shown here, it is interesting to report that they may be correlated to within ±15 percent by the equation

$$\text{Nu} = 0.58(\text{Ra})^{1/4} \tag{7}$$

the Rayleigh number here being made with g in place of $H\Omega^2$. The agreement between the exponent of the Rayleigh number in equation (7) with that in other steady-state correlations could be fortuitous but nevertheless is gratifying.

The trend of the present results for the stationary case appears at first sight not to be in agreement with that reported by Evans and Stefany [9] who found that the heat transfer coefficient for a vertical cylinder was constant over most of the transient period. Their boundary condition, however, was somewhat different from the present one and the parameters were defined differently. However, the present results are consistent with those of Maahs [8] who observed that his heat transfer coefficient increased with increasing time.

The present results for both the steady and rotational cases are satisfactorily correlated on the basis of a quasi-steady situation and this is convincingly demonstrated in part, in Fig. 5. The form of the correlating equation for the rotating geometry is somewhat speculative in that the other pertinent parameters referred to earlier have been omitted. It might be that further refinement in this direction would yield a tighter correlation; however, within the accuracy of the present experimental work the present result must be considered to be adequate.

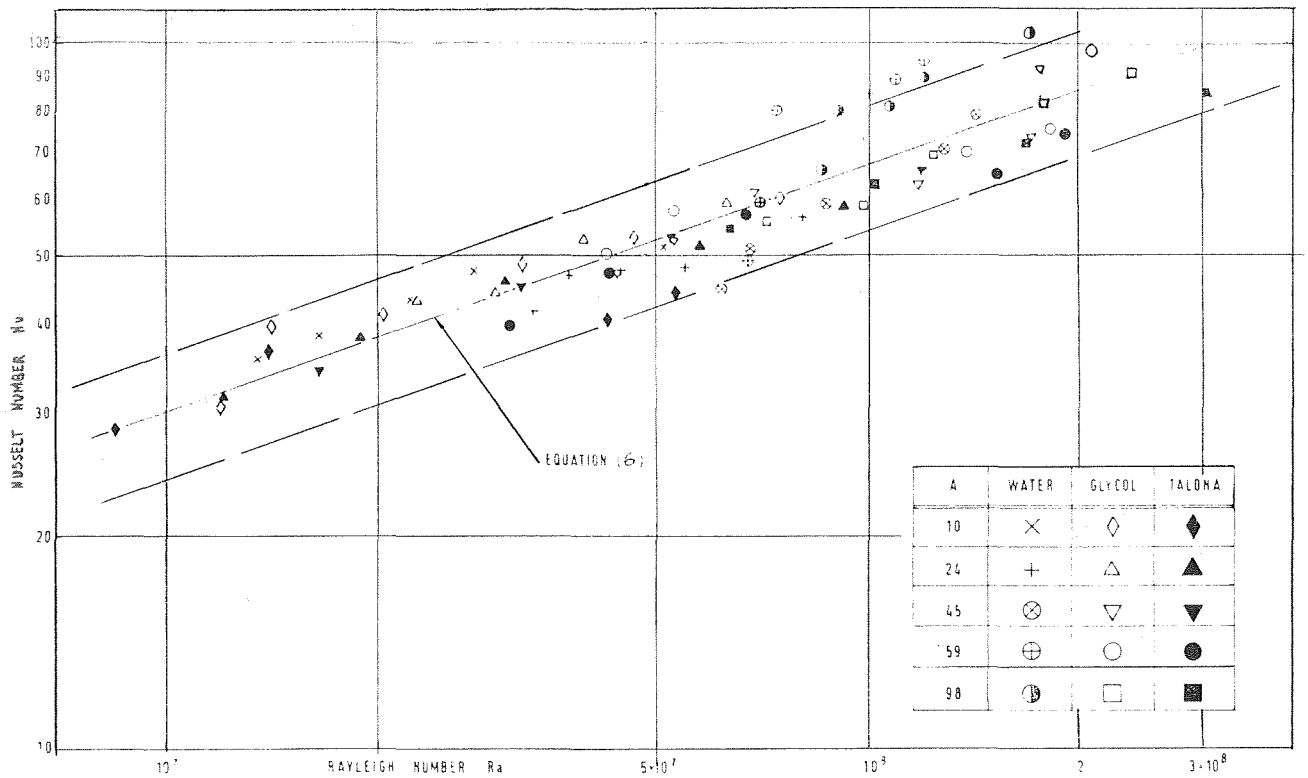

Fig. 5 The correlation of the heat transfer coefficient

Conclusions

An experimental study has been made of the effect of transverse body forces associated with accelerations up to 100 g on transient free convection heat transfer to a fluid in a long duct of circular cross section. The experimental fluids were water, ethylene glycol, and Shell Talona 10 W oil. The transverse force field was produced by revolution of the tube about an axis parallel to its own axis. The free convection effects associated with rotation have first been assessed by comparing the central point temperature history in the actual situation with that when free convection is absent as in pure conduction in the fluid. The comparison was made on the basis of the same wall temperature history. The experimental heat transfer data have been correlated to within ± 20 percent by a simple Nusselt number—Rayleigh number relationship using the idea of quasi-steady conditions.

The experimental temperature measurements indicate the degree to which the flow pattern and hence heat transfer is affected by increases in the force field on rotation, and the dependency on the nature of the fluid. The magnitude of the increases in heat transfer were assessed in the present work by the use of a particular heat transfer coefficient and on this basis up to about $2^1/_2$ times the heat transfer in the earth's gravitational field was observed at about 100 g. The Prandtl number effect was not determined explicitly but the individual heat transfer data were consistent with the behavior of the fluids in gravitational convection as must be expected.

The general conclusion concerning the present observations is that revolution of a fluid system can bring about very marked changes in transient heat transfer; and while an all-encompassing empirical correlation is not possible until more extensive study of all variables has been made, a simplified quasi-steady correlation is feasible for engineering purposes provided the dimensionless parameters are defined in a particular way.

References

1 Bayley, F. J., and Cohen, H., "Heat Transfer Problems of Liquid-Cooled Gas-Turbine Blades," *Proceedings of the Institution of Mechanical Engineers*, Vol. 169, 1955, p. 1063.

2 Martin, B. W., and Cresswell, D. J., "Influence of Coriolis Forces on Heat Transfer in the Open Thermosyphon," *Engineer*, Vol. 204, Dec. 1957, p. 926.

3 Morris, W. D., "Laminar Convection in a Heated Vertical Tube Rotating About a Parallel Axis," *Journal of Fluid Mechanics*, Vol. 21, Part 3, 1965, p. 453.

4 Davies, T. H., and Morris, W. D., "Heat Transfer Characteristics of a Closed Loop Thermosyphon," Third International Heat Transfer Conference, Chicago, AIChE, Aug. 1966.

5 Humphreys, J. F., Morris, W. D., and Barrow, H., "Convection Heat Transfer in the Entry Region of a Tube Which Revolves About an Axis Parallel to Itself," *International Journal of Heat and Mass Transfer*, Vol. 10, 1967, p. 333.

6 Siegel, R., "Transient Free Convection From a Vertical Flat Plate," TRANS. ASME, Vol. 80, 1958, p. 347.

7 Goldstein, R. J., and Briggs, D. G., "Transient Free Convection About Vertical Plates and Circular Cylinders," JOURNAL OF HEAT TRANSFER, TRANS. ASME, Series C, Vol. 86, No. 4, Nov. 1964, p. 490.

8 Maahs, H. G., "Transient Natural Convection Heat Transfer in a Horizontal Cylinder," PhD thesis, University of Washington, 1964.

9 Evans, L. B., and Stefany, N. E., "An Experimental Study of Transient Heat Transfer to Liquids in Cylindrical Enclosures," *Chemical Engineering Progress Symposium Series*, Vol. 62, p. 209.

10 Anderson, B. H., and Kolar, M. J., "Experimental Investigation of the Behavior of a Confined Fluid Subjected to Non-Uniform Source and Wall Heating," NASA T.N. D-2079, Nov. 1963.

11 Bronwell, A., *Advanced Mathematics in Physics and Engineering*, McGraw-Hill, 1st ed., 1953, p. 432.

APPENDIX

The calculation of fluid center-line temperature variation with time due to conduction alone and corresponding to a known wall temperature/time curve was made by means of Duhamel's theorem (see reference [11]).

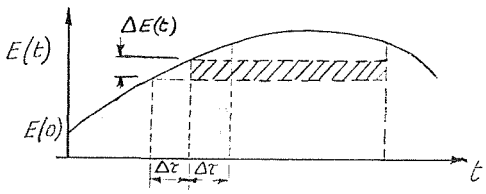

Fig. 6

The response $Y(\tau)$ of a linear system to an arbitrary excitation $E(t)$ can be regarded as a summation of system responses to a succession of step excitations, as shown in Fig. 6.

The response $Y(\tau)$ at time $t = \tau$ to all the step excitations initiated from $t = 0$ to $t = \tau$ is then:

$$Y(\tau) = E(0)B(\tau) + \sum_{t=\Delta\tau}^{t=\tau} \Delta E(t)B(\tau - t) \qquad 0 < t < \tau$$

where $B(\tau - t)$ is the indicial response at time τ, resulting from a unit step excitation initiated at time t.

Considering the present problem of radial heat conduction in an infinite cylinder, the required values of $B(\tau - t)$, the response to a unit step temperature change are available in reference [11] where numerical values obtained from a theoretical solution are tabulated. Hence, by a series of summations the fluid centerline temperature variation with time due to conduction alone was calculated for any observed boundary wall temperature history.

Liquid Droplet Deposition in Two-Phase Flow

R. FARMER
Staff Engineer,
Martin Marietta Corp.,
Denver Division, Denver, Colo.

P. GRIFFITH
Professor of Mechanical Engineering,
Massachusetts Institute of
Technology, Cambridge, Mass.

W. M. ROHSENOW
Professor of Mechanical
Engineering, Massachusetts
Institute of Technology, Cambridge, Mass.

Two-phase annular flow deposition was studied. Experiments were performed to determine where small water droplets in an air stream in a round tube would reach the wall. Results indicated that, for fully accelerated droplets whose diameters were within a factor of two of 150 microns, the number reaching the wall was characteristic of exponential decay with distance downstream. Further, the mean free path to the wall, measured axially, could be taken proportional to droplet diameter. With the assumption that dispersed liquid flow rate in annular two-phase flow regimes consists chiefly of droplets traveling at or near gas velocity, and with arbitrary choices of droplet diameter spectrum and magnitude of entrainment rate, it was possible to derive analytical expressions for mass transfer coefficient, deposition flow rate, dispersed liquid flow rate, mean diameter and spectrum as they all changed downstream. Some experimental measurements by others were successfully reproduced by these expressions. An important result was that droplet size spectrum "hardening" (preferential depletion of small sizes) operates to decrease the deposition rate downstream, especially if there is no longer any entrainment.

Introduction

This investigation began with the primary goal of understanding droplet deposition in adiabatic, air-water annular flow in vertical tubes. This very restricted flow regime has some practical value in its own right, but it is studied most often by researchers trying to understand two-phase flow with heat addition. Air and water at room temperature provide a very convenient means of modeling steam-water flow, at the expense of omitting thermodynamic influences. Despite its convenience, however, adiabatic air-water annular flow is not well understood. Trends for a parameter such as dispersed liquid flow rate are known for changes in inlet conditions, but the only empirical expression for predicting the magnitude of that parameter (of which the authors are aware) was not generally successful [1].[1]

A very simple series of experiments was performed with different sizes of water droplets, in different air flows, to observe the droplet trajectories. The results could be represented by elementary mathematical expressions, and this encouraged further analysis. The analysis yielded expressions for several significant flow parameters, some of which could be compared with the experimental results of others.

The Experiment

The observation of droplet trajectories was carried out with a minimum of equipment:

1 Injection section with accessories

Contributed by the Heat Transfer Division and presented at the Fluids Engineering, Heat Transfer, and Lubrication Conference, Detroit, Mich., May 24–27, 1970, of The American Society of Mechanical Engineers. Manuscript received by the Heat Transfer Division, August 7, 1969; revised manuscript received January 2, 1970. Paper No. 70-HT-1.

[1] Numbers in brackets designate References at end of paper.

Nomenclature

C = concentration, lbm/ft^3
ΔC = concentration difference, lbm/ft^3
C_d = drag coefficient
D = tube diameter, in.
E = entrainment constant, lbm/hr/in.
E' = entrainment constant, lbm/hr/in.^{2}
$G(y)$ = droplet number density, μ^{-1}
$K_n(z')$ = nth order modified Bessell function second kind
N = number of droplets
Re = Reynolds number
V = velocity, ft/sec
W = flow rate, lbm/hr
c = λd, constant for given flow conditions, μ/in.
d = droplet dia, μ
$\bar{d}_v$ = volume mean droplet diameter, μ
$\bar{d}_{vz}$ = volume mean droplet diameter at z, μ
$f_n(z')$ = $2^{-n+1}[(n-1)!]^{-1}(z')^n K_n(z')$, function,—
$f(z)$ = normalizing function
$g(z)$ = normalizing function
g_0 = dimensional constant, lbm ft/lb sec^2
$k(z)$ = local mass transfer coefficient ft/sec
n = numerical order of a function,
p = pressures, psia
$u(z)$ = unit step function at $z = 0$
x = dummy axial variable, in.
x', x'' = dummy axial variables
y = droplet diameter, μ

2 Test section
3 Suction pump with valves, orifice, and piping.

The two sections were made of $^1/_2$-in-ID lucite extruded tubing and are shown in Fig. 1. The injection section was attached at the upper end of the test section by a sealed joint, and both were aligned vertically. Laboratory air was drawn down through both sections by the suction pump. Accessories to the injection section were a velocity probe with manometers for air flow measurement, injection needles for creating the water droplets, and injection syringes for carrying the needles and ejecting the water in small amounts. The injection section was sufficiently long to develop the air flow.

The locations where droplets hit the test section wall were recorded by an MgO layer deposited there by drawing smoke from a burning Mg ribbon through the test section. The holes in the coating could be visually counted, provided they were not too densely spaced, and provided the MgO layer remained intact on the test section wall.

Results

Data were taken for four droplet sizes (volume mean dia $\bar{d}_v$ = 93, 126, 197, and 262μ) and three air velocities (mean velocity V_a = 55, 93, and 111 ft/sec). The droplets, being formed by jet disintegration rather than atomization, had nearly uniform sizes. If the droplets stick to the wall, then the wall count per unit axial length is $-\dfrac{dN}{dz}$, where N is the surviving number of droplets at z. On a semilog plot, the data appears as in Fig. 2. Station number in the figure represents $z + 1/2$ in.

The droplet at injection has a small axial velocity in an air stream at velocity V_a. To calculate the velocity of the droplet at any position downstream, write the force balance:

$$C_d \frac{\pi d^2}{4} \rho_a \frac{(V_a - V_d)^2}{2g_0} = \rho_d \frac{\pi d^3}{6} \frac{dV_d}{dt}. \tag{1}$$

This was integrated numerically using C_d versus Re relation for a solid sphere [2] and starting with an initial droplet velocity of 10 ft/sec. The results are quite insensitive to this assumed initial droplet velocity [5].

For test runs the droplet velocity was calculated using equation (1). In order to correct the deposition density $-dN/dz$ to the magnitude it would have had if the droplets were traveling initially at the air stream velocity, the following corrections were made. Fig. 3 shows a sketch of a possible measured deposition density in actual section lengths of Δz. If the droplets had been initially at the air stream velocity, these deposition points would be farther downstream as shown by the lower sketch. For each section

$$\Delta z_{\text{corrected}} = \frac{V_a}{V_d} \Delta z_{\text{actual}} \tag{2}$$

or

$$z_{n_{\text{corrected}}} = \sum_{i=1}^{n} \left(\frac{V_a}{V_d}\right)_i \Delta z_i. \tag{3}$$

Then the droplet density corresponding to each section would be

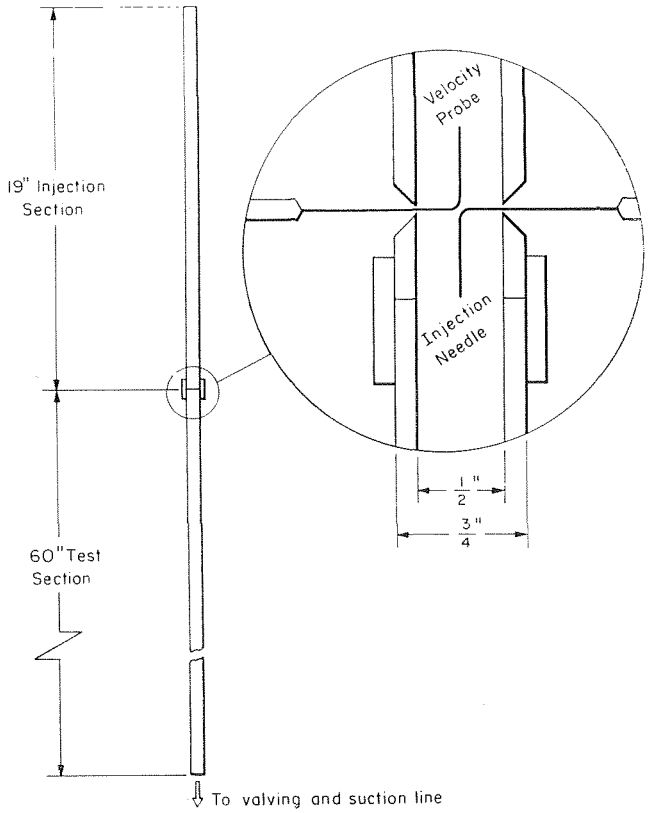

Fig. 1 Injection and test sections

$$\left(-\frac{dN}{dz}\right)_{\text{corrected}} = \frac{V_d}{V_a}\left(-\frac{dN}{dz}\right)_{\text{measured}}. \tag{4}$$

Each datum point of Fig. 2 was corrected in this way. The arrows indicate corresponding points. It can be seen that the data points are scattered about a straight line. Then it follows that

$$-\frac{dN}{dz} = \lambda N \tag{5}$$

or

$$N = N_0 e^{-\lambda z}$$

where λ is the slope of the semilog plot of $-\dfrac{dN}{dz}$ versus z and is called the "deposition constant." Fig. 4 shows the value of λ determined from data plots similar to Fig. 2 for other droplet sizes and air velocities. The data for a given air velocity may be approximated by

$$\lambda = \frac{\text{constant}}{d} \tag{6}$$

which is the equation for each of the three curves shown.

Possible causes of scatter in the data included:

Nomenclature

z = axial variable, in.
z', z'' = axial variables
$\delta(z)$ = deposition rate, lbm/hr/in.
$\xi(z)$ = entrainment rate, lbm/hr/in.
λ = deposition constant, in.$^{-1}$
λ_d = deposition constant for $\bar{d}_v$, in.$^{-1}$
$\lambda(z)$ = deposition parameter, in.$^{-1}$
ρ = density, lbm/ft^3
μ = microns, μ

Subscripts*

L = total liquid
a = air
d = droplet, dispersed liquid
ξ = entrained
0 = initial
avg = averaged

* These subscripts refer the basic parameter to the listed quantity. Definitions with subscripts listed above are exceptions to this last group.

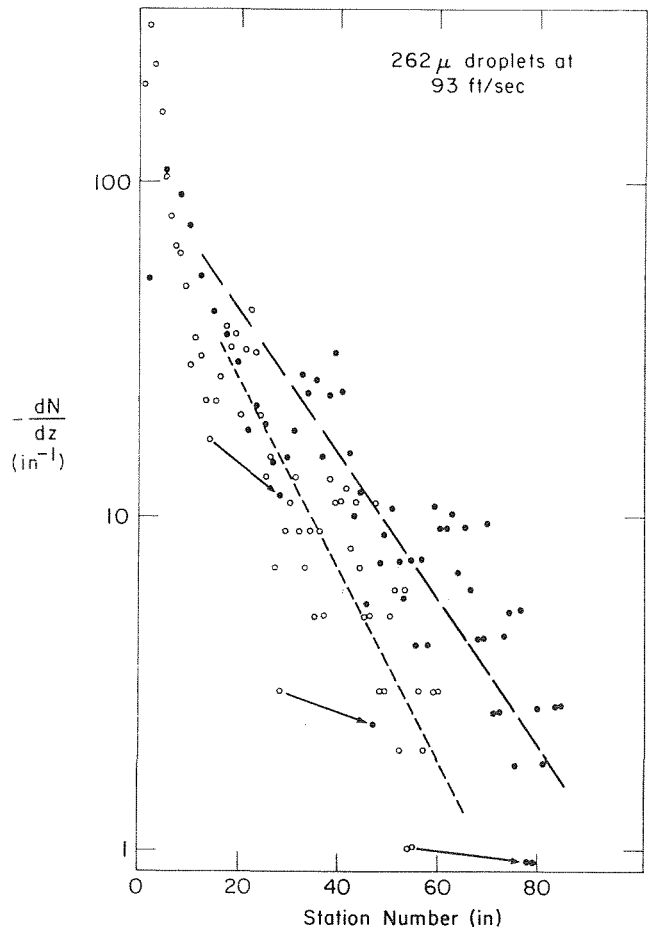

Fig. 2 Raw and corrected wall counts

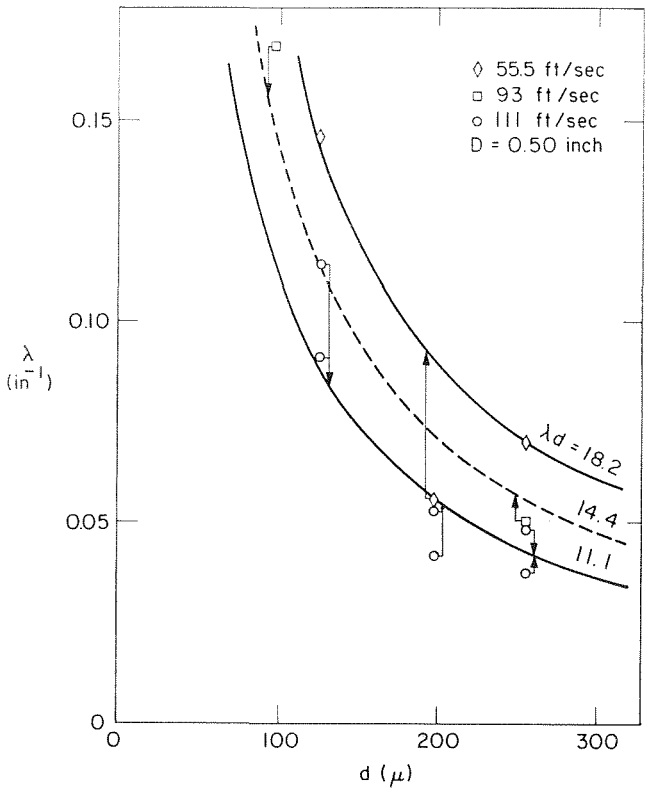

Fig. 4 Summary of results

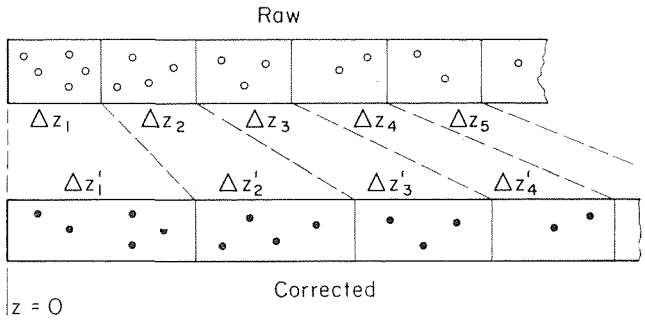

Fig. 3 Sketch of data correction

1 Droplet bounce
2 Droplet evaporation
3 Air flow influence on droplet size at the jet
4 Swirl in air flow
5 Drag coefficient variation due to nonsteady state
6 Needle vibration
7 Electrostatic charge
8 Temperature variation
9 Droplet size spectrum change with length
10 Statistical variations in numbers of droplets hitting the wall, causing data to deviate from true mean behavior.

All except 5 were quantitatively investigated [5]. Only the last two are believed to have contributed significantly to data scatter. The last one predominated and is believed to be responsible for the scatter shown in Fig. 4.

Prediction of Flow Parameters

Consider a dispersed flow with a flow rate of liquid droplets at $z = 0$ of W_{d0} and an entrainment rate of $\xi(z)$ along the tube length. The deposition rate $\delta(yz)$ at any position z resulting from the initial $W_{d0}(y)$ droplets of diameter y is, from equation (5),

$$\delta(y, z) = \lambda W_d(y, z) = \lambda e^{-\lambda z} W_{d0}(y). \tag{7}$$

The deposition rate $\delta(x, y, z)$ at any position z resulting from a droplet entrainment rate $\xi(x, y)$ of droplets of dia y which were entrained at position x between 0 and z is

$$\delta(x, y, z) = \lambda e^{-\lambda(z-x)} \xi(x, y) dx. \tag{8}$$

For a distribution of droplet sizes, define $G(y)$ as the fraction of droplets with dia between y and $y + \Delta y$. The fraction of mass in this diameter range is $G(y)\ (y/\bar{d}_v)^3$, where $\bar{d}_v$ is the volume mean diameter. Then

$$W_{d0}(y) = \left(\frac{y}{\bar{d}_v}\right)^3 G(y) W_{d0}$$

and (9)

$$\xi(x, y) = \left(\frac{y}{\bar{d}_v}\right)^3 G(y) \xi(x)$$

where W_{d0} is the entering dispersed flow rate and $\xi(x)$ is the rate of entrainment of all droplets at x. Integrate equations (7) and (8) with (9) over all droplet sizes and positions x to obtain the deposition rate at any position z:

$$\delta(z) = \int_{y=0}^{\infty} \lambda \left(\frac{y}{\bar{d}_v}\right)^3 G(y) \left\{ e^{-\lambda z} W_{d0} + \int_{x=0}^{z} e^{-\lambda(z-x)} \xi(x) dx \right\} dy. \tag{10}$$

The integration of this function requires knowledge of the magnitude of λ, $G(y)$, and $\xi(x)$.

Solutions have been performed for a number of cases by taking $\lambda y = c$, a constant, as suggested by the experimental data shown in Fig. 4 and equation (6). The droplet size distribution $G(y)$ was taken arbitrarily as that found by Nukiyama and Tanasawa [3]:

$$G(y) = \frac{30}{(\bar{d}_v)^3} y^2 e^{-3.915y/\bar{d}_v} \tag{11}$$

This is the droplet size distribution for the inlet flow W_{d0} and also for the local entrainment at any z.

The solutions made here further assumed that the input $\bar{d}_v$ for the W_{d0} and the entrainment $\xi(x)$ at any x were the same; also W_{d0} was taken as a known boundary condition and $\xi(x)$ was assumed to be known. Solutions for several assumed cases are given in the Appendix.

Once $\delta(z)$ has been found for a given $\xi(z)$ by use of equation (10), then the other parameters of interest can be found as well. First,

$$W_d(z) = W_{d0} + \int_0^z [\xi(x) - \delta(x)]dx. \tag{12}$$

A mass-population weighted mean λ at any location z is

$$\lambda(z) = \int_0^\infty \lambda(y) \left(\frac{y}{\bar{d}_{vz}}\right)^3 G(y, z)dy. \tag{13}$$

It can be shown from equations (10), (12), and (13) that the following identity holds:

$$\lambda(z) = \frac{\delta(z)}{W_d(z)}. \tag{14}$$

Along the flow path the "input" droplet size distribution for the W_{d0} flow and the entrained flow is $G(y)$, equation (11). Because the deposition rate varies with droplet diameter, the size spectrum changes with z.

For the droplets in the initial flow W_{d0} with $G(y)$, the distribution for these droplets downstream, from equation (5), is

$$G_0(y, z) = g(z)e^{-\lambda z}G(y) \tag{15}$$

where $g(z)$ is a normalizing function determined by the requirement that

$$\int_0^\infty G(y, z)dy = 1 \tag{16}$$

For the droplets which go into the stream by entrainment ξ at any z the size distribution of the entering droplets is again taken as $G(y)$. For the entrained flow ξ at any x between 0 and z equation (15) gives the survival spectrum if $e^{-\lambda z}$ is replaced by $e^{-\lambda(z-x)}$. Integrating over the entire upstream length gives the local spectrum

$$G_\xi(y, z) = f(z) \int_0^z e^{-\lambda(z-x)}\xi(x)G(y)dx \tag{17}$$

where $f(z)$ is also determined by equation (16).

At any z the volume mean diameter is calculated by

$$(\bar{d}_{vz})^3 = \int_0^\infty y^3 G(y, z)dy. \tag{18}$$

When both W_{d0} and $\xi(z)$ contribute droplets to the spectrum the local $G(y, z)$ is determined by adding the contributions of each as follows:

$$G(y, z) = \frac{G_0(y, z)\dfrac{W_{d0} - \displaystyle\int_0^z \delta_0(x)dx}{(\bar{d}_{vz})^3_0} + G_\xi(y, z)\dfrac{\displaystyle\int_0^z [\xi(x) - \delta_\xi(x)]dx}{(\bar{d}_{vz})^3_\xi}}{\dfrac{W_{d0} - \displaystyle\int_0^z \delta_0(x)dx}{(\bar{d}_{vz})^3_0} + \dfrac{\displaystyle\int_0^z [\xi(x) - \delta_\xi(x)]dx}{(\bar{d}_{vz})^3_\xi}} \tag{19}$$

where G_0 and G_ξ are determined from equations (15) and (17) and the corresponding $(\bar{d}_{vz})_0$ and $(\bar{d}_{vz})_\xi$ from equation (18); δ_0 is calculated from equation (10) with $\xi = 0$, and δ_ξ is also calculated from equation (10) with $W_{d0} = 0$.

Comparison With Data for Deposition Rates

Data for deposition rates are often reported in terms of a mass transfer coefficient k defined by

$$-\frac{dW_d(z)}{\pi D dz} = k\Delta C = k\frac{W_d(z)}{\frac{\pi D^2}{4}V_a}, \tag{20}$$

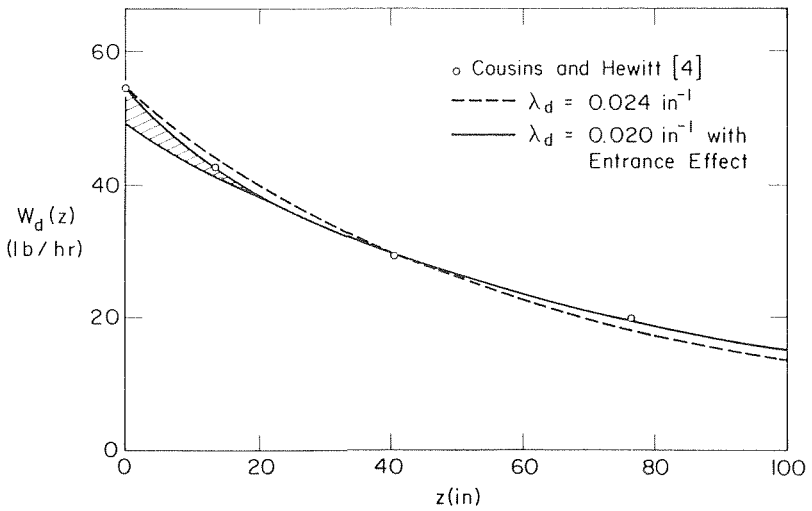

Fig. 5 Calculated $W_d(z)$

where the concentration C at the tube wall is taken as zero. ΔC is the mass concentration of droplets in the stream.

To relate k to λ, write equation (5) as follows:

$$-\left(\frac{1}{\pi D}\right)\frac{dW_d(z)}{dz} = \left(\frac{1}{\pi D}\right)\lambda W_d(z). \tag{21}$$

Then from equations (20) and (21),

$$k = \frac{1}{4}\lambda D V_a. \tag{22}$$

A recent experiment by Cousins and Hewitt [4] gives deposition data which is appropriate for testing the solutions resulting from the analysis above. In the experiment of interest, air and water at room temperature flowed vertically upward together in annular flow through a $1^1/_4$-in-ID tube about 80 ft long. The liquid film was then removed at various distances of 1 to 9 ft from the end of the tube, causing entrainment to go to zero. A film was redeposited downstream of the removal point, by the process of droplet deposition alone, and this film was again removed at the end of the tube. Conditions were:

W_a = 500 lb/hr air
W_L = 175 lb/hr water
p = 29.7 ± 0.1 psia at initial film removal point, z_0, which will be taken as zero in the following figures.

Fig. 5 shows $W_d(z)$ data points from the measurements of Cousins and Hewitt. Two curves are shown, both of which are constructed from the solutions in Table 4 of the Appendix. Hence, the underlying assumptions for these calculations are that upstream entrainment rate was linear and that the droplet size spectrum has approached its corresponding limit.

The first curve (dashed) is the best fit obtainable with the solution $W_d(z) = W_{d0}[f_1(z')]$. The value of λ_d which gave the best fit to the data is 0.024 in.$^{-1}$ Use of this solution is equivalent to the approximation that all entrained droplets, immediately upon entrainment, are well dispersed and fully accelerated to the average air velocity.

The second curve (solid) includes an entrance effect whose contribution is indicated by the shaded area. Here 90 percent

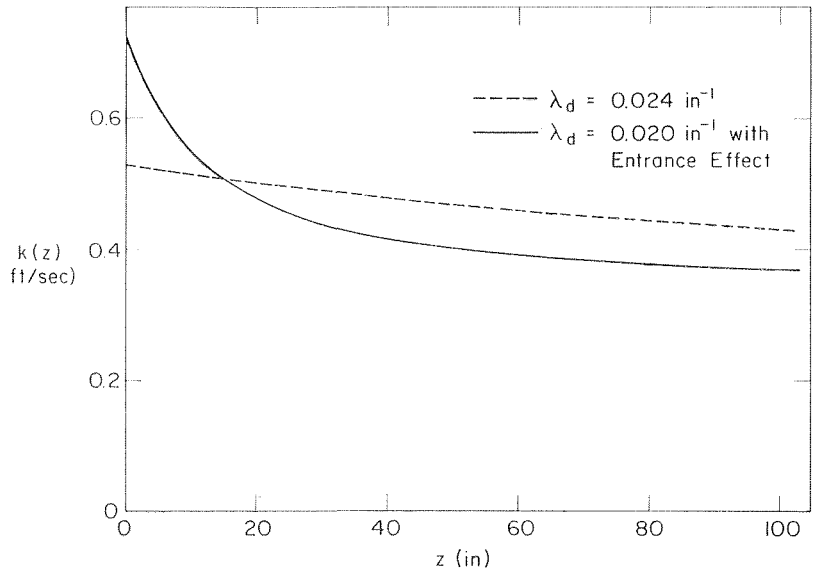

Fig. 6 Calculated k(z)

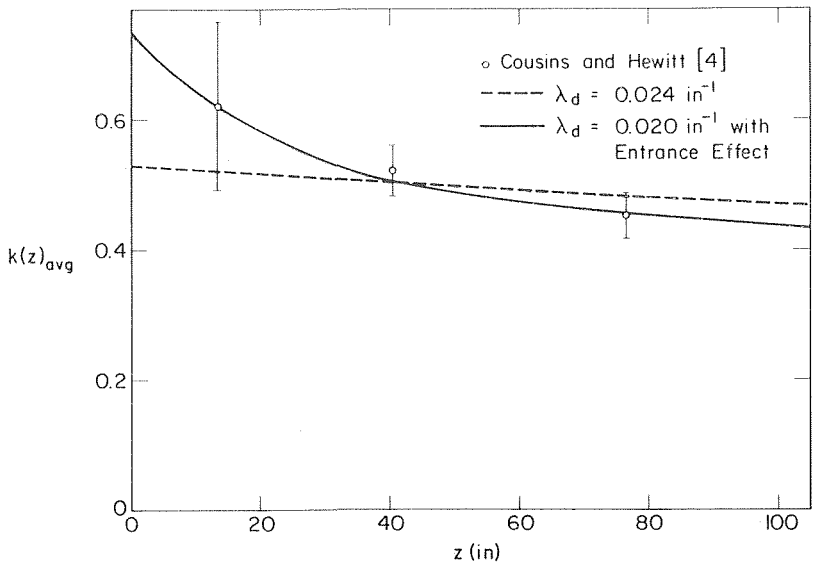

Fig. 7 Calculated average k(z)

of the dispersed flow rate is assumed to consist of fully accelerated and dispersed droplets. The remaining 10 percent is assumed to consist of droplets of a uniform size which lag behind the air flow in such a way that the deposition constant is 5 times as great as λ_d. This correction is made because the drops which have just been entrained would not yet have reached mainstream velocity. Then $W_d(z) = 0.9\, W_{d0}[f_7(z')] + 0.1\, W_{d0}e^{-5\lambda}dz$. It can be seen that the fit of this curve to the data is excellent.

Fig. 6 shows curves for $k(z)$ for each of the above two approximations calculated from equation (22). For the dashed curve, the value of $\lambda(z)$ comes from Table 4 in the Appendix. For the solid curve, $\lambda(z)$ must be calculated from equation (14), with both $\delta(z)$ and $W_d(z)$ consisting of two parts. Table 5 illustrates the details of the calculation.

Fig. 7 shows $k(z)_{\text{avg}}$ data points for the average $k(z)$ between $z = 0$ and $z = z$, plus two curves representing the appropriately averaged values of $k(z)$ shown in Fig. 6. The values must be averaged because the experimenters were in effect measuring deposition over a length of tube from 0 to z. The averaging of the curves is most easily done by writing

$$W_d(z) = W_{d0}e^{-\lambda(z)}\ \text{avg}^z \qquad (23)$$

and solving for $\lambda(z)_{\text{avg}}$.

Then $k(z)_{\text{avg}}$ can be calculated from equation (22). Since $k(z)$ values from the curves do not enter directly, Fig. 7 can be regarded as entirely based on Fig. 5. A good fit in one figure guarantees a good fit in the other.

Examination of the figures indicates that the approximation underlying the second curve appears to be very good. The same approximation was used to reproduce data for other cases, in different sized tubes with different flow conditions [5]. In every instance, the data were successfully matched with curves of apparently correct shape. The only requirements were for numerically appropriate values for $\xi(z)$ and λ_d.

Conclusions

This study has led to many conclusions, the most important ones of which are listed in the following:

1 Experimental evidence indicates that fully accelerated water droplets, over much of the range of sizes expected to carry the bulk of the dispersed liquid in vertical annular flow, tend to reach the wall in simple exponential fashion along the length of a circular tube carrying an air flow, equation (5).

2 Experimental evidence indicates that the tendency to reach the wall, as measured by the magnitude of a deposition constant for each accelerated droplet size, is inversely proportional to droplet size and decreases with increasing air velocity, Fig. 4.

3 With the assumption that dispersed flows are chiefly droplets traveling at gas velocity, one can use the deposition constant to calculate several flow parameters of practical interest, such as dispersed flow rate and deposition rate, Appendix.

4 A droplet size spectrum can be introduced into the analysis to make it more realistic, although the complexity is such that at present it becomes necessary to assume simple forms of entrainment rate to make the analysis tractable.

5 Spectral hardening (depletion of more easily deposited sizes) reduces deposition downstream, causing an increase in dispersed flow rate over the one-size model, Fig. 9. It should be

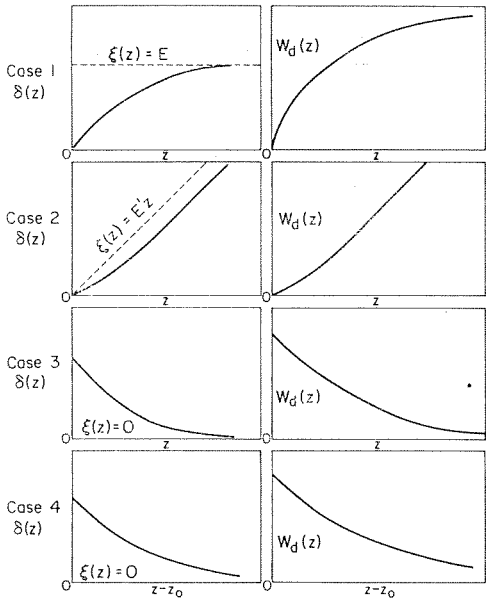

Fig. 8 Shapes for $\xi(z)$, $\delta(z)$, and $W_d(z)$

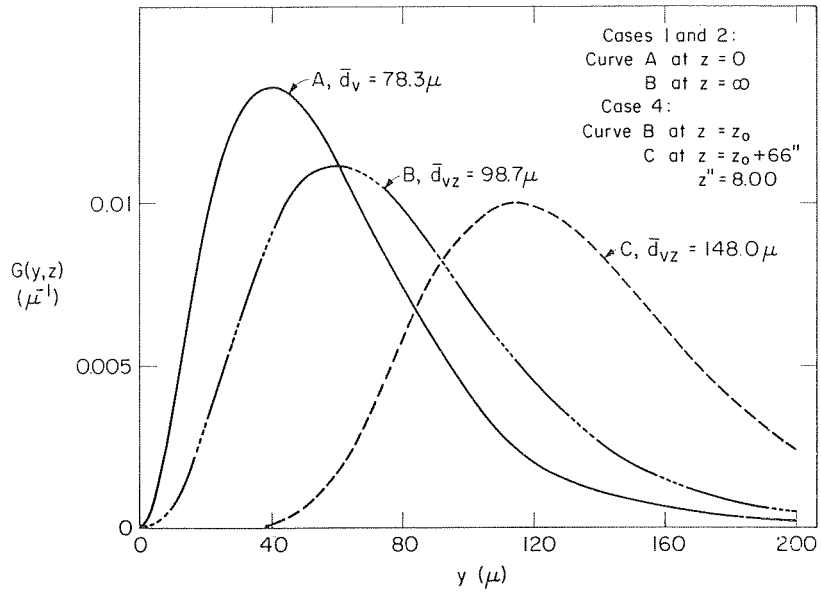

Fig. 9 Downstream spectrum hardening

realized that a similar result would be obtained for any spectrum and for any diametrical dependence in the deposition constant.

6 The parameters calculated by the analysis can be used very successfully to duplicate experimental results of other researchers working on adiabatic annular flow if an "entrance effect" is incorporated in the analysis, Figs. 5, 6, and 7.

APPENDIX

In the following four tables, solutions are presented for these cases:

1 $\xi(z)$ constant, $W_{d0} = 0$
2 $\xi(z)$ linearly increasing, $W_{d0} = 0$
3 $\xi(z) = 0$, $W_{d0} \neq 0$.
4 $\xi(z)$ constant for a long distance, then dropping to zero. The distance is long enough that the droplet spectrum reaches its asymptotic limit, and W_{d0} (if any) has completely died away.

The following notation is used:

1 $f_n(z') = \dfrac{(z')^n}{2^{n-1}(n-1)!} K_n(z')$, where $K_n(z')$ is the nth order modified Bessel function of the second kind.

2 $z' = 2\sqrt{3.915\lambda_d z} = 3.96\sqrt{\lambda_d z}$, dimensionless.

3 $\lambda_d = \dfrac{c}{\bar{d}_v}$.

4 $G(y) = \dfrac{30}{(\bar{d}_v)^3} y^2 e^{-\frac{3.915y}{\bar{d}_v}}$.

5 $G(\infty)$ is an indefinitely hardened spectrum. Only droplets of infinite size are remaining.

6 $z'' = 3.96\sqrt{\lambda_d(z - z_0)}$.

Fig. 8 shows the nature of the results for δ and W_d for the four cases. Fig. 9 shows how the droplet size spectrum changes along the length for cases 1, 2, and 4.

Table 1

$\xi(z)$ = constant

W_{do} = 0

Parameter	Solution	Values at $z = 0$	Values at $z = \infty$	From Equation
$\xi(z)$	E (constant)	E	E	-
$\delta(z)$	$E[1 - f_6(z')]$	0	E	10
$W_d(z)$	$\frac{1.532\,E}{\lambda_d}[1 - f_7(z')]$	0	$\frac{1.532\,E}{\lambda_d}$	12
$\lambda(z)$	$0.653\lambda_d \frac{[1 - f_6(z')]}{[1 - f_7(z')]}$	$0.783\lambda_d$	$0.653\lambda_d$	14
$G(y,z)$	$\frac{39.15\,y^3 e^{-\frac{3.915\,y}{\bar{d}_v}}}{(\bar{d}_v)^4} \frac{[1 - e^{-\frac{cz}{y}}]}{[1 - f_4(z')]}$	$G(y)$	$\frac{1.305\,y}{\bar{d}_v} G(y)$	17, 16
$(\frac{\bar{d}_{vz}}{\bar{d}_v})^3$	$2\frac{[1 - f_7(z')]}{[1 - f_4(z')]}$	1	2	18

Table 2

ξ = linearly increasing with z

W_{do} = 0

Parameter	Solution	Values at $z = 0$	Values at $z = \infty$	From Equation
$\xi(z)$	$E'z$ (linear)	0	$E'z$	-
$\delta(z)$	$E'\{z - \frac{1.532}{\lambda_d}[1 - f_7(z')]\}$	0	$E'[z - \frac{1.532}{\lambda_d}]$	10
$W_d(z)$	$\frac{1.532E'}{\lambda_d}\{z - \frac{1.787}{\lambda_d}[1 - f_8(z')]\}$	0	$\frac{1.532E'}{\lambda_d}[z - \frac{1.787}{\lambda_d}]$	12
$\lambda(z)$	$0.653\lambda_d \frac{z - \frac{1.532}{\lambda_d}[1 - f_7(z')]}{z - \frac{1.787}{\lambda_d}[1 - f_8(z')]}$	$0.783\lambda_d$	$0.653\lambda_d$	14
$G(y,z)$	$\frac{39.15\,y^3 e^{-\frac{3.915y}{\bar{d}_v}}}{(\bar{d}_v)^4} \frac{z - \frac{y}{c}[1 - e^{-\frac{cz}{y}}]}{z - \frac{1.022}{\lambda_d}[1 - f_5(z')]}$	$G(y)$	$\frac{1.305y}{\bar{d}_v} G(y)$	17,16
$(\frac{\bar{d}_{vz}}{\bar{d}_v})^3$	$2\frac{z - \frac{1.787}{\lambda_d}[1 - f_8(z')]}{z - \frac{1.022}{\lambda_d}[1 - f_5(z')]}$	1	2	18

Table 3

$\xi(z)$ = 0

W_{do} ≠ 0

Parameter	Solution	Values at $z = 0$	Values at $z = \infty$	From Equations
$\xi(z)$	0	0	0	-
$\delta(z)$	$0.783\lambda_d W_{do}[f_5(z')]$	$0.783\lambda_d W_{do}$	0	10
$W_d(z)$	$W_{do}[f_6(z')]$	W_{do}	0	12
$\lambda(z)$	$0.783\lambda_d \frac{[f_5(z')]}{[f_6(z')]}$	$0.783\lambda_d$	0	14
$G(y,z)$	$\frac{30\,y^2 e^{-\frac{3.915y}{\bar{d}_v}}}{(\bar{d}_v)^3} \frac{[e^{-\frac{cz}{y}}]}{[f_3(z')]}$	$G(y)$	$G(\infty)$	15,16
$(\frac{\bar{d}_{vz}}{\bar{d}_v})^3$	$\frac{[f_6(z')]}{[f_3(z')]}$	1	∞	18

Table 4

$\xi(z)$ = constant to $z = z_o$

= 0 thereafter

Parameter	Solution	Values at $z = z_o$	Values at $z = \infty$	From Equations
$\xi(z)$	$E[1 - u(z - z_o)]$	E for $z < z_o$ 0 for $z > z_o$	0	-
$\delta(z)$	$0.653\lambda_d W_d(z_o)\ [f_6(z'')]$	$0.653\lambda_d W_d(z_o)$	0	10
$W_d(z)$	$W_d(z_o)\ [f_7(z'')]$	$W_d(z_o)$	0	12
$\lambda(z)$	$0.653\lambda_d \dfrac{[f_6(z'')]}{[f_7(z'')]}$	$0.653\lambda_d$	0	14
$G(y,z)$	$\dfrac{39.15\ y^3 e^{-\frac{3.915\ y}{\bar{d}_v}}}{(\bar{d}_v)^4} \left[e^{-\frac{c(z - z_o)}{y}}\right] [f_4(z'')]$	$\dfrac{1.305\ y}{\bar{d}_v} G(y)$	$G(\infty)$	15, 16
$\left(\dfrac{\bar{d}_{vz}}{\bar{d}_v}\right)^3$	$2\dfrac{[f_7(z'')]}{[f_4(z'')]}$	2	∞	18

References

1 Hinkle, W. D., "A Study in Liquid Mass Transport in Annular Air-Water Flow," ScD thesis in Nuclear Engineering, M.I.T., Cambridge, Mass., 1967.

2 Schlichting, H., *Boundary Layer Theory*, McGraw-Hill, New York, 1960.

Table 5 Calculation of mass transfer coefficient

z	$W_1(z)^{(1)}$	$W_2(z)^{(2)}$	$\lambda_1 W_1(z)^{(3)}$	$\lambda_2 W_2(z)^{(4)}$	$\delta(z)^{(5)}$	$\lambda(z)^{(6)}$	$k(z)^{(7)}$
0	49.05	5.45	0.642	0.545	1.187	0.0217	0.731
3.18	47.0	3.93	0.609	0.393	1.002	0.01970	0.664
7.16	44.7	2.39	0.573	0.239	0.812	0.01726	0.582
12.73	41.6	1.53	0.526	0.153	0.679	0.01577	0.532
19.87	38.0	0.75	0.473	0.075	0.548	0.01416	0.477
28.6	34.1	0.34	0.418	0.035	0.453	0.01312	0.442
39.0	30.1	0.11	0.361	0.011	0.372	0.01232	0.416
50.9	26.2	0.03	0.308	0.003	0.311	0.01186	0.400
79.5	18.8	0	-	0	-	0.01116	0.376
115	12.9	0	-	0	-	0.01063	0.359

1. $W_1(z) = 0.90\ W_{do}[f_7(z')]$, lb/hr.
2. $W_2(z) = 0.10\ W_{do}[e^{-0.100\ z}]$, lb/hr.
3. $\lambda_1(z) = 0.01300 \dfrac{[f_6(z')]}{[f_7(z')]}$, in^{-1}.
4. $\lambda_2(z) = 0.100\ in^{-1}$.
5. $\xi(z) = \lambda_1 W_1 + \lambda_2 W_2$.
6. $\lambda(z) = \delta(z)/[W_1(z) + W_2(z)]$, in^{-1}.
7. $k(z) = \lambda(z)\dfrac{DV}{4} = \lambda(z)\left[\dfrac{1.25\ (108.0)}{4}\right]$, ft/sec.

3 Wade, W. F., "Gas-Atomization Studies by Means of a Rotating-Mirror Camera," ScD thesis in Mechanical Engineering, M.I.T., Cambridge, Mass., 1966.

4 Cousins, L. B., and Hewitt, G. F., "Liquid Phase Mass Transfer in Annular Two-Phase Flow: Droplet Deposition and Liquid Entrainment," AERE-R 5657, 1968.

5 Farmer, R. A., "Liquid Droplet Trajectories in Two-Phase Flow," PhD thesis in Nuclear Engineering, M.I.T., Cambridge, Mass., 1969.

S. Y. AHMAD
Research and Development Engineer,
Advanced Projects and Reactor Physics Division,
Atomic Energy of Canada Ltd.,
Chalk River, Ontario.
Mem. ASME

Axial Distribution of Bulk Temperature and Void Fraction in a Heated Channel With Inlet Subcooling

A theoretical model is developed to determine the axial temperature distribution of subcooled liquid. It is a simple function of a heat transfer and a condensation parameter. The proposed model satisfactorily correlates the measured bulk temperature profiles. The corresponding void fraction is computed by using a new empirical slip correlation, valid in both subcooled and bulk boiling regions. The resulting axial void profile has been compared (over the entire heated length) with steam and water data from six different sources, covering a wide range of pressure, mass flux, surface heat flux, inlet subcooling and channel geometry. The method gives satisfactory agreement with experimental data.

Introduction

The axial void fraction profile for a heated channel with inlet subcooling depends upon the distribution of bulk liquid temperature. Experiments have shown that the boiling subcooled liquid gives rise to a two-phase flow where vapor and subcooled liquid exist simultaneously at a given cross section in the channel. This indicates that for these cases the assumption of thermal equilibrium in calculating void fraction is not applicable. Void profiles in such channels are a complicated function of mass flux, heat flux, inlet subcooling, and channel geometry.

Because of the obvious relationship between void and reactivity it is important to calculate its distribution in liquid-cooled nuclear reactors. Several attempts have been made to determine the axial distribution of void fraction.

On the basis of photographic study Griffith, Clark, and Rohsenow [1][1] were first to propose two separate regions in subcooled boiling. This fundamental investigation has been the basis of most later work. For the first region they suggested that heat was removed simultaneously by single-phase heat transfer mechanism and by condensation of vapor bubbles. By assuming that bubbles always remain in the vicinity of the wall, Griffith, et al. proposed that in the second region the condensing area and therefore the condensing coefficient remained constant. However, recent flow-regime studies show that the bubbles do migrate into the main flow stream for the second subcooled region and the area of vapor condensation does not necessarily remain constant. Later Maurer [2] suggested a linear interpolation between the end of the wall voidage region defined by Griffith, et al. and the point of 40 percent void fraction on the modified Martinelli-Nelson void curve; this arbitrarily chosen boundary was based on experimental observations.

Houghton [3], by neglecting slip velocity, solved the coupled nonlinear differential equations representing the void fraction and the liquid temperature in a heated channel. The solution obtained was a complicated implicit function, and in some cases it predicted that the liquid phase was superheated by as much as 10 deg F—no experimental evidence of such superheating has yet been found.

Bowring [4] subsequently presented a very reasonable physical model to calculate void fraction in the subcooled boiling region. He also showed that for most of the experimental data then available the effect of bubble condensation was negligible—a finding contrary to Houghton's model. Bowring's finding that ϵ, the ratio of agitative heat flux to the evaporative, remains constant does not satisfy the boundary conditions of the subcooled region (because at the bulk boiling boundary $\epsilon = 0$); it thus gives a discontinuity in the void profile.

Lavigne [5] developed a Riccati-type differential equation for the distribution of quality in the subcooled boiling region by assuming that (*a*) the mass of vapor formed per unit length is a function of local subcooling, and (*b*) the rate of condensation of vapor is proportional to the product of its mass and local subcooling. The solution yielded a functional relationship between

[1] Numbers in brackets designate References at end of paper.

Contributed by the Heat Transfer Division for publication (without presentation) in the Journal of Heat Transfer. Manuscript received by the Heat Transfer Division, June 12, 1969; revised manuscript received February 13, 1970. Paper No. 70-HT-T.

true quality and thermodynamic quality. He briefly treated the problem of calculating void fractions, suggesting that the slip ratio can be taken equal to one. The condensation coefficient was simply assumed to be constant for given geometry and pressure.

Zuber, et al. [6] proposed that the bulk liquid temperature distribution be represented either by a hyperbolic tangent function or an exponential function because these functions satisfy the boundary conditions. They derived an expression which predicted void fraction under conditions of thermodynamic equilibrium as well as nonequilibrium.

A more comprehensive approach was next offered by Levy [7]. He determined the point of bubble departure using a bubble force balance and the single-phase liquid turbulent temperature distribution away from the wall. He then postulated a relationship between the true quality and the thermal equilibrium quality on the grounds that it satisfies the boundary conditions. Levy's function can be obtained as a special case of Lavigne's model if the bubble condensation is neglected and if it is assumed that subcooled boiling begins at the point of bubble detachment. For determination of void fraction Levy used the correlation proposed by Zuber and Findlay [8].

Recently Rouhani and Axelsson [9] calculated steam volume fraction in subcooled and quality boiling regions by assuming that (*a*) the supplied heat through the surface is removed by a vapor-liquid exchange mechanism, and (*b*) the rate of heat released by vapor condensation per unit time per unit length is directly proportional to local subcooling. The condensation coefficient was analyzed in detail, and the void correlation of Zuber and Findlay [8] was used. This method requires step-by-step numerical integration, and it does not yield satisfactory results in the case of very low mass flows ($G \leq 0.1 \times 10^6$ lb/hr · ft²).

A generalized subcooled voidage model was next put forward by Sha [10], and more recently a semianalytical correlation was developed by Schmidt [11]. Both these models assume unity slip ratio for the subcooled region.

It appears, therefore, that a more unified approach is needed in predicting volumetric vapor fraction profile along the heated channel. The object of this paper is to present uncomplicated expressions based on simple postulates, which will successfully predict void fraction under conditions of thermal equilibrium as well as nonequilibrium.

Analysis

Hypotheses and Derivation of Temperature Distribution Model. Three distinct regions are recognized in forced convection boiling—the highly subcooled region of wall voidage, the slightly subcooled region of bubble detachment, and the bulk boiling region. The mechanisms of heat removal from the surface in these regions are complex and not yet well understood. In this analysis it is hypothesized that the liquid-phase heat transfer coefficient is distributed as shown in Fig. 1, and it is postulated that:

1 Up to the point A—recognized by the onset of nucleation—the total heat flux is used to raise the liquid bulk temperature, and no vapor is formed. The liquid heat transfer coefficient has the single-phase value h_{sp}.

Nomenclature

A = dimensionless constant defined in equation (21)
A_f = flow area, ft²
B = dimensionless constant defined in equation (24)
B_K = constant defined in equation (18*a*), lb$^{3/2}$/ft$^{5/2}$ hr$^{3/2}$ deg F
C = proportionality constant, hr² · ft²/Btu²
C_0 = distribution parameter used in [8]
C_p = specific heat of liquid, Btu/lb · deg F
C_1 = dimensionless heat transfer parameter defined in equation (12*a*)
C_2 = dimensionless condensation parameter defined in equation (12*b*)
D_e = hydraulic diameter, ft
d = differential sign
G = mass flux, lb/hr ft²
g = acceleration due to gravity, ft/hr²
g_c = conversion factor, lb ft/lb hr²
H_f = liquid saturation enthalpy, Btu/lb
H_{in} = inlet liquid enthalpy, Btu/lb
h_{fg} = latent heat of vaporization, Btu/lb
h_l = subcooled boiling, liquid-phase heat transfer coefficient, Btu/hr ft² deg F
h_{sp} = single-phase heat transfer coefficient, Btu/hr ft² deg F
K = condensation constant defined in equation (18)
K_B = Bankoff's flow parameter used in [21]
K_l = coefficient of liquid thermal conductivity, Btu/ft hr deg F
l = distance along the heated channel such that $0 \leq l \leq l_H$, ft
l_D = position of the onset of bubble detachment measured from inlet, ft
l_H = total heated length, ft
l_{th} = distance at which thermal equilibrium quality becomes zero measured from inlet, ft
P = absolute pressure, lb/in²
P_h = heated perimeter, ft
R_d = radius of bubble at detachment in boiling flow, ft
R_0 = radius of bubble at detachment in pool boiling, ft
S = slip ratio
T = temperature of bulk liquid at position Z, deg F
T_d = temperature of bulk liquid at onset of detachment, deg F
T_{in} = temperature of bulk liquid at inlet, deg F
T_{sat} = saturation temperature, deg F
T_w = temperature of heated wall, deg F
T^+ = dimensionless temperature from reference [16]; = $(T - T_d)/(T_{sat} - T_d)$
ΔT = quenching potential or subcooling at position Z; = $T_{sat} - T$, deg F
ΔT_d = subcooling at onset of detachment; = $T_{sat} - T_d$, deg F
ΔT_{in} = subcooling at inlet; = $T_{sat} - T_{in}$, deg F
ΔT_{sat} = boiling potential; = $T_w - T_{sat}$, deg F
ΔT^* = dimensionless subcooling; = $\Delta T/\Delta T_d$
V_{in} = inlet liquid velocity, ft/hr
X = true vapor weight quality
X_d = thermal equilibrium quality at onset of detachment defined in equation (27)
X_{th} = thermal equilibrium weight quality (also called thermodynamic quality)
Z = position along the heated channel such that $l_D \leq Z \leq l_H$, ft
Z_{sb} = significant boiling length; = $l_H - l_D$, ft
Z^* = dimensionless length; = Z/Z_{sb}
Z^+ = dimensionless distance from reference [16]; = $(l - l_D)/(l_{th} - l_D)$
α = volumetric vapor fraction
ϵ = ratio of agitative heat flux to evaporative heat flux used in reference [4]
μ = dynamic viscosity of liquid, lb/hr ft
ρ = liquid density, lb/ft³
ρ_g = vapor density, lb/ft³
σ = surface tension of liquid, lb/ft
ϕ = heat flux, Btu/hr ft²
ϕ_l = quenching heat flux defined in equation (1), Btu/hr ft²
ϕ_λ = boiling heat flux defined in equation (1), Btu/hr ft²

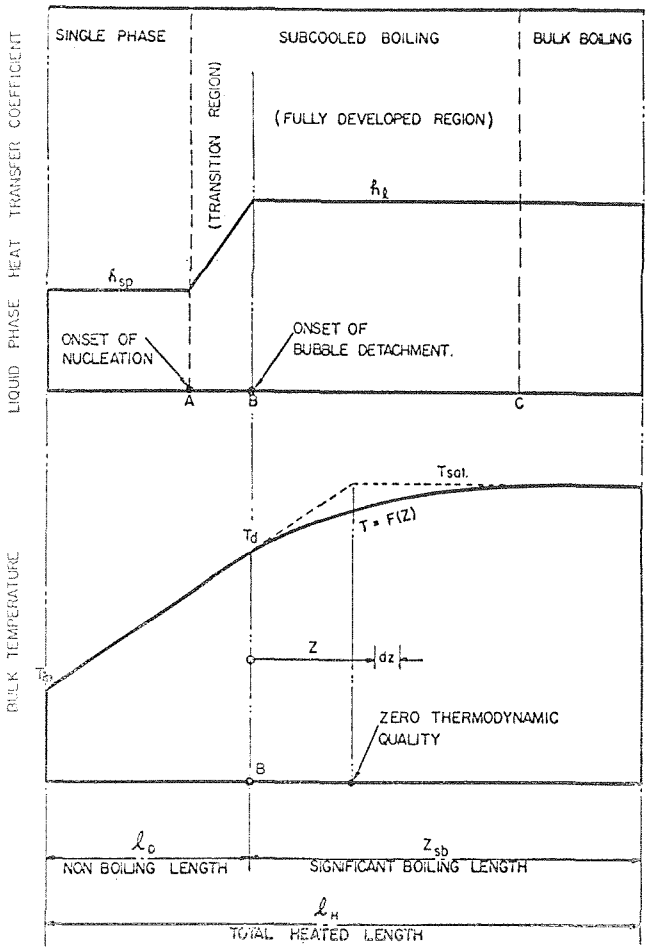

Fig. 1 Schematic representation of heat transfer coefficient and temperature distribution

2 The region AB is a transition region where bubbles are formed but do not grow large enough to detach from the wall and subsequently collapse at the surface. The bubble boundary layer thickness increases with the heated length until the point B is reached where bubbles start to depart from the wall. As a result the net amount of vapor generated to the left of B is very small. The total heat flux is still being utilized in raising the liquid bulk temperature. Because of the growth and collapse cycle of nucleating bubbles the liquid-phase heat transfer coefficient increases significantly from the single-phase value h_{sp} at point A to some maximum value h_l at point B.

3 To the right of B the bubbles detach from the heated wall and are swept downstream, recondensing slowly as they move through the region BC. In cases where the post-detachment condensation of bubbles is not significant, a rapid rise in void fraction is observed. In the region BC the heating of bulk liquid progresses simultaneously with production of vapor but at a reduced rate. The applied heat flux is thus divided into two components and can be written as

$$\phi = \phi_l + \phi_\lambda \tag{1}$$

where ϕ_l is the quenching heat flux, the part responsible for raising the temperature of liquid phase (it is directly proportional to quenching potential ΔT), and ϕ_λ is the boiling heat flux and is a function of boiling potential ΔT_{sat}.

4 At C, which denotes the inception of bulk boiling, the bulk liquid attains saturation, the quenching component of heat flux disappears, and the total heat flux is utilized in formation of vapor.

With the assumed model subsequently defining h_l as an average value of the liquid-phase heat transfer coefficient for region BC, the quenching heat flux can be expressed as

$$\phi_l = h_l \Delta T \tag{2}$$

To simplify the analysis the heated length can be divided into two regions: (a) the nonboiling length, and (b) the significant boiling length. The boundary between the two regions is characterized by the onset of bubble detachment. This point is taken as datum for determining the liquid temperature distribution. A schematic bulk temperature profile is shown in Fig. 1.

If the kinetic and potential energy and pressure terms are neglected, the energy balance for a length dZ of the heated channel with constant flow area can be written as:

For the quenching liquid phase:

$$\left[(1 - x) - dx + \frac{dm_c}{GA_f}\right] GA_f C_p[(T + dT) - T_d] + dxGA_f C_p(T_{sat} - T_d) = (1 - x)GA_f C_p(T - T_d) + dm_c[h_{fg} + C_p(T_{sat} - T_d)] + \phi_l P_h dZ \tag{3}$$

where dm_c is the differential rate of vapor condensation in lb/hr. By neglecting second-order terms the above equation simplifies to

$$(1 - x)C_p \frac{dT}{dZ} + \frac{dx}{dZ} C_p \Delta T = \frac{\phi_l P_h}{GA_f} + \frac{dm_c}{dZ}\left(\frac{h_{fg} + C_p \Delta T}{GA_f}\right) \tag{4}$$

For the boiling phase:

$$(x + dx)h_{fg}GA_f = xh_{fg}GA_f - dm_c \times [h_{fg} + C_p(T_{sat} - T)] + \phi_\lambda P_h dz \tag{5}$$

or

$$h_{fg}\frac{dx}{dZ} = \frac{\phi_\lambda P_h}{GA_f} - \frac{dm_c}{dZ}\left(\frac{h_{fg} + C_p \Delta T}{GA_f}\right) \tag{6}$$

Based on the dynamics of single bubbles, the rate of vapor condensation has been analyzed by the present author [12]. From this analysis the weight of vapor condensed per unit time per unit length is approximately given by

$$\frac{dm_c}{dZ} = K\Delta T\sqrt{Z} \tag{7}$$

where K is a condensation constant.

Combining equations (1), (2), (4), (6), and (7) yields

$$(1 - x)\frac{dT}{dZ} = \frac{\phi P_h}{GA_f C_p} - \frac{h_{fg} + C_p \Delta T}{h_{fg}}\left\{\frac{\phi P_h}{GA_f C_p} - \frac{h_l P_h}{GA_f C_p}\Delta T - K\left(\frac{h_{fg} + C_p \Delta T}{GA_f C_p}\right)\Delta T\sqrt{Z}\right\} \tag{8}$$

The above equation is a first-order nonlinear differential equation. It provides a general relationship for the temperature gradient, and it could be solved by numerical techniques. However, an analytical solution is more desirable and to approximate such a solution two simplifying assumptions are made:

1 $$(1 - x)\frac{dT}{dZ} \simeq \frac{dT}{dZ} \tag{9a}$$

At the beginning of void formation, where $\frac{dT}{dZ}$ is large, the value of x is very small (<1 part in 100 [5]); subsequently as x increases and becomes large the factor $\frac{dT}{dZ} \to 0$; hence the error caused will not be significant.

2 $$h_{fg} + C_p \Delta T \simeq h_{fg} \tag{9b}$$

Since $C_p\Delta T$ is much smaller than h_{fg} the error involved will not be appreciable. At pressures as high as 2000 psia, h_{fg} is at least 5 to 10 times larger than $C_p\Delta T$ [5].

Substitution of equations (9*a*) and (9*b*) into equation (8) reduces it to

$$\frac{dT}{dZ} = \frac{h_l P_h}{GA_f C_p}\Delta T + \frac{Kh_{fg}}{GA_f C_p}\Delta T\sqrt{Z} \tag{10}$$

The above equation is a simplified governing differential equation for the distribution of bulk temperature with initial conditions

$$Z = 0; \qquad \Delta T = \Delta T_d$$

Dimensionless Formulation and Solution. To facilitate analysis and discussion the following quantities are defined:

1 The significant boiling length $Z_{sb} = l_H - L_D$
2 The dimensionless distance $Z^* = Z/Z_{sb}$
3 The dimensionless subcooling $\Delta T^* = \Delta T/\Delta T_d$.

Expressed in these quantities the governing differential equation (10) and the initial conditions transform into

$$\frac{d(\Delta T^*)}{dZ^*} = -\left(C_1 + \tfrac{3}{2}C_2\sqrt{Z^*}\right)\Delta T^* \tag{11}$$

with initial condition $Z^* = 0$, $\Delta T^* = 1$, where C_1 and C_2 are dimensionless parameters and are defined as

$$C_1 \text{ (the heat transfer parameter)} = \frac{h_l P_h Z_{sb}}{GA_f C_p} \tag{12a}$$

$$C_2 \text{ (the condensation parameter)} = \tfrac{2}{3}\frac{Kh_{fg}Z_{sb}^{3/2}}{GA_f C_p} \tag{12b}$$

If the effect of temperature variations on the physical properties of the phases are neglected, the solution of equation (11) with its given initial condition can be readily obtained as

$$\Delta T^* = e^{-(C_1 Z^* + C_2 Z^{*3/2})} \tag{13}$$

The above equation explicitly expresses the distribution of bulk temperature in a heated channel with inlet subcooling.

Determination of Bulk Temperature. To obtain the temperature profile from equation (13), the values of C_1 and C_2 have to be calculated from equations (12*a*) and (12*b*) respectively. There remain three constants to be evaluated:

1 h_l the liquid-phase heat transfer coefficient
2 Z_{sb} the significant boiling length
3 K the condensation constant

The constants h_l and Z_{sb} both depend upon the successful prediction of the point of onset of bubble detachment. At this point the quenching heat flux has its maximum value, because the boiling component is approximately zero. Hence for a uniformly heated channel, the quenching component $\phi_l \simeq \phi$ at bubble detachment. Its substitution in equation (7) gives the liquid-phase heat transfer coefficient as

$$h_l = \frac{\phi}{\Delta T_d} \tag{14}$$

The corresponding position of the onset of bubble detachment is obtained by a simple heat balance, thus

$$l_D = \frac{GA_f}{\phi P_h} C_p(\Delta T_{\text{in}} - \Delta T_d) \tag{15}$$

and the significant boiling length Z_{sb} is expressed as

$$Z_{sb} = l_H - l_D = l_H - \frac{GA_f}{\phi P_h} C_p(\Delta T_{\text{in}} - \Delta T_d) \tag{16}$$

Both equations (14) and (16) can now be evaluated if ΔT_d, the subcooling at onset of detachment, is known. In the next section the methods of calculating ΔT_d are discussed.

Calculation of ΔT_d. Several models [4, 7, 13, 14] are available which predict the subcooling at the onset of bubble detachment. Any of these models could be employed for calculation of ΔT_d but either they do not apply with adequate accuracy, or the physical basis of the models is not compatible with detailed experimental measurements. To overcome these problems a new correlation for predicting onset of bubble detachment has been developed by the present author [15]. It is based on the assumptions presented here, and is thus compatible with this analysis. A detailed discussion of various models and their comparison with experimental data is also given in [15]. The correlation is

$$\frac{h_l D_e}{K_l} = 2.44\left(\frac{GD_e}{\mu}\right)^{1/2}\left(\frac{C_p\mu}{K_l}\right)^{1/3}\left(\frac{H_{\text{in}}}{H_f}\right)^{1/3}\left(\frac{h_{fg}}{H_f}\right)^{1/3} \tag{17}$$

An obvious advantage of such representation is that it is dimensionless. It has been successfully used for Freon-22, although the exponents were obtained from steam and water data only.

By combining equations (14) and (17) the value of ΔT_d is calculated. In some cases the predicted value of ΔT_d may exceed ΔT_{in}. This signifies that the bubble detachment occurs from the start of heated length, and correspondingly $Z_{sb} = l_H$, and $\Delta T_d = \Delta T_{\text{in}}$. It should be noted that the value of $\Delta T_d = \Delta T_{\text{in}}$ is not employed in the calculation of h_l—it is only used in defining the nondimensional quantities. Therefore, a feature of equation (17) is that it provides a physical meaning for the cases where the predicted subcooling at detachment is greater than the inlet subcooling.

Calculation of K. Analytical expressions for the evaluation of K have been obtained by the present author and the method of its calculation has been given in reference [12]. The constant K is expressed as

$$K = 2.79C\frac{B_K R_d P_h \phi^2}{\sqrt{GS}} \text{ (lb/hr deg F ft}^{3/2}\text{)} \tag{18}$$

where C (hr^2 ft^2/Btu^2), a proportionality constant, depends on the liquid and the type of heated surface, and is evaluated from the experimental data.

B_K is a function of fluid properties and it is weakly dependent on pressure.

$$B_K = \frac{(K_l\rho^2 C_p)^{1/2}}{h_{fg}}\left[\frac{gg_c(\rho - \rho_g)\sigma}{\rho^2}\right]^{1/4} \text{(lb}^{3/2}\text{/ft}^{5/2}\text{hr}^{3/2}\text{deg F)} \tag{18a}$$

Note: For steam and water B_K is nearly constant in the pressure range 1 bar to 100 bar and can be approximated by

$$\left.\begin{aligned} B_K &\simeq 71.0 \text{ (lb}^{3/2}\text{/ft}^{5/2}\text{ hr}^{3/2}\text{ deg F)} \\ &\text{for } 14.5 \le P \le 1500 \text{ psia} \end{aligned}\right\} \tag{18b}$$

R_d is the radius of bubble detachment in boiling flow; it is inversely proportional to both pressure and mass flux, and can be approximated from the following equations:

$$R_d/R_0 = 1/(1 + 2V_{\text{in}}{}^n) \tag{18c}$$

where R_0 is the radius of bubble at zero velocity (pool boiling) and is given by

$$R_0 = 1/[(\rho - \rho_g)/(0.09\sigma)]^{1/2} \text{ (ft)} \tag{18d}$$

and

$$\left.\begin{aligned} n &= 3/2 \text{ for } V_{\text{in}} < 1 \text{ ft/sec} \\ n &= 1/3 \text{ for } V_{\text{in}} \ge 1 \text{ ft/sec} \end{aligned}\right\}$$

It is admitted that in determining K the use of the equations given above would achieve only a limited success because of the

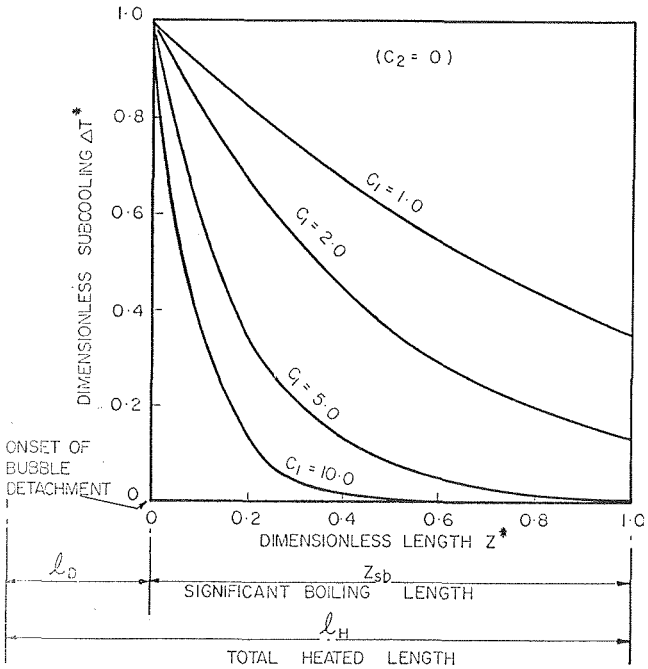

Fig. 2 Effect of heat transfer parameter C_1 on temperature distribution

lack of detailed knowledge regarding growth and nucleation processes. Alternatively, K can be treated as a macroscopic constant and by expressing it as a function of independent variables its value could be determined from experimental data. A similar procedure was adopted by Rouhani [9].

Effects of Operating Variables and Hydraulic Diameter on C_1 and C_2. According to this analysis the distribution of bulk temperature is governed by a heat transfer and a condensation parameter; see equation (13). The qualitative effect of operating variables—pressure, mass flux, heat flux, and inlet subcooling—on the two controlling parameters C_1 and C_2 can now be studied from equations (12a), (12b), (15), (16), (17), and (18). These equations show that C_1 and C_2 vary inversely with pressure but this dependence is quite weak. Strong influence of mass flux is observed in both and they decrease as the mass flux goes up. The effect of heat flux is also quite distinct and C_1 and C_2 increase with increasing heat flux. All operating parameters have a similar effect on both C_1 and C_2 but the former is less sensitive than the latter to changes in mass and heat flux. Inlet subcooling also enters the equations and as it increases C_1 and C_2 decrease; the effect becomes more significant at high degrees of subcooling.

Enlargement of hydraulic diameter reduces the heat transfer parameter C_1 but produces no significant effect on the condensation parameter C_2.

Effect of C_1 and C_2 on Temperature Profile. If the condensation is negligible the equation (13) reduces to

$$\Delta T^* = e^{-C_1 Z^*} \tag{13a}$$

The effect of the heat transfer parameter C_1 on the temperature distribution can now be deduced easily. As C_1 increases in value, ΔT^* converges rapidly to zero, i.e., the thermal equilibrium is restored. The parameter C_1 thus provides a measure of thermal equilibrium.

Computed values of theoretical liquid temperature profiles for $C_1 = 1.0$ to $C_1 = 10.0$ are shown in Fig. 2. It can be seen that for $C_1 \leq 5$ the entire boiling length remains under thermal nonequilibrium, and as the value of C_1 progressively exceeds 5, the thermal equilibrium is restored over greater fractions of the significant boiling length.

The condensation parameter C_2 has an effect similar to C_1, and it is the cumulative effect of both C_1 and C_2 which determines the thermal equilibrium. Large values of C_2 tend to restore the equilibrium and decrease the void fraction. However, if C_2 is not significant compared to C_1, its effect on temperature profile is minimal, and the temperature distribution can be determined from equation (13a).

Comparison of the Temperature Distribution Model With Experimental Data. Measurement of bulk temperature in thermal nonequilibrium two-phase flow is difficult and few data appear in the literature. Recently, however, an excellent and comprehensive experimental study of two-phase flow systems has been reported by Staub, et al. [16].

The equations developed in the present analysis were applied to Staub's data of reference [16]. It was found that for the range of reported test results the effect of post-detachment bubble condensation was only significant where

$$\text{Mass flux} \qquad G < 0.4 \times 10^6 \text{ lb/hr ft}^2$$

This criterion for effective condensation was maintained throughout the analysis.

A comparison of the temperature profiles predicted by equation (13) with Staub's data for three runs is shown in Fig. 3. For low mass flux runs ($G = 0.253 \times 10^6$ lb/hr ft^2) the value of

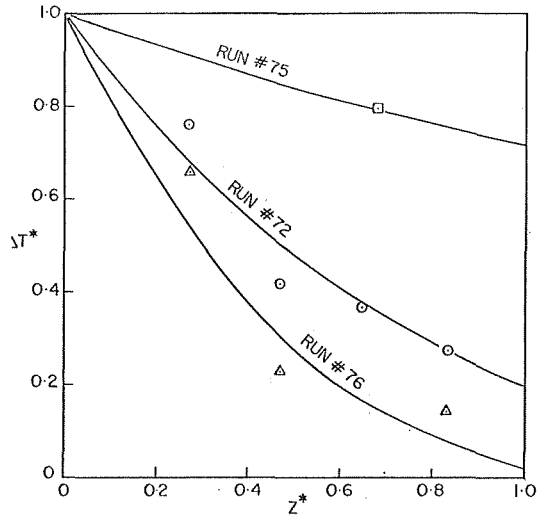

SYMBOL	RUN No.	P (p.s.i.a.)	G x 10⁻⁶ (lb/hr ft²)	Φ x 10⁻⁶ (lb/hr ft²)	ΔTin (°F)	REMARKS
⊙	1-3-T-72	44·8	0·253	0·117	16·5	C_1 = 1·04 C_2 = 0·55
⊡	1-3-T-75	44·8	2·041	0·249	20·5	C_1 = 0·32 NO CONDENSATION
△	1-3-T-76	44·8	0·253	0·234	21·8	C_1 = 1·06 C_2 = 2·20
———	PREDICTIONS FROM EQUATION (13)					

Fig. 3 Comparison of temperature distribution model with data of Staub, et al. at 45 psia

the proportionality constant C was obtained by applying equations (13) through (18) to a single data point of run I-3-T-72.

In view of the fact that the experimental bulk temperatures reported by Staub, et al. [16] were determined from the integration of the measured transverse temperature profiles and that large corrections were applied for conduction error and the presence of vapor phase, the agreement between theory and experiment is remarkably good.

Staub, et al. [16] have also successfully correlated their temperature profile data by a relationship of the following form:

$$T^+ = 1 - e^{-Z^+} \tag{19}$$

Reduced in the nomenclature of the present analysis it becomes

$$1 - \Delta T^* = 1 - e^{-AZ^*} \tag{20}$$

where A is a dimensionless quantity defined as

$$A = \frac{\phi P_h Z_{sb}}{GA_f C_p \Delta T_d} \tag{21}$$

Examination of equations (12a), (15), and (21) shows that if $\Delta T_d < \Delta T_{\text{in}}$ the heat transfer parameter $C_1 = A$. Consequently it can be noted from equations (13) and (20) that for the special case where

$\Delta T_d < \Delta T_{\text{in}}$, and

$C_2 = 0$ (i.e., post-detachment condensation is negligible)

the exponential function used by Staub and the model proposed in this analysis become identical.

In determining the temperature profile from the exponential relationship Staub replaces ΔT_d by ΔT_{in} if the predicted value of the former exceeds the latter. This occurs mainly at low mass flux and inadvertently compensates for the bubble condensation. Thus good approximation would result at low and medium inlet subcoolings. The present model makes no such approximation, using the predicted value of ΔT_d for all cases and taking bubble collapse into account.

Two formulations, the exponential function and the hyperbolic functions, were used by Staub, et al. since both satisfied the boundary conditions. In comparing them they state [16]:

1 That the measured axial liquid temperature distribution appeared to fall closer to the exponential relation than the hyperbolic formulation, and

2 That two-thirds of the data fall within ±10 percent of the exponential relation and all data fall within ±20 percent.

It has been shown that Staub's exponential function is simply a special case of the proposed model. By inference, therefore, it can be stated that the postulates presented in this analysis appear to be valid in the low pressure range covered by Staub, et al.

Experimental results at high pressures are not yet available for comparison. However, the proposed temperature distribution model can be tested using the many void fraction data reported in the literature.

Determination of Void Fraction Profile. The main object of developing a temperature distribution model has been the prediction of void fraction. To make such predictions it is first necessary to calculate (a) the true vapor weight quality, and (b) the slip ratio. Procedures for calculating quality and estimating slip are outlined below.

Calculation of True Vapor Weight Quality. The true quality X at any position Z can be obtained by combining equations (1), (4), and (5) and integrating with initial conditions $Z = 0$, $X = 0$. Thus for uniformly heated channels

$$X = \frac{\phi P_h Z/(GA_f) - C_p(\Delta T_d - \Delta T)}{h_{fg} + C_p \Delta T} \tag{22}$$

or in terms of nondimensional distance and subcooling it can be expressed as

$$X = (AZ^* - 1 + \Delta T^*)/(B + \Delta T^*) \tag{23}$$

where A and B are nondimensional quantities.

A is defined in equation (21) and B is given by

$$B = h_{fg}/(C_p \Delta T_d) \tag{24}$$

Equation (23) predicts true quality in both subcooled and bulk boiling regions. The corresponding thermal equilibrium vapor weight (or thermodynamic) quality X_{th} can be written as

$$X_{th} = (AZ^* - 1)/B \tag{25}$$

As discussed earlier, for cases where $\Delta T_d < \Delta T_{\text{in}}$ and for this case only, the heat transfer parameter $C_1 = A$. And for negligible post-detachment condensation, i.e., $C_2 = 0$, it can be shown by defining

$$X_d = -1/B = -(C_p \Delta T_d)/h_{fg} \tag{26}$$

and by combining equations (13a), (23), (25), and (26) that equation (23) transforms into

$$X = \frac{X_{th} - X_d e^{(X_{th}/X_d - 1)}}{1 - X_d e^{(X_{th}/X_d - 1)}} \tag{27}$$

The above analysis shows that the relationship presented by Lavigne [5] for the case of zero condensation, which was also independently proposed by Levy [7], and presented in the form

$$X = X_{th} - X_d e^{(X_{th}/X_d - 1)} \tag{28}$$

is a good approximation of equation (27) because for most cases

$$X_d e^{(X_{th}/X_d - 1)} \ll 1$$

Thus Lavigne's and Levy's function, equation (28), can be described as an approximation of the present model for the special case where

$$\Delta T_d < \Delta T_{\text{in}}$$

and post-detachment vapor condensation is negligible ($C_2 = 0$).

Evaluation of Slip Ratio. The choice of a suitable slip correlation is important for successful void predictions. Several models both theoretical and empirical are available in the literature, but to date their application to a wide range of data has not been successful. To formulate an adequate slip model the boundaries of flow regimes must be well defined at all pressure levels; current knowledge of such boundaries is still too limited.

A new empirical slip correlation has been developed. The following relationship appears to give the best fit of data in both subcooled and bulk boiling regions:

$$S = \left(\frac{\rho}{\rho_g}\right)^{0.205} \left(\frac{GD_e}{\mu}\right)^{-0.016} \tag{29}$$

for the range

$$P \geq 140 \text{ psia}$$

$$G \geq 0.3 \times 10^6 \text{ lb/hr ft}^2$$

It is recognized that slip ratio is also a function of quality but the dependence is only appreciable at very low qualities. Bartolomei and Georgescu [17] conclude from steam and water experiments at pressures of 200–500 psia and mass fluxes of 0.35×10^6 to 0.9×10^6 lb/hr ft^2 that:

1 The dependence of slip ratio on quality is only observed at lower qualities $X \leq 0.015$, for heated channels, and

2 The slip ratio decreases with increasing pressure and mass flux; a similar trend is shown by equation (29).

The validity of the proposed slip correlation is further substantiated by Thom's analysis [18]. He assumed that slip is simply a function of pressure and obtained a graphical correlation by plotting data of Haywood, et al. [19] and his own data [20]. This graphical relationship can be approximately expressed as

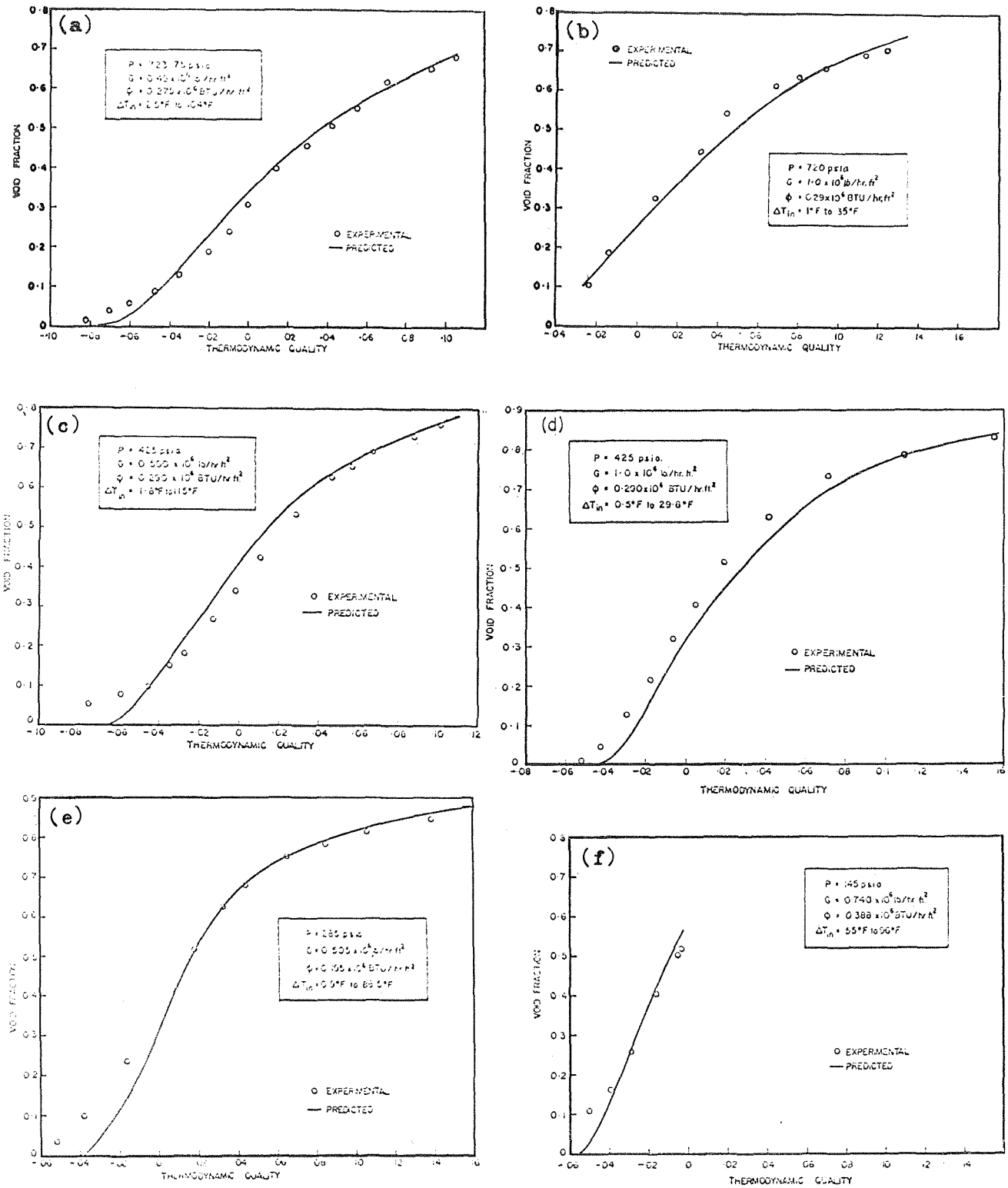

Fig. 4 Comparison of model with Rouhani's medium and high mass flux data

$$S = \left(\frac{\rho}{\rho_0}\right)^{0.2} \tag{30}$$

for 300 psi $\leq P \leq$ 3000 psia.

The proposed empirical correlation will predict a low value of void fraction at very low qualities. A correction of the type proposed by Haywood, et al. [19] could be applied to overcome this shortcoming. However, the effect of the error on the void profile is small and it would be a reasonable approximation to use equation (29) at all qualities.

Recently it has been proposed by Bankoff [21] and Zuber and Findlay [8] that the cross-sectional averaged void fraction is better represented in terms of phase distributions. For most practical cases ($P > 140$ psia and $G > 0.3 \times 10^6$ lb/hr ft^2) the local relative velocity between phases can be neglected—as implied in Bankoff's analysis—and the proposed correlation,

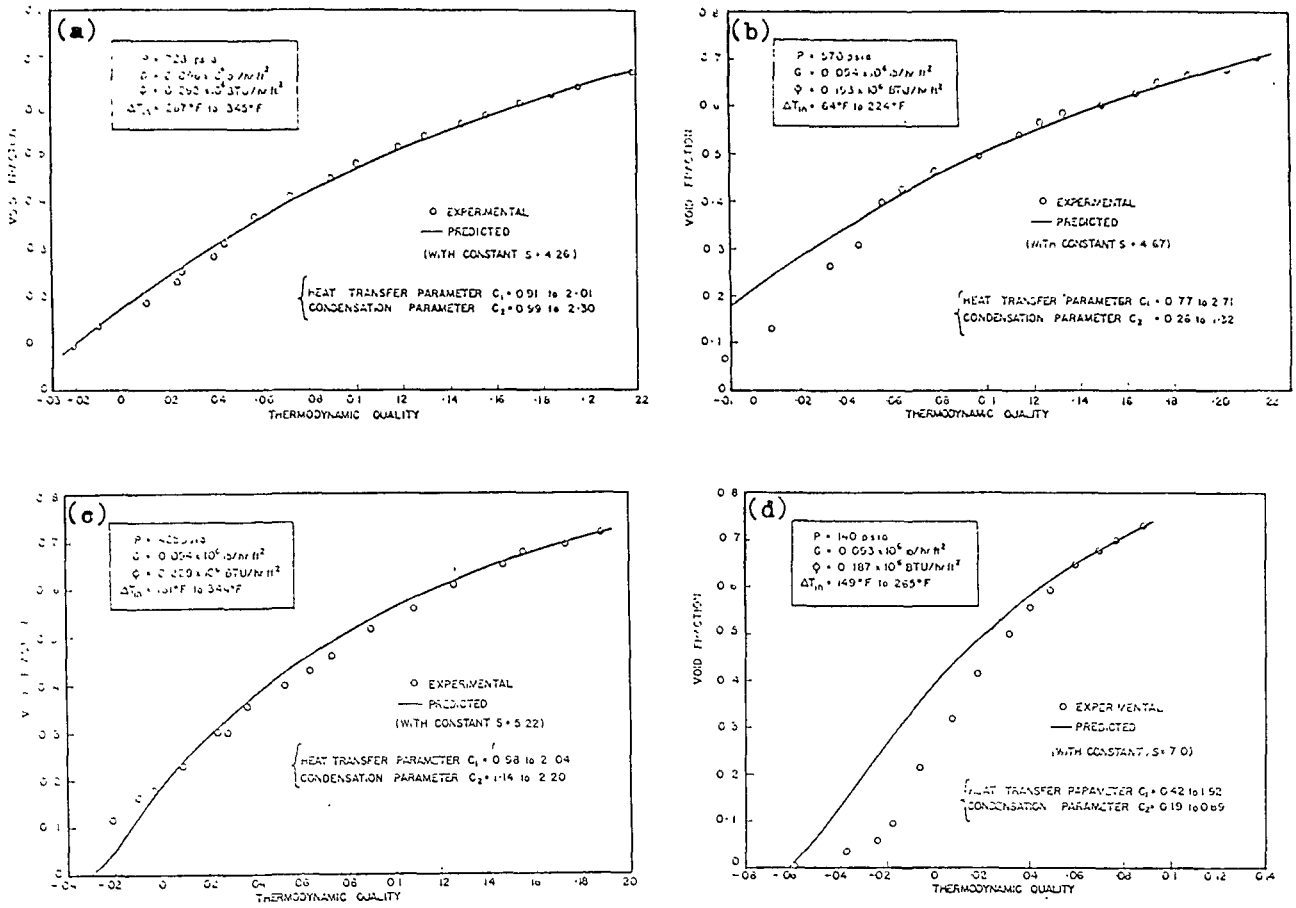

Fig. 5 Comparison of model with Rouhani's low mass flux data

equation (29), can therefore be rewritten in terms of Bankoff's flow parameter K_B and Zuber's distribution parameter C_0 as

$$K_B = \frac{1}{C_0} = 1 + b(1 - \alpha) \tag{29a}$$

where

$$b = \left[\frac{(GD_e/\mu)^{0.016}}{(\rho/\rho_g)^{0.203}} - 1\right] \tag{29b}$$

The above equation satisfies the boundary condition as $\alpha \to 1$ and is consistent with findings of Bankoff [21], Zuber and Findlay [8], and Staub, et al. [16]. However, it is unbounded as $\alpha \to 0$, and a correction may be applied to satisfy this boundary condition; but the effect of this error on the void profile is very small.

Résumé of Void Calculation Procedure. The following three-step method summarizes the analytical procedure discussed above to determine the void fraction profile in a heated channel with inlet subcooling. The method is simple, applicable to both the subcooled and bulk boiling regions, and does not necessitate defining the boundary between the two regions. With the exception of liquid specific heat, all fluid properties are taken at saturation temperature.

Step 1: (*a*) Determine h_l from equation (17); (*b*) calculate ΔT_d from equation (14); if $\Delta T_d > \Delta T_{in}$ then $\Delta T_d = \Delta T_{in}$; (*c*) calculate l_D and Z_{sb} from equations (15) and (16) respectively. (Note: This divides the heated length into nonboiling and significant boiling zones.)

Step 2: (*a*) Evaluate C_1 from equation (12*a*); (*b*) if condensation effect is insignificant then $C_2 = 0$, else, estimate the proportionality constant and compute K from equations (18) through (18*d*), then calculate C_2 from equation (12*b*); (*c*) determine A and B from equations (21) and (24) respectively.

Step 3: For any position l in the heated channel (where $0 \leq l \leq l_H$): (*a*) if $l \leq l_D$ then $Z^* = 0$, else, $Z^* = (l - l_D)/Z_{sb}$; (*b*) calculate the corresponding ΔT^* from equation (13); subsequently determine the true vapor weight quality X from equation (23); (*c*) by estimating slip ratio S from equation (29) or otherwise, compute the corresponding vapor volumetric fraction α from

$$\alpha = \frac{X}{X + (\rho_g/\rho)S(1 - X)} \tag{31}$$

Comparison of Void Prediction With Experimental Data

The methods described in the preceding section were applied to experimental data of references [2, 22–26].

The examination of data showed that the aforementioned criterion of insignificant post-detachment condensation (i.e., $C_2 \simeq 0$ for $G \geq 0.4 \times 10^6$ lb/hr ft^2) was applicable to the entire range of data analyzed. Accordingly the effect of post-detachment bubble condensation was ignored in all cases. The only exception was presented by the very low mass flux ($G \leq 0.1 \times 10^6$ lb/hr ft^2) data of reference [22], where appropriate calculations were made to include the condensation effect.

Fig. 4 shows the comparison of the present model with the experimental data of Rouhani [22] for medium and high mass flux cases ($G = 0.5$ to 1.0×10^6 lb/hr ft^2). It can be seen that the present method accurately predicts void fraction over the entire range of pressure (145 to 720 psia) for medium and high mass flux runs. While the agreement is excellent at high pressures, the model tends to underestimate the void at very low qualities for

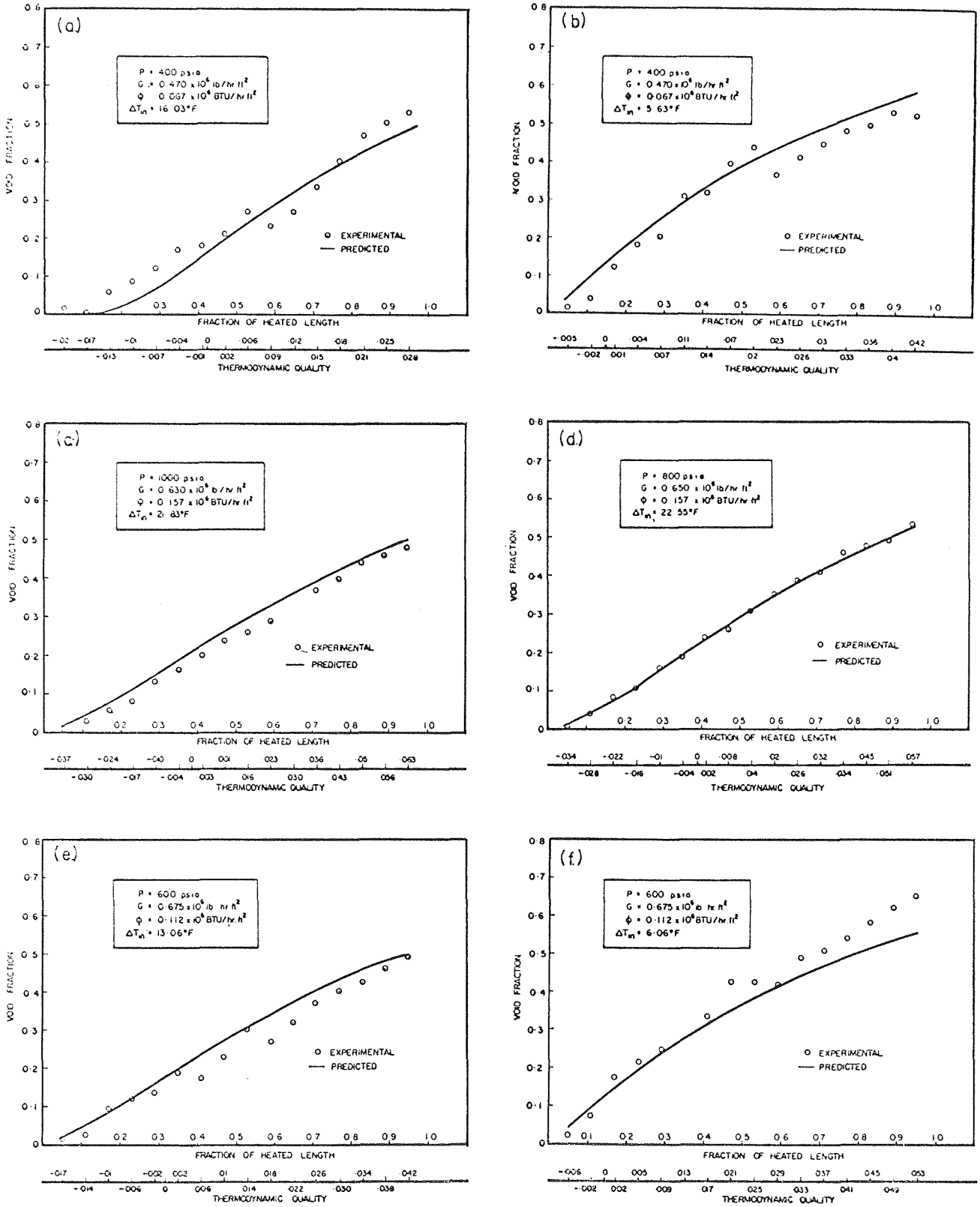

Fig. 6 Comparison of model with Christensen's data

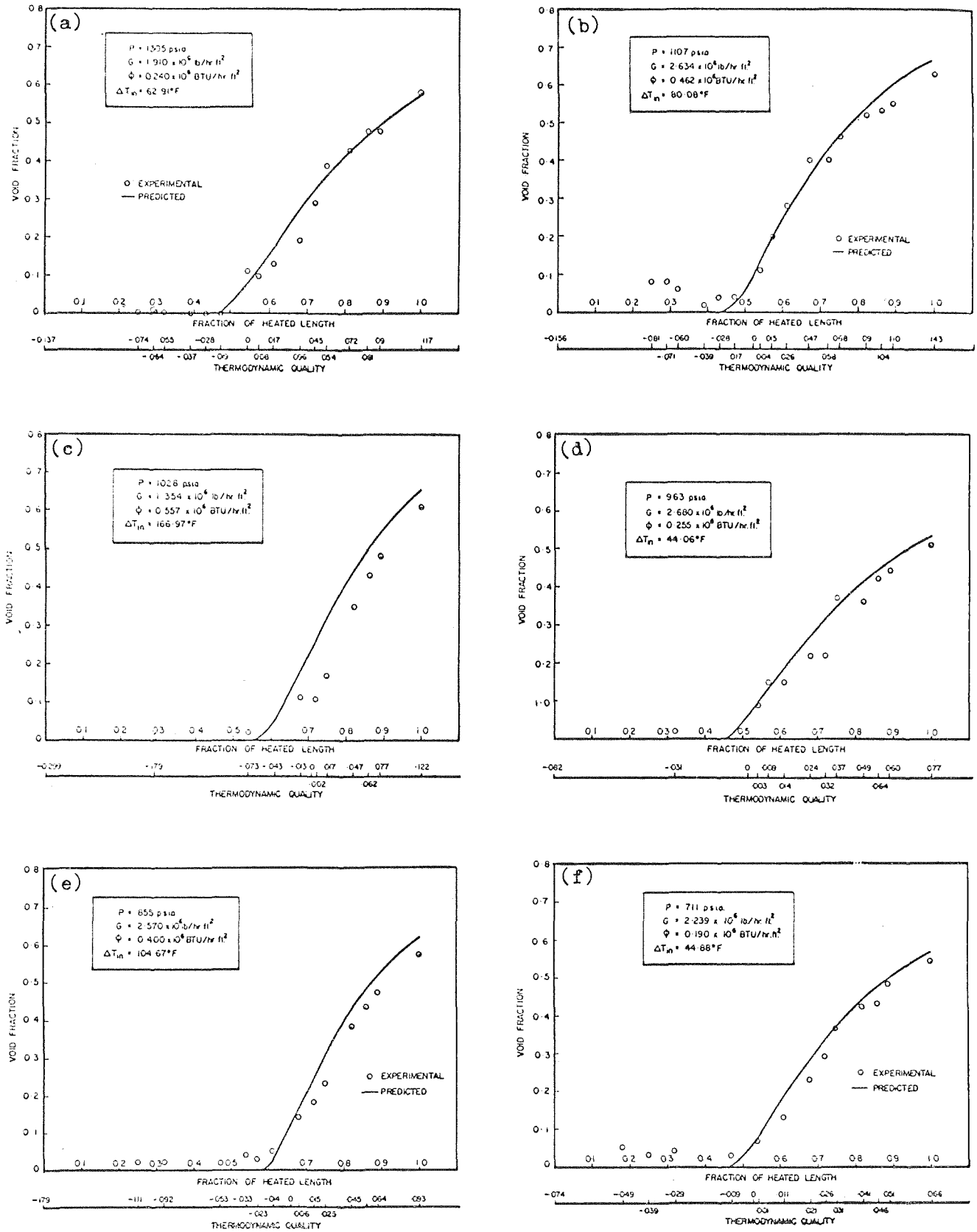

Fig. 7 Comparison of model with data of Foglia, et al.

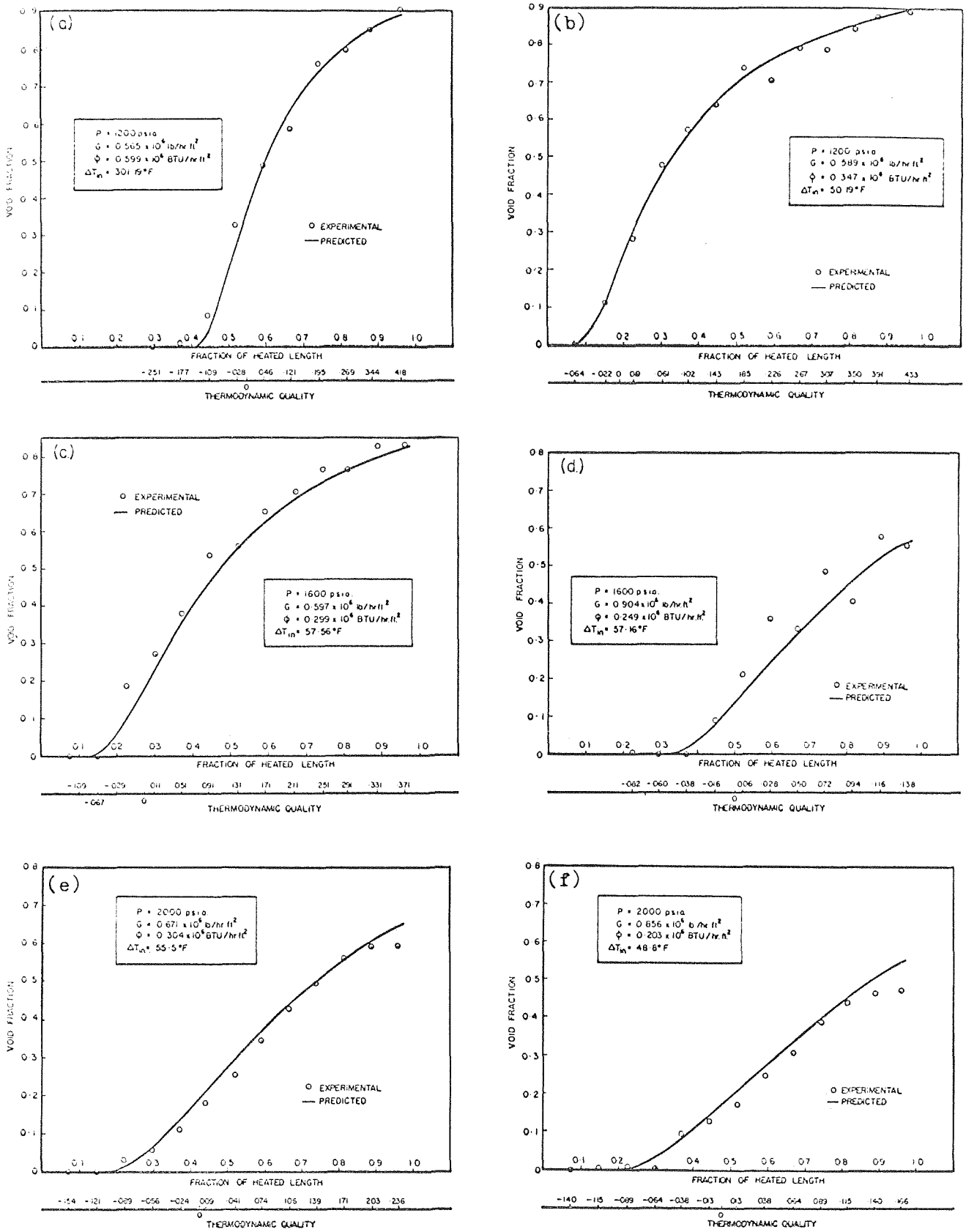

Fig. 8 Comparison of model with Maurer's data

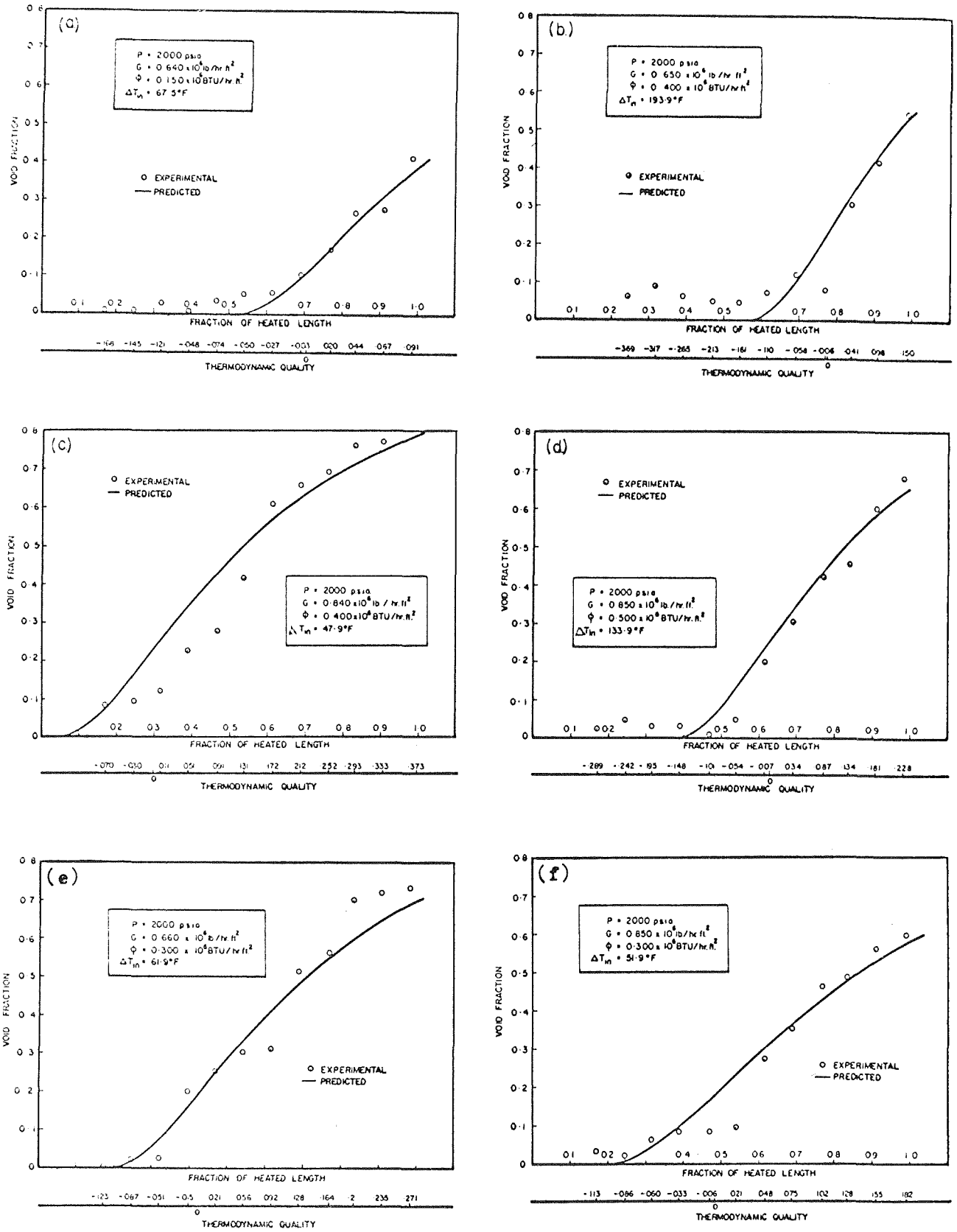

Fig. 9 Comparison of model with data of Egen, et al.

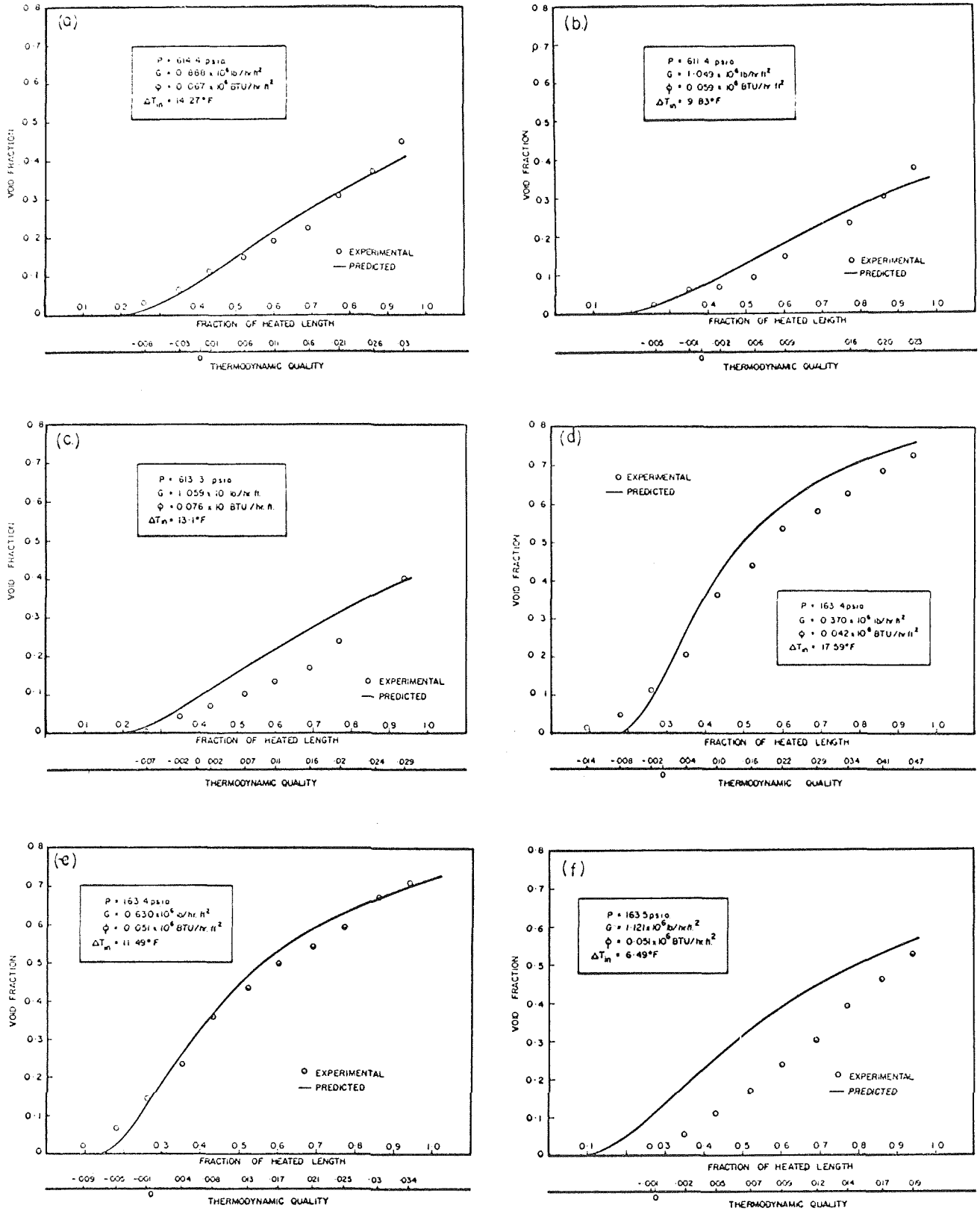

Fig. 10 Comparison of model with data of Marchaterre, et al.

low-pressure cases. This was expected because of the assumption of constant slip ratio.

Rouhani's [22] very low mass flux data ($G \leq 0.1 \times 10^6$ lb/hr ft^2) presented a special problem. It was outside the mass flux range of the proposed slip correlation, equation (29). Hence a constant value of slip was assumed, based on the bulk boiling data. The condensation effect was pronounced at this low level of mass flux and in order to evaluate the condensation constant K from equation (18), the value of proportionality constant C was estimated as $C = 0.15 \times 10^{-6}$ (hr ft/Btu)^2. The ranges of the heat transfer parameter C_1 and the condensation parameter C_2, together with the assumed value of slip, are shown in Fig. 5*a–d*, the low mass flux cases.

In view of the uncertainties in determination of the condensation constant K, caused by lack of detailed knowledge regarding the growth and nucleation processes, the agreement for very low mass flux runs is surprisingly good at high pressures (Fig. 5*a, b, c*); at low pressures ($P \leq 280$ psia) the method tends to overestimate the void fraction in the subcooled region (Fig. 5*d*). This results from the inability of the bubble collapse function used in reference [12] to account for the influence of translational velocity on the bubble collapse. Wittke and Chao [27] have shown that the faster the bubble translates the more rapidly it collapses. Since reduction in pressure increases slip ratio, the bubbles translate faster. Consequently, the actual rate of vapor condensation is much higher and the void fractions are lower than predicted by present analysis.

What is most encouraging is the fact that the present method correctly predicts the experimentally observed trends of Rouhani's void fraction data [22] over the entire range of pressure (10 to 50 bar) and mass flux (0.09 to 1.0 $\times$ 10^6 lb/hr ft^2). Attempts by Levy [7] and Rouhani [9] to correlate the entire flow range of Rouhani's data [22] have not been successful.

The predictions of the proposed model have been further compared with data of Christensen [23] in Fig. 6, Foglia, et al. [24] in Fig. 7, Maurer [2] in Fig. 8, Egen, et al. [25] in Fig. 9, and Marchaterre, et al. [26] in Fig. 10. It may be seen that the model's correspondence with experimental data is excellent over a wide range of pressure (140 to 2000 psia) and mass flux (0.37 to 2.68 $\times$ 10^6 lb/hr ft^2).

It was noted that in a few cases for data of Marchaterre, et al. [26], the model's predictions are higher (Fig. 10*c, d, f*). Two important points emerge from the examination of the poorly correlated cases: (*a*) Most of the data are in the bulk boiling, low-quality region, and (*b*) the measured slip shows a typical trend which does not fit in with any other correlation. These slip values first increase with quality, attain a maximum value, then decrease with quality at the exit of the channel. The reason for this is not clear. However, the conclusions on the comparison of predicted and experimental void fraction data of Marchaterre are consistent with those reached by Gross [28].

Conclusions

1 A method has been developed which predicts a continuous volumetric vapor fraction profile for both subcooled and bulk boiling regions of a heated channel.

2 The method gives satisfactory agreement with experimental void data for various geometries and operating conditions.

3 An analytical expression is derived to predict the bulk temperature profile in a heated channel with inlet subcooling. The effect of bubble collapse on temperature distribution is taken into account. It is shown that the exponential function used by Staub, et al. and the true quality function proposed by Lavigne and Levy are special cases of the proposed model.

4 Satisfactory agreement is shown between the predicted and measured temperature profile.

5 Because of lack of knowledge on flow regime boundaries a tentative generalized correlation for predicting slip has been obtained. This empirical correlation does not account for the effect of quality; nevertheless, the results show that its void predictions are in satisfactory agreement with experimental data. The proposed slip correlation is also expressed in terms of Bankoff's flow parameter and Zuber's distribution parameter. This relationship is consistent with the findings of Bankoff [21], Zuber and Findlay [8], and Staub, et al. [16].

6 A systematic and extensive effort, both analytical and experimental, is required for the understanding of flow regime boundaries and the behavior of slip ratios. Extension of the work reported in reference [16] is needed to obtain simultaneous measurements of velocity, temperature, and void profiles for several geometries and a wide range of operating parameters.

References

1 Griffith, P., Clark, J. A., and Rohsenow, W. M., "Void Volumes in Subcooled Boiling Systems," ASME Paper No. 58-HT-19, 1958.

2 Maurer, G. W., "A Method of Predicting Steady-State Boiling Vapor Fractions in Reactor Coolant Channels," WAPD-BT-19, 1960.

3 Houghton, G., "An Analysis of Vapor Void Profiles in Heated Channels," *Nuclear Science and Engineering*, Vol. 12, No. 3, 1962.

4 Bowring, R. W., "Physical Model Based on Bubble Detachment, and Calculation of Steam Voidage in the Subcooled Region of a Heated Channel," *Institutt for Atomenergi, HPR 10, Halden*, Norway, 1962.

5 Lavigne, P., "Modele d'Evolution du Titre et du Tause de Vide en Ebullition Locale et Zone de Transition," (in French), C.E.A. 2365, 1963.

6 Zuber, N., Staub, F. W., and Bijwaard, G., "Vapor Void Fraction in Subcooled Boiling and Saturated Boiling Systems," *Proceedings 3rd International Heat Transfer Conference*, Chicago, Ill., Paper No. 154, Vol. 5, 1966, p. 24.

7 Levy, S., "Forced Convection Subcooled Boiling—Prediction of Vapor Volumetric Fraction," *International Journal of Heat and Mass Transfer*, Vol. 10, 1967, pp. 951–965.

8 Zuber, N., and Findlay, J. A., "Average Volumetric Concentration in Two-Phase Flow Systems," JOURNAL OF HEAT TRANSFER, TRANS. ASME, Series C, Vol. 87, No. 4, Nov. 1965, pp. 453–468.

9 Rouhani, S. Z., and Axelsson, E., "Calculation of Void Volume Fraction in Subcooled and Quality Boiling Regions," *International Journal of Heat and Mass Transfer*, Vol. 13, No. 2, 1970, pp. 383–393.

10 Sha, W. T., "A Generalized Boiling Void Model," WCAP-7041, 1967.

11 Schmidt, R., "A New Approach to Void Generation in Subcooled Boiling," *ANS Transactions*, Vol. 11, No. 1, 1968.

12 Ahmad, S. Y., "Calculation of the Rate of Vapor Condensation in the Subcooled Region," unpublished notes.

13 Staub, F. W., "The Void Fraction in Subcooled Boiling - Prediction of the Initial Point of Net Vapor Generation," JOURNAL OF HEAT TRANSFER, TRANS. ASME, Series C, Vol. 90, No. 1, Feb. 1968, pp. 151–157.

14 Costa, J., "Mésure de la Perte de Pression per Acceleration et Étude de l'Apparition du Tanx de Vide en Ébullition Locale a Basse Pression," (in French), Note TT No. 244, CENG, Grenoble, 1967.

15 Ahmad, S. Y., "Forced Convection Subcooled Boiling - Prediction of the Onset of Bubble Detachment," unpublished CRNL report, 1969.

16 Staub, F. W., Walmet, G. E., and Niemi, R. O., "Heat Transfer and Hydraulics—The Effects of Subcooled Voids," Final report, NYO-3679-8, 1969.

17 Bartolomei, G. G., and Georgescu, R., "Experimental Study of the Hydrodynamics of Two-Phase Flows in Vertical Pipes," translated by J. E. Barker, *AERE—Trans.*, 1076, 1967.

18 Thom, J. R. S., "Prediction of Pressure Drop During Forced Circulation Boiling of Water," *International Journal of Heat and Mass Transfer*, Vol. 7, 1964, pp. 709–724.

19 Haywood, R. W., Knights, G. A., Middleton, G. E., and Thom, J. R. S., "An Experimental Study of the Flow Conditions and Pressure Drop of Steam-Water Mixtures at High Pressures in Heated and Unheated Tubes," *Proceedings Institution of Mechanical Engineers*, Vol. 175, 1961, pp. 669–748.

20 Thom, J. R. S., "A Study of Pressure Drop and Allied Phenomena During the Flow of a Fluid in the Presence and Absence of Vaporization," Cambridge University Engineering Laboratory, PhD thesis, 1959.

21 Bankoff, S. G., "A Variable Density, Single-Fluid Model for Two-Phase Flow With Particular Reference to Steam-Water Flow," JOURNAL OF HEAT TRANSFER, TRANS. ASME, Series C, Vol. 82, No. 4, Nov. 1960, pp. 265–272.

22 Rouhani, S. Z., "Void Measurements in the Regions of Subcooled and Low Quality Boiling," AE-239, Part 2, 1966.

23 Christensen, H., "Power to Void Transfer Function," ANL-6385, 1961.

24 Foglia, J. J., Peter, F. G., Epstein, H. M., Wooton, R. O., Dingie, D. A., and Chastain, J. W., "Boiling Water Void Distribution and Slip Ratio in Heated Channels," BMI-1517, 1961.
25 Egen, R. A., Dingie, D. A., and Chastain, J. W., "Vapor Formation and Behavior in Boiling Heat Transfer," BMI-1163, 1957.
26 Marchaterre, J. F., Petrick, M., Lottes, P. A., Weatherhead, R. J., and Flinn, W. S., "Natural and Forced-Circulation Boiling Studies," ANL-5735, 1960.
27 Wittke, D. D., and Chao, B. T., "Collapse of Vapor Bubbles With Translatory Motion," ASME Paper No. 66-WA/HT-12, 1966.
28 Gross, T. H., "Vapor Void Fraction and Static Pressure Drop in Forced Convection Boiling with Thermal Nonequilibrium," PhD thesis, Carnegie-Mellon University, Pittsburgh, Pa., 1968.

W. Z. BLACK
Assistant Professor,
School of Mechanical Engineering,
Georgia Institute of Technology,
Atlanta, Ga.

R. J. SCHOENHALS
Professor of Mechanical Engineering,
Purdue University, Lafayette, Ind.

An Experimental Study of Radiation Heat Transfer From Parallel Plates With Direction-Dependent Properties

An experimental study of radiation heat transfer from opposing parallel plates is described. Surfaces composed of many small grooves were used to fabricate plates having direction-dependent radiation properties. These plates possessed a collimated emission pattern which was found to influence significantly the heat transfer rate, the largest observed effects being approximately 40 percent. It appears that somewhat larger alterations could be achieved with further effort. The measurements obtained in this study establish the potential value of specially prepared surfaces for certain applications requiring improved thermal performance.

Introduction

THIS paper describes an experimental investigation of radiation heat transfer from opposing parallel plates with directionally dependent radiation properties, Fig. 1. Each specially prepared directional surface contained many V-groove cavities as shown in Fig. 2. By carefully choosing the various cavity parameters (Fig. 3), such a surface can be made to produce emission which is strongest for small η-values, and is correspondingly weaker at large values of η. For purposes of comparison it should be noted that an ideal diffuse surface exhibits a uniform intensity of emission in all directions.

Surfaces which can be made to produce highly collimated emission patterns offer a means for achieving improved thermal performance of some systems. For example, excessive heat rejection from certain kinds of space vehicles might be considerably reduced if emission from the various surfaces of the vehicle could be collimated so that most of the emitted energy would impinge on other parts of its structure. Conversely, a vehicle requiring a greater cooling rate could be fabricated so that collimated emission from its surfaces would be directed away from its structural components. These kinds of applications have been discussed by Clausen and Neu [1].[1] Favorable thermal performance relies heavily upon the capability to produce surfaces which possess strongly directional radiation properties. Hering [2] has performed detailed calculations for simply arranged surfaces considering the directional properties of both metallic and nonmetallic materials. The results show that total heat transfer rates, determined on this precise directional basis, usually do not differ significantly from corresponding rates calculated when the surfaces are assumed to be diffuse. This is understandable because the deviations from perfectly diffuse emission behavior are slight except for rays making very large angles with the surface normal. Thus it appears that ordinary surfaces tend to

Contributed by the Heat Transfer Division and presented at the Space Technology and Heat Transfer Conference, Los Angeles, Calif., June 21–24, 1970, of THE AMERICAN SOCIETY OF MECHANICAL ENGINEERS. Manuscript received by the Heat Transfer Division, June 13, 1969. Paper No. 70-HT/SpT-1.

[1] Numbers in brackets designate References at end of paper.

Nomenclature

A = area
b = distance from apex to base of cavity
B = distance from apex to top of cavity
h = separation distance between parallel plates
L = length of parallel plates
W = width of parallel plates
T = temperature
ϵ = emissivity
$\epsilon(\eta)$ = directional emissivity
η = angle between an exit ray projected on the plane of Fig. 3 and the normal to the cavity opening area
θ = cavity opening angle
σ = Stefan-Boltzmann constant

Subscripts

c = cold surroundings
h = hemispherical
L = limiting value
opt = optimum value
p = parallel plate
s = cavity side wall

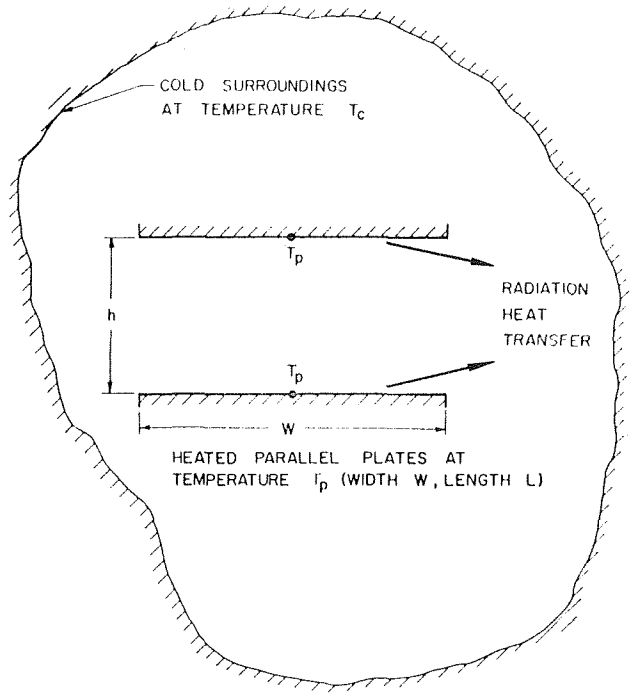

Fig. 1 Surface arrangement for experimental investigation

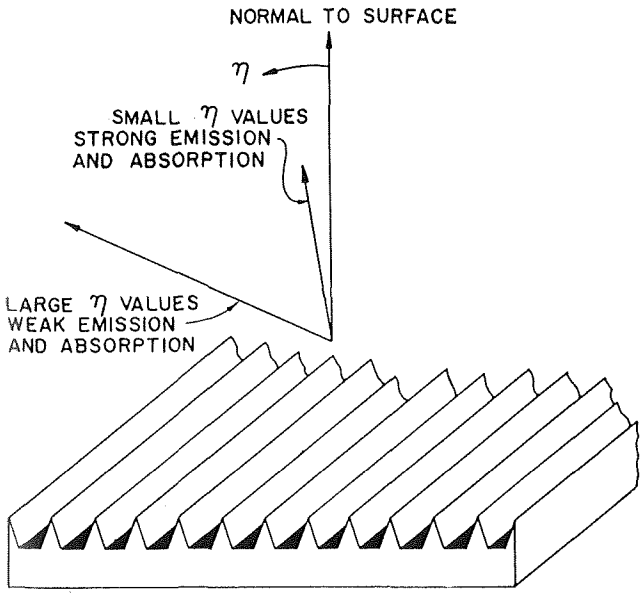

Fig. 2 A directional surface composed of V-groove cavities

scatter most of their emitted energy with a nearly uniform intensity in all directions. As a result, the small magnitude of directional dependency of these surfaces is not sufficient to cause sizeable alterations in the resulting heat transfer rates.

From the previous discussion it is clear that some type of specially prepared surface must be used if radiation heat transfer rates are to be appreciably affected, and this surface must certainly possess radiation properties which are strongly direction-dependent. The directional surfaces fabricated for the present experimental study were found to reduce radiation heat transfer rates by various amounts, depending on geometry, up to a maximum of about 40 percent. This figure represents a very significant reduction and thus establishes the potential value of specially prepared surfaces. It is also concluded, however, that further development is needed in order to produce surfaces which yield more highly collimated emission patterns than were obtained with the V-groove surfaces used in this investigation.

To the authors' knowledge, the experimental data given in this paper represent the first available measurements of radiation heat transfer rates from directional surfaces formed from V-groove cavities. Before proceeding to the description of the experimental program it is appropriate to develop the approach in more detail. The following section provides further discussion of the problem and also presents some information related to the radiation properties of V-groove cavities.

Approach to the Problem

The system illustrated in Fig. 1 was chosen for this study because of its symmetry and simple geometry. These features were desirable from the standpoint of experimentation, and also for ease of interpretation of the measurements. It should be noted at the outset that if the two parallel surfaces are maintained at the same temperature, there can be no net radiation heat transfer between them. For simplicity it is assumed in this discussion that the surroundings are very large relative to the dimensions of the parallel plate system so that emitted radiation which escapes from the plates can be considered to be completely absorbed by the surroundings.

Consider the problem of minimizing heat rejection from the parallel surfaces, due to their radiant emission, to the surroundings. Hypothetically the rate of rejection could be reduced to zero if each surface were to exhibit perfectly collimated emission, provided that the reflected rays behaved similarly. This can be verified by referring to Fig. 4(*a*) which illustrates a situation in which all of the emitted and reflected rays are perpendicular to the two surfaces. If this were the case, then the energy emitted by one surface would be absorbed partially by the opposite surface, and the remainder would be reabsorbed by itself. These absorption processes would occur by means of an infinite number of multiple reflections between the two surfaces. None of the emitted or reflected rays would escape from the parallel plate system, and the rejection rate to the surroundings would therefore be zero. It cannot be expected that any actual surface would behave in this manner, however, so the situation described above

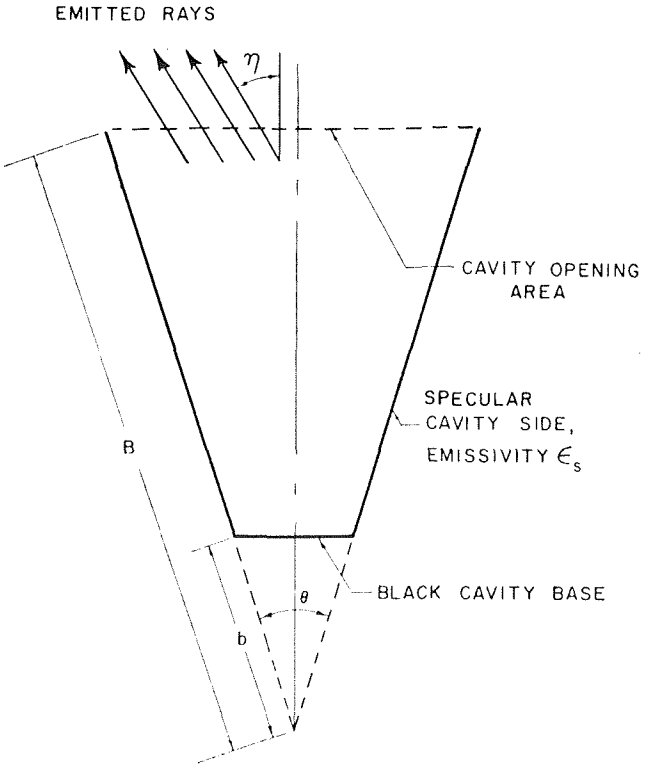

Fig. 3 V-groove geometry

represents an idealized limit which might be approached in reality, but could never be completely attained.

Fig. 4(*b*) illustrates the general case in which a portion of the radiant emission by the lower surface escapes to the surroundings, while the remaining emission strikes the upper surface and is partially absorbed. The energy reflected from the upper surface is also divided into two components, that which escapes to the surroundings and that which returns again to the lower plate. As this process of many reflections between the two surfaces proceeds, the multiple reflected beam becomes weaker and weaker due to absorption and rejection to the surroundings. The initially emitted beam is the strongest, and the greatest absorption rate occurs when the non-rejected portion of this beam is first incident on the upper plate. For this reason it would be expected that the fraction of total emission reabsorbed by the plates would be increased, and the fraction rejected to the surroundings correspondingly decreased, if the emitted energy were distributed most strongly in the near-vertical rays (Fig. 4(*b*)). This would cause almost all of the initial emission of each plate to strike the opposite surface, and the remaining portion of this emission escaping directly to the surroundings would be very small. In addition, if the directional emissivities were quite large for the near-normal directions, then according to Kirchhoff's law the directional absorptivities for these directions would also be large. Thus, the heavy concentration of near-normal emission would immediately strike the opposite surface and be largely absorbed. On the basis of the above discussion it would appear that the total rejection could be substantially reduced by proper consideration of the directional emission properties alone.

Perlmutter and Howell [3] were first to point out that emission from the black base of the cavity shown in Fig. 3 is channeled by the specularly reflecting sides so that the intensity of radiation leaving the cavity is strongest for rays which are nearly vertical. Conversely, the intensity levels were shown to be very low for rays making large angles with the normal to the cavity opening area (that is, for rays which approach a nearly horizontal orientation). Some directional emissivity results were given based on the assumption that the reflecting walls do not absorb or emit. Experiments by Brandenberg and Clausen [4] later substantiated the emission characteristics described by Perlmutter and Howell.

The authors of the present paper extended the analysis of Perlmutter and Howell to include absorbing and emitting side walls based on a detailed study of the variation of the local directional emissivity [5]. The resulting predictions of emission properties were also verified experimentally. Calculations of the radiation heat transfer rate from a surface composed of V-groove

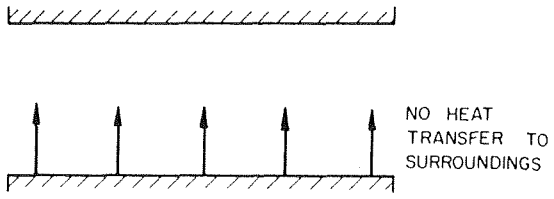

Fig. 4 (*a*) Ideal surfaces possessing perfectly collimated emission

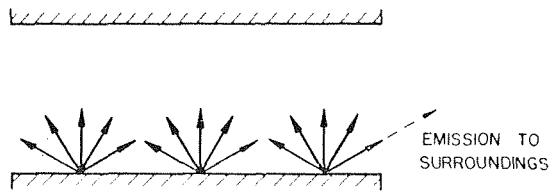

Fig. 4 (*b*) Actual surfaces possessing a realistic directional emission pattern

cavities were performed for a very simple situation involving no multiple reflections. These results showed that for side wall emissivity values readily attainable in practice, alterations in the heat transfer rate of the order of 50 percent should be possible due to the collimated nature of the emission from a cavity-type surface. A complete description of all these items is given in reference [5].

It has been found [6] that cavities possessing very small included angles yield the most collimated emission patterns when the side wall emissivity, ϵ_s, is extremely small. On the other hand, for the practical range of ϵ_s-values (values of 0.05 and above) cavities having an included angle of 45 deg were found to be far more directional than those with $\theta = 5$ deg. For this reason, the directional plates for the present experimental study were fabricated with $\theta = 45$ deg.

Once a choice has been made for θ, the question of a suitable cavity depth still remains. Before responding to this question it is appropriate to establish a means of evaluating the extent to which a given cavity collimates its emission. For this purpose η_L is arbitrarily defined as a limiting angle such that 90 percent of the emitted energy leaves the cavity within the limits of $-\eta_L < \eta < \eta_L$, while only 10 percent leaves at angles larger than η_L. It is clear that surfaces having very small η_L-values are highly directional, while those which possess η_L-values approaching that for a diffuse emitter (64 deg) tend to scatter their emission rather than to collimate it.

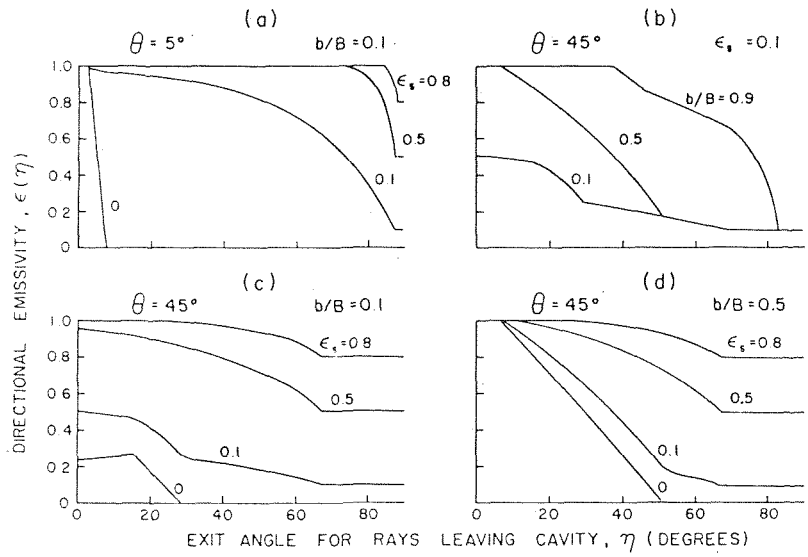

Fig. 5 Analytical predictions of directional emissivity, from reference [5]

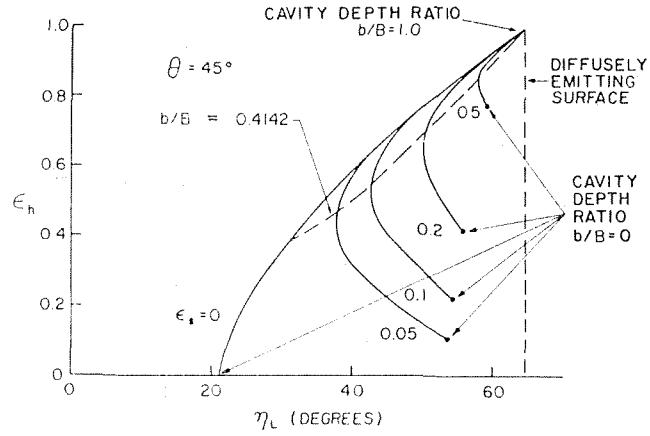

Fig. 6 Values of the limiting angle and hemispherical emissivity for various side wall emissivities and depth ratios, from reference [5]

A surface composed of many cavities possesses a directional distribution of its emission in accordance with information presented in Fig. 5, which was obtained by the authors in a previous study of the radiation properties of cavities [5]. Fig. 6, which is also reproduced from reference [5], gives predicted values of the limiting angle and hemispherical emissivity for cavities having an included angle of 45 deg. These two properties depend upon two additional cavity parameters: the side wall emissivity, ϵ_s, and the cavity depth ratio, b/B. It is clear that for a given value of ϵ_s, there exists an optimum depth ratio, $(b/B)_{opt}$, which gives rise to the minimum possible value of η_L. Also, it has been shown on the basis of an approximate analysis [6] that this optimum condition is closely approached if the depth is determined according to $b/B = \tan(\theta/2)$, which yields $\tan 22^1/_2$ deg = 0.4142 for $\theta = 45$ deg. This approximation is indicated by the dashed line in Fig. 6. Note that the dashed line does indeed pass through the various solid curves at points very close to the minimum η_L-values except for the case of $\epsilon_s = 0$, which is a situation unattainable in practice. Further discussion associated with the property information given in Fig. 6 and additional details concerning the radiation characteristics of V-groove cavities are given in reference [5].

The cavity depth ratio was established as indicated in the above discussion for the grooved surfaces used in the present experimental program. This was done, of course, in order to achieve the maximum possible directionality. The side walls were aluminum for which it was estimated that $\epsilon_s = 0.05$. According to Fig. 6, use of a depth ratio of 0.4142 should be expected to produce an η_L-value slightly under 40 deg and a hemispherical emissivity of about 0.43.

Experimental Apparatus

An experimental apparatus was used to study the effect that specially prepared grooved surfaces (Fig. 7) can have on heat transfer rates. The parallel plate system was enclosed in a hollow-walled copper container which was cooled with liquid nitrogen. This container simulated the cold surroundings. The inside surface was painted with a highly absorbent black velvet paint to minimize reflection of incident radiation escaping from the heated parallel plates. Due to the very low temperature, the emission of the container which was incident on the parallel plate system was essentially negligible. The container and its contents were placed in a vacuum to eliminate convection from the surfaces. The pressure was reduced below 10^{-5}mm of mercury by means of roughing and diffusion pumps. Each plate was 13 in. long and $6^1/_2$ in. wide. The separation distance between the plates was varied, and heat transfer rates were measured for grooved, directional surfaces and for diffusely emitting surfaces. The plates were heated by means of electrical resistance heaters mounted on the back of each surface, and the power required to maintain both plates at a steady temperature of 325 deg F was measured.

Radiation heat losses from the back of each plate and the small conduction losses to the container were determined experimentally by operating the system with the two opposing surfaces placed in direct contact, Fig. 8(*a*), so that no radiant heat transfer could occur from these contacting surfaces. The resulting heat loss value was subtracted from each measurement of the total heat transfer rate obtained when the plates were separated as shown in Fig. 8(*b*). Each measurement, when corrected in this manner, represented only the radiation from the two opposing parallel surfaces to the cold surroundings. For this procedure to be valid, it is necessary that the radiant losses from the back of the plates be constant for all plate separation distances. Although some variation of these losses did occur in the apparatus used, a study of the relative dimensions of the plates and the container revealed that these losses changed very little as the plate separation distance was altered.

The directional surfaces contained many cavities having a depth ratio of approximately 0.41 for reasons discussed in the previous section of the paper. The grooves were constructed by machining completely through a $^1/_4$-in-thick aluminum plate with a 45 deg milling tool. This operation formed a grill-type structure having many triangular cross sections. These grill arrangements, when placed against flat pieces of aluminum painted with black velvet paint, formed the directional surfaces which are shown in Fig. 7. The thermal performance of the directional surfaces was compared with that of painted flat plates having the same hemispherical emissivity. Emission from these painted surfaces can be assumed to be nearly diffuse, in contrast with the collimated emission from the grooved plates. For this reason the flat painted plates are referred to as diffuse surfaces in the remainder of this discussion.

The diffuse surfaces were obtained by first disconnecting the grill-type network from the directional surfaces and removing the black paint. Then, black paint was sprayed on the remaining flat plates in small amounts so that a thin film of paint uniformly covered the plates. The paint thickness was altered in small steps, with intermittent emissivity measurements, until the hemispherical emissivity was very close to the value obtained for the grooved surfaces. By means of this trial and error process,

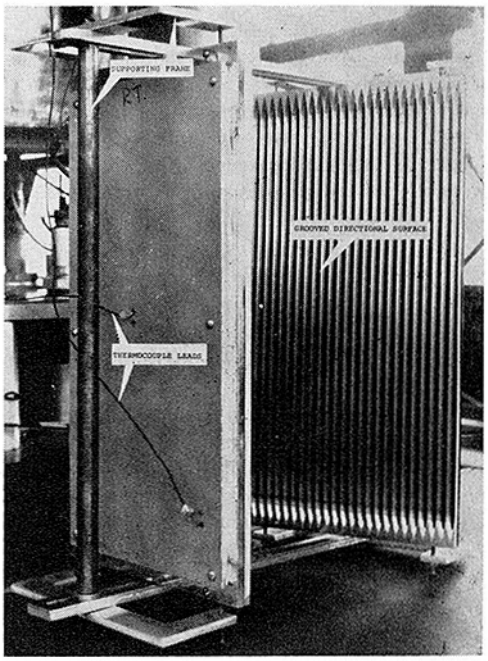

Fig. 7 Directional heat transfer surfaces

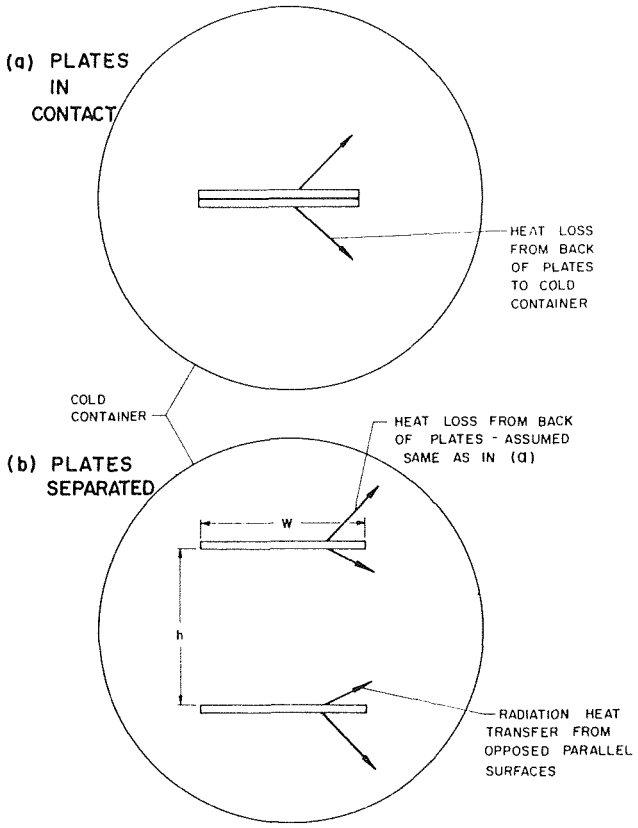

Fig. 8(a) Arrangement used to measure heat transfer losses; (b) arrangement used to measure total heat transfer rate

two identical diffuse surfaces with the proper ϵ_h-value were fabricated. Then, experiments were conducted for the same separation distances as were used with the directional surfaces. The final values of ϵ_h were 0.420 for the directional surfaces and 0.417 for the diffuse surfaces. These hemispherical emissivity values were determined experimentally by placing each plate individually into the apparatus and measuring the total heat transfer rate when the plate was maintained at a prescribed temperature. The heat loss from the back side of each plate, determined as indicated in Fig. 8(*a*), was subtracted from the total value to obtain the loss due to emission from the front face alone. The hemispherical emissivity, ϵ_h, was then calculated from this emission rate, the measured plate temperature, and the front surface area of the plate. It is interesting to note that the measured value of 0.420 is in good agreement with the analytically predicted emissivity for the grooved surfaces which was given in the previous section of the paper.

Results and Discussion

Measurements of the radiation heat transfer rate to the cold surroundings for both the diffuse and the grooved, directional surfaces are compared in Fig. 9. The interpretation of the data is the following. When the plates were placed together ($h/W = 0$) all of the emission was reabsorbed by the two opposing surfaces, and none of this emission escaped to the surroundings. When the separation distance was increased some of this emission did escape, with the remainder being reabsorbed by the emitting surfaces. For any particular separation distance the radiation heat transfer rate from the directional surfaces was always less than that from the diffuse surfaces, despite the fact that the total emission was the same for both pairs of plates. The decrease in heat transfer for the directional plates was due to the collimating influence of the grooves. The largest effects of the directional emission was obtained in the intermediate portion of the range of h/W shown in Fig. 9. In this region the heat transfer rates for the directional surfaces were about 40 percent lower than for the diffuse surfaces.

An analytical prediction of the heat transfer rate from the plates was obtained and is also shown in Fig. 9 for comparison with the measurements made using the flat, diffuse surfaces. In achieving this prediction it was assumed that the container was a nonemitter and a perfect absorber. From the favorable comparison of the experimental and analytical curves it appears that the interior container wall of the apparatus was cold enough and was blackened sufficiently to make these two assumptions realistic. The prediction was made in the conventional manner, considering the plates to be gray and diffuse, and employing radiation shape factor values as are available in standard heat transfer texts. The emissivity value used in making these calculations was 0.417, the measured result obtained for the flat painted surfaces.

It is clear that the measured radiation heat transfer rates from the grooved surfaces were significantly lower than the corresponding rates from the diffuse surfaces when all of the other parameters were maintained the same. This indicates considerable promise for the general technique as a means for controlling radiation heat transfer rates from surfaces. The rates from the grooved surfaces were far removed from the idealized zero rate, as shown in Fig. 9, which is theoretically obtainable with a surface having perfectly collimated emission. This suggests the need for developing practical methods of fabricating surfaces whose emission is more collimated than that possessed by the V-groove surfaces used in the present study.

Conclusions

The following conclusions are established on the basis of the investigation described in this paper:

1 Surfaces composed of V-grooves possess a collimated emission pattern which can be used to significantly affect radiation heat transfer rates. In the experimental program conducted with opposed parallel surfaces, collimation of the emission was found to affect the radiation heat transfer rate by various amounts, depending on the plate spacing, up to a maximum of about 40 percent.

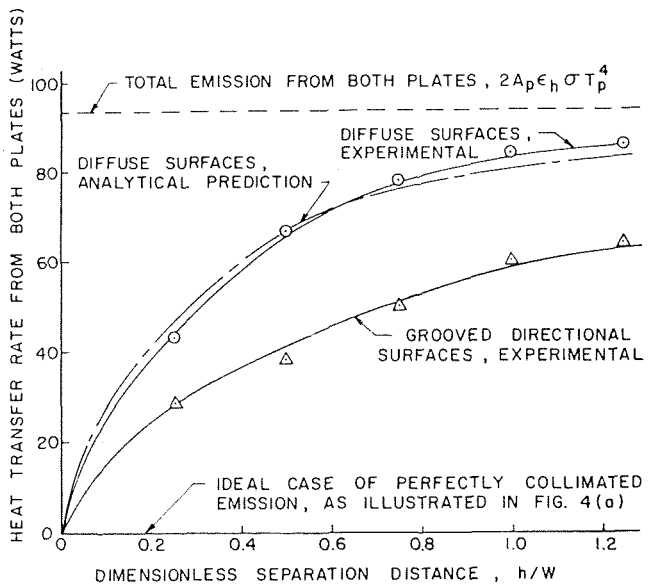

Fig. 9 Measurements of radiation heat transfer rate from opposing parallel plates, plate temperature T_p = 325 deg F

2 It appears that more highly collimated emission could be achieved with further effort. This should make it possible to obtain alterations in heat transfer somewhat larger than those measured during the present study, thus enhancing the usefulness of specially prepared surfaces for acquiring improved thermal performance.

3 Improved methods of fabrication are needed in order to make the technique applicable to these practical situations. In this connection, it should be noted that a novel method for producing a series of deep, thin, parallel grooves has been reported [7].

4 Additional measurements of the type described in this paper would be desirable for the purpose of evaluating newly developed surface configurations as they are conceived.

5 Analytical treatments of the heat transfer characteristics associated with grooved, directional surfaces would be desirable. However, accurate solutions probably would require substantial amounts of computation due to the highly discontinuous nature of the bidirectional reflection properties of the grooves [6].

Acknowledgment

Appreciation is expressed to K. H. Hawks, A. D. Clausen, R. M. Kemp, and R. K. Sanders of Purdue University and to J. G. Knight and J. W. Davis of Georgia Institute of Technology for their helpful assistance in connection with the experimental equipment used for this study.

References

1 Clausen, O. W., and Neu, J. T., "The Use of Directionally Dependent Radiation Properties for Spacecraft Thermal Control," *Astronautica Acta*, Vol. 11, No. 5, Sept.-Oct. 1965, pp. 328–339.

2 Hering, R. G., "Radiative Heat Exchange Between Specularly Reflecting Surfaces with Direction-Dependent Properties," *Proceedings of the Third International Heat Transfer Conference*, Vol. V, Chicago, Ill., 1966, pp. 200–206.

3 Perlmutter, M., and Howell, J. R., "A Strongly Directional Emitting and Absorbing Surface," JOURNAL OF HEAT TRANSFER, TRANS. ASME, Series C, Vol. 85, No. 3, Aug. 1963, pp. 282–283.

4 Brandenberg, W. M., and Clausen, O. W., "The Directional Spectral Emittance of Surfaces Between 200 and 600°C," NASA SP-55, S. Katzoff, ed., 1965, pp. 313–319.

5 Black, W. Z., and Schoenhals, R. J.. "A Study of Directional Radiation Properties of Specially Prepared V-Groove Cavities," JOURNAL OF HEAT TRANSFER, TRANS. ASME, Series C, Vol. 90, No. 4, Nov. 1968, pp. 420–428.

6 Black, W. Z., "Radiative Heat Transfer Characteristics of Specially Prepared V-Groove Cavities," PhD thesis, Purdue University, Lafayette, Ind., Jan. 1968.

7 "Reference Black Body is Compact, Convenient to Use," NASA Tech Brief 63-10004, Apr. 1964.

R. E. HOLMES
Research Engineer,
Battelle Memorial Institute,
Columbus Laboratories,
Columbus, Ohio.
Assoc. Mem. ASME

A. J. CHAPMAN
Professor of Mechanical
and Aerospace Engineering,
Rice University, Houston, Texas.
Mem. ASME

Condensation of Freon-114 in the Presence of a Strong Nonuniform, Alternating Electric Field

The condensation of Freon-114 in the presence of a nonuniform, alternating, 60-cycle, electric field was examined experimentally. The condensing surface was a grounded, cooled flat plate, and the electric field was produced by applying a voltage to a second plate placed above the first. Voltages up to 60 kv were imposed, and nonuniformities in the field were created by varying the angle between the plates. Analytical predictions were made of the expected heat-transfer rate, and reasonable agreement with the experimental data was obtained for voltages less than 40 kv. Above 40 kv the results were unpredictable, but increases in the heat-transfer coefficient as high as ten times that for no field were obtained.

Introduction

In recent years it has been demonstrated by Velkoff and Miller [1][1] and by Choi [2] that electric fields can substantially increase the condensation rate in Freon-113. In Choi's work the condensation was on the inside of the tube with an electrode at the axis of the tube. Using a d-c field Choi found that the heat-transfer coefficient could be increased by as much as a factor of two. Choi attributed the results to an interfacial instability and correlated the results in terms of the most unstable wavelength.

In the work of Velkoff and Miller Freon-113 was condensed on a flat plate and the condensation rate was increased by placing electrodes parallel to the plate with a d-c potential applied to the electrode. They found that the heat-transfer coefficient could be increased by as much as a factor of three. They did not correlate their results, but attributed the increase in coefficient to instabilities caused by the charge buildup on the surface of the liquid film.

In the work described here and in reference [3], the authors sought to eliminate any surface charge buildup by the use of an

[1] Numbers in brackets designate References at end of paper.

Contributed by the Heat Transfer Division and presented at the Fluids Engineering, Heat Transfer, and Lubrication Conference, Detroit, Mich., May 24–27, 1970, of THE AMERICAN SOCIETY OF MECHANICAL ENGINEERS. Manuscript received by the Heat Transfer Division, April 4, 1968; revised manuscript received August 19, 1969. Paper No. 70-HT-6

Nomenclature

A = rms voltage imposed between the two electrodes
$\bar{F}$ = electric field force acting on the condensed liquid which is effective in causing translational accelerations
F = scalar magnitude of $\bar{F}$ parallel to plate
F_b = body force parallel to plate
g = gravitation force per unit mass
g_c = gravitational constant
h = heat-transfer coefficient
k = thermal conductivity of condensed liquid
L = length of the condensing plate in the direction of liquid flow
K = constant defined by equation (3)
K_L = dielectric constant of condensed liquid
K_v = dielectric constant of vapor
q_x = heat transfer between the points $x = 0$ and $x = x$
dq_x = incremental heat transferred in the distance dx
$\bar{r}$ = radial distance from the point where the two plates would intersect if extended
$\hat{r}$ = unit vector in radial direction
ΔT = temperature difference across liquid film
W = plate dimension normal to the direction of flow for the condensing fluid
x = variable distance—often represents distance from top of condensing surface
ϵ_0 = permittivity of free space
λ = latent heat of condensing fluid
μ = viscosity of the liquid
θ_0 = angle between the two electrodes
l_L = density of condensed liquid
l_V = density of vapor
ψ = angle between the surface of the plate and the horizontal

alternating 60-cycle electric field. Nonuniformities were then generated in the field in an effort to create controllable body forces which would cause the liquid to flow down the plate into the intense areas of the field. By a modified Nusselt analysis it was calculated that this should produce a thinner liquid film and an increase in heat-transfer coefficient by a factor of two for Freon-114.

Experiments were performed with Freon-114 to determine if the liquid film could be controlled by the use of the electric field. Although instabilities appeared to be present, the results indicated that to some limited extent the film could be controlled in the manner described. At voltages above 40 kv it was found that the results could not be predicted by the simple analysis used and that coefficients as much as a factor of ten higher than those observed with no field present could be obtained.

Experimental Apparatus

Experimental data was taken for the condensation of Freon-114 on a grounded, flat, cooled surface with an alternating, 60-cycle electric field applied by bringing to a specified rms voltage another flat plate which was placed above the cooled surface (see Figs. 1 and 2). Both surfaces were contained within a pressure vessel. (A schematic of the equipment is given in Fig. 3.)

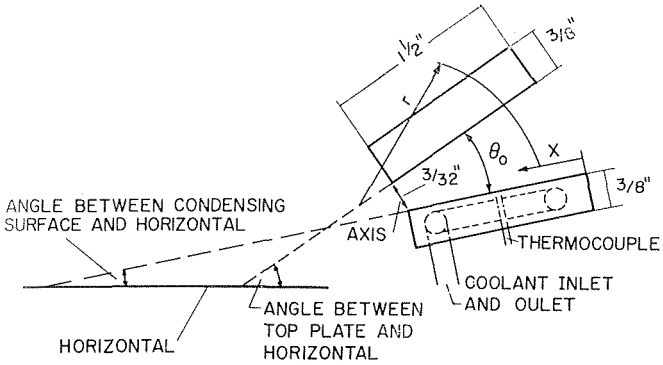

Fig. 1 Condensing surface and electrode

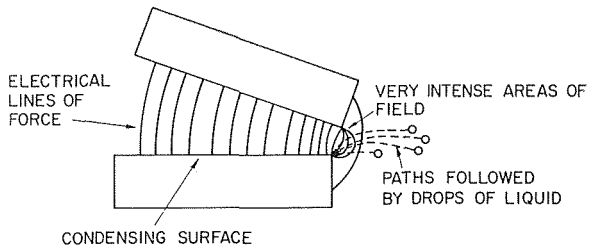

Fig. 2 Charged drops of liquid leaving the condensing surface

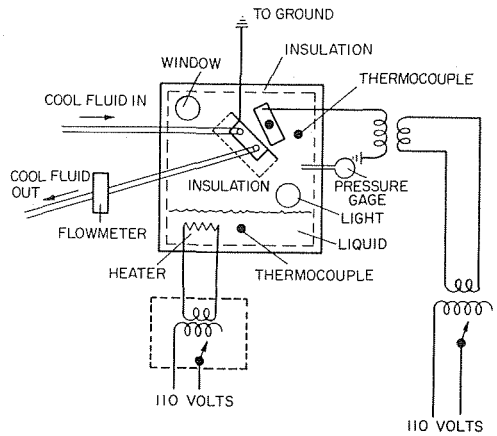

Fig. 3 Diagram of experimental apparatus

The outside of the vessel was insulated to reduce heat losses. The vessel was equipped with a $2^1/_2$-in-dia window through which the experiment could be observed, and a 500-watt electric heater was installed in the bottom of the vessel to boil the Freon-114—the condensing fluid. The power input to this heater could be varied by the use of a variable transformer. The vessel was also equipped with a pressure gage and three thermocouples, which were placed at various locations, making it possible to insure that saturated conditions were maintained.

The cooling surface and the surface located above it, which supplied the electric field, were both made of copper and were plated with silver. The bottom surface was kept cool by passing a cool fluid through it. Both transformer oil and water were used as cooling fluids.

Both plates could be pivoted about an axis that corresponded with the "back" edge of the upper surface of the bottom plate. This is the edge from which the condensed liquid was removed. (This location is marked "axis" in Fig. 1.) By pivoting the plates in this manner, it was possible to maintain a constant distance between the plates along this "back" edge; the separation distance maintained along this edge was $^3/_{32}$ of an inch. The surfaces were 6 in. long parallel to this edge and $1^1/_2$ in. wide normal to it. Tests were run with the angle between the plates at 6 deg with the plates parallel, and the bottom plate was set at angles of 0, 10, and 25 deg, as measured from the horizontal. The results are shown in Figs. 4 through 11. The bottom plate was embedded in plexiglass in an attempt to eliminate all heat losses except those from the top surface. The heat losses associated with these fixtures were taken into account, and the data taken was corrected accordingly. The top plate was also supported by a plexiglass fixture which served as an electrical insulator, so that the top plate could be maintained at a high voltage with negligible losses due to leakage current.

The quantity of heat removed from the condensing surface was measured with a heat balance, while cooling-fluid heat losses were measured by thermocouples placed in the cooling fluid at a point where it entered and left the cool plate. The flow rate through the plate was measured by a precision flow meter. The

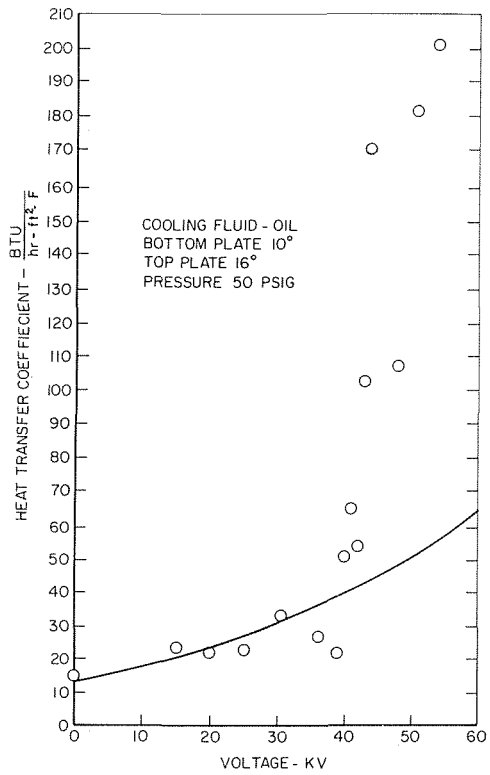

Fig. 4 Heat flux versus applied voltage

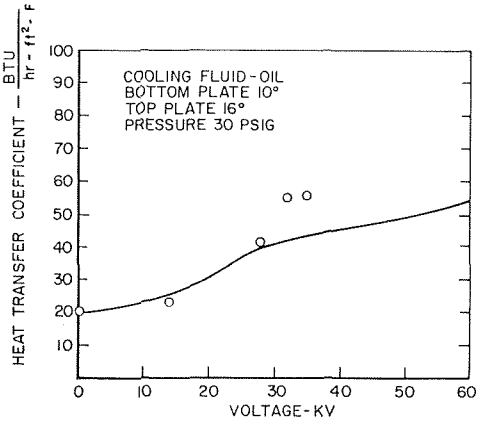

Fig. 5 Heat flux versus applied voltage

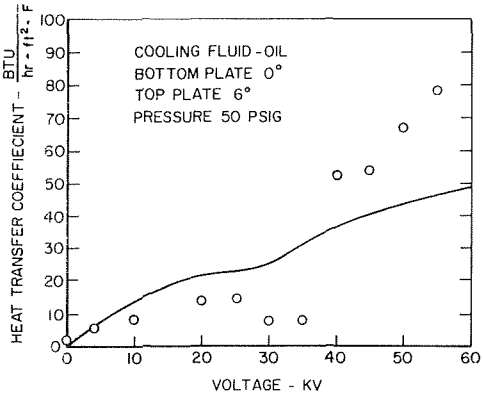

Fig. 6 Heat flux versus applied voltage

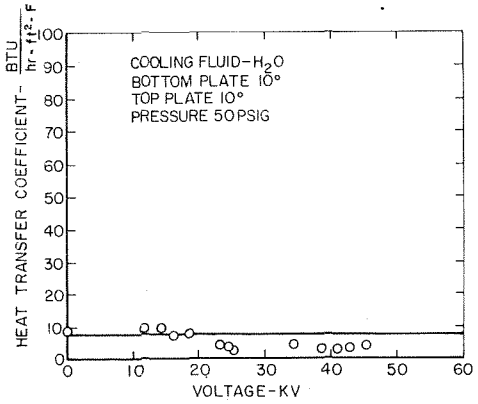

Fig. 7 Heat flux versus applied voltage

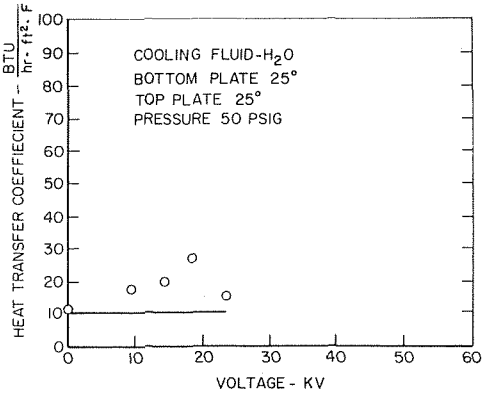

Fig. 8 Heat flux versus applied voltage

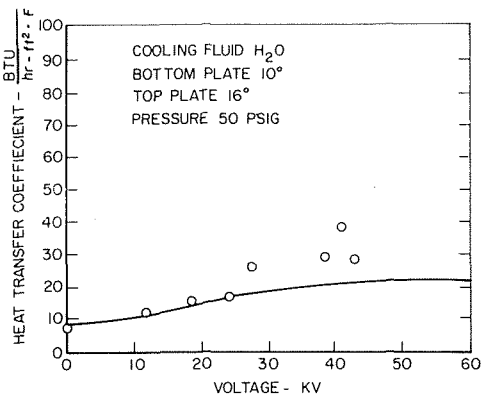

Fig. 9 Heat flux versus applied voltage

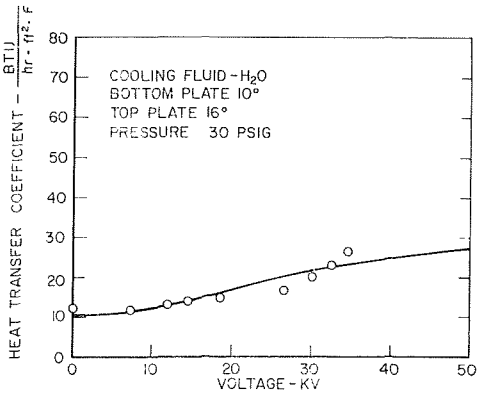

Fig. 10 Heat flux versus applied voltage

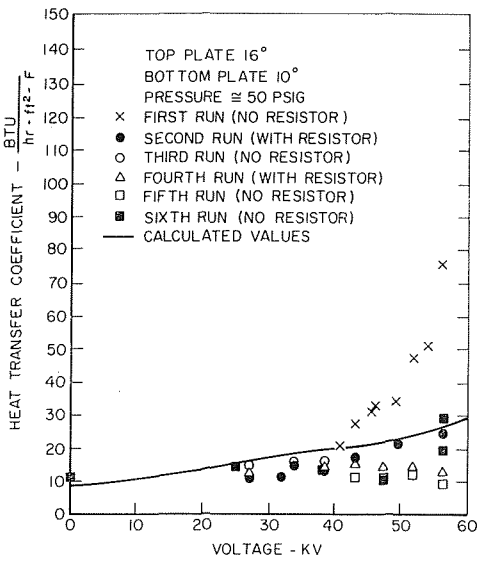

Fig. 11 Heat flux versus applied voltage

difference in temperature between the condensing surface and vapor was assumed to be the temperature difference measured between a thermocouple placed in the vapor near the condensing surface and a temperature measured by a thermocouple embedded in the plate. An analysis is given in reference [3] which illustrates that little error was involved in considering the surface temperature to be uniform at the temperature of the embedded thermocouple.

The voltage applied to the upper plate was supplied by a high-

voltage transformer which was capable of supplying up to 100 kv. The input voltage was applied to the high-voltage transformer on the line leading to the primary of this transformer. One terminal of the secondary coil of the high-voltage transformer was maintained at ground, while the other terminal was the high-voltage terminal to which was fastened the high-voltage line leading into the pressure vessel. A metering circuit was placed between the high-voltage line and ground, which had a current proportional to the applied voltage. This current could then be caused to flow through either of two branches. One of these branches was for the purpose of measuring the rms voltage applied, and the other was for the purpose of observing any sharp peaks or changes in the voltage on an oscilloscope.

Analysis

The purpose of this section is to present approximate analytical predictions for the condensation rate that will occur on a flat plate when an electric field is applied between it and another flat plate inclined at an angle θ_0 to the first plate (see Fig. 1). The approach used is to first assume one has two electrodes with a gas between the electrodes, except for a thin film of liquid covering one of them. By assuming that the interface between the electrodes remains normal to the electric field lines and that no free charges are present, one can establish an effective body force which draws the condensed liquid into the more intense areas of the electric field. For the case considered here this force is given by [3]

$$\bar{F} = (K_V - K_L)\,\epsilon_0 \frac{K_V}{K_L} \frac{A^2}{r^3\theta_0^2}\,\hat{r} \tag{1}$$

where $\bar{F}$ is the electric field force that is effective in causing translational accelerations acting on the liquid at any point.[2]

The condensing heat-transfer coefficient under the conditions described here may be deduced in a manner similar to the modified Nusselt analysis for film condensation. For film condensation with laminar flow on an isothermal flat plate, the modified Nusselt analysis [5] yields the following expression for the incremental heat transferred, dq_x, over a plate strip of length dx:

$$dq_x = \left(\frac{l_L g_c \lambda k^3}{4\mu}\right)^{1/4} F_b^{1/4} W (\Delta T)^{3/4} x^{-1/4} dx \tag{2}$$

in which F_b represents the body force parallel to the condensing surface. Integrating, the heat transferred over a plate length x is

$$q_x = \left(\frac{l_L g_c \lambda k^3}{4\mu}\right)^{1/4} F_b^{1/4} W (\Delta T)^{3/4} \frac{4}{3} x^{3/4} \tag{3}$$

Equations (2) and (3) may be combined to give a form useful for application to the problem at hand:

$$\frac{dq_x}{dx} = \frac{\Delta T}{q_x^{1/3}(3/4)^{1/3}\left(\frac{l_L g_c \lambda k^3}{4\mu}\right)^{-1/3} W^{-1/3} F_b^{-1/3}} \tag{4}$$

For the case described herein, equation (4) may be written

$$\frac{dq_x}{dx} = \frac{\Delta T}{q_x^{1/3} K \left[(l_L - l_v)\frac{g}{g_c}\sin\psi + F\right]^{-1/3}} \tag{5}$$

wherein

$$K = \left(\frac{l_L g_c \lambda k^3}{3\mu}\right)^{-1/3} \tag{6}$$

and F is the scalar component of the electric force field vector given in equation (1). The average heat-transfer coefficient over a plate of length L is then:

$$h = \frac{1}{LW\Delta T}\int_0^L \frac{dq_x}{dx} dx \tag{7}$$

Equations (1), (5), (6), and (7) were used to evaluate, numerically, predicted values of the condensing heat-transfer coefficient with which the experimentally measured values were compared.

Visual Observations

During the process of the experiment, it was possible to observe certain processes through the window on the vessel. It was observed that in the range of 4 or 5 kv, fine "dancing lines" of liquid appeared between the plates. As the voltage between the plates was increased further, the lines grew thinner and a fog seemed to appear between the plates. As the voltage was further increased, the fog between the plates grew darker. In the range of 25 kv, the fog became so heavy that the region between the plates was completely black.

In the case of parallel plates, it was possible to see the liquid being thrown from the plates in the form of small drops or spray. Since it was never possible to observe the back edge of the plate, this observation of the front edge provided a clue as to how the condensed liquid was removed from the edge of the plate. This point will be discussed in more detail later.

Experimental Procedures

Results taken under eight different runs made under different test conditions are shown in Figs. 4 through 11. Also shown in the figures, as solid lines, are the results of the analysis using equations (1) through (7). The first three runs were made with transformer oil as the cooling fluid. The final five were made with water as a cooling fluid. It was found that the oil, which was originally used as a safety precaution, could not remove the heat from the plate fast enough to give a large enough temperature difference between the plate and the vapor to measure coefficients accurately in the high-voltage part of the tests. Each of the data points shown represents an average of three to eight actual readings taken approximately 20 min apart. When the voltage or any other parameter was changed, approximately 45 min were allowed before the first reading was taken.

The region above 40 kv was of particular interest due to the high condensation rate as well as the scatter which occurred in this region. The current flow into the transformer was measured in this region to verify that the heat being removed by the cooling fluid was coming from the condensing Freon and was not due to electrical losses.

Discussion

It is interesting to note that according to the relationships presented for the body forces—neglecting the presence of charged particles—the liquid should collect in the most intense region of the field. In this experiment no means of removing the liquid from the plate were provided; nevertheless, the liquid did not collect. As was noted earlier in the case of the parallel plates, it was possible to see the liquid being thrown from the plates in the form of small drops or spray.

The field is known to be very intense at the corners of the plate, and it is probable that some ionization takes place in this region. Therefore, the polar molecules would then cluster around the resulting charged particles. As the region around the corner becomes rich in these charged particles, the liquid layer in this vicinity would break up and the charged drops would travel along the lines of force normal to the electric field lines. In the vicinity of the edge, the lines of force do not go between the plates as they do in the region interior to the plates. Instead, they tend to flare out as shown in Fig. 2. When the field reverses, the drops do not reverse direction but, due to their momentum, travel a path similar to that shown in Fig. 2.

[2] Reference [4] will be an aid in converting from electrical units to force units.

It is also interesting to note that at the lower voltage levels the experimental results for the case of two nonparallel plates generally agrees well with the analytical prediction. As the voltage is increased beyond 25 kv, the results do not seem to agree quite as well, although in most cases the agreement is satisfactory.

At slightly above 40 kv, the data begin to scatter badly. Several possible explanations for the wide variety in the condensation rates which occurred in this region have been advanced.

Certain phenomena seem particularly likely to have played a part in the high condensation rate. Surface instabilities undoubtedly were of much significance. Such instabilities can lead to a thinning of the liquid film and thus cause increased condensation rates. Evidence has also been advanced that in the range of 40 kv, charged particles begin to appear in the liquid layer in significant quantities for the first time. These particles can interact with the imposed electric field in a number of ways that could give increased coefficients. These possibilities are discussed in some detail in reference [3].

Since this experiment was developed originally to study the effect of the electric field on the condensation coefficient, it was impossible to use the present equipment to gain a detailed knowledge of the local behavior of the liquid layer in the presence of the electric field. It should be borne in mind that the equations presented were developed with some rather stringent assumptions. They give generally good agreement with the case at hand, but their extension to other situations must be done with care.

Summary of Results

Experimental data have been presented which indicate that significant increases in the condensation rate for a dielectric fluid can be achieved by proper use of a nonuniform electric field. An analytical prediction for condensation rate versus voltage, which agrees well with the experimental results in the lower voltage range, has been presented. Such a prediction can not necessarily be expected to hold for all possible electrode geometries and voltage levels. At voltages above 40 kv the data scatter badly, but with newly polished electrodes increases in the heat-transfer coefficient as large as a factor of ten above that for no field were found.

References

1 Velkoff, H. R., and Miller, J. H., "Condensation of Vapor on a Vertical Plate With a Transverse Electrostatic Field," JOURNAL OF HEAT TRANSFER, TRANS. ASME, Series C, Vol. 87, No. 2, May 1965, pp. 197–201.

2 Choi, H. Y., "Electrohydrodynamic Condensation Heat Transfer," JOURNAL OF HEAT TRANSFER, TRANS. ASME, Series C, Vol. 90, No. 1, Feb. 1968, pp. 98–102.

3 Holmes, R. E., "Condensation of a Dielectric Vapor in the Presence of a Nonuniform Electric Field," PhD thesis, Rice University, Houston, Texas, 1967.

4 Panofsky, W. K. H., and Phillips, M., *Classical Electricity and Magnetism*, Addison-Wesley, 1956.

5 Chapman, A. J., *Heat Transfer*, MacMillan, New York, 2nd ed., 1967.

The Departure From Nucleate Boiling in Rod Bundles During Pressure Blowdown

J. O. CERMAK
R. F. FARMAN
L. S. TONG
Westinghouse Electric Corp.,
Atomic Power Division,
Pittsburgh, Pa.

J. E. CASTERLINE
S. KOKOLIS
B. MATZNER
Columbia University,
Engineering Research Laboratories,
New York, N. Y.

Tests were performed in a high pressure heat transfer loop to determine the behavior of transient DNB during pressure blowdown in rod bundles. Water flowed along a 21-rod, 5-ft-long electrically heated rod bundle with a radially nonuniform heat flux distribution. Both steady-state and transient DNB tests were conducted over the following range of operating parameters:

1 *Pressure—750 to 1500 psia*
2 *Inlet temperature—480 to 540 deg F*
3 *Mass velocity—1 × 10⁶ to 3 × 10⁶ lb/hr ft²*
4 *Grid configurations—2*

The data were analyzed using calculated subchannel local velocity and enthalpy as a function of time with proper allowance for the mixing and cross flow within the bundle. Results show that the inception of transient DNB during pressure blowdown can be predicted on the basis of steady-state data.

Introduction

In order to increase the heat flux at which the Departure from Nucleate Boiling (DNB) occurs, mixing promoters (vanes) can be placed on the spacer grid of the rod bundle. These vanes tend to break up bubble boundary layers and force water to contact the heater surface. Thus, two different grid configurations, one with mixing vanes and one without mixing vanes, were tested to assess this mixing-promoter effect.

During a pressure blowdown of a nuclear reactor, the fuel rod will experience DNB and proceed into the transition boiling regime and ultimately film boiling. In the case of a pressurized water reactor, calculations show that the time required for the pressure to reach ambient conditions for the most severe ruptures is generally from 10 to 15 sec. Any pressure decrease below the saturation causes flashing in the fluid. The rate of flashing could perturb the boundary layer to an extent which would alter the local DNB behavior. Transient effects on DNB have been studied by varying rate of change in heat flux and rate of change in flow rate (references [1 and 2]).[1] However, there has previously been no study of the effects of pressure blowdown on DNB. This study was directed to study whether DNB under pressure blowdown can be predicted from steady-state DNB data.

Test Program

The basic objective of this program was to obtain blowdown DNB data in rod bundles to offer a basis upon which to evaluate DNB in the loss of coolant analysis described previously. In addition, it was desired to determine the effect on DNB under steady-state conditions of the mixing provided by mixing vanes on the rod spacer grids as compared to a rod spacer grid without mixing vanes.

The test program was divided into two phases:

1 Steady state and transient DNB determination utilizing the rod spacer grid without mixing vanes.

2 Steady state and transient DNB determination employing the mixing vanes on the rod spacer grid.

Initially steady state data were obtained in both phases to provide a basis of comparison for the results that were to be obtained under the pressure transient portion of the program. Both steady state and transient DNB tests were conducted over the following range of operating parameters:

Contributed by the Heat Transfer Division and presented at the Fluids Engineering, Heat Transfer, and Lubrication Conference, Detroit, Mich., May 24–27, 1970, of The American Society of Mechanical Engineers. Manuscript received by the Heat Transfer Division, July 9, 1968; revised manuscript received October 31, 1969. Paper No. 70-HT-12.

[1] Numbers in brackets designate References at end of paper.

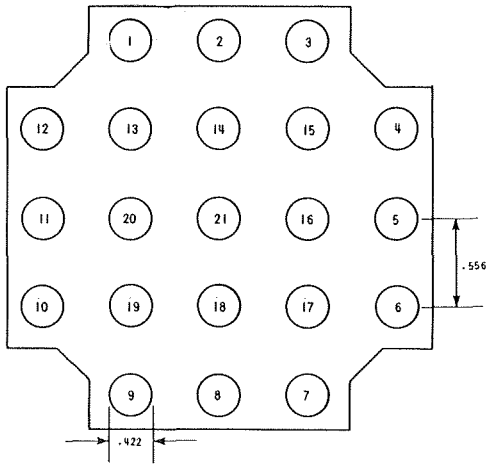

Fig. 1 21-rod square lattice

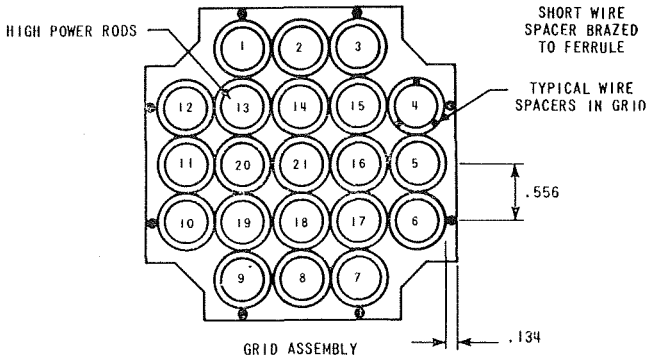

Fig. 2 21-rod square lattice

1 Pressure: 750 to 1500 psia
2 Inlet temperature: 480 to 540 deg F
3 Mass velocity: 1×10^6 to 3×10^6 lb/hr ft^2

Test Section

The test section consisted of a 21-rod bundle in an open channel square array as shown in Fig. 1. The rods were of 0.422 in. OD located on 0.556-in. centers and had a 60 in. electrically heated length. There was a uniform axial power distribution and a non-uniform radial power distribution. The inner 9 rods operated at a heat flux 16 percent greater than the outer 12 rods. A flow housing lined with phenolic asbestos provided the enclosure for the bundle (Fig. 1) and was then enclosed in a pressure housing.

Each heater rod consisted of a stainless steel heater tube silver-brazed at each end to nickel connection rods of the same diameter. The nickel connection rods insured that the power loss was minimal. Inside heater tubes were 0.011 in. thick and the outside heater tubes were 0.009 in. thick. The tubing was filled with Al_2O_3 ceramics to prevent the tubes from collapsing by external pressure.

DNB detection was accomplished with thermocouples inserted in each of the heater tubes $^1/_2$ in. from the outlet end of the heated length. The arrangement of the individual thermocouples was as follows:

1 The thermocouple sheath was silver-soldered onto a copper washer.
2 The copper washer was inserted inside the test element with a forced fit.
3 Ceramics were loaded on both sides of the washer for wall support.

An estimate of the time response of the thermocouples was demonstrated during the transient tests by the time period from the initiation of the transient to the deviation in the rod thermocouple signal. This time period was as small as 0.5 sec indicating that the thermocouple response time is at most 0.5 sec.

Electrical connections to the heater tubes were made at the top by tapered mechanical connections to a nickel terminal plate. The heater tubes extended through O-ring seals at the bottom and individual leads were clamped onto each rod.

The two different grid configurations were tested. The rod spacer without vanes (Fig. 2) consisted of $^1/_2$-in-long hollow cylinders that encompassed the individual heater tube and centered the tube by three longitudinal pins inside each of the cylinders. These short cylinders were brazed together at the points of contact. There were 5 grids on an axial spacing of 10 in. The rod spacer with mixing vanes consisted of Inconel straps brazed together in an egg-crate pattern. Projections from the straps centered the heater tube in its cell. The $^1/_2$-in-long mixing vanes were located on the bottom and top of the grid and were contoured and bent to fit close to the rods. For this phase of the testing there were also 5 grids located on an axial spacing of 10 in.

Test Loop

The experimental tests were conducted in the heat transfer facility at the Chemical Engineering Research Laboratories of Columbia University. This facility consisted of a stainless steel loop operated at a maximum pressure of 1500 psia, fluid temperatures as high as the saturation temperature (596 deg F), and flow rates as high as 300 gpm. The flow rate was measured by a 2-in. Potter flow meter and the pressure was measured by a 0–1500 psi Heise Bourdon-tube pressure gauge. Pressure during the blowdown testing was recorded with a C.E.C. absolute pressure transducer. Inlet test section temperature was measured using a stainless steel sheathed iron constantan thermocouple. Power was supplied from a 3.85-MW d-c power supply with the current being measured by a shunt with readout on a direct-writing oscillograph. The voltage was read directly across the stainless steel portion of the heater tube using voltage taps and the direct-writing oscillograph. Several multi-channel strip-chart recorders monitored all of the heater tube thermocouples Additional information on the test loop is available in [3].

Test Procedure

Steady State. To obtain a steady state DNB measurement the loop was operated at the desired conditions of pressure, inlet temperature, and mass velocity. The power to the test section was gradually increased in small increments. After each step increase in power, the loop was allowed to stabilize at equilibrium conditions. DNB was considered to have occurred whenever a sharp rise was detected in the output of one of the test section thermocouples. Whenever DNB was detected the test section power was reduced and the power (and therefore heat flux) was recorded along with the pressure, flow rate, and inlet temperature. Steady state data were collected over the range in pressure that would be experienced under transient conditions.

Transient. The transient operation was performed by first establishing steady state operation of the loop and then producing a rapid depressurization of the system. Initial steady state conditions were chosen such that generally the heat flux was 2 to 30 percent below the DNB heat flux. Power and test section inlet temperature remained constant up to the point following DNB when the test section power was reduced to prevent phys-

ical burnout to the heater rods. The flow rate generally dropped from 0 to 10 percent during the pressure transient. The system depressurization was accomplished by a solenoid-operated valve which was connected to an electric timer. This valve was connected to the loop at a "T" joint and when it opened the water in the system discharged to atmosphere. In addition, it was necessary to establish a standing dead leg of cold water between the loop and the discharge valve to achieve fast rates of blowdown. The volume of cold water in the dead leg was sufficient to insure that the discharge valve experienced only single-phase flow during the blowdown.

Results

A list of all runs made during the test series is shown in the Appendix for both the simple grid (grid without mixing vanes) and the mixing vane grid. The rod heat flux corresponds to the DNB heat flux under steady state conditions.

Steady State. Steady state DNB data were obtained prior to the transient testing. Since the data points were not all collected at identical operating conditions, it was convenient to present the comparison (Fig. 3) of both data sets with respect to predicted DNB heat flux. Simple grid DNB data from reference [2] is also presented in Fig. 3 since this present study only obtained enough DNB data with the simple grid to show consistency with the previous work. The predicted values of DNB were obtained by calculating local fluid exit conditions and applying the W-3 DNB correlation (references [5 and 6]). Local enthalpy can be determined by using a mixing factor relating local to average enthalpy rise as follows:

$$F_{\text{mixing}} = \frac{\Delta H_{\text{local}}}{\Delta H_{\text{avg}}}$$

It was found using THINC (reference [4]) that values of F_{mixing} of 1.31 and 1.08 may be applied to this bundle with simple grids and mixing vane grids, respectively. This value accounts for both flow redistribution and mixing in this open channel bundle for the range of parameters studied. The effect of the mixing vane grids increases the DNB heat flux compared with simple grids at similar operating conditions. A study of the

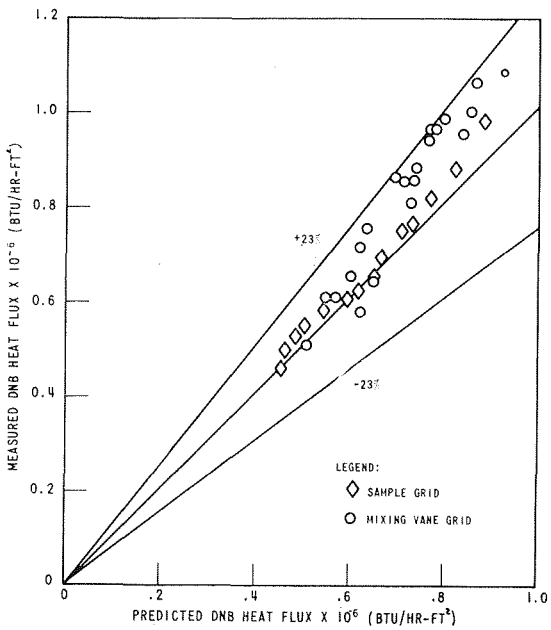

Fig. 3 Steady state DNB heat flux data with simple grids and mixing vane grids

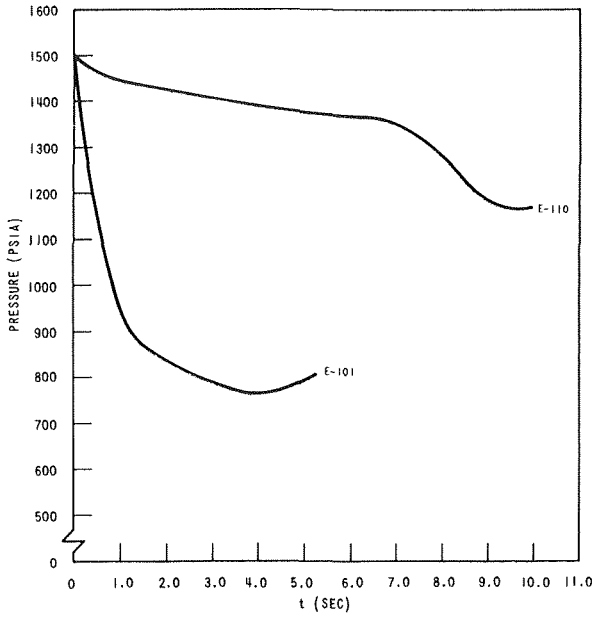

Fig. 4 Pressure blowdown characteristics

mixing vane data shows that greater DNB ratios (measured/predicted) are obtained for the higher mass velocities. These runs have lower outlet qualities than the low mass velocity runs and illustrate a tendency towards increased mixing vane effectiveness on DNB as the local outlet quality decreases. DNB was always observed on the inner rods.

The mixing vane grid reduces the local enthalpy (quality) in the hot channel. This effect should lead to an increase in DNB heat flux as compared to straight vane grids. An empirical mixing parameter called the Thermal Diffusion Coefficient accounts for lateral mixing between channels along the open channel array. The thermal diffusion exchange rate between two channels is given by reference [4] as $\alpha \bar{V}_{ij} \bar{\rho}_{ij} \Delta Z \, (\bar{H}_i - \bar{H}_j)$, where

α = thermal diffusion coefficient (empirically determined).

$\bar{V}_{ij}$ & $\bar{\rho}_{ij}$ = represent average values of coolant enthalpy and density for the combined control volume of channels i and j.

a_{ij} = lateral flow area per unit length between channels i and j.

ΔZ = height of control volume.

H_i = average enthalpy of control volume i.

A study of the effect of the thermal diffusion exchange rate indicates that the effect of mixing alone is not sufficient to explain the behavior of the mixing vane grids and that some other mechanisms are involved. One possible way that the mixing vane grid can effect DNB is by disrupting the bubble boundary layer thereby removing the bubble formation. The bubble layer would thus have to be entirely reestablished on the downstream side of the grid.

An "α" value of 0.076 for the bundle with mixing vane grids was used in the present analysis because previous work reference [4] indicates that a value of 0.076 can be applied to mixing vane grids.

Transient. During the first phase of this study, the initial conditions for runs E-101 and E-110 were very similar, whereas the blowdown history was quite different. During E-101 the system pressure dropped rapidly while during E-110 the pressure decreased slowly. Pressure history for these runs is shown in Fig. 4.

The difference in the rate of blowdown between these two runs is reflected in the earliest time at which an indication of

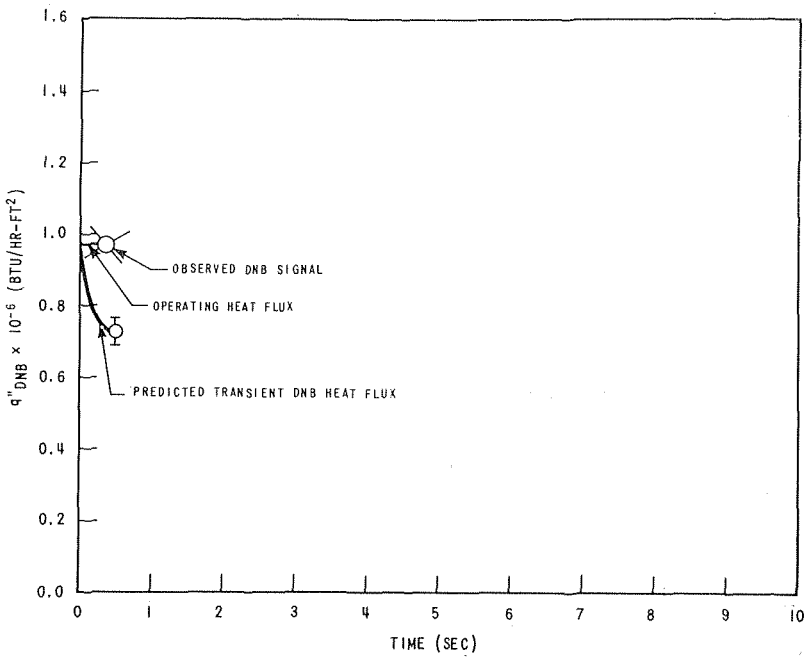

Fig. 5 Transient DNB heat flux during blowdown—run E-101

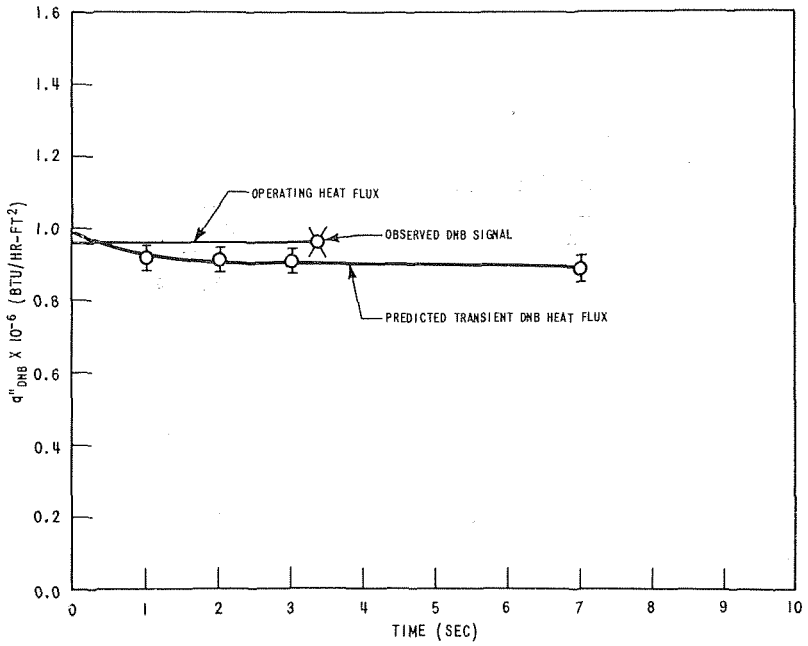

Fig. 6 Transient DNB heat flux during blowdown—run E-110

DNB was apparent. In case E-101 there was an indication of DNB at 0.5 sec following the initiation of the transient, whereas case E-110 indicated DNB at 3.5 sec.

The transient runs were analyzed by computing the average outlet enthalpy as a function of time with transient pressure inlet temperature and flow characteristics supplied as boundary conditions. This can be determined by using the CHICKIN (reference [7]) computer program. Hot channel local enthalpy can then be determined by use of the mixing factor defined previously. The steady state DNB data was used to predict the transient DNB at the same local conditions. DNB heat fluxes predicted in this manner for cases E-101 and E-110 are shown in Figs. 5 and 6, respectively, along with the time corresponding to the experimental observation of DNB. The predictions based on the steady state data agree with the observed transient DNB observation within the assertion of 5 percent accuracy and probable detector response time.

During the second phase of this study, fifteen transient runs were performed with mixing vane grid bundles. Each of the mixing vane grid transient runs was analyzed on the basis of the steady state data, using the same technique as was used for the simple grid analysis. Typical results are shown in Figs. 7 through 12. The remainder of the runs are presented in the Appendix. As in the simple grid analysis, a plus or minus five percent un-

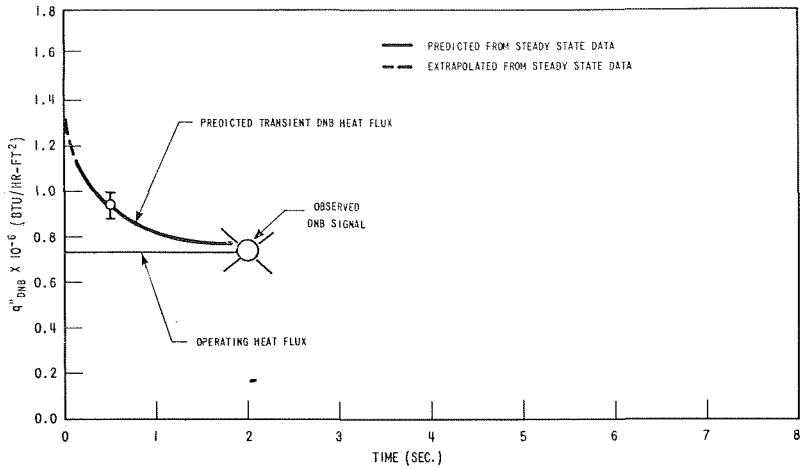

Fig. 7 Transient DNB heat flux during blowdown—run 149.2

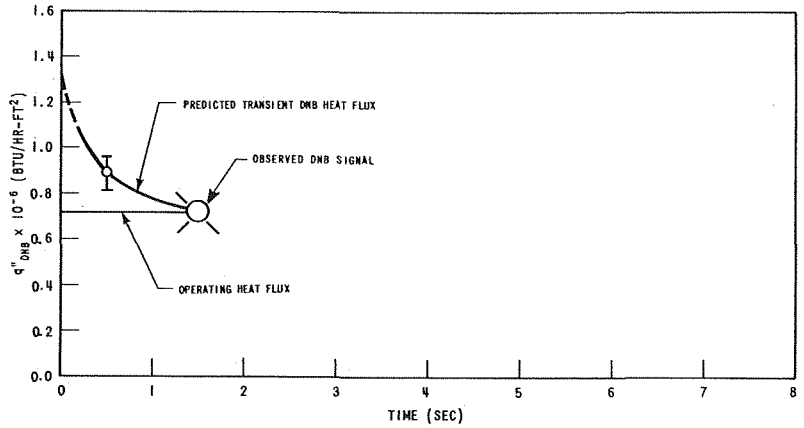

Fig. 8 Transient DNB heat flux during blowdown—run 150

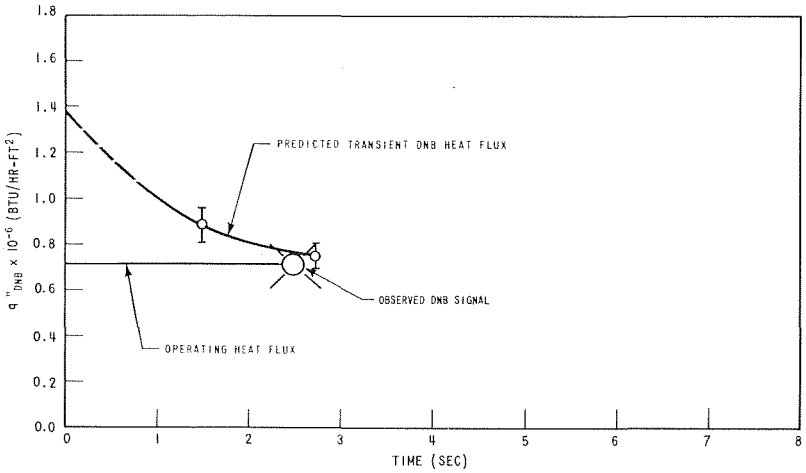

Fig. 9 Transient DNB heat flux during blowdown—run 151

certainty band was assigned to the predicted transient DNB heat flux and represents the general reproducibility of the DNB measurements. Accordingly, DNB is predicted to occur whenever the envelope of the predicted DNB heat flux matches the operating heat flux of the rod bundle. The predicted time for DNB and the times of observed DNB signals are shown in Table 1 for each case.

In the majority of the runs (F-149.2, F-150, F-151, F-153, F-154, F-156, F-158, F-161.2, F-162) the time at which DNB occurred was equal to or greater than the predicted time of DNB.

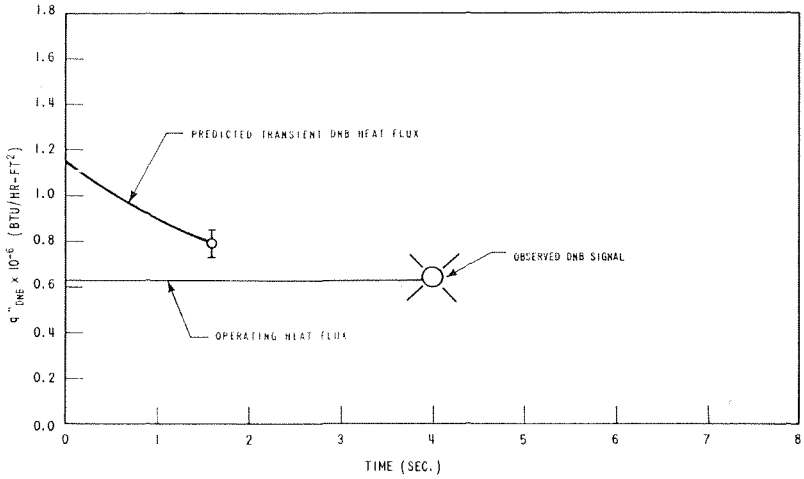

Fig. 10 Transient DNB heat flux during blowdown—run 153

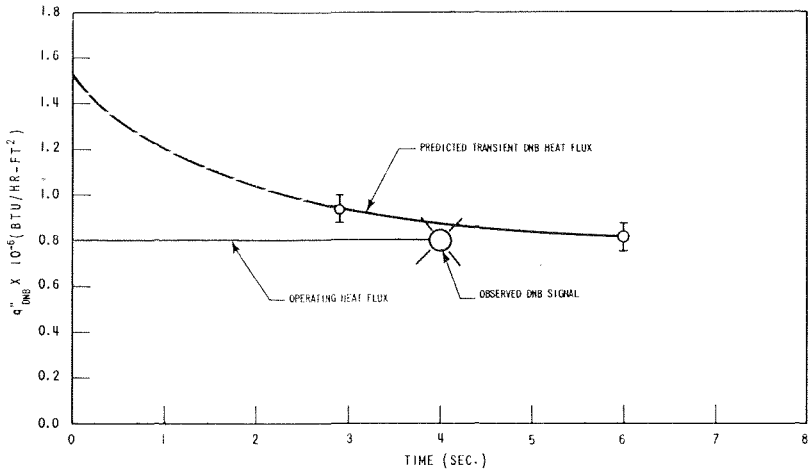

Fig. 11 Transient DNB heat flux during blowdown—run 158

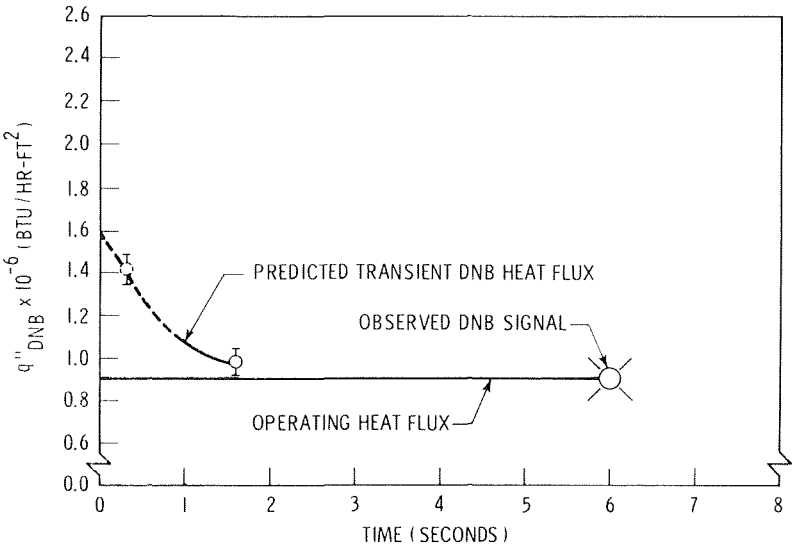

Fig. 12 Transient DNB heat flux during blowdown—run 162

Table 1

Run Number	Earliest Predicted DNB Time	Observed DNB Time
F-149.1	2.1	not observed
F-149.2	1.3	2.0
F-150	1.1	1.5
F-151	2.4	2.5
F-153	3.5	4.0
F-154	1.25	1.5
F-156	.7	1.0
F-157	5.0	not observed
F-158	4.0	4.0
F-160	5.0	not observed
F-161.1	5.0	not observed
F-161.2	1.3	7.0
F-161.3	4.5	not observed
F-161.4	4.7	not observed
F-162	1.8	6.0

This result represents a conservative prediction of the transient DNB heat flux.

Of the remaining six runs (F-149.1, F-157, F-160, F-161, F-161.3, F-161.4) it was predicted that DNB should occur but it was not observed, which is conservative from the point of view of estimating the occurrence of transient DNB. If DNB does not actually occur, then no physical damage can result. Thus it is concluded that transient DNB behavior can be predicted from steady state DNB data.

Conclusions

1 Mixing vane grids produce higher DNB heat fluxes as compared with simple grids. The effectiveness of the mixing vane grids is to reduce the enthalpy rise in the subchannel of the hot rod and to break up the bubble layer along the hot rod.

2 Transient DNB behavior of rod bundles can be predicted by using the steady state DNB data from the same geometry and under the same local fluid conditions.

3 The subchannel analysis is proper for use of determining transient DNB heat fluxes as well as the steady state heat fluxes.

References

1 Tong, L. S., Bishop, A. A., Casterline, J. E., and Matzner, B., "Transient DNB Test on CVTR Fuel Assembly," ASME Paper No. 65-WA/NE-3, 1965.

2 Tong, L. S., Chelemer, H., Casterline, J. E., and Matzner, B., "Critical Heat Flux (DNB) In Square and Triangular Array Rod Bundles," JSME 1967 Semi-International Symposium, Tokyo, pp. 25–34.

3 Bonilla, C. F., and Casterline, J. E., "Department of Chemical Engineering, Engineering Research Laboratories, Heat Transfer Research Facility," Internal Publication, Department of Chemical Engineering, Columbia University, 1965.

4 Weisman, J., Wenzel, A. H., Tong, L. S., Fitzsimmons, D., Thorne, W., and Batch, J., "Experimental Determination of the Departure from Nucleate Boiling on Large Rod Bundles at High Pressure," *Chemical Engineering Progress Symposium Series*, Vol. 64, No. 82, 1968, p. 114.

5 Tong, L. S., "DNB Predictions for an Axially Non-Uniform Heat Flux Distribution," *Journal of Nuclear Energy*, Vol. 21, 1967, pp. 241–248.

6 Tong, L. S., Currin, H. B., Larsen, P. S., and Smith, O. B., "Influence of Axially Non-Uniform Heat Flux on DNB," AIChE Preprint 17, Eighth National Heat Transfer Conference, Los Angeles, 1965.

7 CHIC-KIN, "A Fortran Program for Intermediate and Fast Transients in a Water Moderated Reactor," V. A. Redfield, WAPD-TM-479, Jan. 1965.

APPENDIX

EXPERIMENTAL DATA

SIMPLE GRID

Run No.	Inlet Temp. (°F)	Mass Flow Rate ($\#/lb\ ft^2$)$\times 10^{-6}$	Pressure (psia)	Rod Heat Flux ($Btu/hr\ ft^2$)$\times 10^{-6}$	Operating Conditions
E-87	522.0	1.487	865	0.685	S.S.*
E-88	482.0	1.490	665	0.791	S.S.
E-89	523.0	1.499	1500	0.586	S.S.
E-90	480.0	1.485	1500	0.694	S.S.
E-91	522.0	2.511	874	0.813	S.S.
E-92	522.0	2.485	665	0.905	S.S.
E-93	482.0	2.215	1000	0.929	S.S.
E-94	481.5	2.556	1500	0.968	S.S.
E-95	522.0	2.535	1500	0.791	S.S.
E-96	523.0	3.010	1500	0.876	S.S.
E-97	522.0	3.029	1200	0.835	S.S.
E-98	521.0	2.500	1500	0.717	S.S.
E-100	483.0	2.539	1500	0.990	S.S.
E-101	480.0	2.546	1500	0.970	Trans.**
E-104	522.0	2.523	1500	0.827	S.S.
E-107	519.0	2.532	1200	0.837	S.S.
E-108	521.0	2.510	1000	0.887	S.S.
E-109	522.0	2.752	900	0.883	S.S.
E-110	482.0	2.528	1500	0.964	Trans.

*Steady State

**Transient

MIXING VANE GRID

Run No.	Inlet Temp. (°F)	Mass Velocity ($\#/hr\ ft^2$)$\times 10^{-6}$	Pressure (psia)	Rod Heat Flux ($Btu/hr\ ft^2$)$\times 10^{-6}$	Operating Conditions
F-119	540	1.03	1500	0.505	S.S.
F-120	518	1.02	1500	0.599	S.S.
F-121	522	1.03	1250	0.594	S.S.
F-122	517	1.03	1000	0.582	S.S.
F-123	502	1.01	1500	0.603	S.S.
F-124	482	1.01	1500	0.649	S.S.
F-125	482	1.01	1250	0.638	S.S.
F-126	480	1.01	1000	0.656	S.S.
F-127	479	1.00	750	0.632	S.S.
F-128	518	1.54	1500	0.578	S.S.
F-129	520	1.54	1500	0.707	S.S.
F-130	521	1.52	1250	0.684	S.S.
F-131	522	1.52	1000	0.631	S.S.
F-132	482	1.53	1500	0.847	S.S.
F-133	480	1.53	1250	0.799	S.S.
F-134	481	1.51	1000	0.730	S.S.
F-135	480	1.52	750	0.720	S.S.
F-136	542	2.03	1500	0.753	S.S.
F-137	522	2.04	1500	0.857	S.S.
F-138	522	2.55	1000	0.808	S.S.
F-139	522	2.56	1250	0.872	S.S.
F-140	524	2.51	1500	0.959	S.S.
F-141	542	3.02	1500	0.957	S.S.
F-142	524	2.98	1500	0.998	S.S.
F-143	509	3.02	1500	1.078	S.S.
F-144	500	2.05	1500	0.941	S.S.
F-145	481	1.90	1500	0.982	S.S.
F-146	480	2.55	750	0.841	S.S.
F-147	480	2.53	1000	0.951	S.S.
F-148	484	2.52	1250	1.052	S.S.
F-149.1	481	1.53	1500	0.697	Trans.
F-149.2	481	1.53	1500	0.719	Trans.
F-150	483	1.53	1500	0.718	Trans.
F-151.1	480	1.53	1500	0.719	Trans.
F-152	523	1.53	1000	0.596	S.S.
F-153	520	1.59	1500	0.614	Trans.
F-154	522	1.53	1500	0.619	Trans.
F-155	522	2.54	1250	0.856	S.S.
F-156	522	2.55	1500	0.856	Trans.
F-157	522	2.54	1500	0.794	Trans.
F-158	522	2.54	1500	0.816	Trans.
F-160	484	2.55	1500	0.871	Trans.
F-161.1	482	2.55	1500	0.883	Trans.
F-161.2	482	2.54	1500	0.908	Trans.
F-161.3	482	2.54	1500	0.922	Trans.
F-161.4	482	2.54	1500	0.941	Trans.
F-162	478	2.56	1500	0.918	Trans.

J. C. MOLLENDORF
NSF Trainee, Cornell University, Ithaca, N. Y.

B. GEBHART
Professor of Mechanical Engineering, Cornell University, Ithaca, N. Y.
Mem. ASME

An Experimental Study of Vigorous Transient Natural Convection

External natural convection transient response leading to transition and established turbulent flow is determined experimentally and compared with the laminar double-integral theory predictions for processes wherein all transient effects are important. The theory is shown to give very accurate predictions during the laminar portion of the transient, and temperature overshoot is not observed experimentally. In addition, several unexpected and very interesting observations were made concerning the stability of the flow as it proceeds to turbulence. The first main observation is that the propagating leading edge effect serves as a very effective moving boundary layer trip and triggers the resulting turbulence. Also for the less extreme condition (less vigorous transient) there is a relaminarization of the boundary layer. Explanations of these observations are proposed in the light of recently acquired results of linear stability theory analysis for small disturbances.

Introduction

For the past few years transient natural convection has been the object of increased, intensive study. This is probably due, at least in part, to the recent technological applications of such flows: for example, the natural convection flow over the fuel rods in a nuclear reactor. All previous work in transients has dealt with laminar flows and, although some attention has been given to cylindrical geometries, most of the work (both analytical and experimental) has been concerned with a vertical, flat plate configuration. In the earliest theoretical studies the thermal capacity of the element was neglected, and the main object of research in transient natural convection has been to predict or measure the thermal response subsequent to the imposition of a specified initial condition (usually a step in temperature or heat flux at the solid-fluid interface). Of considerable concern was whether or not the temperature during the transient response rose above the final steady-state value, i.e., temperature overshoot. Although the early studies provided much information about transients, definitive conclusions regarding transient response were hampered by inconsistent results and, until recently, the history of transient natural convection has not been without opposing views with regard to the question of temperature overshoot.

In 1961, Gebhart [1][1] developed a double-integral method for

Contributed by the Heat Transfer Division and presented at the Fluids Engineering, Heat Transfer, and Lubrication Conference, Detroit, Mich., May 24–27, 1970, of The American Society of Mechanical Engineers. Manuscript received by the Heat Transfer Division, May 21, 1969; revised manuscript received January 8, 1970. Paper No. 70-HT-2.

[1] Number in brackets designate References at end of paper.

Nomenclature

a = parameter determining the division of thermal energy input between the wall and the fluid $a = (\rho c_p k)^{1/2} c''$

b = generalizing factor for time

c'' = thermal capacity of element per unit surface area

c_p = specific heat

f = frequency of naturally occurring disturbances

g = gravitational acceleration

G* = flux Grashof parameter G* = $5(\mathrm{Gr}^*/5)^{1/5}$

Gr = Grashof number based on L and $\overline{\Delta t}$, $\mathrm{Gr} = \dfrac{g\hat{\beta}L^3\overline{\Delta t}}{\nu^2}$

Gr* = flux Grashof number based on L, $\mathrm{Gr}^* = \dfrac{g\hat{\beta}L^4q''(\tau)}{k\nu^2}$

Gr_x = local value of the Grashof number $\mathrm{Gr} = \dfrac{g\hat{\beta}x^3\Delta t}{\nu^2}$

Gr_x^* = local value of the flux Grashof number $\mathrm{Gr}_x^* = \dfrac{g\hat{\beta}x^4q''(\tau)}{k\nu^2}$

k = thermal conductivity

l = half-thickness of foil

L = height of element

M = derivative of generalized temperature distribution

N = number of fringes

p = test section pressure

(*Continued on next page*)

external natural convection transients for a vertical surface having finite and arbitrary thermal capacity per unit surface area c'' and negligible internal relative heat transfer resistance in the direction normal to the surface, subjected to a possibly time-dependent but spatially uniform (over the element height) internal energy generation rate $q''(\tau)$ per unit surface area. An energy input condition with an arbitrary element thermal capacity is much more realistic than the application of a step in temperature or in flux at the fluid-solid interface. In 1963, Gebhart [2] showed that the response characteristics are very much affected by the element thermal capacity. In fact this feature results in regimes of natural convection transient response as c'' decreases, from quasi-static, through actual convection transients, to essentially a conduction-type of initial response. Moreover, in 1967, Gebhart, Dring, and Polymeropoulos [3] compared various measured transients with the double-integral theory presented by Gebhart [1]. The experimental data gathered in [3] as well as the data of Gebhart and Adams [4], Goldstein and Eckert [5], and Lurie and Johnson [6] showed excellent agreement with the double-integral theory for a wide range of experimental conditions. The validity of the agreement is supported by the fact that the data covered a broad range of conditions and fluids and was measured by several completely different types of apparatus. Consequently, this recent work has shown quite conclusively that for reasonable starting conditions and completely laminar transients, temperature overshoot does not occur for a vertical surface for a very wide range of circumstances.

Nevertheless, it is not unreasonable to question the existence of extreme response characteristics for circumstances unlike those previously considered. One such circumstance is that of a transient which is not completely laminar. Such a transient was studied experimentally in this work. This experiment, similar to that reported in [3], was performed at much higher Grashof numbers to observe any transition or turbulence which might occur in a rapidly accelerating and highly unstable laminar flow.

For the natural convection transient which occurs subsequent to an input to an element of finite thermal capacity, the integral theory analysis of response [2], substantially supported by experimental results, as indicated above, predicts that true convection transients occur for values of the generalized thermal capacity, Q, in the interval $0.1 \leq Q \leq 1.0$. In this regime, the modification of the initial one-dimensional field into the final two-dimensional field by the propagating leading edge effect, see Goldstein and Briggs [7] and Gebhart and Dring [8], and the adjustment of the resulting two-dimensional field to the appropriate steady-state one are very complicated flow processes and at this time are not completely understood. It is an experimental study of a transient of this third type which is the basis of this work.

This study concerned specifically temperature response characteristics in a very vigorous transient which begins in a laminar flow which becomes unstable and at final steady state is primarily turbulent. The questions are: Is disturbance amplification delayed, is transition delayed, do any such delays lead to extreme temperature excursions in the heated element which generates the flow, etc.

In addition, certain of the transient circumstances studied here showed several very surprising flow characteristics. We feel that these observations may be explained in terms of recently acquired understanding of several transient and stability mechanisms of natural convection flows.

New Measurements

Since we are concerned here with vigorous transients to unstable and turbulent flow, it is necessary to observe circumstances wherein $\mathrm{Gr} \gg 10^9$ locally during the transient. It is noted here that all previously reported transient natural convection experiments were such that $\mathrm{Gr} \leq 3.98 \times 10^9$. They were entirely laminar.

A convenient way to assess the applicable range of an experimental apparatus for studying transients was presented in [3]. Using the known physical constraints of the apparatus, a region can be isolated in a Gr-Q plot, where Q is the generalized thermal capacity and is roughly a ratio of the thermal capacities of the foil and fluid. The apparatus used in this experiment is the 8-in. Mach-Zehnder interferometer described in [9]. The limits imposed by the interferometer and pressure system are the upper and lower limits in pressure (18 to 1.2 atm), the observable plate length limit (18 in.), the maximum number of interferometer fringes which may be distinguished, and the minimum number of fringes which would give accurate temperature determinations. In addition, temperature differences were limited to 100 deg F to limit fluid property variations. The gas was purified bottled nitrogen. In the same manner as [3] these limiting relations are derived and the following results are obtained.

Pressure:	$\mathrm{Gr} \geq (9.4 \times 10^8)Q^4$	$p \geq 1.2$ atm
	$\mathrm{Gr} \leq (4.7 \times 10^{13})Q^4$	$p \leq 18$ atm
Fringes:	$\mathrm{Gr} \leq (6.2 \times 10^{10})Q^{-4/3}$	$N \leq 120$
	$\mathrm{Gr} \geq (6.6 \times 10^8)Q^{-4/3}$	$N \geq 4$
Temperature difference:	$\mathrm{Gr} \leq (1.13 \times 10^9)Q^{-1/4}$	$\overline{\Delta t} \leq 100$ deg F

These are plotted in Fig. 1, along with all previously measured transient conditions. The Gr-Q area within the polygon is accessible. It may be seen that Grashof numbers of over 10^{11} can be obtained within these constraints.

With normal optics, the maximum number of fringes that can be counted is approximately 30. The figure of 120 is exceedingly high. This limit of 120 fringes was interpreted using laminar theory. It is reasonable to assume that there should be fewer than 120 fringes in the established turbulent flow because turbulent transport is more effective than laminar. Neverthe-

Nomenclature

Q = constant related to element storage capacity $Q = \dfrac{c''}{\rho c_p L M}\,[b\,\mathrm{Gr}^*\,\sigma]^{1/5}$

Q^* = see [12], $Q^* = \dfrac{\sigma}{5}\,\dfrac{(\rho l c_p)\ \text{foil}}{(\rho x c_p)\ \text{fluid}}$

$q''(\tau)$ = instantaneous energy generation rate per unit of element surface area

t' = nondimensionalized time $t' = \alpha\sqrt{\tau}$

T = generalized time in transient $T = \dfrac{\alpha\tau}{2}\,[b\,\mathrm{Gr}^*\,\sigma]^{2/5}$

U^* = $\nu\,\mathrm{G}^{*\,2}/5x$

x = distance along the plate

x' = nondimensionalized distance along plate $x' = (ka^5/g\hat{\beta}q''\sqrt{\alpha})x_{p,\max}$

$x_{p,\max}$ = distance leading edge effect propagates up the surface in time τ

α = thermal diffusivity

β = dimensionless frequency $\beta = \bar{\beta}\delta/U^*$

$\bar{\beta}$ = $2\pi f$

$\hat{\beta}$ = volumetric coefficient of thermal expansion

δ = $5x/\mathrm{G}^*$

θ_0 = instantaneous local temperature maximum

$\bar{\theta}_0$, $\bar{\psi}$, $\overline{\Delta t}$ = average over height of element

λ = wavelength of naturally occurring disturbance

ν = kinematic viscosity

ρ = fluid density

σ = Prandtl number

τ = time

ψ = temperature excess ratio

Subscripts

0 = at plate surface

∞ = at infinite time during transient

l = pertains to laminar theory

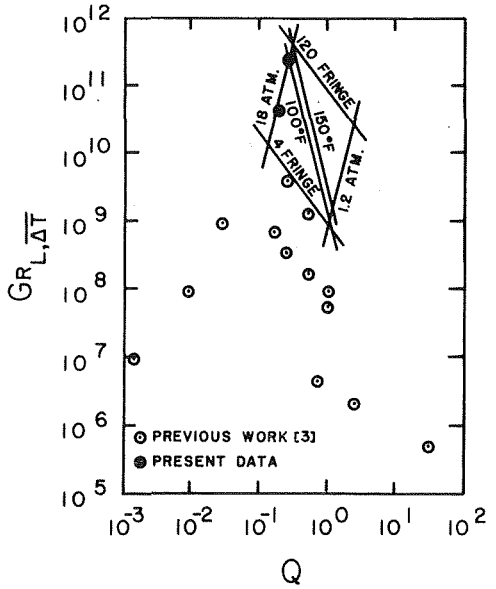

Fig. 1 Previously measured transients and currently reported ones

less, since there was no way of knowing exactly how many fringes could be expected, it seemed desirable and probably necessary to expand the field with an anamorphic lens system. Both prismatic anamorphs and cylindrical lens systems were investigated. Finally a system similar to that of Buchelle and Goossens [10] was chosen. The addition of this lens system provided the capability of anamorphically enlarging the field normal to the surface by as much as 24:1.

The surface was constructed by stretching a piece of $19^3/_4$-in. by 2-in. by 0.0005-in. Inconel-600 foil between two knife edges. The knife edge assembly was then mounted in a positioning apparatus which in turn was placed in the pressure vessel. The foil and positioning apparatus was equipped with motor-driven adjustments for remote foil alignment. The foil was subjected to a step in current and the resulting convection layers on both sides of the foil were observed between the length interval of 10 to 18 in. by the 8-in. Mach-Zehnder interferometer. Transient response was recorded in a 16-mm movie of the transient interferogram.

Time was recorded during the transient by an electrical timer which was focused into the movie camera, along with interferograms, by means of mirrors and lenses. The timer was triggered at the instant when the step in current was applied by means of a double switch. The quality of the step in current was determined by monitoring the plate current on an oscilloscope. The scope was triggered by a needle connected to the power switch. That is, when the step in current was applied, the transient response of the power supply was recorded. The needle was positioned so that the scope was triggered slightly before the switch made contact. This response indicated that the power supply time constant is approximately 80 microsec, which is within the specifications of the manufacturer of the power supply and is very fast compared with even the fastest transient studied here.

The temperature field is determined from interferograms which were recorded during the transient by means of a high-speed movie camera. A shutter speed of 80 frames per sec was used, and the camera was allowed to attain full speed before power was applied to the foil. Consequently, many frames showing the unheated foil and field were available. These "unheated frames" are distortion-free and are used as a reference when analyzing optical distortion present at high heating rates. A piece of brass, accurately machined in the form of a symmetrical "staircase" (see Figs. 5 and 6) was used to provide known reference dimensions in the field. Two experimental conditions were studied, corresponding to heating rates of 269 and 29.4 Btu/hr ft^2.

Results

The instantaneous foil temperature was obtained by counting fringes into the foil, and using the relation between fringe shift and temperature change, which, for the conditions studied, was 1.35 deg F/fringe. While the fringes were counted, they were also recorded as a function of distance, from the fixed and known dimensions in the field. Comparison between heated and unheated conditions showed no observable changes in the known reference dimensions in the field for the lower heating rate used. This was not the case for the higher heating rate. The data obtained at the higher heating rate (necessary for very vigorous transients) exhibited a phenomenon resulting in a disappearance of the field in the vicinity of the foil. The amount of disappearance was noted to increase as the time increased (i.e., as the plate got hotter) during the transient.

The cause of this disappearance is unknown at the present time. The possibility of refraction errors is being investigated, but such analysis is not applied here. The basic idea used in refraction error analysis is to calculate the deflection of a light ray produced by a refractive index gradient normal to the light path and consider the resulting relative retardation as the ray proceeds to the photographic film. A much simpler means of arriving at a quantitative answer is to use instead an extrapolation procedure for the distorted part of the field.

Several methods of extrapolation were tried and it proved desirable to find a method that considers all the data points and allows some freedom in the choice of the degree of the interpolating polynomial. Such a method is polynomial regression. This is a standard subroutine in the IBM library which fits a "best curve" to data by finding the polynomial which best represents the data in a least-squares sense. The method was applied to both sides of the foil, for each time considered, and the two resulting values of foil temperature agreed to within a few percent. While the higher heating rate data exhibited distortion which required correction, the lower heating rate did not.

Both experimental conditions studied are in the "true" convection transient region, as defined by a range of the generalized thermal capacity, Q, of $0.1 < Q < 1.0$, see [2]. The values of the generalized thermal capacity, Q, for the higher and lower heating rates used in this experiment are 0.25 and 0.16, respectively. These correspond to Grashof numbers based on length, L, and average temperature difference, $\overline{t\Delta}$, of 2.52×10^{11} and 4.30×10^{10}, respectively.

Time during the transient is expressed in terms of a generalized time variable, $T = \dfrac{\alpha\tau}{L^2}(b\,\mathrm{Gr}^*\,\sigma)^{2/5}$, where α is the thermal diffusivity of the gas, τ is the actual time, L is the plate length, b is a generalizing factor for time, Gr* is the flux Grashof number, and σ is the Prandtl number. The instantaneous local temperature maximum, θ_0, is obtained directly from the interpretation of the interferograms. From the experimental operating conditions, the expected laminar, steady-state temperature excess averaged over the plate height, $\theta_{0,\infty,l}$ was calculated. This predicted value was compared with the experimentally observed value where laminar, steady-state conditions prevailed, i.e., the relaminarization of the lower heating rate transient. Comparison shows that the predicted temperature excess is within 8 percent of the experimental for this case, suggesting perhaps that edge effects are of little importance. It is also noted that before turbulence sets in, the boundary layer thickness is less than one-eighth of the plate width. The temperature excess ratio, ψ, is then given by $\psi = \theta_0/\theta_{0,\infty,l}$. By averaging ψ over the plate height (denoted $\bar{\psi}$) and by expressing generalized time by T/Q, experimental response data points were compared with the laminar theory. Since only the upper 8 in. of the foil were observable experimentally, the average was taken only over this

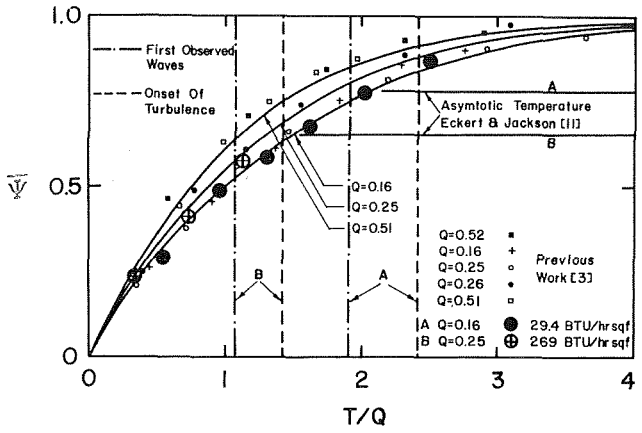

Fig. 2 **Comparison of calculated and measured temperature responses in the true transient regime**

upper portion of the foil. This will result in no error during the early (one-dimensional conduction) part of the transient response since the surface is at uniform temperature at this time. It is also pointed out that for an eventual steady laminar flow the error of such an averaging technique would be about 11 percent. However, the flow becomes turbulent long before such an extreme condition is reached. After that no average response characteristics are calculated. Therefore, the errors in estimated instantaneous average surface temperatures are much less than 11 percent. In addition, it was noted that temperature gradients along the foil were very small. Response curves for the two conditions studied are compared with laminar response theory in Fig. 2. Since a fringe count was unobtainable as the flow became more chaotic, response data is shown up to the onset of transition.

Also, in Fig. 2, demarcations are shown indicating the time at which the first observed disturbances and the onset of turbulence occur. Even though an accurate count of the fringes is not available as the waves amplify greatly (for the higher heating rate only) because of the very confused nature of the flow field, a careful count is possible up to this point. The onset of turbulence occurs at a value of $\bar{\psi}$ of 0.90 and 0.65 for the lower and higher heating rates, respectively. Note that both of these values of $\bar{\psi}$ are less than the laminar steady-state values ($\bar{\psi} = 1$). This is expected since turbulent transport is a more effective means of removing heat. Also the transport effectiveness is shown to increase (0.90 versus 0.65) as the vigor of the turbulence increases, as expected. This is further substantiated by calculating the final foil temperature for turbulent flow using a correlation proposed by Eckert and Jackson [11] for $Gr > 10^{10}$. These resulting asymptotic values are shown on Fig. 2 for the two heating rates examined here. Note that the higher heating rate data seem to match this asymptote, whereas the lower heating rate data overshoot the prediction by about 10 percent. This may be due to the fact that for the lower heating rate a miscount of one fringe would cause such a discrepancy, since there are only about nine fringes for this case. The data can also be compared with that of Bayley [12]. For the case of the higher heating rate the correlation of Bayley is about 3 percent lower than that of Eckert and Jackson. For the lower heating rate case it is about 11 percent lower. So for the more vigorous transient, there is little distinction between the present data and those of both Bayley and Eckert and Jackson. However, for the lower heating rate, the present data agree more closely with those of Eckert and Jackson. More recent studies such as Warner [13] and Vliet and Liu [14] show agreement with Bayley, whereas Cheesewright [15] compares more favorably with the prediction of Eckert and Jackson.

Additional Observations

The first important observation from the interferogram movie is that, as the initially one-dimensional convection field is supplanted, through the leading edge effect, by a two-dimensional field, the local flow carries periodic disturbance waves of a single wavelength which amplify very quickly and explode into transition and turbulent flow (see Fig. 5). The second important observation is that the established turbulent boundary layer is later quickly swept away (lower heating rate only) by an apparently undisturbed laminar flow coming from the upstream region of the foil (see Fig. 6).

We think that the characteristics referred to first above may be explained through a combination of: known characteristics of leading edge effect propagation, the instability properties of such boundary layers, and the selective (or filtering) mechanisms of disturbance amplification in such flows. The second observation referred to above, i.e., that the turbulent boundary layer is subsequently swept away by an undisturbed laminar flow coming from the upstream region of the foil, is also consistent with what we know from experimentation with such flows.

Approximate values of Gr_x, Gr_x^*, the frequency f, and the wavelength λ, of the observed waves which precede turbulence are tabulated along with the time at which they were observed. By using a nondimensionalized frequency $\beta = \tilde{\beta}\delta/U^*$, where $\tilde{\beta} = 2\pi f$, $\delta = 5x/G^*$, and $U^* = \nu G^{*2}/5x$ and the flux Grashof parameter $G^* = 5(Gr^*/5)^{1/5}$, the naturally occurring disturbance data can be compared with the linear stability theory for small disturbances. In such a manner, the specific points 1, 4, 5, and 7 are located on such a neutral stability (β versus G^*) plot of Knowles and Gebhart [16] along with related data of Polymeropoulos and Gebhart [17] in Fig. 3. At the present time, amplification characteristics are not known for the region where the data lies. Nevertheless, judging from stability plots for another Prandtl number (see Dring and Gebhart [18]), it is not unreasonable to assume that the data (for both heating rates) lie in the region where disturbances are highly amplified. In addition, several lines of constant frequency amplification, as the disturbance is convected downstream, corresponding to the various frequencies of the experimental data are shown. Furthermore, the natural disturbance data of Polymeropoulos and Gebhart [17] are shown on Fig. 3 and are consistent with the inferences mentioned in the foregoing.

As time in the transient increases, the first observed waves are seen to amplify a great deal, and before the flow explodes into turbulence (higher heating rate), "spike-like" disturbances protrude intermittently from the boundary layer (see Fig. 5).

Approximate values of Gr_x, Gr_x^*, the frequency f, and the wavelength, λ, for naturally occurring disturbances

Point	Time (sec)	Location (in.)	Wavelength (in.)	Frequency (Hz)	Grashof number	Flux Grashof number
1	1.45	15	1	4.6	6.48×10^{10}	2.94×10^{13}
2	1.58	$16\frac{1}{4}$	$\frac{3}{4}$	4.6		
3	1.80	17	$\frac{3}{4}$	6.0		
4	1.90	18	$\frac{3}{4}$	6.0	1.19×10^{11}	6.09×10^{13}
5	4.00	13	$1\frac{1}{2}$	2.0	9.12×10^{9}	1.79×10^{12}
6	4.58	15	$1\frac{1}{2}$	2.0		
7	5.06	18	$1\frac{1}{2}$	2.0	2.76×10^{10}	6.65×10^{12}

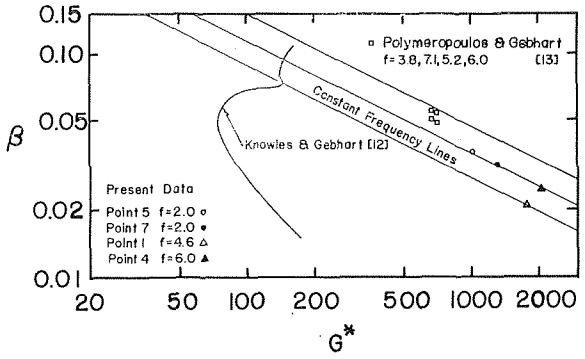

Fig. 3 Location of first observed naturally occurring disturbances on β versus G* stability plot

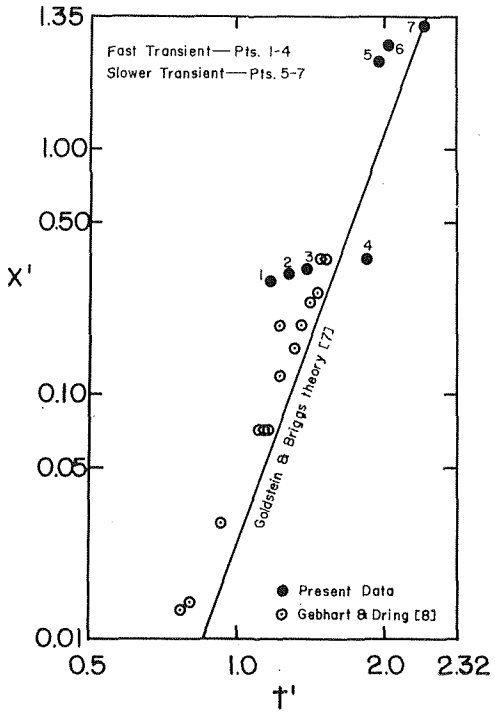

Fig. 4 Comparison of first observed waves to the leading edge propagation rate theory and other data

Also, the amplification appears to be accompanied by a steepening of the waves, see the interferograms of Fig. 5. The extremeness of this steepening effect was observed to be related to the vigor of the transient. For the lower heating rate condition examined here, the steepening rate and amount is relatively mild, but for the very vigorous condition, it is extreme. As the field becomes more chaotic, an accurate count of the fringes is unobtainable for the higher heating rate for times after transition.

By defining a nondimensionalized distance along the plate, x', and a nondimensionalized time, t', as $x' = (ka^5/g\hat{\beta}q''\sqrt{\alpha})x_{p,\max}$ and $t' = a\sqrt{\tau}$, where "a" is a parameter determining the division of thermal-energy input between the wall and the fluid $(\rho c_p k)^{1/2}/c''$, Gebhart and Dring [8] have shown that the leading edge propagation rate theory of Goldstein and Briggs [7] can be reduced to an $x' - t'$ diagram. Calculations reveal that the first observed periodic disturbances convected by and propagating in the flow appear to be associated with the propagating leading edge effect. In Fig. 4 the locations of the propagating disturbances at various times are shown as points, compared to the theory of leading edge effect propagation on the $x' - t'$ diagram, in the manner of [8], applicable to such a laminar transient. The agreement is sufficiently close to suggest that the disturbances are generated in the transition from one- to two-dimensional laminar flow. Similar disturbances are also seen in the interferogram at 3 sec of the sequence shown in [8].

Conclusions

Despite the high Grashof numbers of the experimental conditions studied, Fig. 2 shows that the laminar double-integral theory gives very accurate predictions for the laminar portion of the transient response for both the higher and lower heating rates used in this experiment. In addition, the measured temperature does not rise above the predicted laminar response value for the conditions studied here, i.e., $\sigma = 0.72$, $Q = 0.25$, $Q = 0.16$. It should be cautioned, however, that this may not be the case for conditions at large values of σ and Q. These conditions may be more susceptible to temperature overshoot because of the relatively high thermal capacity of the foil and low thermal diffusivity of the fluid.

Although the primary purpose of this work was to study the thermal response in a vigorous transient, much unexpected and very interesting information was also obtained.

In the light of stability theory it would be asked why disturbances generated as they are here would have the observed, or any particular, wavelength and frequency. It is apparent, from other studies, that if the generated disturbance has a more complicated form, certain of the constituent harmonies would, in effect, be selectively amplified due to the particular characteristics of unstable laminar boundary layers of this type. This "filtering" characteristic, or selectivity, has been shown in both theory and in measurement. See [18] and [19] for evidence of such disturbance behavior in a liquid having a Prandtl number of 6.7. In future publications a like characteristic will be shown for gases, both from theory in general and from experimental observations of the amplification of naturally occurring disturbances. The frequency of the observed, i.e., rapidly amplified disturbances, here are exactly what one would expect from such considerations. The mechanism is then that the complicated disturbance of the leading edge effect is decomposed, by selective amplification and damping, into a dominant frequency.

Another question is: Why does this disturbance not outrun or fall behind the propagating leading edge effect? Again instability theory provides an explanation. The calculated maximum disturbance velocities of the frequencies having the highest amplification rates are comparable to the maximum base flow velocity, see [16] and [18]. The leading edge effect is calculated to propagate at the maximum velocity. Therefore the two effects are tied together.

The above explanation in terms of disturbance filtering and amplification, of a more complicated disturbance associated with the leading edge effect, may be restated as though the propagating leading edge effect amounts to a very effective moving boundary layer trip.

It is necessary to point out that the above explanation is not at this time definitive because the stability calculations referred to above are for steady base flows, not for the transients under observation here. However, we believe, in the light of work in transient instability in similar flows, see [20], that the above conjectures are reasonable.

In addition, we should like to propose certain hypotheses regarding the relaminarization of the boundary layer.

We have seen, in numerous experiments, that amplifying disturbances and transition are usually not present in flows until far beyond the location of incipient instability, see, e.g., [17], and that the amount of delay is highly variable and probably associated with the natural disturbance level in the experimental environment. Now, the test apparatus used in the experiment under discussion here has always yielded results suggestive of an extremely low level of natural disturbances. It is proposed, therefore, that the relaminarization which we see here occurs

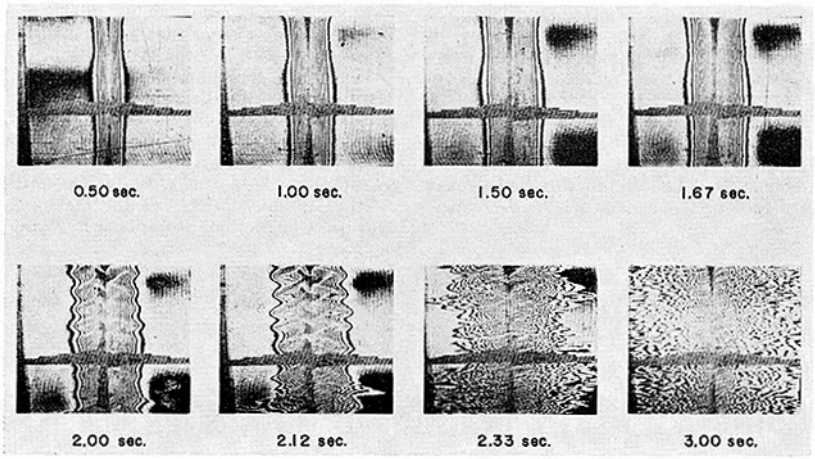

Fig. 5 Interferograms at various times during the convection transient $q'' = 269$ Btu/hr ft^2, $Q = 0.25$, $Gr_{L,\overline{\Delta t}} = 2.52 \times 10^{11}$, $p = 17.97$ atm

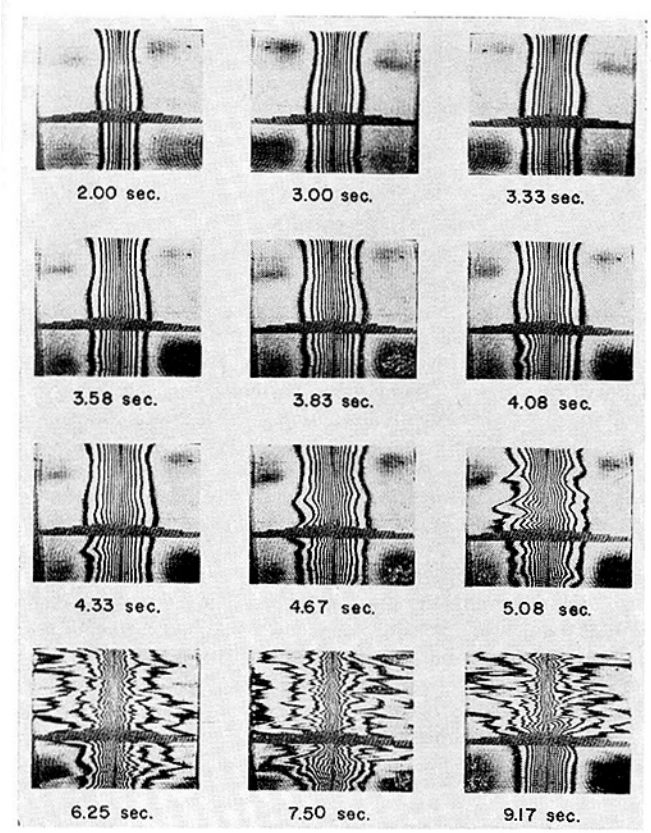

Fig. 6 Interferograms at various times during the convection transient $q'' = 29.4$ Btu/hr ft^2, $Q = 0.16$, $Gr_{L,\overline{\Delta t}} = 4.30 \times 10^{10}$, $p = 17.97$ atm

because the upstream boundary region is offered no additional (or later) disturbances, and, as a result, amplifies none. Disturbances are generated by the turbulence but the short period and the configuration of the flow did not, at this low energy intensity, result in a sustaining feedback mechanism. This is in contrast with forced flow circumstances in which the external flow, and other sources such as mechanical vibration, continually offer a disturbance spectrum to the unstable upstream laminar boundary layer. In forced flow, a relaminarization results, presumably, from the local boundary region flow regaining the conditions for a laminarly stable configuration. We would expect that, in this natural convection configuration, a steady location of transition and steady turbulence would result in an environment possessing a significant level of natural and feedback disturbances and that the Grashof number of transition would be less, the higher the amplitude of the disturbances present.

It is noted here that the much more vigorous flow circumstance did not show a restoration of a laminar boundary layer. Our tentative conclusion is that the initially established turbulent flow was sufficiently vigorous to feed back into the unstable upstream laminar boundary layer disturbances of sufficient amplitude to lead to more-or-less continuous transition.

Acknowledgment

The authors wish to acknowledge the support of this research by the National Science Foundation under Research Grant GK1963.

References

1 Gebhart, B., "Transient Natural Convection from Vertical Elements," JOURNAL OF HEAT TRANSFER, TRANS. ASME, Series C, Vol. 83, No. 1, Feb. 1961, p. 61.

2 Gebhart, B., "Transient Natural Convection from Vertical Elements—Appreciable Thermal Capacity," JOURNAL OF HEAT TRANSFER, TRANS. ASME, Series C, Vol. 85, No. 1, Feb. 1963, p. 10.

3 Gebhart, B., Dring, R. P., and Polymeropoulos, C. E., "Natural Convection from Vertical Surfaces, the Convection Transient Regime," JOURNAL OF HEAT TRANSFER, TRANS. ASME, Series C, Vol. 89, No. 1, Feb. 1967, p. 53.

4 Gebhart, B., and Adams, D., "Measurements of Transient Natural Convection on Flat Vertical Surfaces," JOURNAL OF HEAT TRANSFER, TRANS. ASME, Series C, Vol. 85, No. 1, Feb. 1963, p. 25.

5 Goldstein, R. J., and Eckert, E. R. G., "The Steady and Transient Free Convection Boundary Layer on a Uniformly Heated Vertical Plate," *International Journal of Heat and Mass Transfer*, Vol. 1, 1960, p. 208.

6 Lurie, H., and Johnson, H. A., "Transient Pool Boiling of Water on a Vertical Surface With a Step in Heat Generation," JOURNAL OF HEAT TRANSFER, TRANS. ASME, Series C, Vol. 84, No. 2, May 1962, p. 217.

7 Goldstein, R. J., and Briggs, D. G., "Transient Free Convection about Vertical Plates and Circular Cylinders," JOURNAL OF HEAT TRANSFER, TRANS. ASME, Series C, Vol. 86, No. 4, Nov. 1964, p. 490.

8 Gebhart, B., and Dring, R. P., "The Leading Edge Effect in Transient Natural Convection From a Vertical Plate," JOURNAL OF HEAT TRANSFER, TRANS. ASME, Series C, Vol. 89, No. 5, Aug. 1967, p. 274.

9 Gebhart, B., and Knowles, C. P., "Design and Adjustment of a 20 cm. Mach-Zehnder Interferometer," *The Review of Scientific Instruments*, Vol. 37, 1966, p. 12.

10 Buchelle, D. R., and Goossens, H. R., "Lens System Producing Unequal Magnification in Two Mutually Perpendicular Directions," *The Review of Scientific Instruments*, Vol. 25, 1954, p. 262.

11 Eckert, E., and Jackson, T. W., NACA Report 1015, 1951.

12 Bayley, F. J., "An Analysis of Turbulent Free-Convection Heat-Transfer," *Proceedings, Institution of Mechanical Engineers*, Vol. 169, 1955, p. 2.

13 Warner, C. Y., PhD thesis, University of Michigan, 1966.
14 Vliet, G. C., and Liu, C. K., "An Experimental Study of Turbulent Natural Convection Boundary Layers," JOURNAL OF HEAT TRANSFER, TRANS. ASME, Series C, Vol. 91, No. 4, Nov. 1969, p. 517.
15 Cheesewright, R., "Turbulent Natural Convection from a Vertical Plane Surface," JOURNAL OF HEAT TRANSFER, TRANS. ASME, Series C, Vol. 90, No. 1, Feb. 1968, p. 1.
16 Knowles, C. P., and Gebhart, B., "The Stability of the Laminar Natural Convection Boundary Layer," *Journal of Fluid Mechanics*, Vol. 34, 1968, p. 657.
17 Polymeropoulos, C. E., and Gebhart, B., "Incipient Instability in Free Convection Laminar Boundary Layers," *Journal of Fluid Mechanics*, Vol. 30, 1967, p. 225.
18 Dring, R. P., and Gebhart, B., "A Theoretical Investigation of Disturbance Amplification in External Laminar Natural Convection," *Journal of Fluid Mechanics*, Vol. 34, 1968, p. 551.
19 Dring, R. P., and Gebhart, B., "An Experimental Investigation of Disturbance Amplification in External Laminar Natural Convection Flow," *Journal of Fluid Mechanics*, Vol. 35, 1969, p. 447.
20 Gunness, R. C., Jr., and Gebhart, B., "Stability of Transient Natural Convection," to appear in *Physics of Fluids*.

G. M. FULS
Senior Engineer,
Westinghouse Electric Corp.,
Bettis Atomic Power Laboratory,
Pittsburgh, Pa. Mem. ASME

G. E. GEIGER
Associate Professor,
Department of Mechanical Engineering,
University of Pittsburgh,
Pittsburgh, Pa. Mem. ASME

Effect of Bubble Stabilization on Pool Boiling Heat Transfer[1]

It is an established phenomenon that bubbles can be stabilized in a vertically vibrating liquid column. The effect of bubble stabilization on the rate of pool boiling heat transfer is experimentally investigated. With the liquid and heating surface vibrating as a unit, the data indicates a decrease of up to 12 percent in the temperature difference necessary for a given heat flux within the range of frequencies from 200 to 300 cps. The experimental results and comparison with results of previous investigators show that the effect is unique and not due simply to the vibrations per se.

Introduction

Bubble stabilization in a vertically vibrating liquid column and the effects of vibration on pool boiling heat transfer have both separately been known and under investigation for a number of years. However, the combined phenomena have not previously been investigated despite the fact that in many practical applications, such as ship propulsion units, the entire system will vibrate.

It is the purpose of this paper to present data on the effects of bubble stabilization on the rate of heat transfer and to show that this effect is distinct from the effect of vibration only on the rate of heat transfer.

The analytical developments of a criterion for bubble stabilization are reported in the literature. A comprehensive bibliography and discussion of the phenomenon are presented by Fuls [1].[2] For a given frequency of sinusoidal vertical oscillation, there corresponds a unique amplitude for a given depth of immersion that will prevent small bubbles from either rising or falling. A decrease in amplitude will permit the bubble to rise and an increase in amplitude will cause it to fall. The relationship between the amplitude and frequency developed by Fuls [1] is

$$\left\{\frac{\omega^2 x_0}{g}\,\frac{\sin\dfrac{2\omega z}{c}}{\dfrac{\omega z}{c}\left(1+\cos\dfrac{\omega L}{c}\right)}\right\}^{1/2} = \left\{\frac{\mu e}{3}\left(1-\frac{\rho_v}{\rho_L}\right)\left(1-\frac{\omega^2}{\Omega^2}\right)2\gamma\left(1+\frac{P_u+\dfrac{2\sigma}{a}}{\rho_L g z}\right)\right\}^{1/2} \quad (1)$$

An extensive survey of the literature on the effects of vibrations on heat transfer was presented in Bergles and Morton [2]. This survey was brought up to date by Fuls [1] with particular emphasis on pool boiling heat transfer. Only a brief summary of these surveys will be presented here to demonstrate that the effect of bubble stabilization is not the same effect associated with a critical intensity, as reported by previous investigators.

Where there are spatial gradients of fluctuating velocity products, such as those generated by a relative oscillatory motion between a solid body and a fluid, a steady flow will result. In general, this steady flow is referred to as acoustic streaming, particularly if the flow is laminar. A useful introduction to acoustic streaming and acoustics in general is given by Richardson [3]. Increasing the intensity of oscillation beyond some critical value will result in some portion of the flow becoming turbulent. This

[1] This work in part was used by Dr. Fuls in fulfillment of the Doctor of Philosophy Degree thesis requirements of the University of Pittsburgh.

[2] Numbers in brackets designate References at end of paper.

Contributed by the Heat Transfer Division and presented at the Fluids Engineering, Heat Transfer, and Lubrication Conference, Detroit, Mich., May 24–27, 1970, of The American Society of Mechanical Engineers. Manuscript received at ASME Headquarters, October 17, 1969. Paper No. 70-HT-4.

Nomenclature

A = area
C = constant
c = speed of sound
c_L = specific heat of liquid
g = gravitational constant
H_{fg} = heat of vaporization
k_L = thermal conductivity of liquid
L = depth of liquid column
P_u = ullage pressure
q = heat flux
T_{sat} = saturation temperature
T_w = wall temperature
x_0 = amplitude of vibration
z = vertical displacement from liquid free surface
γ = ratio of specific heats of gas in bubble
μ_e = coefficient of apparent mass of bubble in expansion
μ_L = viscosity of liquid
ρ_L = mass density of liquid
ρ_v = mass density of vapor
σ = surface tension
Ω = natural frequency of bubble
ω = radial frequency of vibration

type of turbulent flow in conjunction with natural convection heat transfer is referred to as thermoacoustic streaming [4, 5]. Thermoacoustic streaming is characterized by vortex shedding from the heated element and is similar to a von Karman vortex street.

Superposition of acoustic streaming on natural convection heat transfer would be expected to have some effect on the rate of heat transfer. The effect was analytically predicted and experimentally verified by Blankenship and Clark [6, 7], and Eshghy, Arpaci, and Clark [8] to be a small decrease in the rate of heat transfer. Experimental data from both investigations, however, demonstrated that increasing the vibrational Reynolds number beyond the laminar flow region resulted in very rapid increases in the rate of heat transfer to values well above those corresponding to no vibrations. Since the Reynolds number is directly proportional to the intensity of the vibrations, it is understandable why the intensity was recognized as an important parameter in the effects of vibrations on heat transfer. It becomes obvious upon examination of the data that the critical intensity necessary to increase the rate of heat transfer is the intensity necessary for the transition from laminar to turbulent boundary flow over the heating element. Since the change in the rate of heat transfer in the laminar flow region is only a few percent and the change in the turbulent region, or above the critical intensity, may be several hundred percent for the same increment of intensity change, it is not surprising that most investigators report no effect below the critical intensity.

Fand and Kaye [4] reported a critical intensity of 0.36 ft/sec when transferring heat from a 0.75-in. horizontal cylinder in a sound field. Fand and Kaye [5] later reported a critical intensity of 0.3 ft/sec for a 0.875-in. horizontal cylinder vibrating vertically. The two critical intensities vary by 20 percent, but assuming the same kinematic viscosities, the Reynolds numbers vary by about three percent. The similarity in the vibrational Reynolds numbers reinforces the concept that the critical intensity should be replaced by a critical or transitional Reynolds number.

Turbulence may also be generated in the boundary layer of the heating element by bubble formation. Fand [9] reported that the critical intensity for increased heat transfer to a liquid from a cylinder subjected to acoustic vibrations was directly related to the ability to cause cavitation. Wong and Chon [10] arrived at the same conclusion using analogous equipment. They reported that as the temperature of the liquid approached incipient boiling, the critical intensity decreased. Above this temperature the critical intensity increased very rapidly. This indicated that the growth and departure of the bubbles in boiling was causing turbulence and the contributions of the vibrations in increasing the turbulence rapidly diminished in importance with increased bubble action. McQuiston and Parker [11] presented a graph of the temperature difference between the heated surface and the bulk liquid temperature versus the vibrational acceleration at various heat fluxes. At 14,000 Btu/hr ft^2, the critical intensity was about 0.3 ft/sec at 50 cps and, for the limited data, the critical intensity appeared to be proportional to the heat flux. Price and Parker [12] reported data over the same range of parameters but with a larger diameter boiling surface, and no effect of vibrations was reported. The implication is that the critical intensity is not a function of heat flux but a function of heat generated, and consequently vapor generated, per unit axial length of heater surface. In all these references either the fluid or surface vibrated, but not both. The effect of vibrations resulted from a relative motion between the heated surface and the fluid.

Experimental Apparatus

A schematic of the experimental apparatus is shown in Fig. 1. The electrically heated test section was mounted in a glass tank by two heavy copper electrodes. This in turn was mounted on an electro-dynamic shaker so that the heated surface and the fluid moved as a unit. This minimized the relative velocity between the two. The shaker had a frequency range from 20 to 520 cps. The maximum amplitude of vibration of the unloaded shaker was 0.5 in. and 0.002 in. at 20 and 520 cps, respectively. The maximum amplitude at intermediate frequencies formed a straight line between these reference points on a log-log plot. The frequency was continuously variable over the range and the amplitude was independently adjustable up to its maximum. The characteristic of the shaker was such that the maximum amplitude decreased with increasing load.

The frequency of vibration was read directly from an integral meter and the amplitude was determined by a calibrated velocimeter. The power dissipated by the heating element was determined by the voltage drop across the central portion of the element and current through a precision shunt. The temperatures were measured by thermocouples and a potentiometer. The bulk fluid temperature was measured by a thermocouple probe and the surface temperatures by internally mounted thermocouples. These are shown in the cross section of the heating element in Fig. 2. The surface temperature thermocouples were resistance welded to the inner surface and tested to insure accurate readings. More importantly, if the weld area is significant, the thermocouple reading will be affected by the voltage gradient in the test section. By pulsing the test section in air with a given

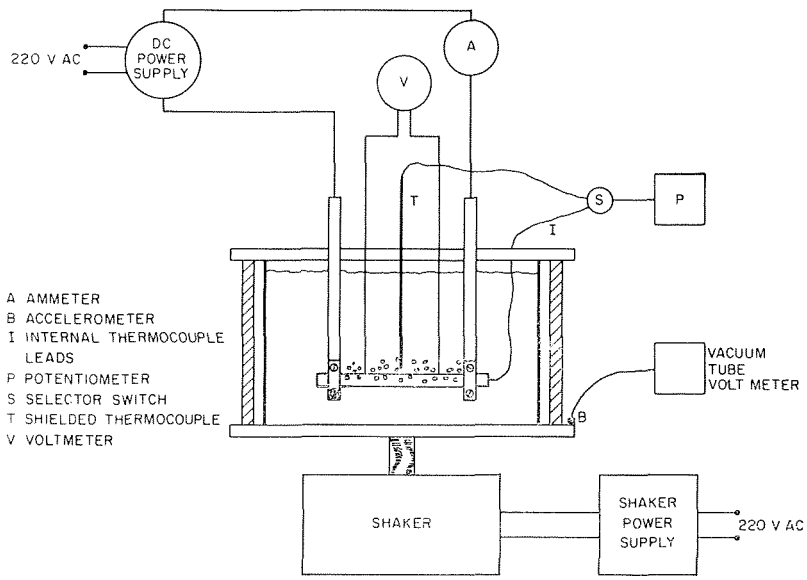

Fig. 1 Experimental apparatus schematic

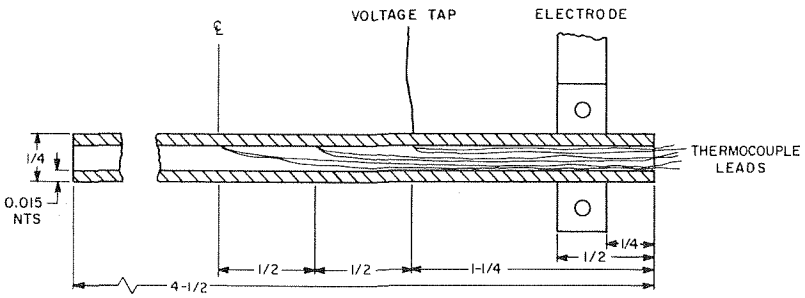

1/4" OD W/0.015" WALL BY 4-1/2" LONG STAINLESS STEEL

2" CENTRAL SECTION FOR DATA HAS VOLTAGE TAPS AND THREE THERMOCOUPLES
END OF TUBES WILL BE SEALED WITH SUITABLE MATERIAL TO PREVENT HEAT TRANSFER BUT WILL HAVE VENT SUFFICIENT FOR PRESSURE RELIEF

Fig. 2 Test section

amperage for a short given period of time, the rate of temperature change in the test section will be approximately proportional to the rate of electrical energy input. Further, if the thermocouple is effected by the voltage gradient, a step change in temperature indication will be observable when the current is interrupted. Continuous strip chart recording of the thermocouple reading showed excellent correlation between the rate of temperature change and electrical energy input and no discernable step change in temperature when the current was interrupted.

To prevent heat transfer from the inner surface and obtain a true surface temperature of the element, plastic tubing was slipped over the ends, sealed with silicone rubber, and vented to the atmosphere. This tubing also served as a conduit for the thermocouple leads. Guard heaters on the outer surface of the tank were provided to control heat losses to ambient and thus permit closer control of the bulk fluid temperature. However, even this did not prevent spurious convective currents in the vicinity of the test elements. The close proximity of the thermocouple probe to the test element permitted close monitoring of the actual temperature to which the heat was transferred. Any data with an indicated bulk temperature outside the specified control band were discarded.

The fluid was deionized water.

Experimental Results

(a) Speed of Sound. Analytical predictions of the stabilization criterion from equation (1) are strongly influenced by the speed of sound. The properties of the experimental apparatus provided a very simple method of determining the speed of sound. As previously stated, the maximum attainable amplitude of vibration was a function of both the load and frequency of vibration. If the load on the vibrator was constant, the amplitude of vibration would monotonically decrease as the frequency increased. However, because of the compressibility of the void-free liquid column, standing waves could be generated so that either a node or antinode could be generated at the bottom of the tank. This resulted in relative peaks and valleys in the amplitude versus frequency and by simple wave analysis based on these results, a speed of sound of 275 ft/sec was determined for this system.

(b) Behavior of Bubbles. The immediate effect on boiling by very low amplitude vibrations is to break up the larger bubbles into smaller ones. As the amplitude of vibration is increased, the rate of rise of the bubbles decreases, which had been analytically predicted by Fuls [1]. The bubbles also show a tendency to migrate to the center of the liquid column. These effects become more pronounced with increasing amplitude until the small bubbles agglomerate at some depth below the surface prior to venting. Further increases in amplitude increase both the depth at which agglomeration occurs and the size of the agglomeration necessary for venting. The agglomerates are essentially spherical in shape and are very agitated. The size and depth of the agglomeration continue to increase with amplitude until the boundary of the agglomeration becomes tangent to the top of the heating element. At this point, the agglomeration loses its apparent attraction for the center of the liquid column. Agglomeration begins anywhere along the top of the heating element, moves rapidly along the top of the heating element gathering mass and volume until it reaches sufficient size to vent to the surface. Theoretically, further increasing the amplitude should force agglomeration to a greater depth. This does not occur, possibly because of changes in the characteristics of the liquid column from the presence of the agglomeration and from cavitation in the vicinity of the heating elements. This differs from the theoretical analysis since the analysis was based on a homogeneous liquid with only a single small bubble present.

It is not known whether the increase in the rate of heat transfer, discussed below, is the result of the highly agitated agglomeration being in the vicinity of the heated surface, the result of the agglomeration moving across the surface, or a recombination of the two.

(c) Heat Transfer. Experimental heat transfer data was obtained both with and without vibrations at a bulk pool temperature of 210 $\pm$ 0.5 deg F. Sufficient amplitude of vibration to bring the point of agglomeration down to tangency with the heating element could only be achieved over a relatively narrow range of frequencies because of limitations of the vibrator. Data were taken at frequencies of 200, 250, and 300 cps. The lowest heat flux investigated was 5000 Btu/hr ft^2 and the highest was at 80,000 Btu/hr ft^2, the limit of the power supply. Sufficient vapor was generated at all conditions so that some vapor always reached the free surface.

A typical set of data is presented in Fig. 3. These data are for a nominal heat flux of 15,000 Btu/hr ft^2 and a vibration frequency of 300 cps. The abscissa indicates the elapsed time and the ordinate, in the form of a film coefficient, is the ratio of the heat flux to the temperature difference between the inside surface of the heating element and the bulk fluid temperature. The two periods of operation with amplitudes of vibration of 0.0012 and 0.0010 in., respectively, are both preceded and followed by periods without vibration for normalization. The effect on the rate of heat transfer of the larger amplitude is very pronounced. However, the effect of the smaller amplitude is comparatively slight. In fact, it is almost within the scatter of the normalizing data. Vibration at an amplitude of less than 0.0010 in. has no effect on the rate of heat transfer.

Over the range of heat fluxes where bubble stabilization had an effect on heat transfer, the effect occurred only over a very narrow range of amplitudes for a given frequency. The amplitude of vibration that corresponds to the greatest effect on heat transfer also corresponds to the minimum amplitude necessary to cause agglomeration to occur tangent to the top surface of the heating element. Deviation from this minimum amplitude, either above or below, eliminated this effect.

A summary of the heat transfer data is presented in Table 1

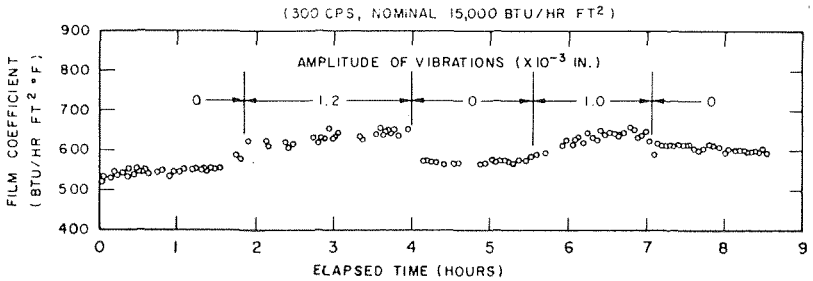

Fig. 3 Film coefficient of heat transfer versus time

Table 1 Summary of heat transfer data

Heat Flux (Btu/hr.ft.^{2}) Nominal	Heat Flux (Btu/hr.ft.^{2}) Average	Frequency (cps.)	Amplitude ($X10^{-3}$in.)	Film Coefficient (Btu/hr.ft.^{2} °F)
5,000	5,200	-	-	220
10,000	10,900	200	0	350
			1.3-1.5	350
			0	360
			0.9-1.2	360
		250	0	360
			1.3-1.5	360
		300	0	350
			1.0-1.2	350
15,000	15,400	200	0	530
			0.9	560
		250	0	475
			1.5	520
		300	0	570
			1.2	640
20,000	20,600	200	0	575
			1.2	595
		250	0	610
			1.5	650
		300	0	575
			1.2	615
40,000	40,300	200	0	1180
			1.2	1220
		250	0	1160
			1.5	1210
		300	0	1250
			1.2	1350
60,000	60,600	200	0	1580
			0.9-1.5	1580
		250	0	1580
			1.3-1.5	1580
		300	0	1600
			1.0-1.2	1600
80,000	81,200	-	-	2010

It should be noted that the data in the table and the remaining figures have been corrected for the temperature drop through the wall of the heating element. It is significant that, where an effect occurred, the amplitude of vibration causing the effect was not a function of heat flux but only a function of frequency of vibration. The tabular data are presented graphically in Figs. 4, 5, and 6. The simultaneous changes of both vibration and nonvibration data are not unusual but are typical of heat transfer data. It was for this reason normalizing nonvibration data were obtained before and after each operation, with a given frequency and amplitude of vibration. This effect is demonstrated by the nonvibration data of Fig. 3 where it begins at about 525 Btu/hr ft² deg F at time zero and increased to above 600 after seven hours. This variation is aggravated by the necessity of periodically changing the water and polishing the test element surface.

Consistent with current literature, these figures present the heat flux as a function of the temperature difference between the heater surface and bulk fluid temperature. The heat transfer data without vibrations was correlated with the Rohsenow [13] equation,

$$\frac{c_L(T_w - T_{sat})}{H_{fg}} = C\left[\frac{q/A}{\mu_L H_{fg}}\sqrt{\frac{\sigma}{g(\rho_L - \rho_v)}}\right]^n \left(\frac{c_L\mu_L}{k_L}\right)^{1.7} \quad (2)$$

For the no vibration data of the table, corrected for the temperature drop through the wall, the coefficient, C, has a value of 0.0146 and the exponent, n, has a value of 0.15. The vibration data was normalized to this correlation by taking the same percent decrease in temperature difference caused by vibrations at the given heat flux. The normalized data is shown in Fig. 7.

Additional heat transfer data were taken at a heat flux of 5000 Btu/hr ft² with and without vibrations. These data were to demonstrate the difference between the effect on heat transfer from bubble stabilization and the effect on heat transfer from the critical intensity reported by other investigators and discussed in the introduction. These data are shown in Fig. 8 with the data of 10,000 and 15,000 Btu/hr ft². Consistent with the results of previous investigators, once an effect is evident at the lowest heat flux, the rate of heat transfer continues to increase with increase in amplitude and, therefore, intensity and vibrational acceleration. Also consistent with the results of Wong and Chon [10] and McQuiston and Parker [11], the critical intensity increases rapidly with heat flux and at 10,000 Btu/hr ft² there is no effect on the rate of heat transfer from vibrations over the range of intensities attainable. Further increasing the heat flux to 15,000 Btu/hr ft² results in an effect on the rate of heat transfer from bubble stabilization. Unlike the turbulence triggering mechanism of the critical intensity, further increasing the amplitude and intensity does not result in a continuing increase in the rate of heat transfer. On the contrary, further increasing the amplitude of vibration causes a decrease in the rate of heat transfer back to its original value.

(d) Stabilization Amplitude. The amplitude of vibration at which the effect on the rate of heat transfer was obtained and, therefore, the minimum amplitude to stabilize individual bubbles at the surface of the heating element is correlated with the theoretical predictions of equation (1) in Fig. 9. The correlation at 300 cps is very good, but the correlation deteriorates as the frequency is decreased to 200 cps. Equation (1) was based on the assumptions that the liquid was homogeneous and that the pressure waves induced by the oscillations propagating as plane waves. The nature of the experimental conditions precluded approximating these assumptions.

The effect of the vapor on the predicted stabilization amplitude would be particularly pronounced near a frequency of 190 cps

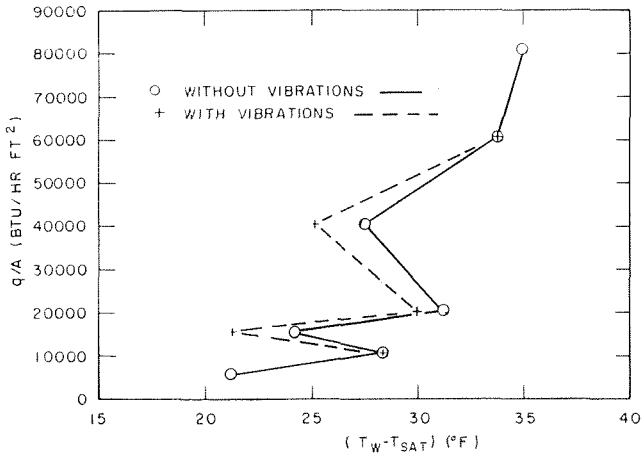

Fig. 4 200 cps test data

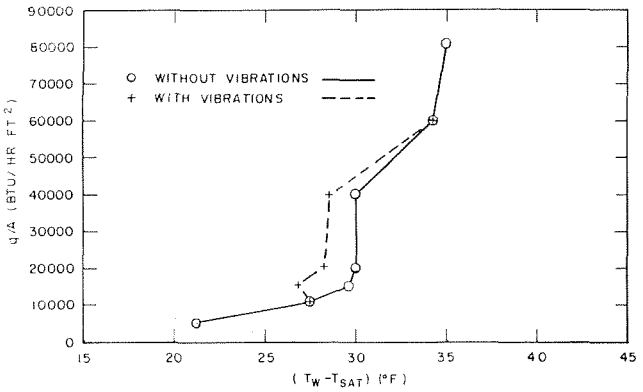

Fig. 5 250 cps test data

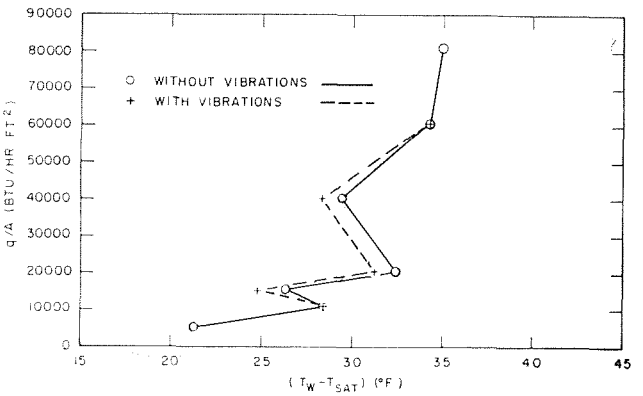

Fig. 6 300 cps test data

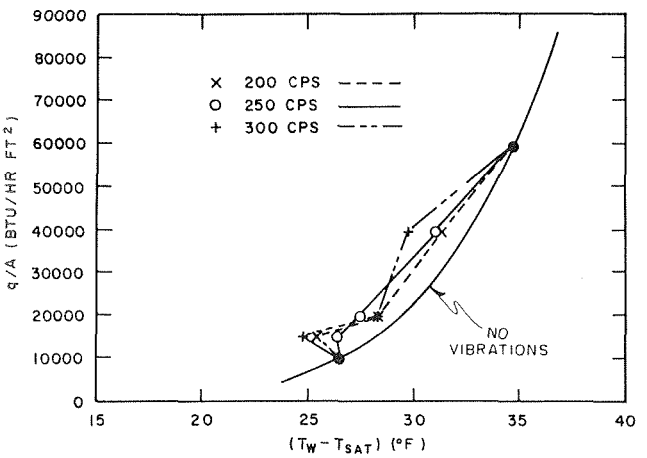

Fig. 7 Normalized test data correlated with best fit

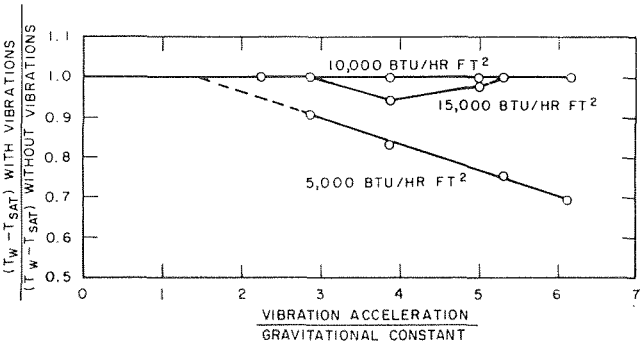

Fig. 8 Effect of heat flux on heat transfer phenomenon at 200 cps

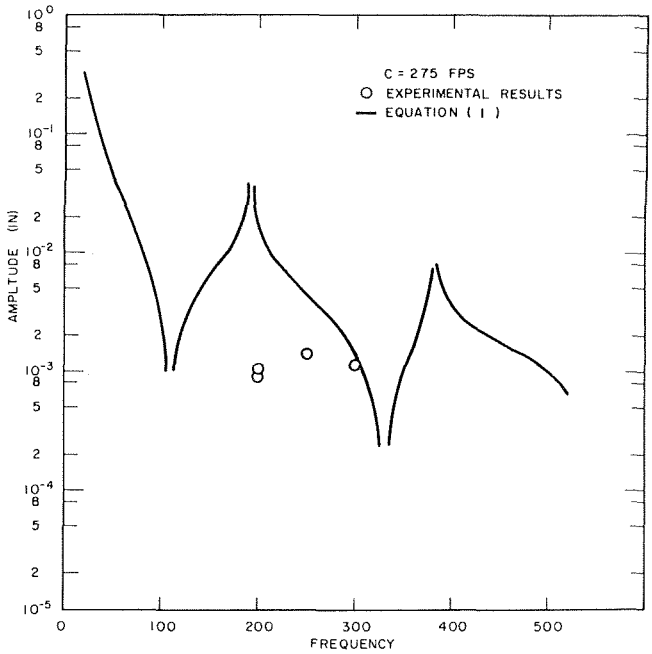

Fig. 9 Stabilization criteria comparison of theoretical predictions and experimental results

since this frequency corresponds to a resonant pressure amplitude at the depth of the test section. The predicted large pressure changes would be dissipated by the compressibility of the gas and the same compressibility would distort the plane wave propagation of the disturbances.

Conclusions

The effect of bubble stabilization decreases by up to 12 percent, the temperature difference necessary for a given heat flux within the range of frequencies of 200 to 300 cps. The data taken at the low heat flux have shown that the effect on the rate of heat transfer is not the same effect associated with a critical intensity as reported by previous investigators.

Good correlation between the experimental stabilization amplitude and theory has been shown, provided pressure resonance is avoided. Near the resonant frequency the theoretical predictions understandably break down because the compressibility of the agglomeration was not accounted for in the analysis.

References

1 Fuls, G. M., "Bubble Dynamics in a Vertically Vibrating Field and Their Effect on Pool Boiling Heat Transfer," PhD dissertation, University of Pittsburgh, 1968.

2 Bergles, A. E., and Morton, H. L., "Survey and Evaluation Techniques to Augment Convective Heat Transfer," *M.I.T., Department of Mechanical Engineering*, Report No. 5382-32, Feb. 1965.

3 Richardson, P. D., "Effects of Sound and Vibration on Heat Transfer," *Applied Mechanics Review*, Vol. 20, No. 3, 1967, pp. 201–217.

4 Fand, R. M., and Kaye, J., "The Influence of Sound on Free Convection From a Horizontal Cylinder," JOURNAL OF HEAT TRANSFER, TRANS. ASME, Series C, Vol. 83, No. 2, May 1961, pp. 133–148.

5 Fand, R. M., and Kaye, J., "The Influence of Vertical Vibrations on Heat Transfer by Free Convection From a Horizontal Cylinder," *International Development of Heat Transfer*, ASME, 1961, p. 490.

6 Blankenship, V. D., and Clark, J. A., "Effects of Oscillation on Free Convection From a Vertical Finite Plate," JOURNAL OF HEAT TRANSFER, TRANS. ASME, Series C, Vol. 86, No. 2, May 1964, pp. 149–158.

7 Blankenship, V. D., and Clark, J. A., "Experimental Effects of Transverse Oscillations on Free Convection From a Vertical Finite Plate," JOURNAL OF HEAT TRANSFER, TRANS. ASME, Series C, Vol. 86, No. 2, May 1964, pp. 159–165.

8 Eshghy, S., Arpaci, V. S., and Clark, J. A., "The Effect of Longitudinal Oscillations on Free Convection From Vertical Surfaces," *Journal of Applied Mechanics*, Vol. 32, TRANS. ASME, Vol. 87, Series E, No. 1, March 1965, pp. 183–191.

9 Fand, R. M., "The Influence of Acoustic Vibrations on Heat Transfer by Natural Convection From a Horizontal Cylinder in Water," JOURNAL OF HEAT TRANSFER, TRANS. ASME, Series C, Vol. 87, No. 2, 1965, pp. 309–310.

10 Wong, S. W., and Chon, W. J., "Effects of Ultrasonic Vibrations on Heat Transfer to Liquids by Natural Convection and Boiling," Preprint 47A, Sixtieth Annual Meeting, AIChE, Nov. 1967.

11 McQuiston, F. C., and Parker, J. D., "Effects of Vibration on Pool Boiling," ASME Paper No. 67-HT-49, ASME-AIChE Heat Transfer Conference, ASME, Aug. 1967.

12 Price, D. C., and Parker, J. D., "Nucleate Boiling on a Vibrating Surface," ASME Paper No. 67-HT-58, ASME-AIChE Heat Transfer Conference, ASME, Aug. 1967.

13 Rohsenow, W. M., "A Method of Correlating Heat Transfer Data for Surface Boiling Liquids," TRANS. ASME, Vol. 74, 1952, pp. 969–976.

D. M. McELIGOT
Associate Professor.
Assoc. Mem. ASME

S. B. SMITH
Research Assistant.
Presently, Engineer,
U. S. Air Force Flight Test Center,
Edwards AFB, Calif.

Energy, Mass and Momentum Transfer Laboratory,
Aerospace and Mechanical Engineering Department,
The University of Arizona,
Tucson, Ariz.

C. A. BANKSTON
Staff Member,
Los Alamos Scientific Laboratory,
Los Alamos, N. Mex.
Assoc. Mem. ASME

Quasi-Developed Turbulent Pipe Flow With Heat Transfer

Available literature on wall friction and heat transfer for gas flow strongly heated in the downstream region of tubes shows disagreement between analysis and experiments. Possible explanations are examined quantitatively, then the governing equations are treated in more complete form than in previous analyses. Results compare favorably with existing experiments for nonreacting, high-Reynolds-number, turbulent flow of a gas with negligible natural convection and with a constant wall heat flux imposed.

Introduction

THE results of the few available analyses on the strong heating of gases, flowing turbulently through circular tubes, do not agree with experimental measurements in the downstream region. This paper examines the discrepancies. For the first time, the downstream behavior is predicted by a numerical analysis which solves the complete, coupled, partial-differential, boundary-layer equations describing the problem. In the process, additional information is developed (*a*) pointing out the importance of basic phenomena left out of previous analyses, and (*b*) discriminating between various generalized models of turbulent flow. Finally, analytical prediction is usefully improved so that trends observed in experiments are represented more closely than by previous analyses.

The level of the investigation is that suggested as feasible by Spalding [1],[1] and the numerical method was partially incited by his work [2]. Since the theory of turbulence is not yet well in hand even for adiabatic, fully developed, pipe flow, at this time we do not expect to obtain a basic understanding of the structure of the turbulence occurring in a situation which is many-

Contributed by the Heat Transfer Division and presented at the Fluids Engineering, Heat Transfer, and Lubrication Conference, Detroit, Mich., May 24–27, 1970, of THE AMERICAN SOCIETY OF MECHANICAL ENGINEERS. Manuscript received by the Heat Transfer Division, July 31, 1968; revised manuscript received July 22, 1969. Paper No. 70-HT-8.

[1] Numbers in brackets designate References at end of paper.

Nomenclature

$\triangleq$ = defined as
( ) = function of
A_{cs} = cross-sectional area, $\pi D^2/4$
c_p = specific heat at constant pressure
D = diameter
$\dot{E}$ = total enthalpy flow rate at position x
G = mass flow velocity, $\dot{m}/A_{cs}$
g_c = dimensional constant; e.g., 32.17 (ft)(lbm)/(lbf)(sec^2)
H = enthalpy; $H_b \triangleq \dot{E}/\dot{m}$
h = convective heat-transfer coefficient, $q_w''/(T_w - T_b)$
k = thermal conductivity
l = mixing length
$\dot{m}$ = mass flow rate
m, n = exponents in equation (1)
p = pressure
q_w'' = wall heat flux, positive from wall to gas
r = radial coordinate
T = absolute temperature; $T_b \triangleq T(H_b, p)$
u = gas velocity in axial direction
V = gas bulk velocity, G/ρ_b
v = gas velocity in radial direction
x = axial coordinate
y = transverse coordinate, $r_w - r$
δ^* = displacement thickness, $r_w[1 - \sqrt{\dot{m}/(\pi r_w^2 \rho_c u_c)}]$
ϵ = eddy diffusivity; ϵ_m, for momentum, e_h, for heat
κ = constant in turbulence models
μ = viscosity
ν = kinematic viscosity, μ/ρ
ρ = density; $\rho_b \triangleq \rho(H_b, p)$
τ = shear stress
f = friction factor, $\tau_w/(G^2/2g_c\rho_b)$; f_{app}, apparent friction factor, $-\frac{D}{4}\frac{d}{dx}\left(p + \frac{G^2}{g_c\rho_b}\right)\Big/(G^2/2g_c\rho_b)$
l^+ = mixing length, $l\sqrt{\tau_w g_c/\rho}/\nu$
Nu = Nusselt number, hD/k
$\bar{p}$ = pressure deficit, $g_c(p_i - p)/\rho_i V_i^2$
Pr = Prandtl number, $\mu c_p/k$

fold more complicated. Instead the scientific approach is constrained to the "method of multiple working hypotheses" to obtain useful predictions [3]. Some level of empiricism is necessary to obtain solutions; the present numerical method has the advantage of focusing the empiricism directly on the unknown phenomena, the representation of the turbulent transport behavior. However, before developing completely new models as hypotheses, it seems best to test existing turbulent-flow models to see which, if any, are adequate for a variety of flows. The present work thus evaluates their extension to the class of flows next described.

Idealized Problem. In this paper attention is focused on the downstream, or "quasi-developed," region beyond the region of thermal entry effects. For turbulent flow with constant fluid properties, simplifications in the governing equations can lead to essentially invariant nondimensional temperature profiles in this region [4]. However, with strong heating, the fluid properties vary and the same simplifications cannot be made, although experiments show that the thermal-entry effects still appear unimportant beyond a length of 20 to 40 tube diameters [5, 6], providing the thermal boundary condition is independent of distance.

Turbulent, nonreacting, low-velocity flow of a semiperfect gas is considered in this analysis, with the assumption of a constant wall heat flux whose magnitude causes significant variation of the temperature-dependent fluid properties. The flow region with a high Reynolds number is studied so that an approximation that the viscous sublayer is thin will be valid.

Discrepancies Between Analyses and Experiments. To date, only a few analyses have been conducted on the internal turbulent flow of a gas with varying properties. Botje [7], Jackson [8], and Sze [9] used slight variations of Deissler's solution [10] for hypothetical, fully established temperature and velocity profiles, i.e., quasi-developed. Assuming a velocity profile, Magee obtained a numerical solution for the energy equation from the thermal entrance [11]. All these analyses were based on Deissler's eddy diffusivity model. The results of these analyses may be expressed in the form common to experimental presentations.[2]

$$\frac{\mathrm{Nu}}{\mathrm{Nu}_{cp}} = \left(\frac{T_w}{T_b}\right)^n \text{ and } \frac{f}{f_{cp}} = \left(\frac{T_w}{T_b}\right)^m \tag{1}$$

For these Deissler-like analyses the exponents of *both* the friction-factor prediction and the Nusselt-number prediction are approximately the same, $m = n \simeq -0.3$. Magee found $n \simeq -0.4$, but since he arbitrarily selected a correlation of the Deissler velocity profile to describe his flow field, no friction-factor predictions are provided in his thesis.

[2] The subscript, *cp*, indicates the normalizing parameter is evaluated from the constant-properties correlation at the same Reynolds and Prandtl numbers. In this paper these parameters are evaluated at the gas bulk temperature.

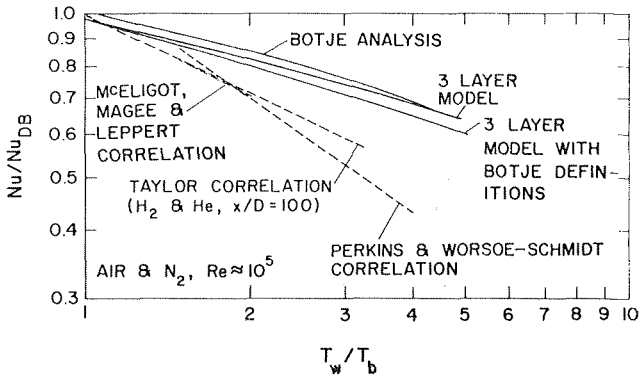

Fig. 1(a) Heat transfer

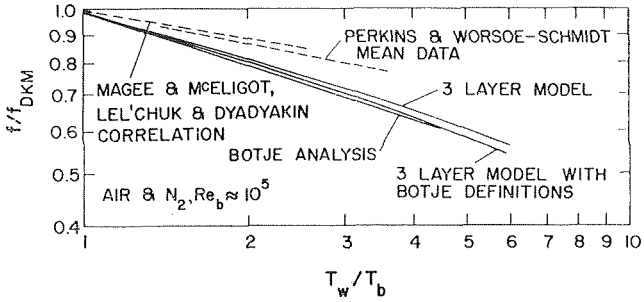

Fig. 1 Comparison between "fully developed" analyses of Deissler-Botje [7] and of Smith-Martinelli [15], and experimental correlations of Perkins and Worsoe-Schmidt [6], of Taylor [12], of Lel'chuk and Dyadyakin [35], and of McEligot, Magee, and Leppert [5]

Fig. 1(b) Wall friction. f calculated from $(\partial u/\partial y)_w$.

In examining the results of experiments we have confined our attention to those investigations in which results have been obtained at local positions in the downstream region and for which the initial condition for the thermal entry was a fully developed, turbulent flow with a large Reynolds number. Such investigations have been reported by McEligot, Magee, and Leppert [5], by Perkins and Worsoe-Schmidt [6], and by Taylor [12]. The results of these three experimental investigations are summarized in Fig. 1, which also indicates the predictions of Botje's analysis [7], which is typical of the type described above. Typically, most of the data show the heat-transfer exponent to range from -0.5 to -0.7 while the friction exponent is only about -0.1 to -0.3 with the bulk of the data grouping around -0.2.

Thus the comparison shows that the observed reduction in Nu is more severe than predicted by the analyses. And it appears that f is reduced less. Resolving these two discrepancies is the major goal of this work.

Nomenclature

q^+ = wall heat flux parameter; q_i^+, inlet, $q_w''/(Gc_{p,i}T_i)$; q_x^+, local, $q_w''/(Gc_{p,x}T_{b,x})$

Q^+ = local heat flux parameter, $q_w''r_w/(k_bT_b)$

$\bar{r}$ = radial distance, r/r_w

Re = Reynolds number, $4\dot{m}/(\pi D\mu)$

u^+ = axial velocity parameter, $u/\sqrt{\tau_w g_c/\rho}$

$\bar{x}$ = axial distance, x/D

y^+ = transverse-distance parameter, $y\sqrt{\tau_w g_c/\rho}/\nu$

y_l^+ = constant in turbulence models; laminar sublayer thickness in three-layer model

Subscripts

b = evaluated at bulk temperature

bu = evaluated at edge of buffer layer

c = evaluated at center line

cp = evaluated from constant-properties prediction, e.g., $\mathrm{Nu}_{cp,\mathrm{DB}} = 0.021\ \mathrm{Re}^{0.8}\mathrm{Pr}^{0.4}$ (or $\mathrm{Nu}_{\mathrm{DB}}$)

DB = modified Dittus-Boelter, references [5, 18]

DKM = Drew, Koo, and McAdams, reference [34]

eff = effective

i = inlet

l = evaluated at edge of laminar sublayer

vD = van Driest

w = evaluated at wall

x = evaluated at x

y = evaluated at transverse position y

The absence of a subscript on gas properties indicates properties evaluated at gas bulk temperature.

Unless otherwise defined, an overscore indicates the variable has been normalized through division by its inlet value, e.g., $\bar{\rho} = \rho/\rho_i$.

Possible Explanations. One might suggest various explanations for the discrepancies noted above. Some of these possibilities are examined briefly in the paragraphs below, whereas others will be scrutinized at greater length in the context of the results of the numerical analysis.

(a) Experimental Uncertainty or Error. Since most of the experiments have been conducted to obtain design correlations, a wide range of subsonic gas flow has been covered in the literature. However, little effort has been exerted to conduct measurements for systematic comparison with the analyses. In general, the best heat-transfer data for strong heating have uncertainties of at least ±10 percent, and local friction data are even less accurate. When the predictions are plotted as in Fig. 1, it becomes evident that the temperature ratio, T_w/T_b, must be greater than two before the differences between analyses and heat-transfer data are greater than 10 percent. Perkins and Worsoe-Schmidt, and Taylor [6, 12] have made local heat-transfer measurements downstream of the thermal-entry region at higher temperature ratios. These independent studies both show that the Nusselt number is significantly smaller than indicated by an exponent of -0.3 (equation (1)), i.e., the magnitude of the exponent is greater for the data. Taylor could not measure local friction parameters with his apparatus, but Perkins and Worsoe-Schmidt did; they show a scatter for m from -0.1 to -0.3, with most downstream measurements about -0.2 or less. (The difficulty in obtaining experimental friction factors is discussed further in Appendix A.) The heat-transfer data of these two independent studies suffice to show that the analyses are not adequate.

(b) Difference in Definitions. The perceptive reader will note that Botje [7], Deissler and Eian [13], and the experimentalists [5, 6] differ in their definitions of bulk temperature and velocity and hence, of Re_b, f, and Nu_b. The resulting differences are quantified in Fig. 1 and they are shown to be insignificant. (The three-layer model, under which the definitions are compared, is a variable-properties extension of Martinelli's approach [14, 15].)

Another difficulty remains for f. The analyst, calculating velocity profiles, is able to obtain the wall shear stress from the velocity gradient. On the other hand, the laboratory scientist lacks this information so he calculates the one-dimensional, "apparent wall shear stress" of Shapiro and Smith [16],

$$\tau_{w,\text{app}} \triangleq -\frac{D}{4}\frac{d}{dx}\left\{p + \frac{G^2}{g_c\rho_b}\right\} \tag{2}$$

The difference may be phrased in terms of the momentum flux gradient as

$$\frac{f_{\text{app}}}{f} = \frac{\tau_{w,\text{app}}}{\tau_w} = \frac{-\frac{r_w}{2}\frac{dp}{dx} - \frac{r_w}{2}\frac{G^2}{g_c}\frac{d}{dx}\left\{\frac{1}{\rho_b}\right\}}{-\frac{r_w}{2}\frac{dp}{dx} - \frac{1}{r_w g_c}\frac{d}{dx}\left\{\int_0^{r_w}\rho u^2 r dr\right\}} \tag{3}$$

With severe heating, distortions in $u(r, x)$ and $\rho(r, x)$ thus lead to differences between f and f_{app} for the same flow. However, the quasi-developed analyses do not provide, or even consider, axial gradients. Accordingly, evaluation of this possible explanation for the friction-factor discrepancy is deferred until the results of the present numerical program are discussed.

(c) Eddy-Diffusivity Ratio. The eddy-diffusivity ratio has not been measured for conditions of strong heating. In the quasi-developed analyses it has been taken as unity. Kendall and coworkers have suggested values of 0.75 and 1.0 for ϵ_m/ϵ_h [17]. When the former value is used with constant fluid properties, the predicted Nusselt number is too high, about 10–20 percent higher than the modified Dittus-Boelter correlation [5, 17].[3] A value of unity leads to reasonable heat-transfer and friction predictions over a wide range of Reynolds number [8, 19, 20, 21]. However, the possibility remains that the eddy-diffusivity ratio effectively varies with increased heating (i.e., with T_w/T_b). Careful profile measurements may provide the answer in the future, but the task of determining $\epsilon_m(r)/\epsilon_h(r)$ within ±5 percent is extremely difficult even for near-ambient temperature conditions. Additional effects, such as axial and transverse conduction along the probe structure and thermal radiation from the wall to the probe, make meaningful measurements at high heating rates even more complex. For calculations in this work, the hypothesis of equal eddy diffusivities will be retained.

(d) Different Turbulence Models. Most analytical predictions of heat-transfer parameters and wall shear stress for forced-convective turbulent flow are based on generalization of data obtained for adiabatic, incompressible flow. Analysts have thus tried to extend the results of a specific case to the general situation, which is analogous to an attempt of deriving a basic principle from a single observation. For example, Spalding and Chi have listed over 20 generalizations proposed by various authors for external, turbulent flow with compressibility effects [22]. Kendall, et al., examined another extensive group of generalized turbulent-flow models for applications with surface mass addition [17]. Essentially, only the Deissler eddy-diffusivity model has been applied for the class of flows treated here.

In a preliminary, quasi-developed analysis, Smith [15] extended Martinelli's three-layer model [14] to include consideration of transverse property variation. In contrast to the previous quasi-developed analyses, he also allowed the effective viscous sublayer thickness, y_l^+, to vary with the heating rate. His results are a slight improvement (Fig. 1) but do not resolve the two discrepancies being attacked.

Study of additional turbulence models is accomplished with the present numerical analysis.

(e) Incomplete Governing Equations. In the quasi-developed analyses, the transverse velocity is neglected and the integrated mass flow is used to calculate the Reynolds number. Thus the continuity equation is not involved when the profiles are obtained. Also, Jackson shows that, with constant properties, the assumption of a linear $q''(r)$ corresponds to slug flow in the axial convective term of the energy equation [8]. These analyses treat the axial momentum equation in about the same manner as the energy equation, i.e., $\tau(r)$ is taken to be the same form as derived from constant-property, parallel flow. Consequently, the axial momentum change term is effectively ignored.

For a flow to be "fully developed" the nondimensional velocity profile must be invariant. Such a situation may occur for internal adiabatic flow of an incompressible fluid, and then the momentum change term is identically zero. But heated gas expands; and because it expands at an axial rate that varies as the axial heating rate varies, the resulting axial-velocity gradient becomes successively more important with increased heating. Since the governing equations are coupled, the effects are not confined to the velocity profile, but also modify the solutions for the other dependent variables.

A more subtle, but more important, point is that the same axial-momentum term provides the connection to the upstream history of the flow. Without it, a fictitious condition of instantaneous development is implied for each axial position. Since the local Reynolds number decreases due to the heating along the channel, the velocity profile would be expected to change even if there were no other effects: Adiabatic profiles show successively thicker viscous sublayers as the Reynolds number is reduced. In the important wall region, the velocities would change axially, and the convective momentum term should therefore be included if possible. With the flow in this continually developing condition, each axial position might be pictured as the entry of a tube with an initial velocity profile that is characteristic of incompletely established flow at higher Re. One might expect heat-transfer and friction parameters to be increased rather

[3] The modification consists in using 0.021 as the coefficient when applied to gases.

than decreased (relative to results derived under fully developed, constant-property assumptions).

Conspectus. To see whether possible explanations (*d*) and (*e*) lead to lower Nusselt numbers and higher friction factors than previous analyses, the governing boundary-layer equations—all coupled by temperature-dependent fluid properties—are solved numerically from the thermal entrance. A variety of turbulence models are tested against a single strong heating run representing demanding conditions. Models found inadequate are eliminated from further consideration. Predictions from one of the surviving models are then presented for a wide range of heating rates and entering Reynolds numbers; these predictions are compared to other data also representing a wide range of conditions. Finally, possible implications to "basic understanding" of the general theory of turbulence are suggested.

Solutions of Boundary-Layer Equations

Governing Equations. The usual equations for axisymmetric boundary-layer flow at low speeds can be written in nondimensional form as follows:

For continuity,

$$\frac{\partial(\bar{\rho}\bar{u})}{\partial\bar{x}} + \frac{2}{\bar{r}}\frac{\partial(\bar{\rho}\bar{v}\bar{r})}{\partial\bar{r}} = 0 \tag{4a}$$

For x momentum,

$$\bar{\rho}\bar{u}\frac{\partial\bar{u}}{\partial\bar{x}} + 2\bar{\rho}\bar{v}\frac{\partial\bar{u}}{\partial\bar{r}} = \frac{d\bar{p}}{d\bar{x}} + \frac{4}{\mathrm{Re}_i}\frac{1}{\bar{r}}\frac{\partial}{\partial\bar{r}}\left(\bar{r}\bar{\mu}_{\mathrm{eff}}\frac{\partial\bar{u}}{\partial\bar{r}}\right) \tag{4b}$$

For energy,

$$\rho\bar{u}\frac{\partial\bar{H}}{\partial\bar{x}} + 2\bar{\rho}\bar{v}\frac{\partial\bar{H}}{\partial\bar{r}} = \frac{4}{\mathrm{Re}_i\mathrm{Pr}_i}\frac{1}{\bar{r}}\frac{\partial}{\partial\bar{r}}\left(\bar{r}\frac{\bar{k}_{\mathrm{eff}}}{\bar{c}_p}\frac{\partial\bar{H}}{\partial\bar{r}}\right) \tag{4c}$$

The additional relation necessary to make the set of equations determinate in the absence of a y-momentum equation is the integral continuity equation,

$$\int_0^1 \bar{\rho}\bar{u}\bar{r}d\bar{r} = \frac{1}{2} \tag{4d}$$

The boundary conditions are the no-slip and impermeable-wall conditions,

$$\bar{u}(1, \bar{x}) = 0 \text{ and } \bar{v}(1, \bar{x}) = 0 \tag{4e}$$

and the specified wall heat flux condition,

$$\left(\frac{\partial\bar{H}}{\partial\bar{r}}\right)_w = \frac{q^+\,\mathrm{Re}_i\mathrm{Pr}_i\bar{c}_{p,w}}{2\bar{k}_w} \tag{4f}$$

The auxiliary equations are

$$\bar{\mu}_{\mathrm{eff}} = \bar{\mu}\left(1 + \frac{\epsilon_m}{\nu}\right) \tag{4g}$$

$$\frac{\bar{k}_{\mathrm{eff}}}{\bar{c}_p} = \frac{\bar{k}}{\bar{c}_p}\left(1 + \mathrm{Pr}_i\frac{\bar{\mu}\bar{c}_p}{\bar{k}}\frac{\epsilon_h}{\nu}\right)$$

Method of Solution. Finite-difference equations approximating equation (4) were carefully derived from basic principles to

Table 1 Characteristics of turbulence models used

"Title"/Reference	Basic Representation	κ	y_ℓ^+	Range	Prediction for Constant Properties, $\mathrm{Re}=10^5$ $\mathrm{Nu}/\mathrm{Nu}_{DB}$	f/f_{DKM}	Identification
Reichardt "local" [31,32]	$\frac{\epsilon}{\nu_y} = \frac{\kappa}{6}\left[y_y^+ - y_\ell^+\tanh\frac{y_y^+}{y_\ell^+}\right]\left[2 - \frac{y}{r_w}\right]\left[1+2\left(1-\frac{y}{r_w}\right)^2\right]$	0.4225	11.0	Wall → ℄	0.945	0.989	R-ℓ
Reichardt modified "wall"	Same except replaced y_y^+ by y_w^+ in argument of tanh	Same	Same	Same	Same	Same	Not Shown
Reichardt "wall"	$\frac{\epsilon}{\nu_w} = \frac{\kappa}{6}\left[y_w^+ - y_\ell\tanh\frac{y_w^+}{y_\ell^+}\right]\left[2 - \frac{y}{r_w}\right]\left[1+2\left(1-\frac{y}{r_w}\right)^2\right]$	Same	Same	Same	Same	Same	R-w
Three layer-modified Martinelli [14,15]	See Reference [15]	0.4	--	--	0.964	0.993	3L
Sparrow, Hallman and Siegel "local" [25]	$\epsilon = n^2 uy\left(1 - e^{-\frac{n^2uy}{\mu/\rho}}\right)$; $n = 0.124$ $\frac{\epsilon}{\nu_y} = \kappa y_y^+\left(1 - \frac{y}{r_w}\right) - 1$	0.36	26.0	$y_y^+ < y_\ell^+$ $y_y^+ > y_\ell^+$	0.943	0.984	SHS-ℓ
Sparrow, Hallman and Siegel "wall"	Viscous sublayer same (except range); Core: $\frac{\epsilon}{\nu_w} = \kappa y_w^+(1 - \frac{y}{r_w}) - 1$	0.36	26.0	$y_w^+ < y_\ell^+$ $y_w^+ > y_\ell^+$	Same	Same	SHS-w
van Driest "local" [33]	$\ell = \kappa y\left[1 - \exp(-y_y^+/y_\ell^+)\right]$	0.4	26.0	Wall → ℄	1.03	1.06	vD-ℓ
van Driest "wall"	Same except replaced y_y^+ by y_w^+ in argument of exp	Same	Same	Same	Same	Same	vD-w
Kendall et al. "local" [17]	$\frac{d\ell_y^+}{dy_y^+} = \frac{\kappa y_y^+ - \ell_y^+}{y_\ell^+}\sqrt{\frac{\tau_y}{\tau_w}}$	0.42	11.83	Wall → ℄	1.03	1.06	K w/o C-ℓ
Kendall et al. "wall"	$\frac{d\ell_y^+}{dy_y^+} = \frac{\kappa y_y^+ - \ell_y^+}{y_\ell^+}\frac{\sqrt{\tau_y/\rho_y}}{\sqrt{\tau_w/\rho_w}}$	Same	Same	Same	Same	Same	K w/o C-w
Kendall w/Clauser "wall" [17]	Wall region same form as Kendall et al. "wall"; Core (or wake): $\epsilon + \nu = 0.018\,u_c\delta^*$	0.44	11.83	$\epsilon + \nu \le 0.018\,u_c\delta^*$	0.939	1.00	K w/C-w

insure that momentum, energy, and mass were, in fact, conserved between adjacent elemental control volumes associated with the nodes.

The numerical representations of the rate equations are chosen so that the energy equation and the momentum equation are linear and implicit when phrased for algebraic solution. Only the transverse diffusion terms and the axial convective terms are used in setting up the coefficients of the unknown quantities; all other terms are included in the "source" term (except pressure). Thus, stability is insured in the recursive solution of the resulting tridiagonal matrices [23]. The governing equations are solved successively and are then iterated to handle the nonlinearities caused by the temperature-dependent property variation (as well as by the axial convective term in the momentum equation).

Fluid properties are entered as power-law functions, dependent on enthalpy or temperature. In accordance with an assumed low Mach number, the pressure-dependence of the density is neglected. For this paper, only air properties were approximated: $(\mu/\mu_i) \simeq (T/T_i)^{0.67}$; $(k/k_i) \simeq (T/T_i)^{0.805}$; $(c_p/c_{p,i}) \simeq (T/T_i)^{0.095}$; and $(\rho/\rho_i) \simeq (T_i/T)$. The trial turbulence models are entered as subprograms; "effective" viscosity and thermal conductivity are formed as sums of molecular and turbulent contributions for use in the general program.

Mesh spacing was varied in both the radial and axial directions. To conserve computer time, mesh parameters were chosen to give heat-transfer and wall-friction results within about ± 1 percent of converged values. This level of accuracy is deemed adequate for the comparative purposes of the present paper and for development of the design predictions. Computers used were the IBM 7072, the CDC 6400, and the CDC 6600, with production runs completed on the latter. Details of the numerical procedure may be found in reference [24].

Definitions of output parameters are those used by the laboratory scientist and, therefore, are convenient for the designer. The Nomenclature presents the pertinent definitions explicitly.

Turbulent-Transport Models. Eleven models were investigated. Some are popular and familiar while others are less well known. No effort was made to run all models that have been suggested. Instead, versions were selected that were typical of particular classes of generalized turbulent-transport models.

The models chosen are listed in Table 1. Extensive subscripting is used to denote explicitly the reference temperature at which the properties are evaluated. For example, the subscript "y" indicates they are evaluated pointwise across the stream, i.e., at the temperature corresponding to the local value of the transverse coordinate. All versions are one-dimensional in their basic representation; this implies axial similarity of the transport model—an assumption which is not believed to be generally valid for developing flows, but often is operationally useful.

Ideally, a generalized turbulent-transport model should base its predictions solely on pointwise conditions and gradients in the stream. In particular, any direct dependence on the transverse coordinate should be eliminated for complete generalization: the function $\epsilon(y)$ would thus be obtained by integration. One such attempt is the von Karman similarity hypothesis which Deissler used for the turbulent core [10]. Unfortunately, the computer program was unstable with the Deissler model; the modified Martinelli treatment (mentioned earlier) and a version presented by Sparrow, Hallman, and Siegel [25] were therefore applied instead. The former agrees with the Deissler-Botje "fully developed" predictions at $\mathrm{Re} \simeq 10^5$, and the latter agrees with the Deissler prediction for constant fluid properties. Another treatment, which is partially independent of y, is the version proposed by Kendall and co-workers [17] for boundary layers with blowing or suction. They obtain the mixing length by integrating the function $dl^+(y^+, l^+)/dy^+$ shown in Table 1.

Constants κ and $y_l{}^+$, used in the various representations cited in the foregoing, are those proposed by the original authors except where the form is modified. The resulting constant-property predictions are compared to empirical correlations in Table 1. No attempt was made to adjust the constants to yield identical predictions for all models since gas experiments presently lack the precision necessary to confirm absolute parameters within ± 5 percent. This lack of a common asymptote as T_w/T_b approaches unity does not hamper the later comparisons.

Selection of a Turbulent-Transport Model. To study the relative behavior of the various models under strong heating, each was tested at the boundary conditions of Run 140 in the experiments of Perkins and Worsoe-Schmidt [6]. While agreement with a single run cannot confirm a model, disagreement is sufficient to eliminate a model if confidence in the data exists. In this section most models are eliminated and in a later section the best remaining is tested over a wider range.

Run 140 was the most extreme run for which detailed data were available to the authors. The wall-to-bulk-temperature ratio peaked at >7. Compressibility effects were minimized by basing the heat-transfer coefficient on adiabatic wall temperature, and the properties were calculated at the local bulk static temperature. Consequently, the data were reduced to coincide approximately with the assumptions of the present analysis. Further, the definitions used for the one-dimensional parameters were known to be the same as applied in this paper.

Fig. 2 demonstrates the comparisons. Experimental downstream data are shown together with the axial variation of wall heating rate chosen for the analysis—a series of ramp functions connecting the values of q_w'' reported. Brackets on the data represent the current authors' guess of experimental uncertainties; Perkins and Worsoe-Schmidt do not present estimated uncertainties.

From the Nusselt-number plot it is clear that the eddy diffusivity correlation models do not lead to satisfactory predictions. For each one tested, the reduction of Nu is much less than that shown by the data. These results also show that the earlier quasi-developed results were misleading. For example, with the three-layer model, solution of the complete boundary-layer equations leads to $(\mathrm{Nu}/\mathrm{Nu}_{cp}) \simeq (T_w/T_b)^{-0.11}$, whereas the exponent is about -0.3 when solved under the fully developed assumption. These two observations are among the important results of the present study.

The magnitudes of Nusselt numbers predicted with the mixing-length models are in better agreement with the experiment, perhaps as a consequence of the dependence on the local velocity gradient which is retained in mixing-length models. While the representation of a mixing-length model is one-dimensional, it enters the calculations as

$$\epsilon = l^2|\partial u/\partial y|$$

so there is pointwise dependence on $\partial u/\partial y$ which is a function of both x and y. In contrast, when eddy-diffusivity correlations are used directly, they are primarily geometry-dependent.

The reductions predicted with the mixing-length models based entirely on pointwise fluid properties are not as great as those obtained with models which retain some dependency on wall conditions. In the van Driest version, it is seen that the exponential term causes more effective damping at the same value of y if y^+ is evaluated with wall properties rather than with local properties. Therefore, an additional effect is introduced which reduces the mixing length as T_w/T_b is increased. Comparable behavior is noticeable in the versions derived from Kendall, et al. While these observations do not agree with the desire for completely local models, the results with wall-property dependency appear to be operationally more useful. Agreement with the experimental Nusselt numbers seems best for the "van Driest-wall" model (but only by a slight margin over the Kendall model). This model was therefore chosen for the further predictions and for further comparison to experiment.

Whether the Deissler model would provide better agreement is open to question. For the turbulent core, it includes con-

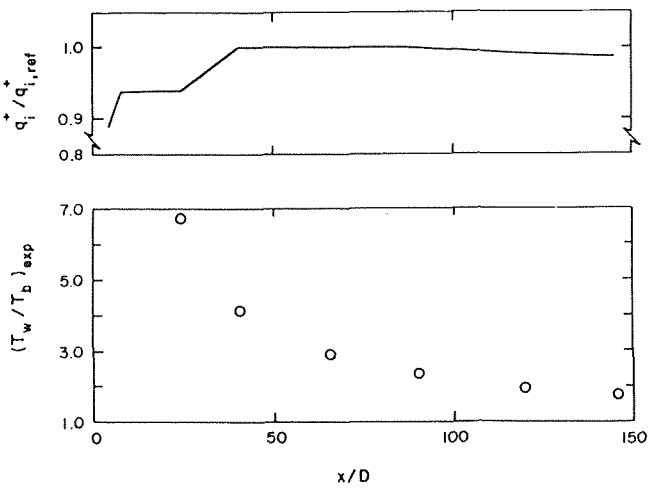

Fig. 2(a) Assumed axial wall heat flux variation

Fig. 2(b) Experimental wall-to-bulk-temperature ratio

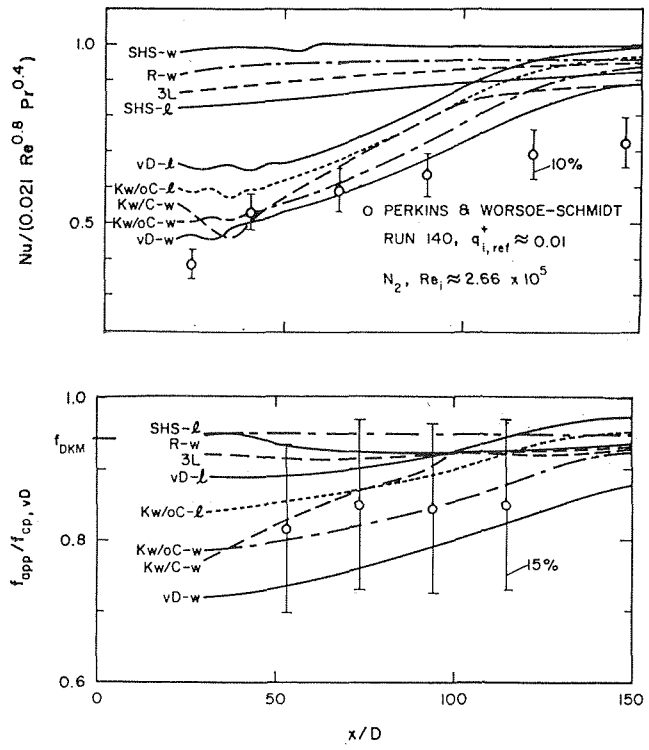

Fig. 2(c) Downstream, normalized heat-transfer predictions

Fig. 2(d) Downstream, normalized wall friction predictions

Fig. 2 Numerical predictions for various turbulence models compared to data of Perkins and Worsoe-Schmidt [6]. Identification of models as in Table 1.

siderations of local velocity gradients as the mixing-length models do. However, near the all-important wall, its effective viscosity is comparable to the values used in the modified three-layer model and in the Sparrow, Hallman, and Siegel model; these two models do not agree with the data very well.

The results for apparent friction factor with the various models are inconclusive in the sense that the data do not determine preferred models. As the heating rate is increased, the experimental friction factors inherently become more uncertain and less important as demonstrated in Appendix A.

It is significant that the predicted reduction in friction factor is definitely less than the reduction in Nusselt number when the complete boundary-layer equations are solved. The reader should recall that the "fully developed" analyses did not lead to this result and that this deficiency was one of the major reasons which prompted this study. Thus, it is concluded that axial effects should be included in the formulation of the problem when treating strongly heated, turbulent, internal gas flows.

Predictions From Numerical Analysis

Basis of Predictions. With the van Driest mixing-length model (using wall properties in the exponential term) chosen as the best of the models studied, a number of predictions were made. After studying the heat-transfer results the trends are compared to a wide range of data. In the calculations, wall heat flux was maintained constant in the axial direction and a 40-dia long unheated entry section preceded the heating region. The Reynolds number for entering flow was varied from 5×10^4 to 5×10^5, and q_i^+ ranged from 0.001 to 0.02. Exponents for air were employed, and the Prandtl number for entering flow was taken as 0.7. Runs with exponents of 0.0 provided constant-properties predictions for normalization.

Heat Transfer. The primary results are the normalized downstream Nusselt numbers plotted in Fig. 3 against the property-variation parameter, T_w/T_b. This is the form that the experimentalist often uses for correlation purposes. The symbols represent the start of the plot for each run, at about 40 dia from the start of heating. The results are plotted as solid lines, which progress to the left of the symbol since T_w/T_b decreases downstream. The most severe heating situation shown extends from $(T_w/T_b) \simeq 4.3$ at 40 dia to $\simeq 1.2$ at 300 dia.

Two regions are apparent on the figure. As each run proceeds it approaches an asymptotic curve downstream. One may envision this asymptotic behavior as an approximate parabola with the vertex upward on the logarithmic plot. Joining this curve are other curves representing the transition from the higher Nusselt numbers expected in the immediate thermal entry. At a given heating rate, q_i^+, these transitional curves seem to coincide regardless of the entering Reynolds number. As q_i^+ increases, the axial location of the point of juncture varies with both q_i^+ and Re_i. At low q_i^+ and/or at low Re_i, a length of 40 dia seems enough while at the higher values over 80 and 120 dia are sometimes necessary. The asymptotic behavior is in approximate agreement with the correlation proposed by Kutateladze and Leont'ev [26].

Comparison to Experiment. Some of the existing disagreement between experimental correlations may be explained in terms of Fig. 3. Various publications suggest different coefficients and exponents in their correlations [5, 6, 12]. Since Fig. 3 does not show a simple power-law dependence, experimental correlations presented in such form will represent only the region in which their data are massed. Thus, at low heating rates the film-temperature reference is adequate, as demonstrated by McEligot in an educational paper [27]. The downstream data of Perkins and Worsoe-Schmidt ranged from $(T_w/T_b) \simeq 3$ to $(T_w/T_b) \simeq 1.5$, and their correlation consequently shows a steeper slope and higher intercept [6]. The maximum q_i^+ of McEligot, Magee, and Leppert, about 0.004, was in between the values of these two studies, and so was the correlation. These correlations are seen to be consistent with the trends of Fig. 3.

Taylor [28] and Dalle Donne and Bowditch [29] suggest correlations with the exponent on the temperature ratio presented as a function of axial position. This approach is shown by Fig. 3 to be unnecessary in the aysmptotic region, but may be useful in the transition zone from thermal entry to asymptotic region.

Fig. 4 represents an approximate comparison between the tabulated data of Perkins and Worsoe-Schmidt [6] and the cur-

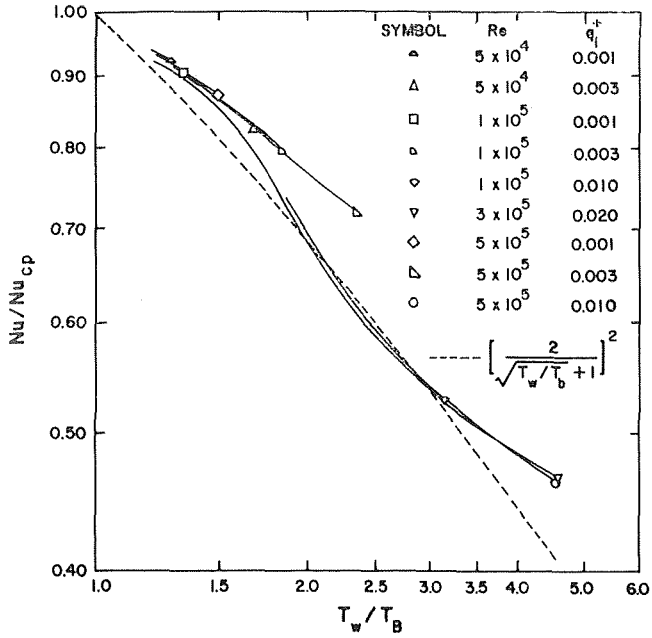

Fig. 3 Downstream heat-transfer predictions of current numerical analysis, air properties, $x/D \gtrsim 40$. Symbol is shown at $x/D \simeq 40$ for each run.

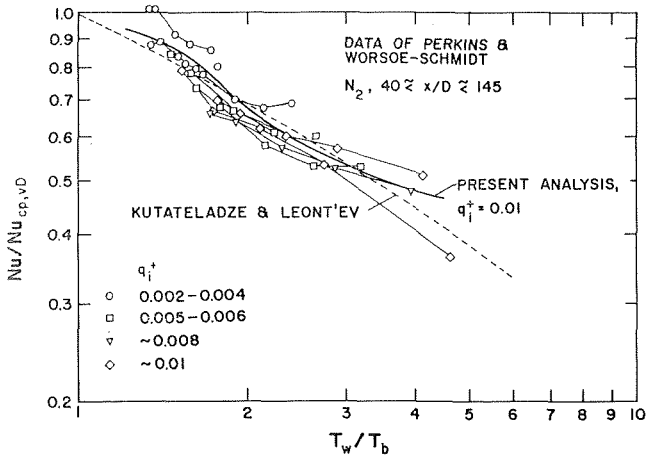

Fig. 4 Comparison of present heat-transfer predictions to experiment [6]. Light lines connect data points on same run. Dashed line is approximate correlation recommended by Kutateladze and Leont'ev [26].

rent analysis.[4] Rather than testing the model against a single, strongly heated run only, these data cover the ranges $0.002 \lesssim q_i^+ \lesssim 0.01$ and $76{,}000 \lesssim \mathrm{Re}_i \lesssim 270{,}000$. Further, Taylor [30] has shown that these data agree with his correlation of his own data for helium and hydrogen, so Fig. 4 may be considered an indirect comparison with Taylor's data. The boundary condition for the analysis was constant heat flux while the data show slight variations. Also, air properties were used in the numerical program rather than the properties of precooled nitrogen of the experiments. But the agreement is heartening. For the most part, the trends of the data are as noted earlier when discussing Fig. 3. In particular, the curves for individual runs have the

[4] The coordinates of Fig. 4 provide a less sensitive test than those of Fig. 2, but they are the ones normally used by the laboratory scientist. Note that a calculated local Nusselt number which is larger than an experimental observation will result in a predicted T_w/T_b which is smaller than the observation and, therefore, the two points in the plane of Fig. 4 may fall near the same curve even though the predicted and experimental wall temperatures differ considerably.

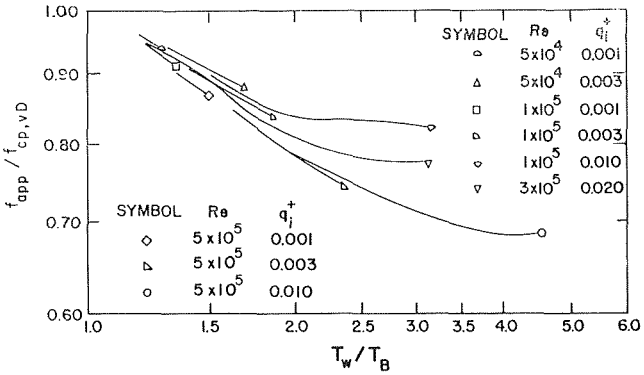

Fig. 5 Downstream apparent friction-factor predictions of current numerical analysis, air properties, $x/D \gtrsim 40$. Symbols as in Fig. 3.

same shape in both sets of results. However, the bulk of the downstream data falls below the asymptotic part of the analytical curve. Whether this problem is due to experimental error or to an inadequacy in the analysis has not been determined. The simple relation suggested by Kutateladze and Leont'ev [26] is shown for comparison; agreement is about as good as with our relation since theirs approximately agrees with our current analytical results. Design application of the results is discussed in Appendix B.

Wall Friction. The effect of heating rate upon apparent friction factor is exhibited in Fig. 5. As pointed out earlier, the trends are about the same as those observed for heat transfer, but the magnitude of the reduction is less. Since the reduction is only slight, designers need not be overly concerned about the effect of property variation on pressure drop, provided they calculate the acceleration term correctly.

Friction factor becomes an item of major concern when used in establishing the validity of an analysis. In the Introduction, contradictions were pointed out between the analyst's evaluation of friction factor and that of the laboratory scientist. In Fig. 5 the apparent friction factor is presented because this parameter, rather than f based on the true wall shear stress, corresponds to experiment and design usage. However, for the most extreme heating situation studied in this series ($q_i^+ = 0.02$), the difference in these two friction factors downstream only amounted to 5 percent at $(T_w/T_b) = 2.5$ and decreased as T_w/T_b approached unity. Of the two, f_{app} is higher, i.e., the reduction is less, and its exponent in a power-law correlation would therefore be slightly less. However, 5 percent at $(T_w/T_b) = 2.5$ represents a difference of about 0.06 in the exponent. From Fig. 5 one may estimate an exponent of about -0.25 for a power-law correlation of f_{app} downstream.

In relation to the stated goals of this paper, an interesting cycle appears in the study of the friction results. Initially, the quasi-developed analyses based on eddy-diffusivity models overpredicted the reduction in friction factor when compared to the mean data. The present solutions of the complete boundary layer equations then showed the eddy-diffusivity models to predict too small a reduction in both f and Nu (Fig. 2). Finally, with the chosen mixing-length model, the prediction of f_{app} is only slightly lower than our estimate of the mean trend of the data, and the predicted f, based on $\partial u/\partial y)_w$, is approximately the same as the quasi-developed results with eddy-diffusivity models (exponent about -0.3). Thus, if the difference in definitions had been quantified for the quasi-developed analyses, one might have erroneously concluded that this difference was the proper explanation. However, the major discrepancy in Nu would have remained.

Discussion

Since basic understanding of the physics of fully developed, adiabatic pipe flow is not yet well in hand, it would be presump-

tuous to expect to gain a basic understanding of the turbulence structure in this more difficult problem. The numerical program of this paper is a means of solution once structure theorists have hypotheses from which transport models can be derived (if models cannot be derived, the theory is not of much value). Further, from our results one can perhaps establish some bounds that structure theories must meet if they are ever extended to the present problem. For example, if a theory predicts a model equivalent to Reichardt's version [31, 32] when treating variable-property gas flows, then the theory is inadequate. On the other hand, if a model comparable to the "van Driest-wall" model is derived, the theory may be valid.

It is observed that the use of wall conditions in the van Driest "damping term" leads to better predictions than use of local conditions. Thus, the viscous sublayer must be thicker than one would anticipate from adiabatic measurements. Whether the reason is a reduction in turbulence production or more rapid decay of turbulence or both remains to be determined. The consequent distortions of velocity and temperature profiles evidently are sufficiently large, in the important wall region, that correlations of ϵ_m or $u^+(y^+)$ based on adiabatic, fully developed measurements are of little value.

The need for complete boundary-layer equations, in place of the quasi-fully developed approximations, demonstrates the importance of the upstream "history" of the temperature and velocity distributions even far downstream. Since an approximate, asymptotic result appears, it is possible that an approximate similarity analysis could be developed for the downstream region without solving through the thermal entry. But any such analysis must include the axial convective terms in a realistic manner.

The improvement attained with the present numerical analysis for strong heating rates can perhaps best be seen in terms of the predicted temperature differences. Transformation from the usual data presentation to the consequent design prediction is shown in Fig. 6. Above a heating rate which leads to a measured T_w/T_b of about 2, the improvement is substantial. In that range, Fig. 4 shows the present analytical results may be approximated by an exponent of -0.55 in a correlation of T_w/T_b and the data group around -0.6. As an example, at a design heating rate (Q_b^+/Nu_{cp}) of 1, changing from a prediction based on the quasi-fully developed analyses (exponent $\simeq -0.3$) to the present results shows the predicted temperature difference to increase by 35 percent. For the same conditions, changing from the present analysis to a correlation based on the data would only increase the predicted temperature difference by about 10 percent. However, the authors would be the last to claim that the present method is the ultimate. It is evident from Fig. 2(*c*) that further improvement is necessary far downstream for strongly heated runs. While the trends seem to be predicted well, the magnitude of Nu appears to return toward the constant-property prediction too rapidly. Better predictions will probably require the development of better turbulent transport models; two- or three-dimensional versions may even be necessary.

Conclusions

The present numerical program for the solution of the coupled, partial-differential, boundary-layer equations provides a substantial improvement over previous analyses for the prediction of downstream Nusselt numbers for turbulent gas flow through tubes with strong property variation, when the effective transport properties are derived from a version of van Driest's mixing-length model. In addition, the following significant observations may be made:

(*a*) Previously, data showed that property variation had a stronger effect on Nu than on f while analyses based on fully developed assumptions predicted approximately equal effects. Solving the complete boundary-layer equations with axial effects resolved this discrepancy.

(*b*) The previous discrepancy in predicting the exponent in the function $\mathrm{Nu}/\mathrm{Nu}_{cp}$ was resolved, for the most part, by solving the complete boundary-layer equations with axial effects plus selection of an alternate turbulence model.

(*c*) The eddy-diffusivity models tested are inadequate for the class of flows studied. Mixing-length models fared better.

(*d*) Approximate, asymptotic behavior of Nu versus T_w/T_b is found for the downstream region, but the distance to approach it is a function of q_i^+ and Re_i.

Acknowledgment

Work at Los Alamos was performed under the auspices of the U. S. Atomic Energy Commission, while work at the University of Arizona was supported primarily by the U. S. Army Research Office—Durham, and partially by an institutional grant from the National Aeronautics and Space Administration and by the U. S. Army Mobility Equipment Research and Development Center, Ft. Belvoir. The aid of the Computer Centers at both institutions is appreciated.

References

1 Spalding, D. B., "Theories of the Turbulent Boundary Layer," *Applied Mechanics Reviews*, Vol. 20, 1967, p. 735.

2 Patankar, S. V., and Spalding, D. B., "A Finite Difference Procedure for Solving the Equations of the Two-Dimensional Boundary Layer," *International Journal of Heat and Mass Transfer*, Vol. 10, 1967, pp. 1389–1411.

3 Chamberlin, T. C., "On the Method of Multiple Working Hypotheses," *Journal of Geology*, Vol. 5, 1897, p. 837.

4 Kays, W. M., *Convective Heat and Mass Transfer*, McGraw-Hill, New York, 1966.

5 McEligot, D. M., Magee, P. M., and Leppert, G., "Effect of Large Temperature Gradients on Convective Heat Transfer: The Downstream Region," JOURNAL OF HEAT TRANSFER, TRANS. ASME,

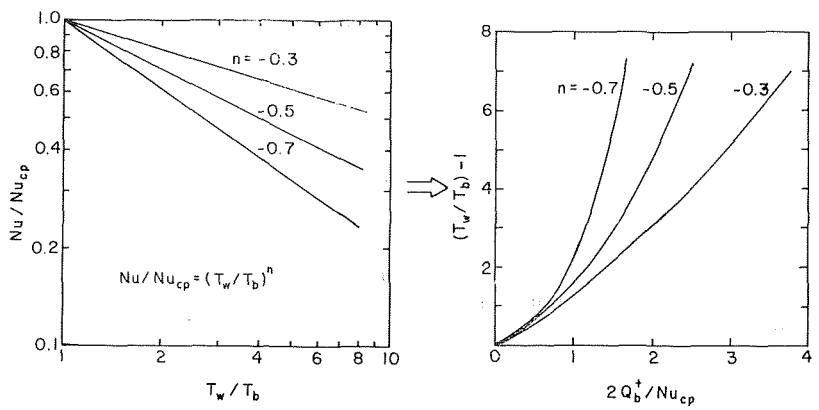

Fig. 6 Transformation of empirical correlations to design predictions for known heating rate and bulk temperature

Series C, Vol. 87, No. 1, Feb. 1965, p. 67.
6 Perkins, H. C., and Worsoe-Schmidt, P. M., "Turbulent Heat and Momentum Transfer for Gases in a Circular Tube at Wall-to-Bulk Temperature Ratios to Seven," *International Journal of Heat and Mass Transfer*, Vol. 8, 1965, p. 1011. Data tabulated in Tech. Report SU 247-7, Mech. Eng. Dept., Stanford University, Sept. 1964.
7 Botje, J. M., "An Experimental and Analytical Investigation of Heat Transfer by Forced Convection in Turbulent Flow for Air, Carbon Dioxide and Helium," PhD thesis, Purdue University, 1956.
8 Jackson, J. D., "A Theoretical Investigation into the Effects of Surface/Gas Temperature Ratio for Fully Developed Turbulent Flow of Air, Helium and Carbon Dioxide in Smooth Circular Tubes," ARC 22,784, FM 3084, Great Britain, 1961, DDC AD 269 066.
9 Sze, B. C., "The Effect of Temperature Dependent Fluid Properties on Heat Transfer in Circular Tubes," PhD thesis, Stanford University, 1957.
10 Deissler, R. G., "Analysis of Turbulent Heat Transfer, Mass Transfer and Friction in Smooth Tubes at High Prandtl and Schmidt Numbers," NACA Report 1210, 1955.
11 Magee, P. M., "The Effect of Large Temperature Gradients on Turbulent Flow of Gases in the Thermal Entrance Region of Tubes," PhD thesis, Stanford University; TID-22247, 1964.
12 Taylor, M. F., "Experimental Local Heat Transfer Data for Precooled Hydrogen and Helium at Surface Temperature up to 5300 deg R," NASA TN D 2595, 1965.
13 Deissler, R. G., and Eian, C. S., "Analytical and Experimental Investigation of Fully Developed Turbulent Flow of Air in a Smooth Tube with Heat Transfer with Variable Fluid Properties," NACA TN 2629, 1952.
14 Martinelli, R. C., "Heat Transfer to Molten Metals," TRANS. ASME, Vol. 69, 1947, p. 947.
15 Smith, S. B., "Prediction of the Influence of Variable Properties on Nusselt Number and Friction Factor for Fully Developed Turbulent Flow of Air in Tubes at High Reynolds Numbers," M.S.E. Report, Aerospace and Mechanical Engineering Department, University of Arizona, 1967.
16 Shapiro, A. H., and Smith, R. D., "Friction Coefficients in the Inlet Length of Smooth Round Tubes," NACA TN 1785, 1948.
17 Kendall, R. M., Rubesin, M. W., Dahm, T. J., and Mendenhall, M. R., "Mass, Momentum, and Heat Transfer within a Turbulent Boundary Layer with Foreign Gas Mass Transfer at the Surface. Part I—Constant Fluid Properties," Vidya Report No. 111, 1964, DDC AD 619 209.
18 McAdams, W. H., *Heat Transmission*, 3rd ed., McGraw-Hill, New York, 1954, p. 219.
19 McEligot, D. M., Ormand, L. W., and Perkins, H. C., "Internal Low Reynolds-Number Turbulent and Transitional Gas Flow With Heat Transfer," JOURNAL OF HEAT TRANSFER, TRANS. ASME, Series C, Vol. 88, No. 2, May 1966, p. 239.
20 Kinney, R. B., and Sparrow, E. M., "Turbulent Pipe Flow of an Internally Heat Generating Fluid," JOURNAL OF HEAT TRANSFER, TRANS. ASME, Series C, Vol. 88, No. 3, Aug. 1966, p. 314.
21 Black, A. W., and Sparrow, E. M., "Experiments on Turbulent Heat Transfer in a Tube With Circumferentially Varying Thermal Boundary Conditions," JOURNAL OF HEAT TRANSFER, TRANS. ASME, Series C, Vol. 89, No. 3, Aug. 1967, p. 258.
22 Spalding, D. B., and Chi, S. W., "The Drag of a Compressible Turbulent Boundary Layer on a Smooth Flat Plate with and without Heat Transfer," *Journal of Fluid Mechanics*, Vol. 18, 1964, p. 117.
23 Richtmyer, R. D., *Difference Methods for Initial Value Problems*, Interscience, New York, 1957.
24 Bankston, C. A., and McEligot, D. M., "A Numerical Method for Solving the Boundary Layer Equations for Gas Flow in Circular Tubes with Heat Transfer and Property Variations," Technical Report LA-4149, Los Alamos Scientific Laboratory, 1969.
25 Sparrow, E. M., Hallman, T. M., and Siegel, R., "Turbulent Heat Transfer in the Thermal Entrance Region of a Pipe With Uniform Heat Flux," *Applied Scientific Research*, Vol. 7A, 1957, p. 37.
26 Kutateladze, S. S., and Leont'ev, A. I., *Turbulent Boundary Layers in Compressible Gases*, Arnold, London, 1964.
27 McEligot, D. M., "Internal Gas Flow Heat Transfer with Slight Property Variation," *Bulletin of Mechanical Engineering Education*, Vol. 6, 1967, p. 251.
28 Taylor, M. F., "Correlation of Local Heat Transfer Coefficients for Single Phase Turbulent Flow of Hydrogen in Tubes with Temperature Ratios to 23," NASA TN D 4332, 1968.
29 Dalle Donne, M., and Bowditch, F. H., "High Temperature Heat Transfer," *Nuclear Engineering*, Vol. 8, 1963, p. 20.
30 Taylor, M. F., Discussion on paper 28, *Proceedings, Third International Heat Transfer Conference*, Vol. VI, 1966, p. 102.
31 Reichardt, H., "Complete Representation of Turbulent Velocity Distribution in Smooth Pipes," *Z. Angew. Math. Mech.*, Vol. 31, 1951, p. 208.
32 Reynolds, H. C., "Internal Low Reynolds Number Turbulent Heat Transfer," PhD thesis, University of Arizona, 1968.
33 van Driest, E. R., "On Turbulent Flow Near a Wall," *Journal of Aeronautical Science*, Vol. 23, 1956, p. 1007.
34 Drew, T. B., Koo, E. C., and McAdams, W. H., "The Friction Factor for Clean, Round Pipes," *Trans. AIChE*, Vol. 28, 1932, p. 56.
35 Lel'chuk, V. L., and Dyadyakin, B. V., "Heat Transfer from a Wall to a Turbulent Current of Air Inside a Tube and the Hydraulic Resistance at Large Temperature Differentials," *Problems of Heat Transfer*, AEC-tr-4511, 1962, p. 114.

APPENDIX A

Insignificance of Friction Factor

The design engineer is interested in the friction factor to predict pressure drop and, hence, pumping power or inlet pressure. In most designs for gas-cooled nuclear power reactors and nuclear rocket reactors, for example, the pressure in the coolant passages is sufficiently high to render compressibility effects unimportant. Therefore, with the definitions listed in the Nomenclature plus the assumption that $(\Delta p/p) \ll 1$, one-dimensional force and energy balances lead to

$$-\frac{d\{p/(\rho V^2/^2g_c)\}}{d\{x/D\}} \simeq 8q_x{}^+ + 4f_x \tag{5}$$

The subscript x indicates that the definitions are based on properties at the local axial position. The first term on the right side represents the acceleration of the flow due to heating while the second term arises from the familiar wall friction.

For turbulent adiabatic flow the friction factor typically lies between 0.004 and 0.008; as we have seen, heating reduces this factor slightly. The parameter $q_x{}^+$ increases as the heating rate is increased, and the fraction of the pressure drop caused by friction consequently decreases. For the conditions of Run 140 by Perkins and Worsoe-Schmidt [6], friction would account for about one-sixth of the pressure gradient near the entrance and for only about one-half at the exit. A 10 percent error in friction factor is worth about 5 percent at the exit and less than 2 percent near the entrance! Thus the paradox arises that as the heating is increased its effect on wall friction increases but its importance declines.

Conversely, as the heating rate increases, so does the difficulty in obtaining accurate friction factors from experiments. Usually, pressure drop is measured rather than wall shear stress. At a specified Reynolds number and density, the frictional pressure drop decreases with heating while overall pressure drop increases. The percent uncertainty in friction factor increases both for this reason and because the uncertainty in bulk temperature affects the calculation of acceleration pressure drop. Again, for Run 140, 2 percent uncertainty in pressure gradient at the entrance leads to a 12 percent uncertainty in local friction factor.

APPENDIX B

Design Application

The asymptotic results from the van Driest mixing-length model can be adapted for application at several levels of precision. An explicit, or noniterative, prediction would be desirable. However, Fig. 3 would seem to dispel this possibility because the asymptotic curve appears to be predominantly a function of T_w/T_b. On the other hand, the nondimensional rate equation

$$Q^+ = \frac{\mathrm{Nu}}{2}\left(\frac{T_w}{T_b} - 1\right) \tag{6}$$

shows the relationship between T_w/T_b and Q^+ explicitly. Since the present asymptotic curve is approximated by the correlation of Kutateladze and Leont'ev [26], this equation may be written

$$Q^+ \simeq \frac{\mathrm{Nu}_{cp}}{2}\left[\frac{2}{\sqrt{\frac{T_w}{T_b}} + 1}\right]^2\left(\frac{T_w}{T_b} - 1\right) \tag{7}$$

or, for the range of interest,

$$\frac{T_w}{T_b} \approx \left[1 - \frac{Q^+}{2\mathrm{Nu}_{cp}}\right]^{-10/3} \tag{8}$$

Thus, for feasibility studies, the wall temperature can be calculated directly once the bulk temperature is determined from an energy balance. (The reader is reminded that equation (7) itself is approximately valid only on the asymptotic downstream curve, e.g., $(T_w/T_b) \gtrsim 1.6$ for moderate $q_i{}^+$, or $(T_w/T_b) \gtrsim 3$ for "high" $q_i{}^+$.)

For design studies the engineer may fit power-law correlations to his range of interest in Fig. 3 and use an iterative procedure to determine the wall temperature. If more precise predictions are desired, the computer program is listed in reference [24].

The results reported are for constant wall-heat-flux boundary conditions (or nearly so: Run 140 of reference [6]). There is no guarantee that these results for downstream conditions would provide adequate predictions for strongly varying wall heat flux. The latter condition is, in effect, a continuous thermal entry.

J. T. POGSON

J. H. ROBERTS

Research Engineers,
The Boeing Co., Seattle, Wash.

P. J. WAIBLER

Professor of Mechanical Engineering,
University of Washington, Seattle, Wash.

An Investigation of the Liquid Distribution in Annular-Mist Flow

The results of an experimental investigation of the average liquid film thickness are presented for vertical upward annular-mist two-phase flow, with and without heat transfer. The effects on the film thickness for variations in vapor flow rate, liquid flow rate, vapor density, and heat transfer are described. A correlation equation is presented for the local time-averaged thickness and for the droplet size distribution. In addition, an equation is given for the liquid film flow rate as a function of the average film thickness.

Introduction

TWO-PHASE vapor-liquid mixtures form a variety of patterns while flowing in tubes. These flow patterns are classified according to the spatial distribution of the liquid and the vapor. In one such pattern, annular-mist flow, the liquid flows along the tube walls in the form of a thin film while the central vapor core carries dispersed drops of liquid. This may occur for ratios of the vapor flow to the total flow rate ranging from a few percent to nearly 100 percent.

Attempts at predicting heat transfer coefficients or pressure drop with and without heat transfer for annular-mist flow have been largely empirical. Solutions usually rely on an analogy between single- and two-phase flow [1].[1] The accuracy of calculations based on such models has been found to be on the order of ±30 percent. In addition, these correlations can safely be used only for similar flow conditions and for the same fluids used in the experiments. Therefore, it seems logical that more detailed investigations of the liquid-vapor flow should precede further attempts at the analytical prediction of the heat transfer and pressure drop. Before accurate mathematical models for the flow dynamics may be hypothesized, the liquid distribution must be described, i.e., percent of the liquid in the form of droplets, number, size, and spatial distribution of the droplets, along with the droplet velocity distribution.

There is limited experimental data for the determination of the local liquid distribution. Most of this data is from the recent studies of Collier, Gill, Hewett, et al., [2] through [7]. Their data consists of local liquid film thickness measurements, liquid film flow rate data, and droplet concentration distributions for air-water mixtures flowing vertically in tubes. McManus [8] has also published the results of his investigations for horizontal flow of air-water mixtures flowing in adiabatic tubes. Very little data has been found for droplet sizes in confined two-phase flows. Additional information is needed, particularly for single-component, two-phase flow, for the prediction of the thickness of the annular liquid film and the liquid distribution, with and without heat transfer. This investigation was directed toward measuring the liquid film thickness and the droplet size distribution for annular mist flow.

Experimental Apparatus

1 Liquid Film Thickness. A schematic diagram of the open flow loop constructed for the liquid film thickness investigation is shown in Fig. 1. This apparatus allowed the independent variation of the test section pressure, steam flow rate, water flow rate, and heat flux. The data taken or directly calculable were: the local instantaneous and time-averaged annular liquid film thickness, the test section pressure drop, the outside wall temperature, and the inlet steam and water properties.

Essentially dry and saturated steam was throttled to the desired operating pressure and passed through a cyclone separator and a ten-micron filter before flowing into the test section. The steam flow rates were determined by weighing the condensed vapor, and a constant rate held by observation of the pressure drop across a sharp-edged orifice.

The distilled water used to form the annular liquid film on the

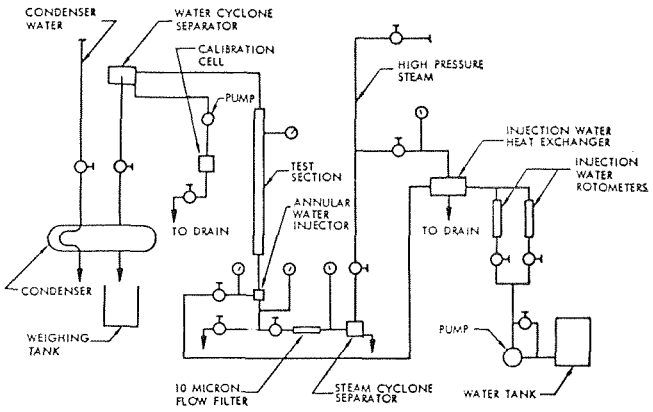

Fig. 1 Flow loop schematic

[1] Numbers in brackets designate References at end of paper.

Contributed by the Heat Transfer Division and presented at the Fluids Engineering, Heat Transfer, and Lubrication Conference, Detroit, Mich., May 24–27, 1970, of THE AMERICAN SOCIETY OF MECHANICAL ENGINEERS. Manuscript received at ASME Headquarters, November 3, 1969. Paper No. 70-HT-11.

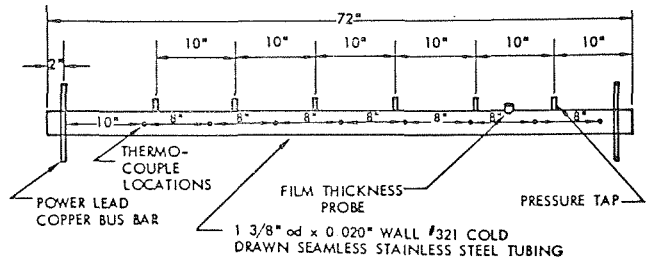

Fig. 2 Test section

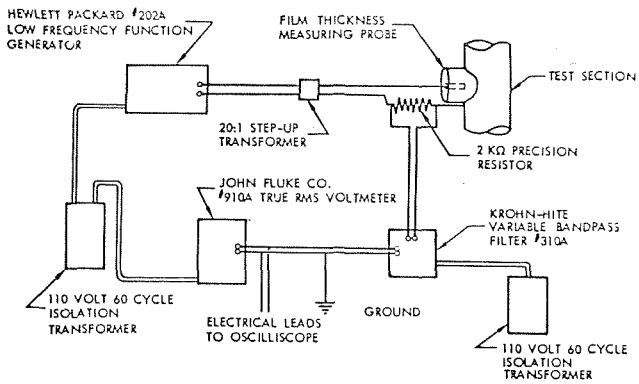

Fig. 3 Electric circuit schematic

wall of the test section was pumped through rotometers and a heat exchanger to the water injector. The flow rate could be varied from 10 to 500 lbm/hr, and the temperature controlled to correspond to the saturation temperature of the saturated steam flowing through the injector. Both the steam and water flow rates were then corrected to account for the removal of the steam superheat resulting from the throttling process.

The annular two-phase mixture formed in the injector flowed concurrently upward through the test section and into a second cyclone separator. The liquid from this separator was used for calibration of the test section film thickness probe. After passing through the cyclone separator, the steam and water flowed through a valve to a condenser. This valve permitted control of the test-section pressure.

Test Section. The test section was constructed from a six-foot length of cold-drawn type 321 stainless steel tubing, 0.020-in. wall thickness, $1^3/_8$ in. OD, Fig. 2. Two electrical power bus bars were silver-soldered to the ends of the tube for the d-c heating current. Electrical isolation of the test section was provided by mounting it in "Teflon" insulating supports at each end.

Six pressure taps were connected to water seal pots by nylon tubing. A 0–100-psi Heise pressure gauge with 0.1-psi divisions was connected to the downstream pressure tap, which was also used as the reference pressure tap and connected to the tube side of all five well-type manometers. The five remaining pressure taps were connected to the well-side of each of the five manometers.

Water Injector. A water injector was designed and built which allowed the addition of water to form an annular film on the tube wall. The water was introduced through either or both of two annular slots, 0.035 in. in width, forming an angle of 2.5 deg with the pipe wall.

Liquid Film Thickness Probe. The film probe was made by forcing a tungsten wire through the axis of a short glass cylinder heated to the plastic stage. The glass rod and wire was then cut into two halves, identical at the cut face. An outer electrode, made of an annular nickel band, was forced over each piece of the $^1/_2$-inch glass rod. The unit selected as the measuring probe was held in a hole in the tube wall by a metal saddle and screw cap arrangement and ground in place to the exact contour of the inner tube wall so that no discontinuity existed. In operation, the electrical resistance between the inner and outer electrodes was proportional to the film thickness.

Deviations from linearity due to the slight three-dimensional nature of the film and possible capacitive circuit effects were eliminated by use of a reference or calibration probe cell.

Calibration Cell. The calibration cell consisted of a watertight box in one wall of which the duplicate probe was mounted. The probe was faced by a spring-loaded flat glass plate whose spacing from the probe plate could be varied by the longitudinal movement of a wedge. A longitudinal wedge movement of 0.0232 in. resulted in a 0.001-in. change in the spacing. The water pumped through this gap was the fluid stripped from the test-section flow, and therefore of the same electrical conductivity.

Liquid Film Probe Electronics. Fig. 3 is a schematic diagram of the electrical circuit for both the test section liquid film thickness probe and the calibration cell. Experience proved that the best excitation was a 150-v, 300-cps sine wave. A narrow band pass filter was used to reduce extraneous noise from the heating current and other sources. The resulting signal, the voltage drop across a 2000-ohm resistor, had a noise level of less than 1 millivolt.

2 Droplet Size Distribution. To obtain data on the droplet size distribution, the flow system was modified to strip the liquid film from the wall of the tube and vent the flow to the atmosphere at the top of the test section. In the region near the exit the flow was undisturbed and droplets could be photographed using

Nomenclature

A_T = free surface area of the control volume ($2\pi\delta x(R - y)$)
b = size parameter in distribution equations
B = scale constant in distribution equations
b_s = constant, (0.091) in Sleicher's momentum diffusivity equation
C_3 = constant in the correlation equations
D_p = diameter of the tube (1.335 in I.D.)
F_s = surface forces
n = exponent of the density ratio
Re = Reynolds number
Re'_l = superficial liquid Reynolds number ($4W_l/D_p\pi\nu_v$)
R = tube radius, 0.6675 in.
$\bar{l}$ = average liquid film thickness
$\bar{l}^+$ = nondimensional average liquid film thickness, $\frac{\bar{l}u^*}{\nu}$
u^+ = nondimensional velocity $= u/u^*$
$\bar{u}$ = average velocity
u^* = shear velocity $\sqrt{\tau_w g_c/\rho_l}$
v_i^* = shear velocity $\sqrt{\tau_i g_c/\rho_l}$
x = distance along the tube axis, see Fig. 13
y = distance normal to the tube wall, see Fig. 13
y^+ = nondimensional distance normal to the tube wall, $\frac{yu^*}{\nu}$
W = flow rate
α = $(dp/dx + \rho_l g/g_c)$
δ = distribution parameter in distribution equations
η = thickness of the laminar and buffer layers
η^+ = nondimensional thickness of the laminar and buffer layers, $\frac{\eta u^*}{\nu}$
ϵ = eddy diffusivity
μ = dynamic viscosity
ν = kinematic viscosity
ξ = ratio $\eta/\bar{l}$
ρ = density
τ = shear
ϕ = $\mu\alpha g_c/\rho_l{}^2 u^{*3}$
χ = constant

Subscripts

$c.v.$ = control volume
i = interface
iv = vapor interface
l = liquid
lf = liquid film
n = normal to the tube wall
m = average
w = wall
r.m.c. = root mean cube

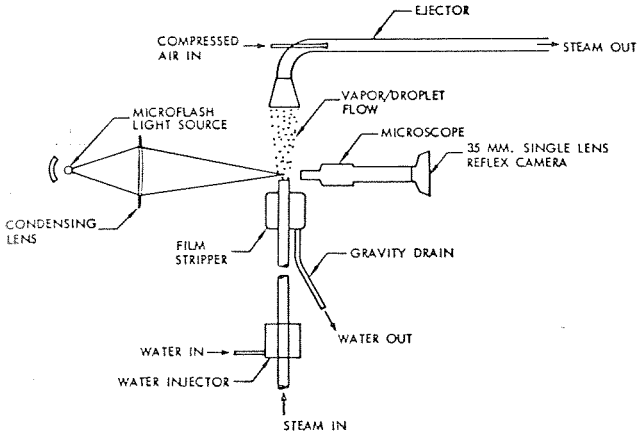

Fig. 4 Schematic of photography apparatus

a high-resolution optical system and a high-speed flash lamp. A schematic of the apparatus is shown in Fig. 4. The flow rate of the steam was controlled at 300 lbm/hr and the water flow rate was varied from 100 to 300 lbm/hr.

Camera and Optics. A Carl Zeiss stereomicroscope with a range of magnification from 10× to 200× provided an optical system which was used to experimentally determine the optimum magnification and depth of field relationships. The microscope could accept both a Polaroid film back and a 35-mm focal-plane-shutter camera. The Polaroid back allowed a convenient preliminary check-out of the system alignment and a means of taking quantitative data. The 35-mm camera with the available range of film speeds and resolution provided a means of taking high-quality photographs at a lower magnification, which could be subsequently enlarged without reduction in the depth of field. The 35-mm camera with an optical system magnification of 14.3× provided photographs of a field 2.50 by 1.72 mm with a depth of field of 1.70 mm. Exact magnification of the system was determined by photographing a Zeiss stage micrometer just prior to taking data. The photograph of the scale was later enlarged at the same time as the droplet photographs and provided a scale for measuring droplets. Enlargement to a 4 × 5-in. print produced an image of approximately 500× magnification for analysis.

Depth of field for the camera and optical system was determined on an optical bench. The camera and lenses were firmly mounted at one end with a fixed light source focused at the objective plane. A 25-micron-diameter wire was attached to a sliding stand on the bench which was moved through the plane of focus by a micrometer screw. By moving the wire loaded with a small attached droplet through the range of focus in small increments, with a photograph at each position, the extent of the range was determined for each camera and film type. At some level of distortion a subjective judgment was made that the drop was just barely in focus. This photograph then was retained as a comparator, and was held beside the droplet photographs when the analysis of droplet sizes was made. It was found to be relatively easy to decide whether a particular drop was in focus with the comparator photograph alongside.

In obtaining droplet size distributions, it is not necessary that the exact diameter be measured, but that the droplet be sufficiently resolved that it can be classified into size groups. For instance, if droplets are to be classified into size groups of 20 microns, it is only necessary to know their size to the nearest 20 microns; that is, the fuzzy edge of the droplet image should be no greater than one-half the size of the classification increment. With this criteria the error becomes smaller with the larger size drops.

Illumination. A microflash lamp with a peak intensity of 5×10^7 candlepower and a duration of 0.5 microsec from $1/4$ peak to $1/4$ peak was used. This duration allows a drop traveling 100 fps to move only about 15 microns, or roughly three times the diameter of the smallest drop anticipated. Measurements across the width of the streak permitted the diameter of even very small droplets to be determined. The lamp was aligned with the camera axis such that the droplets were silhouetted against a bright background. A converging lens was used to focus a bright spot of light at the objective plane. By this method not only was the sharpest resolution of the droplet edge possible, but the most light reached the film providing the brightest illumination for the highly enlarged subject and the highest contrast.

Liquid Distribution Analysis

The liquid distribution in annular-mist flow may be determined from the average liquid film thickness, the liquid film velocity profile, and the quality of the total flow. Since the average film thickness is generally unknown, an equation which would correlate the data was developed for this parameter. In addition, an expression is derived for the film flow rate using a modified shear profile, in comparison to that presented in references [10–12].

The drag of the dispersed core is the driving force which causes the liquid to flow along the tube wall. Equating approximate values for the shear across the vapor-liquid interface, an expression relating the vapor interfacial shear to bulk flow parameters can be obtained.

The vapor-liquid core can be thought of as the flow of a gas in a roughened tube and a resistance coefficient written in the Blasius form. Writing the shear, τ_{iv}, in terms of the vapor properties, tube diameter, and the vapor Reynolds number gives

$$\tau_{iv} = \frac{C_l \mu_v^2 \mathrm{Re}^a}{\rho_v \bar{l}^2}$$

An expression for the liquid interfacial shear is obtained by examining the wall shear. The wall shear is governed by the velocity gradient at the wall, and the magnitude of the velocity gradient in the laminar sublayer is affected by the vapor-liquid interface. A similar influence may be produced with liquid flowing in the tube at a greatly increased rate. One might then suspect the Blasius shear equation to hold for the liquid wall shear.

$$\tau_{wl} = C_2 \rho_l \bar{u}_{ml}^2 \mathrm{Re}_l^{-b}$$

where

$$\bar{u}_{ml} = W_{lf}/(\rho_l \pi D_p \bar{l})$$

and

$$\mathrm{Re}_{lf} = 4W_{lf}/(\pi D_p \mu_v)$$

The relationship between the wall shear and the interfacial shear was determined from a momentum balance as $\tau_{il} = \tau_w + \alpha \bar{l}$. In the case of very thin films, the term $\alpha \bar{l}$ may be neglected since it will be less than 10 percent of the wall shear. Thus the liquid interfacial shear was set equal to the wall shear in order to simplify the resulting film thickness equation. The validity of this simplification is discussed in the presentation of the results. The approximate interfacial shear then becomes

$$\tau_{il} = \frac{C_2' \mu_l^2 \mathrm{Re}_l^{b'}}{\rho_l \bar{l}^2}$$

where $b' = (2 - b)$ and C_2' is a constant.

Equating the two equations for the interfacial shear and then simplifying gives:

$$\bar{l} = \left[C_3 \frac{\mathrm{Re}_{lf}^{b'}}{\mathrm{Re}_v^a} D_p^2 \frac{\mu_l^2}{\mu_v^2} \frac{\rho_v}{\rho_l} \right]^{1/2} \tag{1}$$

In equation (1), the liquid film flow rate is included as a parameter (i.e., the liquid film Reynolds number, Re_{lf}). However, since the liquid film flow rate is one of the unknown parameters still to be determined, an expression relating w_{lf} to

known flow quantities is needed. Such a relationship could not be obtained from basic principles due to the complex and yet unknown mechanisms causing entrainment.

A search of the literature indicated the following parameters have been used in accounting for the interfacial roughness in two-phase flow: $\left(\frac{\sigma g_c}{\mu_v \bar{u}_v}\right)$, (Re'_l), (ρ_v/ρ_l). All of the variables considered to be important for this investigation occur in these three dimensionless groups. An empirical grouping was used to obtain an expression for the liquid film flow rates.

$$\frac{W_{lf}}{w_l} = C_4 \left(\frac{\sigma g_c}{\mu_v \bar{u}_v}\right)^e \mathrm{Re}'_l{}^{(-d)} (\rho_v/\rho_l)^f$$

This expression can be written in terms of the Reynolds numbers and fluid properties as,

$$\mathrm{Re}_{lf} = C'_4 \mathrm{Re}'_l{}^{(1-d)} \mathrm{Re}_v{}^e \left(\frac{D_p \sigma g_c \rho_v}{\mu_v{}^2}\right)^e \left(\frac{\rho_v}{\rho_l}\right)^f \qquad (2)$$

Combining equation (1) and (2) gives

$$\frac{\bar{l}}{D_p} = C \frac{\mathrm{Re}'_l}{\mathrm{Re}_v{}^z} \frac{\mu_l}{\mu_v} \left(\frac{\rho_v}{\rho_l}\right)^n \left(\frac{D_p \sigma g_c \rho_v}{\mu_v{}^2}\right)^k$$

The exponents s, z, n, k, and the constant C, must be evaluated from experimental data and are described in the discussion of the results.

The deviation of the liquid film flow rate equation follows from the description of the film shear profile. A pictorial diagram of the annular liquid film with its wavy interface is shown in Fig. 13.

Applying the momentum theorem for the control volume *c.v.*, shown in Fig. 13, and simplifying, the shear-stress distribution is,

$$\tau = \tau_w + y\alpha + \rho_{c.v.} \frac{u(y)v(y)}{g_c} + \frac{1}{A_T} \frac{\partial}{\partial \theta} [\text{mass } (\theta)\bar{u}(\theta)]_{c.v.} \frac{-F_s}{A_T}$$

The first two terms on the right-hand side in the foregoing equation can be computed from generally known two-phase flow parameters, such as the flow rates and pressure loss. However, the other terms on the right-hand side, the convective momentum terms, and surface forces are not known *a priori*. These three terms require that the interfacial wave characteristics be prescribed for their evaluation. It is the effect of the convective momentum and interface surface forces which have been omitted in other studies [10–13].

For low liquid flow rates, both the wave amplitudes and frequencies are small, and the terms involved may be omitted with small error. As the liquid flow rate increases, so does the amplitude of the waves and possibly the wave frequency. Therefore, the convective momentum terms and surface forces may be important at the larger liquid flow rates. Hewitt's calculated flow rates, [12], when compared with his air-water data [3], indicate such an effect. That is, the calculated film flow rates are less than the experimental values when the liquid flow rate is increased.

Another approximation was made in this study in an attempt to retain the effect of the convective momentum terms at the larger liquid flow rates, (i.e., those cases in which the quantity $(\tau_{il} - \tau_w)$ becomes of the same order of magnitude as τ_w). In forming the approximation it is useful to examine the momentum terms. Very near the wall, in the liquid film, the convective momentum terms become very small and tend to zero as the wall is approached. The reason for the decreasing importance near the wall is that the influence of the wave structure, the wave troughs, and the radial liquid velocity is negligible in this region. This is especially true in the laminar and buffer liquid layers. Near the interface, however, in the turbulent liquid layer, these terms are significant. The method used to account for the convective terms was to increase the shear near the interface by use of the following modified shear profile:

$$\tau_i = \tau_w + \alpha l \quad \text{for} \quad 0 \le y \le \eta$$

and

$$\tau(y) = \tau_i \quad \text{for} \quad \eta \le y \le \bar{l}$$

In conjunction with the foregoing, the interface was assumed to be smooth, thus eliminating the surface forces. In the foregoing profile η is defined as the thickness of the combined laminar and buffer layers.

The significance of the previous assumptions (constant shear stress in the turbulent layer and a smooth interface) is an average value of shear has been applied across the turbulent layer. This average shear value tends to compensate for the shear deficiency near the interface (caused by the omission of the convective momentum and surface terms) by increasing the shear in the region near the buffer layer.

The shear-stress distribution in the buffer and laminar layer now becomes, retaining the requirement for a continuous shear distribution,

$$\tau = \tau_w + \alpha \frac{\bar{l}}{\eta} y \qquad 0 \le y \le \eta$$

and in the turbulent layer,

$$\tau = \tau_w + \alpha \bar{l} \qquad \eta \le y \le \bar{l}$$

Using this liquid film shear distribution, a liquid velocity distribution and film flow rate can be derived. Writing the general equation for the shear in terms of viscosity and momentum eddy diffusivity, one has

$$\tau = \frac{1}{g_c} (\mu + \epsilon\rho) du/dy$$

Sleicher's [14] momentum eddy-diffusivity equation, used by Davis to predict downward liquid film flow rates, was used for the eddy viscosity in the laminar and buffer layers,

$$\epsilon = \nu b_s{}^2 y^{+2} \qquad 0 \le y \le \eta$$

For the turbulent liquid layer, Prandtl's equation was used,

$$\epsilon = \chi^2 y^2 \left|\frac{du}{dy}\right|; \quad \eta \le y \le \bar{l}$$

Substituting the eddy diffusivity into the general shear equation and integrating gives an equation for the velocity profile. The liquid film flow rate can thus be obtained by integrating the resultant velocity profile.

$$\frac{W_{lf}}{2\pi R \mu_l} = \int_0^{30} u^+ dy^+ + \int_{30}^{t^+} u^+ dy^+$$

Performing the integration yields, for $t^+ < 30$,

$$W_l = 2\pi R \mu_l \left[\tan^{-1}(b_s y^+) \left(\frac{\xi\phi}{b_s{}^3} + \frac{\eta^+}{b_s}\right) + \ln(1 + b_s{}^2 y^{+2}) \left(\frac{\xi y^+ \phi}{2b_s{}^2} - \frac{1}{2b_s{}^2} - \frac{y^+ \xi\phi}{b_s{}^2}\right)\right]$$

For $t^+ > 30$,

$$W_{lf} = 2\pi R \mu_l \left[\tan^{-1}(b_s \eta^+) \left(\frac{\xi\phi}{b_s{}^3} + \frac{\eta^+}{b_s}\right) + \ln(1 + b_s{}^2 \eta^{+2}) \left(\frac{\xi \eta^+ \phi}{2b_s{}^2} - \frac{1}{2b_s{}^2}\right) - \frac{\eta^+ \xi\phi}{b_s{}^2} + \frac{v_i{}^*}{u^*} \frac{\bar{l}^+}{\chi} \times \left(\ln \frac{t^+}{\eta^+} - 1\right) + u^+(\eta^+)(t^+ - \eta^+) + \frac{v_i{}^*}{u^*} \frac{\eta^+}{\chi}\right]$$

Discussion of Results

Liquid Film Thickness. The data of those tests in which saturated injection water was used are presented in graphical form for il-

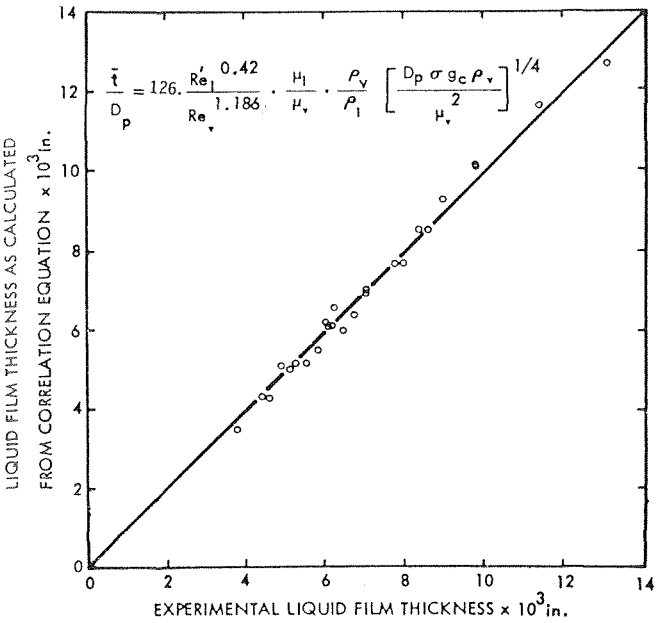

Fig. 5 Correlation of the liquid film thickness for saturated water injection

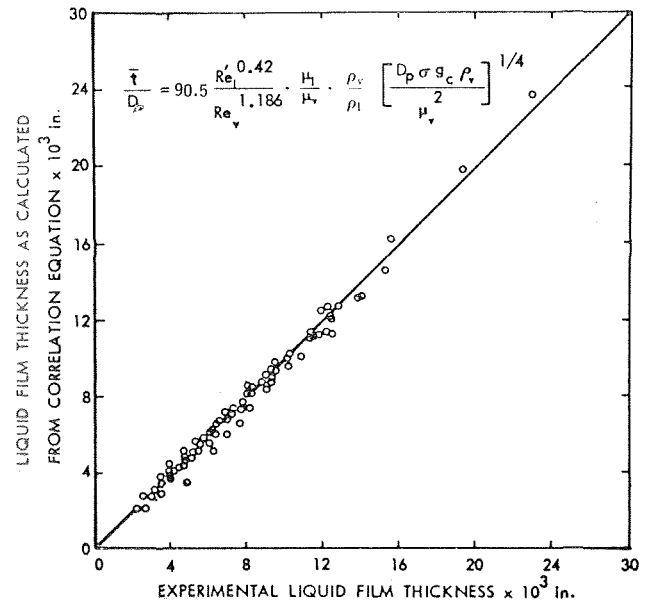

Fig. 6 Correlation of the liquid film thickness for subcooled water injection

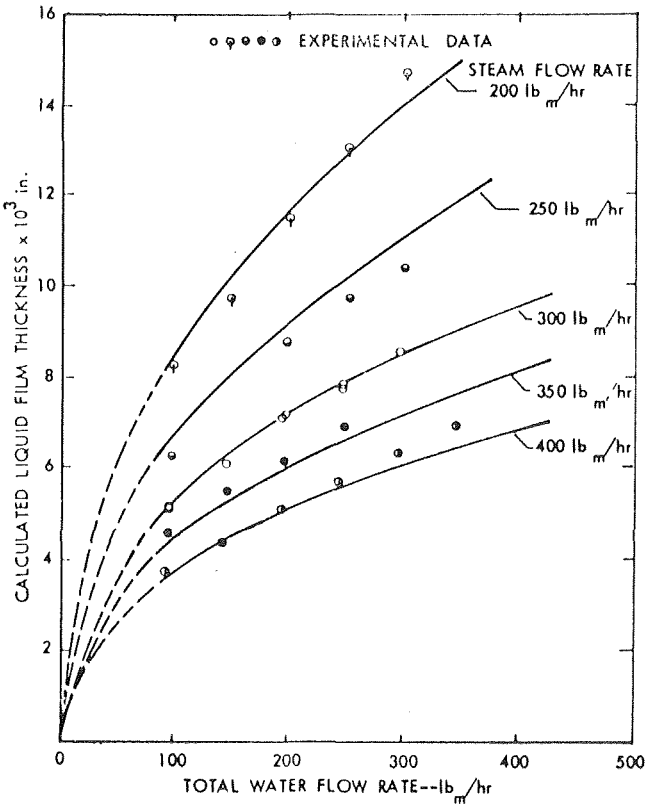

Fig. 7 A comparison of the liquid film thickness with the water flow rate for various steam flow rates

lustrative purposes. The adiabatic data are presented in Figs. 5 and 6 to show the correlation of the liquid film thickness for both saturated and subcooled water injection. Data was taken at three pressure settings for the subcooled water injection, 30, 40, and 50 psia. The saturation tests were run at 30 psia.

The liquid film thickness data was reduced on an IBM 7094 computer. A curve fit based on the method of least squares was used to determine the unknown constant and the exponent of the vapor Reynolds number. The other exponents were determined by hand calculations.

For saturated water injection the correlation is

$$\frac{\bar{l}}{D_p} = 126 \frac{\mathrm{Re}'^{0.42}_l}{\mathrm{Re}_v^{1.186}} \frac{\mu_l}{\mu_v} \frac{\rho_v}{\rho_l} \left(\frac{D_p \sigma g_c \rho_v}{\mu_v^2}\right)^{1/4}$$

For subcooled water injection (T_w = 84 deg F), the data correlation becomes

$$\frac{\bar{l}}{D_p} = 90.5 \frac{\mathrm{Re}'^{0.42}_l}{\mathrm{Re}^{1.186}} \frac{\mu_l}{\mu_v} \frac{\rho_v}{\rho_l} \left(\frac{D_p \sigma g_c \rho_v}{\mu_v^2}\right)^{1/4}$$

The difference in the constants, 126 and 90.5, for the foregoing two correlation equations was attributed to the condensation that occurred for subcooled water injection. During the injection of saturated water only small mass-transfer rates were present in arriving at a saturation state for the steam and water compared to the subcooled injection.

This difference in the mass-transfer rates was reflected in the test-section pressure pulsations. Pressure pulsations of ±0.5 psi or larger were not uncommon during subcooled injection. The pressure pulsations were rarely as large as ±0.5 psi and were generally about ±0.3 psi during saturated injection. The larger pressure pulsations observed for the subcooled injection are common during condensation processes.

These increased pressure pulses indicate increased instability of the liquid film. An increased disturbance level can cause the presence of large waves that would not otherwise be present [15]. These larger waves are different from the usual ripple waves and have been called "disturbance waves," [16]. Thus, with the increased instability in the liquid film and the tendency toward large disturbance waves, more liquid would be entrained for subcooled water injection than during saturated injection. This increased entrainment rate, combined with condensation in the dispersed core due to droplets, would cause a larger percentage of the water to be in the form of droplets. Hence the film liquid flow rate and film average thickness would be decreased.

Fig. 7 shows the variation of the average water film thickness as a function of the steam and water flow rates. As this figure illustrates, the film thickness decreases with an increase in steam flow rate. A cross-plot of the data, shown in Fig. 8, if extrapolated, indicates a minimum film thickness will be obtained for large steam flow rates. This condition, however, was not observed. Instead, as the minimum film thickness appeared to be reached for the larger steam flow rates, the continuous water film tended to break up into separate rivulets flowing along the tube wall. This situation was noted for water injection flow rates of W_l = 50 lb_m/hr and W_l = 25 lb_m/hr. In addition, the aforementioned minimum film thickness varied with the water flow rate.

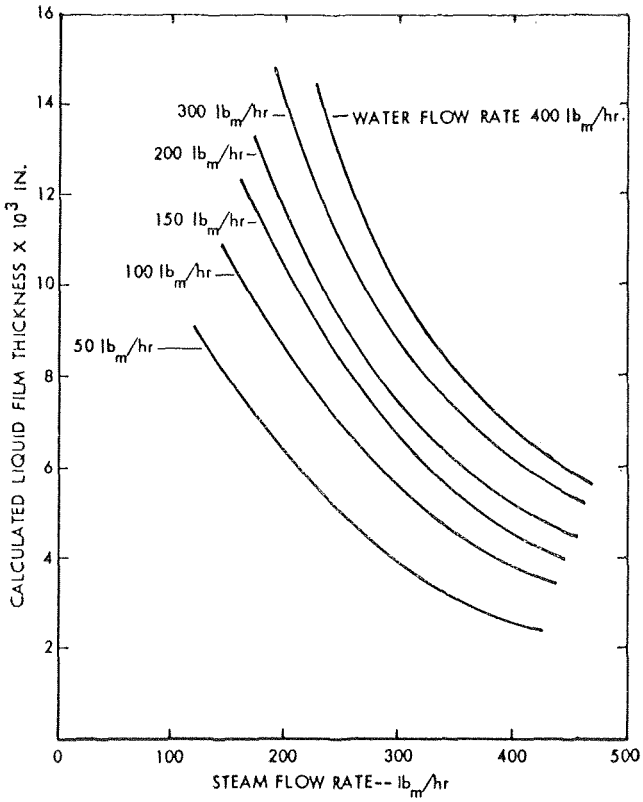

Fig. 8 A comparison of the liquid film thickness with the steam flow rate for various water flow rates

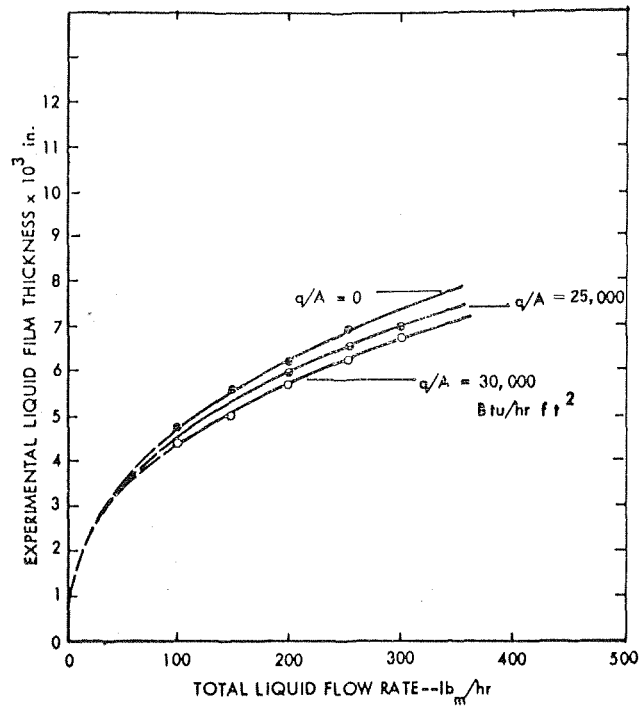

Fig. 9 A comparison of the liquid film thickness with the liquid flow rate—heat transfer as a parameter—steam flow rate 350 lb_m/hr

A similar condition to that described in the previous paragraph was noted by Chien and Ibele [17] in their experimental pressure-drop measurements. In their case a sharp discontinuity occurred in the static pressure gradient curve. This was attributed to a change in flow pattern from annular-mist flow to mist flow. Hewitt and Lacey [18] have also observed the breakup of a continuous water film into the form of rivulets in their recent studies.

In the development of the liquid film thickness equation, an assumption concerning the relative magnitudes of the interfacial shear and wall shear was made, i.e., $\tau_{il} = \tau_{wl}$. Although this approximation is erroneous for larger film flow rates, the effect on the resultant film thickness equations is less serious since the constant and exponents were determined from all of the data. Even for the cases in which τ_{il} was 50 percent greater than τ_{wl}, the correlation equations predicted film thicknesses with no noticeable decrease in accuracy.

The scatter of the film thickness data about the correlating curve is well within the limits of the experimental measurements, the accuracy of which was estimated to be ± 7 ten-thousandths of an inch. As may be noted, the percentage error in the film thickness data is greater for small values of film thickness. This is because the experimental error remained nearly constant for all of the data taken, with only a slight dependency on the magnitude of thickness. A digital program used for curve fitting the film thickness data also computed mean standard deviation values. A comparison of the calculated film thickness values to the experimental film thickness data yielded a mean standard deviation of less than three percent for both the saturated and subcooled injection water cases.

Fig. 9 compares the liquid film thickness with heat transfer as a parameter. As is shown in Fig. 9, for a decrease in heat flux from 30,000 to 25,000 Btu/hr ft², the small decrease in film thickness between $q/A = 30{,}000$ and $q/A = 0$ was halved. During the test runs with a heat flux of 30,000 Btu/hr ft², the difference between the wall temperature and the saturation temperature was near that required for nucleation. With constant heat flux conditions, nucleation can cause "dry-out," resulting in a large increase in the test section wall temperature and possibly physical destruction of the tube. Therefore, heat fluxes greater than 30,000 Btu/hr ft² were not attempted.

A heat flux of 30,000 Btu/hr ft² caused a decrease of approximately 10 percent in the annular water film thickness. This reduction in the film thickness may be attributed to not only the decrease in the water viscosity and surface tension as the correlation equation indicates, but probably also to an increase in the interfacial waviness. This increased disturbance of the vapor-liquid interface may be a result of the decrease in water viscosity and surface tension [15] and the mass transfer occurring at the interface.

Average water film thicknesses measured during the investigation were generally greater than dimensionless y^+ values of 30. Typical y^+ values were about 80. It may therefore be assumed that liquid films extended into the turbulent region. In the turbulent region the convective transfer of energy and momentum is the controlling mechanism. Thus the extension of the annular liquid film into the turbulent region supports and explains the success of various investigators in the correlation of their heat transfer data by single-phase convective heat transfer models.

A comparison of the calculated liquid film flow rates to the total liquid flow rates, with the steam flow rate as a parameter, are shown in Fig. 10. At the lower steam flow rates, below 200 lb_m/hr, the calculated film flow rate is equal to the total liquid flow rate. As the steam flow rate increases, the difference between the total liquid flow rate and the calculated film flow rate ($W_l - W_{lf}$) increases. This difference is the predicted entrained liquid flow rate. Hence the greater the steam flow rate, the greater the entrainment.

However, for low liquid flow rate, $W_l < 100$ lb_m/hr, the calculated film flow rate and total liquid flow rate are again nearly equal. This indicates that the liquid interface was relatively smooth, since entrainment is believed to result from shearing the tips of large waves. Fig. 11 supports this concept. This figure is a picture of an oscilloscope trace for the instantaneous voltage drop across the film thickness measuring probe. This instantaneous voltage drop is a measure of the height of the interface waves. For the same steam flow rate, 400 lb_m/hr, it may be noted from the time traces that the amplitude of the waves decreases as the liquid flow rate decreases. At a liquid flow rate of 100 lb_m/hr the time traces are relatively smooth, thus reducing

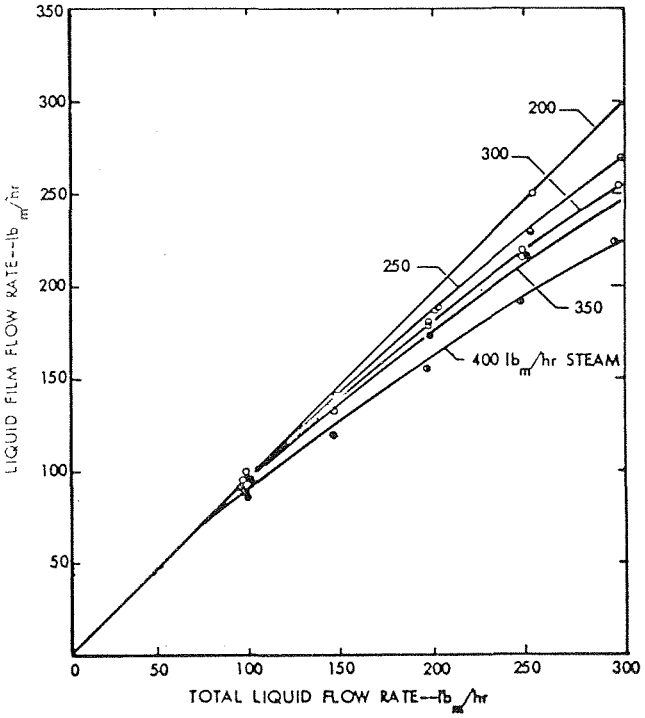

Fig. 10 Liquid flow rate for saturated water injection

Table 1 Droplet size distribution from photographic analysis

STEAM FLOW RATE lb_m/hr	WATER FLOW RATE lb_m/hr	NUMBER OF PHOTOS	TOTAL NO. OF DROPS	DROPS 0-20 μ	DROPS 21-40 μ	DROPS 41-60 μ	DROPS 61-80 μ	DROPS 81-100 μ	DROPS 101-120 μ	MEAN DIA. μ	ROOT MEAN CUBE DIA. μ
300	300	9	70	6	33	19	7	4	1	42	52
300	250	7	97	7	51	27	8	2	2	40	49
300	200	6	43	3	22	11	3	2	2	43	55
300	150	5	33	2	17	7	3	3	1	44	56
300	100	6	27	3	16	7	1	1	0	39	34
TOTALS		33	270	21	139	71	22	11	6		

the opportunity for entrainment.

Droplet Size Distribution. The results of an analysis of a set of photographs taken of the dispersed steam-water droplet mixture flowing vertically upward in the adiabatic tube are shown in Table 1. The sampling represents a total of 44 photographs, of which nine were rejected because of equipment malfunction and two contained no drops sufficiently in focus to be counted.

The Nukiyama-Tanasawa droplet size distribution function that was developed for atomizing fuel sprays, [9], has the form

$$\Delta n/\Delta x = B\bar{x}^2 e^{-b\bar{x}^\delta}$$

where Δn is the fraction of the total number of droplets found in the size interval and $\Delta\bar{x}$ is the size increment, B is a scale constant, b is the size parameter with dimension $\bar{x}^{-\delta}$, and δ is the distribution parameter. By differentiating the expression and setting the result equal to zero, b can be evaluated from the data. Combinations of B and δ were examined and by trial and error were fit to the data with the resulting equation:

$$\Delta n/\Delta\bar{x} = 0.0003\bar{x}^2 e^{-0.08\bar{x}}$$

A plot of this function is shown with the data in Fig. 12. The curve shows good agreement with the data at droplet sizes 30 microns and above. Mismatch at the lower end can be attributed to the different mechanism of droplet formation in an atomizer spray and to the evaporation from the droplet surface for fuels which would produce more droplets in the smallest size increment.

Mean diameters of the droplets were calculated and are shown in Table 1. The mean diameter is the arithmetic mean, while

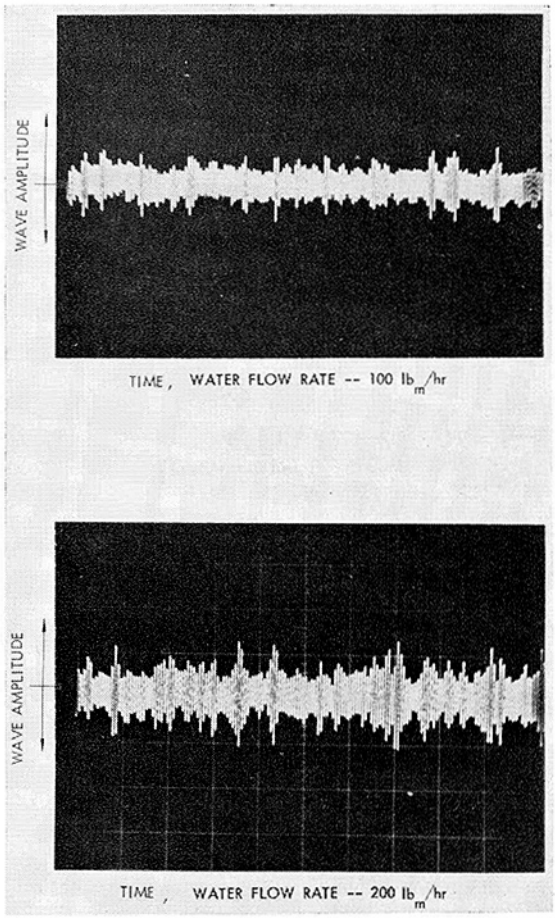

Fig. 11 Variation in film thickness for steam flow rate of 400 lb_m/hr

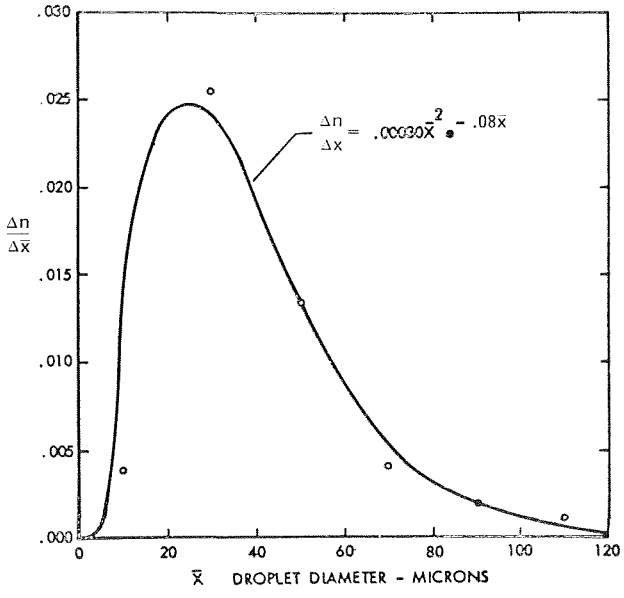

Fig. 12 Droplet size distribution compared to Nukiyama-Tanasawa

the root cube diameter shown was calculated as follows:

$$\bar{x}_{\text{r.m.c.}} = [\Sigma\Delta n_i\bar{x}_i^3]^{1/3}$$

where Δn_i is the fraction of the total number of droplets counted in the ith size interval and $\bar{x}_i$ is the arithmetic mean diameter of the size interval. This value is significant as it is the cube-weighted diameter, proportional to the mass of the droplet, which is of interest in heat transfer. For all liquid-gas flow rates investigated the most probable droplet diameter was 30 microns.

An inspection of the tabulated results shows that there is very

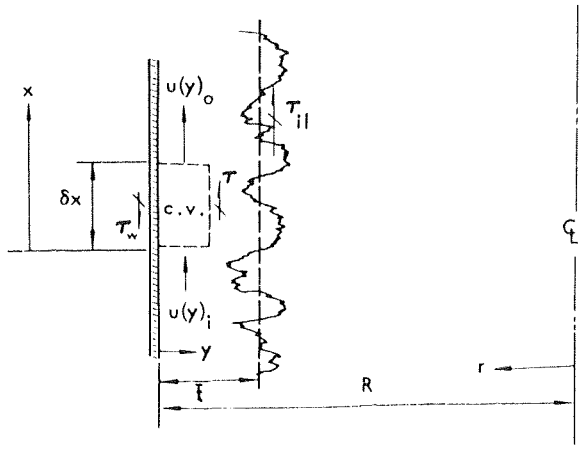

Fig. 13 Liquid film model

little deviation in the mean diameter or in the distribution of droplet sizes for the different flow rates. The exception occurs at the lowest water flow rate, 100 lb mass per hour. At this flow rate the concentration of droplets is very small, and it appears that the deviation in the data is due to an insufficient number of photographs.

Conclusion

The results of this investigation permit the following conclusions to be made about the liquid distribution in annular-mist two-phase flow.

1 The method of liquid injection, as well as the presence of mass transfer, affects the value of the correlation constant. In the case of subcooled injection-caused pressure pulsations, an increased entrained liquid flow rate results.

2 Heat transfer was found to have only a small effect on the liquid film thickness, less than ten percent. When the wall temperature increases to a value which can result in nucleation, the liquid film will be disrupted and "dry-out" can occur. Energy transfer rates of 30,000 Btu/hr ft^2 were found to be near the value of flux required for nucleation.

3 The shear profile developed for the annular liquid film predicts an increased film flow rate for those cases in which the film weight is the same order of magnitude as the wall shear, in comparison to those equations given by Anderson-Mantzouranis or Hewitt [12]. At the larger values of wall shear the proposed film flow rate equations reduce to those suggested by Anderson-Mantzouranis [10].

4 The droplet size distribution for the quality range investigated, 50 to 80 percent, is independent of the quality. The mean droplet diameter is 41 microns with a most probable diameter of 30 microns.

Acknowledgment

This study was carried out under the sponsorship of the Department of Mechanical Engineering, University of Washington, and represents a portion of the Doctoral thesis of J. T. Pogson [19] and the Master of Science thesis of J. H. Roberts [20].

References

1 Davis, E. J., "Heat Transfer to High Quality Steam-Water," Doctoral Dissertation in Chemical Engineering, University of Washington, Seattle, Wash., June 1960.

2 Collier, J. G., and Hewitt, G. F., "Data on the Vertical Flow of Air Water Mixtures in the Annular and Dispersed Flow Regions. Part II: Film Thickness and Entrainment Data and Analysis of Pressure Drop Measurements," *Trans. of the Institute of Chemical Engineers*, Vol. 39, 1961, p. 127.

3 Gill, L. E., and Hewitt, G. F., "Further Data on the Upwards Annular Flow of Air-Water Mixtures," *AERE R 3935*, 1962.

4 Gill, L. E., Hewitt, G. F., and Lacey, P. M. C., "Data on the Upwards Annular Flow of Air-Water Mixtures," *Chemical Engineering Science*, Vol. 20, 1965, pp. 71–88.

5 Hewitt, G. F., King, I., and Lovegrove, P. C., "Hold-up and Pressure Drop Measurements in the Two-Phase Annular Flow of Air-Water Mixtures," *British Chemical Engineering*, May 1963.

6 Gill, L. E., et al., "Sampling Probe Studies of the Gas Core in Annular Two-Phase Flow—I," *Chemical Engineering Science*, Pergamon Press, Vol. 18, 1963, pp. 525–535.

7 Gill, L. E., Hewitt, G. F., and Lacey, P. M., "Sampling Probe Studies of the Gas Core in Annular Two-Phase Flow—II," *Chemical Engineering Science*, Pergamon Press, Vol. 19, 1964, pp. 665–682.

8 McManus, H. N., Jr., "Local Liquid Distribution and Pressure Drop in Annular Two-Phase Flow," ASME Paper No. 61-Hyd-20, June 1960.

9 Mugele, R. A., and Evans, H. D., "Droplet Size Distribution in Sprays," *Industrial and Engineering Chemistry*, Vol. 43, No. 6, June 1951, pp. 1317–1324.

10 Anderson, G. H., and Mantzouranis, B. G., "Two-Phase (Gas-Liquid) Flow Phenomena I," *Chemical Engineering Science*, Vol. 12, 1960.

11 Calvert, S., and Williams, B., "Upward Concurrent Annular Flow of Air and Water in Smooth Tubes," AIChE *Journal*, Vol. 1, 1955, p. 78.

12 Hewitt, G. F., "Analysis of Annular Two-Phase Flow: Application of the Dukler Analysis to Vertical Upward Flow in a Tube," AERE-R3680, 1961.

13 Dukler, A. E., "Fluid Mechanics and Heat Transfer in Vertical Falling-Film Systems," *Chemical Engineering Progress Symposium Series*, Vol. 56, No. 30, (Heat Transfer-Storrs), 1960, pp. 1–10.

14 Sleicher, C. A., "Experimental Velocity and Temperature Profiles for Air in Turbulent Pipe Flow," TRANS. ASME, Vol. 80, 1958, p. 693.

15 Ostrach, S., and Koestel, A., "Film Instabilities in Two-Phase Flows," A.I.Ch.E., Preprint No. 45, 6th National Heat Transfer Conference, Aug. 1963.

16 Taylor, N. H., Hewitt, G. F., and Lacey, P. M. C., "The Motion and Frequency of Large Disturbance Waves in Annular Two-Phase Flow of Air-Water Mixtures," *Chemical Engineering Sciences*, Vol. 18, 1963, pp. 537–553.

17 Chien, Sze-Foo, and Ibele, W., "Pressure Drop and Liquid Film Thickness of Two-Phase Annular and Annular-Mist Flows," JOURNAL OF HEAT TRANSFER, TRANS. ASME, Series C, Vol. 86, No. 1, Feb. 1964, p. 89.

18 Hewitt, G. F., and Lacey, P. M. C., "The Breakdown of the Liquid Film in Annular Two-Phase Flow," *International Journal of Heat and Mass Transfer*, Vol. 8, 1965, pp. 781–791.

19 Pogson, J. T., "An Investigation of the Liquid Distribution in Vertical Co-current Two-Phase Annular Mist Flow With Heat Transfer," Doctoral dissertation in Mechanical Engineering, University of Washington, Seattle, Wash., June 1966.

20 Roberts, J. H., "A Photographic Technique to Determine the Droplet Size Distribution in Two-Phase Gas-Liquid Flow," Master of Science thesis, University of Washington, Seattle, Wash., June 1966.

journal of heat transfer

technical briefs

This section consists of contributions of 1500 words or less (about 2 1/2 double-spaced typewritten pages, including figures). Technical Briefs will be reviewed and approved by the specific division's reviewing committee prior to publication. After approval such contributions will be published as soon as possible, normally in the next issue of the Journal.

Minimum Film-Boiling Point for Several Light Hydrocarbons

C. THOMAS SCIANCE[1] and C. PHILLIP COLVER[2]

Nomenclature

g = acceleration
g_c = gravitational constant
q_{min} = minimum film-boiling heat flux
P_r = reduced pressure
ΔT_{min} = minimum film-boiling temperature difference, $T_w - T_{sat}$
λ = heat of vaporization
μ = viscosity
ρ = density
σ = surface tension

Subscripts

f = vapor film; properties evaluated at average between wall and saturation temperature
l = liquid; properties evaluated at saturation temperature
v = vapor; properties evaluated at saturation temperature

THE minimum film-boiling point, sometimes called the second critical point or Leidenfrost point, has been the subject of only a very few experimental studies. Even fewer studies have been conducted over a pressure range, and the results from three Russian studies [4–6][3] appear to be the only data reported at elevated pressures. It is the purpose of this short note to present data for the minimum film-boiling heat flux and the corresponding ΔT_{min} for several pure light hydrocarbons over a wide pressure range. Results are compared with the widely referenced minimum film-boiling correlations of Berenson [1, 2]. This work was part of a larger study of nucleate-boiling heat transfer and burnout [7, 8] and film-boiling heat transfer [7, 9] for methane, ethane, propane, and butane between 1 atm and the critical pressure.

Experimental

The apparatus and general operating procedures have been detailed elsewhere [7–9]. Briefly, boiling took place from a gold-plated, 0.811-in-dia by 4-in-long cylinder, heated electrically and suspended horizontally inside a 1-gal pressure vessel. Minimum film-boiling heat fluxes were determined from electrical current and voltage measurements. Temperature differences at the corresponding minimum heat fluxes were determined as the difference between the heater surface temperatures, as extrapolated from internal heater thermocouple measurements, and the saturated liquid temperature.

A very effective means of obtaining the data was developed. It is well known that in some cases nucleate and film boiling may exist simultaneously, particularly on wires [3]. It was surprising to find that this effect could also be observed on the relatively large-diameter heater used in this work. On several occasions, it was clearly observed in the sight glass that one end of the heater was in film boiling and the other end in nucleate boiling, with an almost perfect demarcation line in the center of the heater. The first time this condition existed it was suspected that the heater was malfunctioning, since temperature measurements located only 0.75 in. on either side of the center of the heater indicated radically different temperatures. It was observed, too, that the same end of the heater almost always dropped into nucleate boiling first.

This last observation provided the means for obtaining accurate minimum film-boiling data. A digital voltmeter was connected to display one of the internal temperatures near the boiling surface on the end of the heater which regularly fell back into the nucleate regime first. As the heater power was decreased in increments, it was observed that that particular internal temperature began decreasing slower and slower as the ΔT_{min} was approached, until a sudden transition to nucleate boiling caused the temperature to drop sharply. This enabled the heater to be stabilized at a heat flux just above the minimum, so that a small decrease in flux would cause a drop into film boiling. This method had the great advantage over other methods tried in that both the heat flux and the ΔT_{min} could be closely approximated.

Results and Discussion

Minimum heat-flux data for the hydrocarbons studied are shown in Figs. 1–4, and represent measurements carried out over the pressure range $0.05 < P_r < 0.8$. Data symbols, connected vertically at a given reduced pressure, represent a single minimum heat-flux measurement. Transition from film boiling to nucleate boiling took place on reducing the heat flux suddenly from the value shown by the upper data symbol to the lower value. Those points representing large flux changes were taken before the technique described above was developed. It is noted that the solid line representing the smoothed data for each substance goes through a maximum somewhere in the pressure range $0.3 < P_r < 0.4$.

The data in Figs. 1–4 are compared with the following equation, originally proposed by Zuber and Tribus [10] and later modified by Berenson [1], to represent the minimum heat flux:

$$q_{min} = 0.09\,\rho_f \lambda_f \left[\frac{g(\rho_l - \rho_v)}{(\rho_l + \rho_v)}\right]^{1/2} \left[\frac{g_c \sigma}{g(\rho_l - \rho_v)}\right]^{1/4} \quad (1)$$

[1] E. I. du Pont de Nemours & Co., Orange, Texas; formerly, School of Chemical Engineering and Materials Science, University of Oklahoma, Norman, Okla.

[2] School of Chemical Engineering and Materials Science, University of Oklahoma, Norman, Okla.

[3] Numbers in brackets designate References at end of Technical Brief.

Contributed by the Heat Transfer Division of THE AMERICAN SOCIETY OF MECHANICAL ENGINEERS. Manuscript received by the Heat Transfer Division, Feb. 2, 1970.

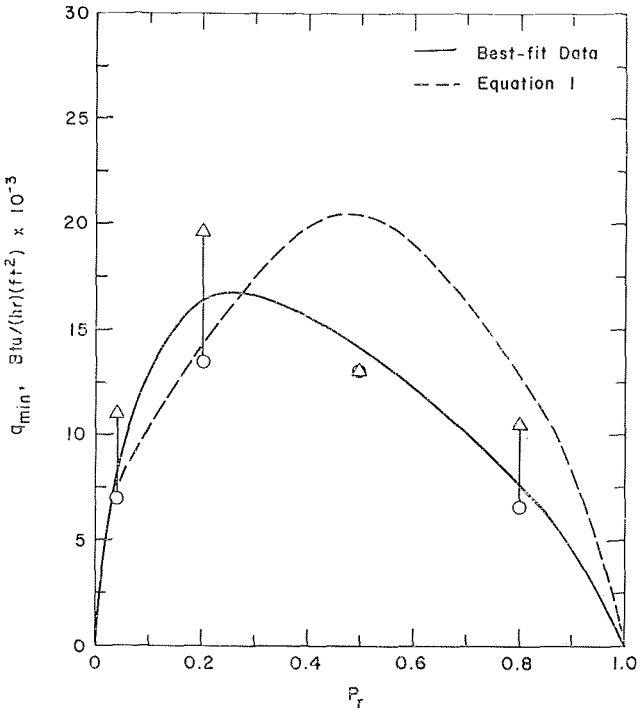

Fig. 1 Methane minimum heat-flux data compared with equation (1)

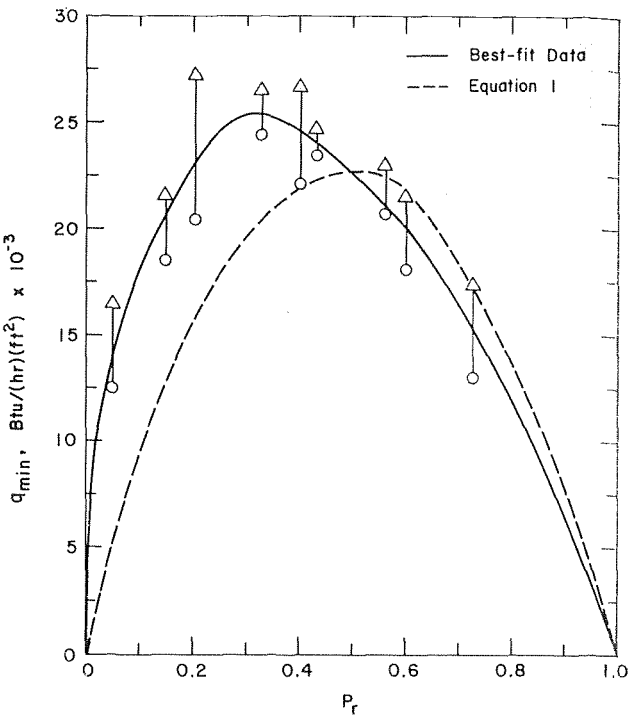

Fig. 3 Propane minimum heat-flux data compared with equation (1)

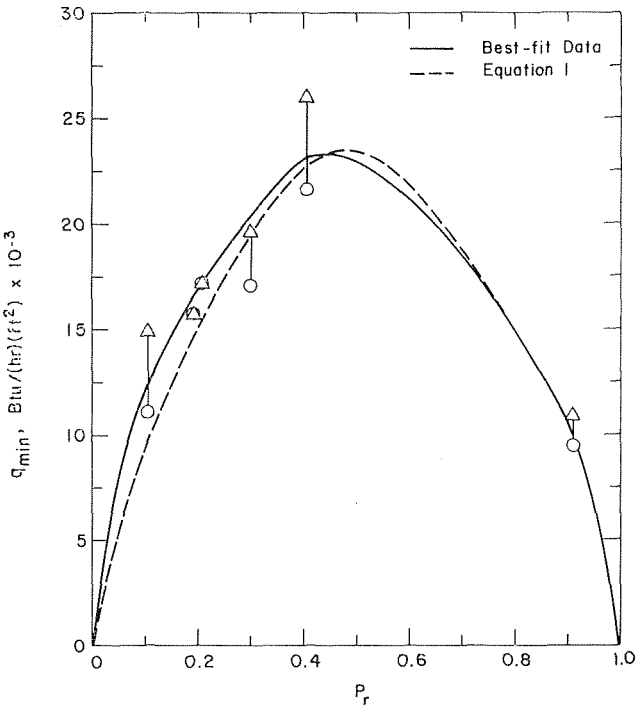

Fig. 2 Ethane minimum heat-flux data compared with equation (1)

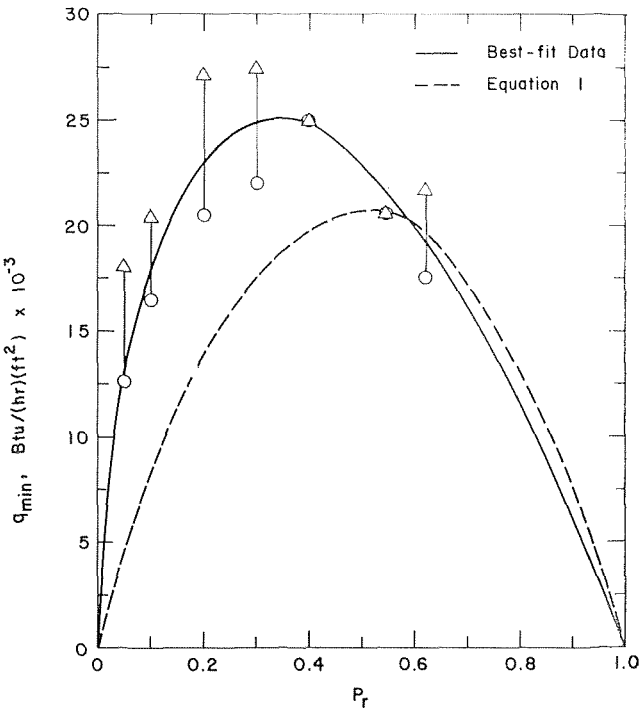

Fig. 4 Butane minimum heat-flux data compared with equation (1)

Good order-of-magnitude agreement is achieved; however, generally the equation underpredicts the data for reduced pressures below 0.4. Aside from the ethane data, where very good agreement is obtained over the full pressure range, the equation overpredicts the data for reduced pressures above 0.5.

Temperature differences at the minimum heat flux, ΔT_{min}, are compared in Fig. 5 with the following equation proposed by Berenson [2]:

$$\Delta T_{\min} = 0.127 \frac{\rho_f \lambda_f}{k_f} \left[\frac{g(\rho_l - \rho_v)}{(\rho_l + \rho_v)}\right]^{2/3} \times \left[\frac{g_c \sigma}{g(\rho_l - \rho_v)}\right]^{1/2} \left[\frac{\mu_f}{g(\rho_l - \rho_v)}\right]^{1/3} \quad (2)$$

Unfortunately only a few values for the ΔT_{min} could be measured; nonetheless, there seems to be order-of-magnitude agreement with

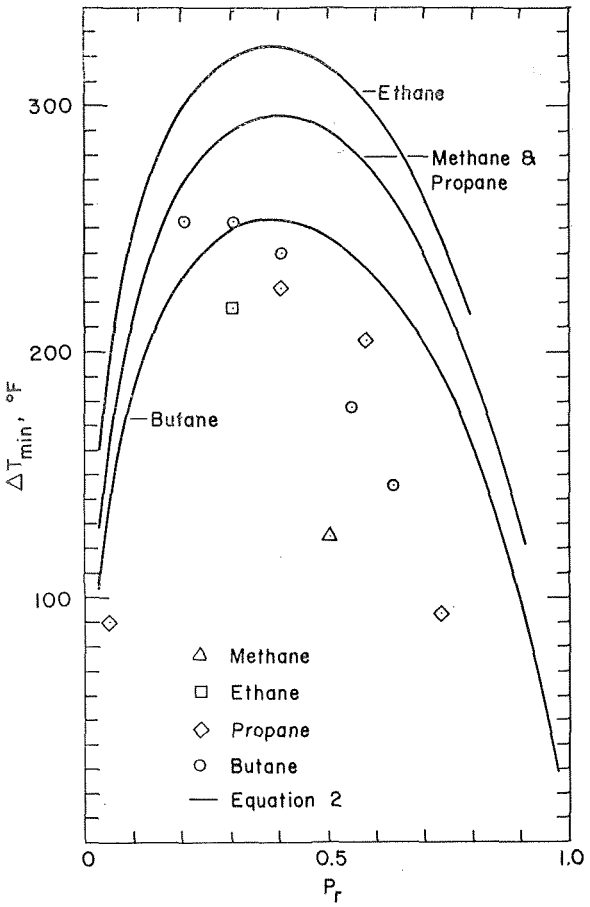

Fig. 5 Minimum temperature difference data compared with equation (2)

equation (2). The predicted ΔT_{min} is too high at high reduced pressures.

References

1 Berenson, P. J., "Transition Boiling Heat Transfer From a Horizontal Surface," M.I.T. Heat Transfer Laboratory Report No. 17, Cambridge, Mass., March 1, 1960.

2 Berenson, P. J., "Film-Boiling Heat Transfer From a Horizontal Surface," JOURNAL OF HEAT TRANSFER, TRANS. ASME, Series C, Vol. 83, No. 3, August 1961, pp. 351–358.

3 Farber, E. A., and Scorah, R. L., "Heat Transfer to Water Boiling Under Pressure," TRANS. ASME, Vol. 70, May 1948, p. 369.

4 Kovalev, "An Investigation of Minimum Heat Fluxes in Pool Boiling of Water," *International Journal of Heat and Mass Transfer*, Vol. 9, 1966, p. 1219.

5 Kutateladze, S. S., ed., "Problems of Heat Transfer During Change of State," Atomic Energy Commission Report No. AEC-TR-3405, May 1962.

6 Morozov, V. G., "An Experimental Investigation of the Cessation of Film Boiling of a Liquid on a Submerged Heating Surface," *Int. Chemical Engineering*, Vol. 3, No. 1, January 1963, pp. 48–51.

7 Sciance, C. T., Colver, C. P., and Sliepcevich, C. M., "Pool Boiling of Methane Between Atmospheric Pressure and the Critical Pressure," *Advances in Cryogenic Engineering*, Plenum Press, New York, Vol. 12, 1967, pp. 395–408.

8 Sciance, C. T., Colver, C. P., and Sliepcevich, C. M., "Nucleate Pool Boiling and Burnout of Liquefied Hydrocarbon Gases," *Chemical Engineering Progress Symposium*, Vol. 63, No. 77, 1967, pp. 109–114.

9 Sciance, C. T., Colver, C. P., and Sliepcevich, C. M., "Film Boiling Measurements and Correlation for Liquefied Hydrocarbon Gases," *Chemical Engineering Progress Symposium*, Vol. 63, No. 77, 1967, pp. 115–119.

10 Zuber, W., and Tribus, M., "Further Remarks on the Stability of Boiling Heat Transfer," UCLA Report No. 58-5, January 1958.

Contribution to the Calculation of Oscillatory Boundary Layers

V. L. SHAH[1]

Nomenclature

U = velocity of oscillation
U_1 = velocity amplitude of oscillation
u = longitudinal velocity component in boundary layer
v = velocity in boundary layer normal to wall
x = coordinate parallel to surface
y = coordinate normal to surface
ω = frequency of imposed oscillation
ψ = stream function
ν = kinematic viscosity
δ_{ac} = ac boundary layer thickness
η = dimensionless distance from surface, equation (5*d*)

Introduction

THE NOTE contains an explicit expression for the third term of the series expansion for the flow field in a boundary layer exposed to an oscillating free stream. The method of solution is that conceived by Schlichting [1].[2]

Prefatory Remarks

Schlichting [1] considered the problem of determining the flow pattern in a boundary layer created by an oscillating free stream of the form

$$\begin{aligned} U(x,t) &= U_1(x)\cos\omega t \\ &= \text{real part of } U_1(x)e^{i\omega t} \end{aligned} \tag{1}$$

He linearized the problem by postulating the following series for the stream function:

$$\psi = \psi_1 + \psi_2 + \psi_3 + \ldots = \sqrt{\frac{2\nu}{\omega}}\, U_1(x) \sum_{n=1}^{n=\infty} \chi_n(\eta,t) \tag{2}$$

Here each one of the additive terms $\psi_1, \psi_2, \ldots, \psi_n$ yields the corresponding velocity components in the usual way. Hence putting

$$u_n = \frac{\partial \psi_n}{\partial y} \text{ and } v_n = -\frac{\partial \psi_n}{\partial x} \tag{3}$$

guarantees that the equation of continuity is satisfied.

Each one of the components u_n satisfies the differential equation of motion with the convective terms assumed known, and computed from a knowledge of the lower-order terms, that is, up to and including u_{n-1}. In his classic paper, Schlichting derived explicit expressions for ψ_1 and ψ_2. These turned out to be

$$\psi_1 = \sqrt{\frac{2\nu}{\omega}}\, U_1(x)\zeta_1(\eta)e^{i\omega t} \tag{4a}$$

and

---

[1] Assistant Professor, Energetics Department, University of Wisconsin, Milwaukee, Wis.; formerly, Research Assistant, Division of Engineering, Brown University, Providence, R. I.

[2] Numbers in brackets designate References at end of Technical Brief.

Contributed by the Heat Transfer Division of THE AMERICAN SOCIETY OF MECHANICAL ENGINEERS. Manuscript received by the Heat Transfer Division, July 23, 1970.

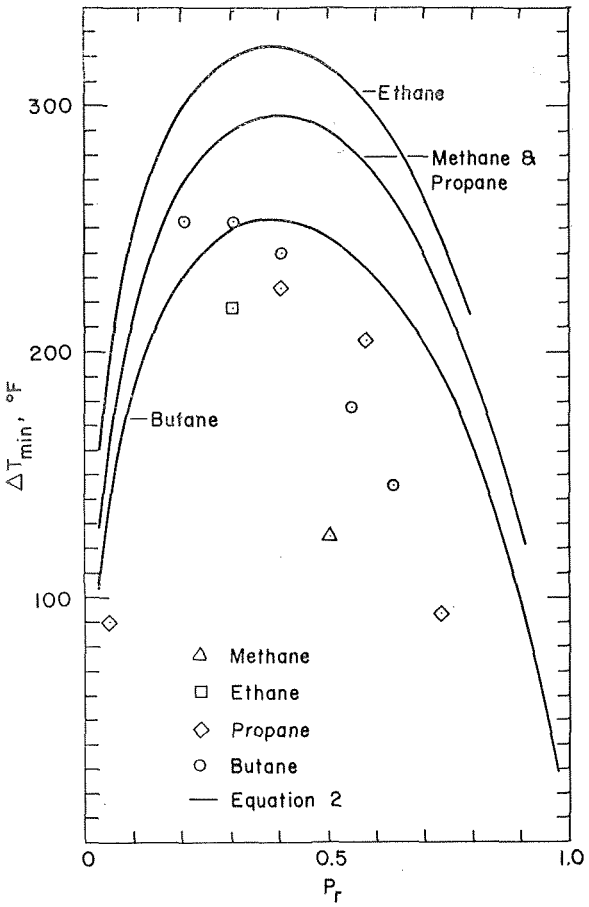

Fig. 5 Minimum temperature difference data compared with equation (2)

equation (2). The predicted ΔT_{min} is too high at high reduced pressures.

References

1 Berenson, P. J., "Transition Boiling Heat Transfer From a Horizontal Surface," M.I.T. Heat Transfer Laboratory Report No. 17, Cambridge, Mass., March 1, 1960.

2 Berenson, P. J., "Film-Boiling Heat Transfer From a Horizontal Surface," JOURNAL OF HEAT TRANSFER, TRANS. ASME, Series C, Vol. 83, No. 3, August 1961, pp. 351–358.

3 Farber, E. A., and Scorah, R. L., "Heat Transfer to Water Boiling Under Pressure," TRANS. ASME, Vol. 70, May 1948, p. 369.

4 Kovalev, "An Investigation of Minimum Heat Fluxes in Pool Boiling of Water," *International Journal of Heat and Mass Transfer*, Vol. 9, 1966, p. 1219.

5 Kutateladze, S. S., ed., "Problems of Heat Transfer During Change of State," Atomic Energy Commission Report No. AEC-TR-3405, May 1962.

6 Morozov, V. G., "An Experimental Investigation of the Cessation of Film Boiling of a Liquid on a Submerged Heating Surface," *Int. Chemical Engineering*, Vol. 3, No. 1, January 1963, pp. 48–51.

7 Sciance, C. T., Colver, C. P., and Sliepcevich, C. M., "Pool Boiling of Methane Between Atmospheric Pressure and the Critical Pressure," *Advances in Cryogenic Engineering*, Plenum Press, New York, Vol. 12, 1967, pp. 395–408.

8 Sciance, C. T., Colver, C. P., and Sliepcevich, C. M., "Nucleate Pool Boiling and Burnout of Liquefied Hydrocarbon Gases," *Chemical Engineering Progress Symposium*, Vol. 63, No. 77, 1967, pp. 109–114.

9 Sciance, C. T., Colver, C. P., and Sliepcevich, C. M., "Film Boiling Measurements and Correlation for Liquefied Hydrocarbon Gases," *Chemical Engineering Progress Symposium*, Vol. 63, No. 77, 1967, pp. 115–119.

10 Zuber, W., and Tribus, M., "Further Remarks on the Stability of Boiling Heat Transfer," UCLA Report No. 58-5, January 1958.

Contribution to the Calculation of Oscillatory Boundary Layers

V. L. SHAH[1]

Nomenclature

U = velocity of oscillation
U_1 = velocity amplitude of oscillation
u = longitudinal velocity component in boundary layer
v = velocity in boundary layer normal to wall
x = coordinate parallel to surface
y = coordinate normal to surface
ω = frequency of imposed oscillation
ψ = stream function
ν = kinematic viscosity
δ_{ac} = ac boundary layer thickness
η = dimensionless distance from surface, equation (5*d*)

Introduction

THE NOTE contains an explicit expression for the third term of the series expansion for the flow field in a boundary layer exposed to an oscillating free stream. The method of solution is that conceived by Schlichting [1].[2]

Prefatory Remarks

Schlichting [1] considered the problem of determining the flow pattern in a boundary layer created by an oscillating free stream of the form

$$U(x,t) = U_1(x)\cos\omega t = \text{real part of } U_1(x)e^{i\omega t} \tag{1}$$

He linearized the problem by postulating the following series for the stream function:

$$\psi = \psi_1 + \psi_2 + \psi_3 + \ldots = \sqrt{\frac{2\nu}{\omega}}\,U_1(x)\sum_{n=1}^{n=\infty}\chi_n(\eta,t) \tag{2}$$

Here each one of the additive terms $\psi_1, \psi_2, \ldots, \psi_n$ yields the corresponding velocity components in the usual way. Hence putting

$$u_n = \frac{\partial\psi_n}{\partial y} \text{ and } v_n = -\frac{\partial\psi_n}{\partial x} \tag{3}$$

guarantees that the equation of continuity is satisfied.

Each one of the components u_n satisfies the differential equation of motion with the convective terms assumed known, and computed from a knowledge of the lower-order terms, that is, up to and including u_{n-1}. In his classic paper, Schlichting derived explicit expressions for ψ_1 and ψ_2. These turned out to be

$$\psi_1 = \sqrt{\frac{2\nu}{\omega}}\,U_1(x)\zeta_1(\eta)e^{i\omega t} \tag{4a}$$

and

---

[1] Assistant Professor, Energetics Department, University of Wisconsin, Milwaukee, Wis.; formerly, Research Assistant, Division of Engineering, Brown University, Providence, R. I.

[2] Numbers in brackets designate References at end of Technical Brief.

Contributed by the Heat Transfer Division of THE AMERICAN SOCIETY OF MECHANICAL ENGINEERS. Manuscript received by the Heat Transfer Division, July 23, 1970.

$$\psi_2 = \sqrt{\frac{2\nu}{\omega}}\,\frac{U_1}{\omega}\,\frac{dU_1}{dx}\,[\zeta_{2a}(\eta)e^{2i\omega t} + \zeta_{2b}(\eta)] \tag{4b}$$

where

$$\zeta_1 = -\frac{1-i}{2} + \eta + \frac{1-i}{2}\,e^{-(1+i)\eta} \tag{5a}$$

$$\zeta_{2a} = \frac{1+i}{4\sqrt{2}}\,e^{-\sqrt{2}(1+i)\eta} + \frac{i}{2}\,\eta e^{-(1+i)\eta} - \frac{1+i}{4\sqrt{2}} \tag{5b}$$

$$\zeta_{2b} = -\frac{1}{8}\,e^{-2\eta} - \frac{3}{2}\,e^{-\eta}\cos\eta - e^{-\eta}\sin\eta - \frac{\eta}{2}\,e^{-\eta}\sin\eta - \frac{3}{4}\,\eta + \frac{13}{8} \tag{5c}$$

and[3]

$$\eta = y\left(\frac{\omega}{2\nu}\right)^{1/2} \tag{5d}$$

It turns out that an explicit expression can also be obtained for ψ_3.

Equations

The differential equation for the third term is

$$\frac{\partial u_3}{\partial t} - \nu\,\frac{\partial^2 u_3}{\partial y^2} = -u_1\,\frac{\partial u_2}{\partial x} - u_2\,\frac{\partial u_1}{\partial x} - v_1\,\frac{\partial u_2}{\partial y} - v_2\,\frac{\partial u_1}{\partial y} \tag{6}$$

with the boundary conditions

$$\left.\begin{aligned} &u_3 = 0;\ v_3 = 0 \text{ at } y = 0\\ &u_3 = 0 \text{ at } y = \infty \end{aligned}\right\} \tag{6a}$$

Kestin, Persen, and Shah [2] have given the general expression for the nth component of the stream function. In the present case we put

$$\psi_3 = \sqrt{\frac{2\nu}{\omega}}\,\frac{U_1^2}{\omega^2}\,\frac{d^2U_1}{dx^2}\,[\zeta_{3a}(\eta)e^{3i\omega t} + \zeta_{3b}(\eta)e^{i\omega t}] + \sqrt{\frac{2\nu}{\omega}}\,\frac{U_1}{\omega^2}\left(\frac{dU_1}{dx}\right)^2[\zeta_{3c}(\eta)e^{3i\omega t} + \zeta_{3d}(\eta)e^{i\omega t}] \tag{7}$$

We can now write down the expressions for the third-order velocity components:

u_3 = real part of

$$\left\{\frac{U_1^2}{\omega^2}\,\frac{d^2U_1}{dx^2}\,[\zeta_{3a}'(\eta)e^{3i\omega t} + \zeta_{3b}'(\eta)e^{i\omega t}] + \frac{U_1}{\omega^2}\left(\frac{dU_1}{dx}\right)^2[\zeta_{3c}'(\eta)e^{3i\omega t} + \zeta_{3d}'(\eta)e^{i\omega t}]\right\} \tag{7a}$$

and

$$v_3 = \text{real part of}\left\{-\sqrt{\frac{2\nu}{\omega}}\left[\frac{U_1^2}{\omega^2}\,\frac{d^3U_1}{dx^3} + \frac{2U_1}{\omega^2}\,\frac{dU_1}{dx}\,\frac{d^2U_1}{dx^2}\right][\zeta_{3a}(\eta)e^{3i\omega t} + \zeta_{3b}(\eta)e^{i\omega t}] - \sqrt{\frac{2\nu}{\omega}}\left[\frac{1}{\omega^2}\left(\frac{dU_1}{dx}\right)^3 + \frac{2U_1}{\omega^2}\,\frac{dU_1}{dx}\,\frac{d^2U_1}{dx^2}\right] \times [\zeta_{3c}(\eta)e^{3i\omega t} + \zeta_{3d}(\eta)e^{i\omega t}]\right\} \tag{7b}$$

[3] Schlichting [1] has used the definition $\eta = y\left(\frac{\omega}{\nu}\right)^{1/2}$ and so the values of ζ_1, ζ_{2a}, and ζ_{2b}, presented here, differ from those of Schlichting by a factor of $\sqrt{2}$.

Substitution of equations (7*a*, *b*) in the left-hand side of equation (6) leads to the following four ordinary differential equations for the auxiliary functions ζ_{3a}, ζ_{3b}, ζ_{3c}, and ζ_{3d}:

$$\zeta_{3a}''' - 6i\zeta_{3a}' = 2\zeta_1'\zeta_{2a}' - 2\zeta_1''\zeta_{2a} \tag{8a}$$

$$\zeta_{3b}''' - 2i\zeta_{3b}' = 2\zeta_1'\zeta_{2b}' - 2\zeta_1''\zeta_{2b} \tag{8b}$$

$$\zeta_{3c}''' - 6i\zeta_{3c}' = 4\zeta_1'\zeta_{2a}' - 2\zeta_1''\zeta_{2a} - 2\zeta_1\zeta_{2a}'' \tag{8c}$$

$$\zeta_{3d}''' - 2i\zeta_{3d}' = 4\zeta_1'\zeta_{2b}' - 2\zeta_1''\zeta_{2b} - 2\zeta_1\zeta_{2b}'' \tag{8d}$$

The boundary conditions are

$$\left.\begin{aligned} &\zeta_{3a} = \zeta_{3a}' = 0;\ \zeta_{3b} = \zeta_{3b}' = 0;\\ &\zeta_{3c} = \zeta_{3c}' = 0;\ \zeta_{3d} = \zeta_{3d}' = 0;\\ &\zeta_{3a}' = \zeta_{3b}' = \zeta_{3c}' = \zeta_{3d}' = 0 \text{ at } \eta = \infty \end{aligned}\right\} \text{ at } \eta = 0 \tag{8e}$$

Here, the prime denotes differentiation with respect to η.

Solutions

Equations (8*a–d*) have been solved for the functions ζ_{3a}, ζ_{3b}, ζ_{3c}, and ζ_{3d}. We obtain

$$\zeta_{3a} = [1-i]\left\{\left(\frac{5}{16\sqrt{3}} + \frac{1+2\sqrt{2}}{16(\sqrt{2}+1)} - \frac{1}{4}\right) - \frac{5}{16\sqrt{3}}\,e^{-\sqrt{3}(1+i)\eta} - \frac{1}{4\sqrt{2}}\,e^{-\sqrt{2}(1+i)\eta} - \frac{1}{8}\left[(1+i)\eta - \left(1+\frac{1}{\sqrt{2}}\right)\right]e^{-(1+i)\eta} + \frac{1-\sqrt{2}}{16(\sqrt{2}+1)}\,e^{-(\sqrt{2}+1)(1+i)\eta} + \frac{1}{8}\,e^{-2(1+i)\eta}\right\} \tag{9a}$$

$$\zeta_{3b} = \left[\frac{1}{8}\,(2-i)\eta^2 - \frac{1}{8}\,(1+2i)\eta + \frac{1}{1200}\,(608-521i)\right]e^{-(1+i)\eta} - \left[\frac{1}{8}\,\eta + \frac{1}{16}\,(5+7i)\right]e^{-(1-i)\eta} - \frac{i}{80}\,e^{-(3+i)\eta} - \frac{1}{48}\,(1-i)\,e^{-2(1+i)\eta} - \left[\frac{1}{20}\,(2+i)\eta + \frac{1}{200}\,(47+96i)\right]e^{-2\eta} - \frac{3}{4}\,i\eta + \frac{1}{600}\,(37+806i) \tag{9b}$$

$$\zeta_{3c} = -\frac{3}{16\sqrt{3}}\,(\sqrt{2}+1)(1-i)e^{-\sqrt{3}(1+i)\eta} - \left[\frac{1}{2}\,\eta - \frac{1+\sqrt{2}}{4\sqrt{2}}\,(1-i)\right]e^{-\sqrt{2}(1+i)\eta} + \left[-\frac{1}{4}\,(1+i)\eta^2 + \frac{1}{4}\,\eta + \frac{1-3\sqrt{2}}{8\sqrt{2}}\,(1-i)\right]e^{-(1+i)\eta} + \frac{3-2\sqrt{2}}{16(\sqrt{2}+1)}\,(1-i)e^{-(\sqrt{2}+1)(1+i)\eta} + \frac{(1-i)}{16\sqrt{6}(\sqrt{2}+1)}\,(12+9\sqrt{2}-7\sqrt{6}+2\sqrt{3}) \tag{9c}$$

and

$$\zeta_{3d} = \left[\frac{i}{12}\,\eta^3 + \frac{1}{16}\,(11+3i)\eta^2 + \frac{1}{16}\,(16-13i)\eta + \frac{1}{800}\,(903-951i)\right]e^{-(1+i)\eta} + \left[-\frac{1}{20}\,(3+4i)\eta\right.$$

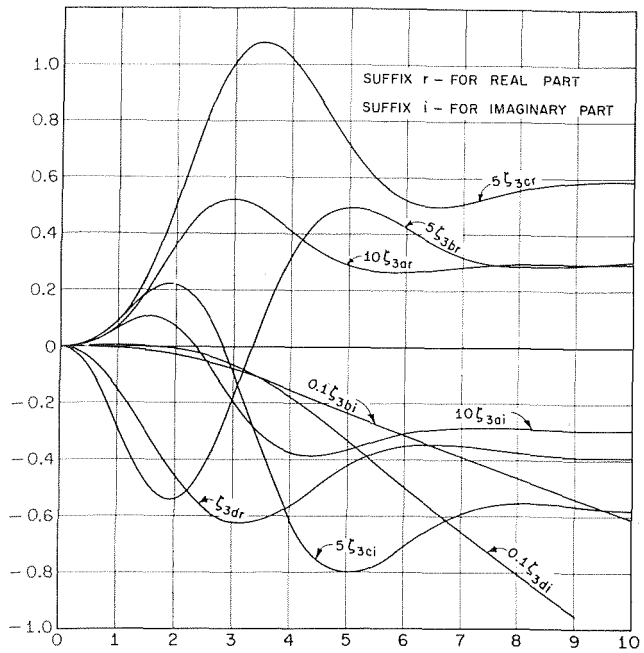

Fig. 1 Functions of the third approximation (stream functions)

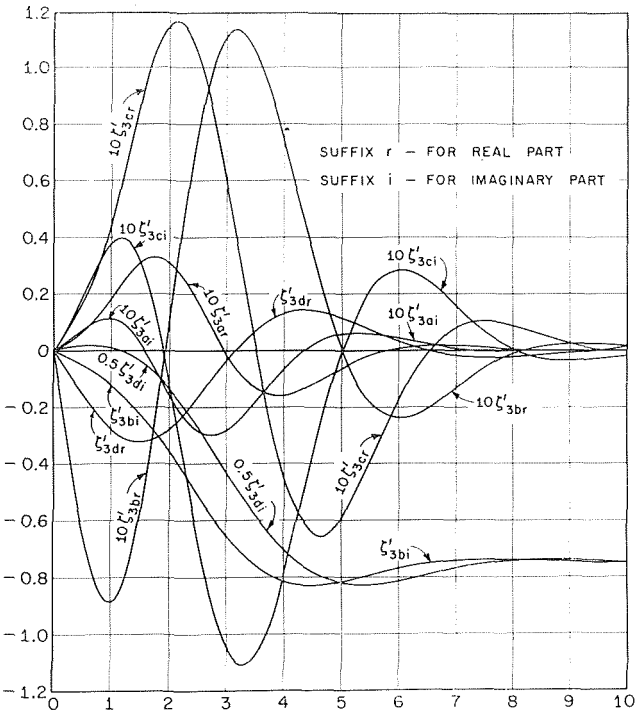

Fig. 2 Functions of the third approximation (longitudinal velocity)

$$+\frac{1}{200}(12-159i)\Big]e^{-2\eta}-\Big[\frac{1}{8}(1-i)\eta^2+\frac{1}{8}(9+2i)\eta+\frac{1}{16}(13+31i)\Big]e^{-(1-i)\eta}+\frac{1}{80}e^{-(3+i)\eta}-\frac{3}{2}i\eta+\frac{1}{800}(-311+3137i) \quad (9d)$$

The functions for the velocity component u_3 are:

$$\zeta_{3a}'=\Big[\frac{1}{4}(1+i)\eta-\frac{2\sqrt{2}+1}{4\sqrt{2}}\Big]e^{-(1+i)\eta}+\frac{5}{8}e^{-\sqrt{3}(1+i)\eta}+\frac{1}{2}e^{-\sqrt{2}(1+i)\eta}+\frac{\sqrt{2}-1}{8}e^{-(\sqrt{2}+1)(1+i)\eta}-\frac{1}{2}e^{-2(1+i)\eta} \quad (10a)$$

$$\zeta_{3b}'=\Big[-\frac{1}{8}(3+i)\eta^2+\frac{1}{8}(3+i)\eta-\frac{1}{1200}(1279+387i)\Big]e^{-(1+i)\eta}+\Big[\frac{1}{8}(1-i)\eta+\frac{1}{8}(5+i)\Big]e^{-(1-i)\eta}-\frac{1}{80}(1-3i)e^{-(3+i)\eta}+\frac{1}{12}e^{-2(1+i)\eta}+\Big[\frac{1}{10}(2+i)\eta+\frac{1}{100}(37+91i)\Big]e^{-2\eta}-\frac{3}{4}i \quad (10b)$$

$$\zeta_{3c}'=\frac{3}{8}(\sqrt{2}+1)e^{-\sqrt{3}(1+i)\eta}+\Big[\frac{1}{2}i\eta^2-\frac{3}{4}(1+i)\eta+\Big(1-\frac{1}{4\sqrt{2}}\Big)\Big]e^{-(1+i)\eta}+\Big[\frac{1}{\sqrt{2}}(1+i)\eta-\Big(1+\frac{1}{\sqrt{2}}\Big)\Big]e^{-\sqrt{2}(1+i)\eta}+\frac{2\sqrt{2}-3}{8}e^{-(\sqrt{2}+1)(1+i)\eta} \quad (10c)$$

and

$$\zeta_{3d}'=\Big[\frac{1}{12}(1-i)\eta^3-\frac{1}{8}(4+5i)\eta^2-\frac{1}{16}(7-3i)\eta-\frac{1}{400}(527+301i)\Big]e^{-(1+i)\eta}+\Big[\frac{1}{10}(3+4i)\eta-\frac{1}{100}(27-139i)\Big]e^{-2\eta}-\frac{1}{80}(3+i)e^{-(3+i)\eta}+\Big[-\frac{1}{4}i\eta^2+\frac{1}{8}(9-5i)\eta+\frac{1}{8}(13+7i)\Big]e^{-(1-i)\eta}-\frac{3}{2}i \quad (10d)$$

Conclusions

The real and imaginary parts of functions of the third approximation are shown plotted in Figs. 1 and 2. The variation in the flow field due to this additional third approximation is shown in Figs. 3*a* and 3*b*.

We can see that the order of magnitude of the third approximations is small in the region within the *ac* boundary layer thickness $\delta_{ac}=\sqrt{2\nu/\omega}(\eta=1)$ of the oscillatory motion but by no means negligible. We can further see that the third approximation is periodic and does not contribute anything to the secondary steady flow.

The availability of the terms ψ_1, ψ_2, and ψ_3 allows us to write down the first four terms of the Fourier series expansions for the velocity components in the form

$$u=\frac{1}{\omega}U_1\frac{dU_1}{dx}\zeta_{2b}'(\eta)+\Big[U_1\zeta_1'(\eta)+\frac{U_1^2}{\omega^2}\frac{d^2U_1}{dx^2}\zeta_{3b}'(\eta)+\frac{U_1}{\omega^2}\Big(\frac{dU_1}{dx}\Big)^2\zeta_{3d}'(\eta)\Big]e^{i\omega t}+\Big[\frac{1}{\omega}U_1\frac{dU_1}{dx}\zeta_{2a}'(\eta)\Big]e^{i2\omega t}+\Big[\frac{U_1^2}{\omega^2}\frac{d^2U_1}{dx^2}\zeta_{3a}'(\eta)+\frac{U_1}{\omega^2}\Big(\frac{dU_1}{dx}\Big)^2\zeta_{3c}'(\eta)\Big]e^{i3\omega t} \quad (11a)$$

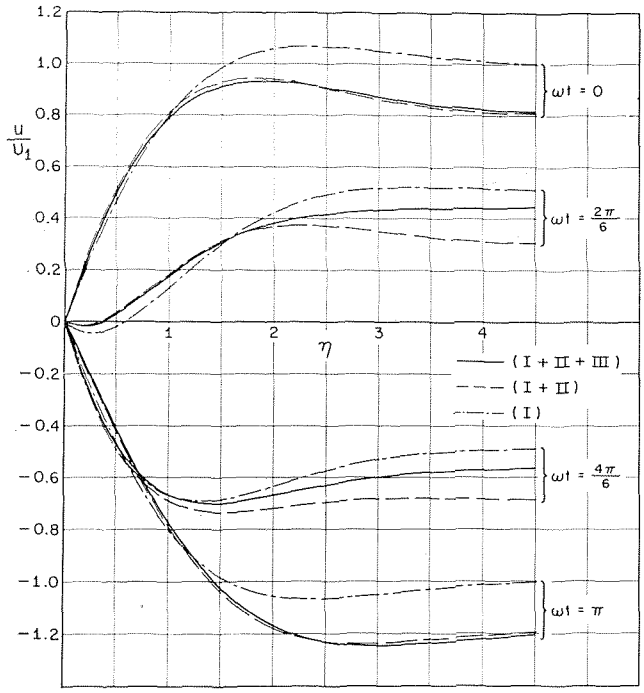

Fig. 3a Transient curve of boundary layer flow with (I), (I + II), and (I + II + III) approximations for $\frac{1}{\omega}\frac{dU_1}{dx} = \frac{1}{4}$ and $\frac{U_1}{\omega^2}\frac{d^2U_1}{dx^2} = \frac{1}{16}$

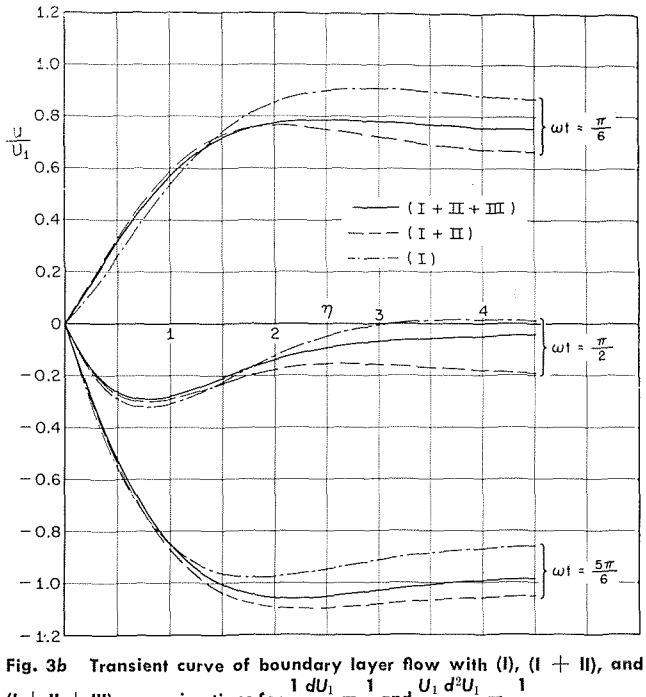

Fig. 3b Transient curve of boundary layer flow with (I), (I + II), and (I + II + III) approximations for $\frac{1}{\omega}\frac{dU_1}{dx} = \frac{1}{4}$ and $\frac{U_1}{\omega^2}\frac{d^2U_1}{dx^2} = \frac{1}{16}$

$$v = -\sqrt{\frac{2\nu}{\omega}}\frac{1}{\omega}\left\{U_1\frac{d^2U_1}{dx^2} + \left(\frac{dU_1}{dx}\right)^2\right\}\zeta_{2b}(\eta)$$
$$-\left[\sqrt{\frac{2\nu}{\omega}}\frac{dU_1}{dx}\zeta_1(\eta) + \sqrt{\frac{2\nu}{\omega}}\left\{\frac{U_1^2}{\omega^2}\frac{d^3U_1}{dx^3} + \frac{2U_1}{\omega^2}\frac{dU_1}{dx}\frac{d^2U_1}{dx^2}\right\}\right.$$
$$\left.\times\,\zeta_{3b}(\eta) + \sqrt{\frac{2\nu}{\omega}}\left\{\frac{1}{\omega^2}\left(\frac{dU_1}{dx}\right)^3 + \frac{2U_1}{\omega^2}\frac{dU_1}{dx}\frac{d^2U_1}{dx^2}\right\}\zeta_{3d}(\eta)\right]e^{i\omega t}$$
$$-\left[\sqrt{\frac{2\nu}{\omega}}\frac{1}{\omega}\left\{U_1\frac{d^2U_1}{dx^2} + \left(\frac{dU_1}{dx}\right)^2\right\}\zeta_{2a}(\eta)\right]e^{i2\omega t}$$
$$-\left[\sqrt{\frac{2\nu}{\omega}}\left\{\frac{U_1^2}{\omega^2}\frac{d^3U_1}{dx^3} + \frac{2U_1}{\omega^2}\frac{dU_1}{dx}\frac{d^2U_1}{dx^2}\right\}\zeta_{3a}(\eta)\right.$$
$$\left.+\sqrt{\frac{2\nu}{\omega}}\left\{\frac{1}{\omega^2}\left(\frac{dU_1}{dx}\right)^3 + \frac{2U_1}{\omega^2}\frac{dU_1}{dx}\frac{d^2U_1}{dx^2}\right\}\zeta_{3c}(\eta)\right]e^{i3\omega t} \quad (11b)$$

Acknowledgments

The author wishes to thank Prof J. Kestin, Division of Engineering, Brown University, for his guidance and encouragement. The work was performed with the financial assistance of the Aeronautical Research Laboratory of Scientific Research, U. S. Air Force, Contract AF 33(616-7749), under the technical supervision of Dr. M. Scherberg. Dr. R. DiPippo prepared the computer program for all functions.

References

1 Schlichting, H., "Berechnung ebener periodischer Grenzschichtstroemungen," *Physik. Zeitschr.*, Vol. 33, 1932, p. 327.

2 Kestin, J., Persen, L. N., and Shah, V. L., "The Transfer of Heat Across a Two-Dimensional, Oscillating Boundary Layer," *Zeitschrift für Flugwissenschaften*, H. Schlichting 60th Anniversary Volume, 1967.